Diffuse Radio Recombination Line Emission on the Galactic plane

A thesis submitted to The University of Manchester for the degree of
Doctor of Philosophy
in the Faculty of Engineering and Physical Sciences

2011

Marta Isabel Rocha Alves

School of Physics and Astronomy

Contents

Word count: $\sim 40,000$

List of Figures

List of Tables

List of Acronyms

Below is a list of acronyms used throughout this thesis:

AIPS Astronomical Image Processing System

ATCA Australia Telescope Compact Array

BGs Big Grains

CHVC Compact High Velocity Clouds

CMB Cosmic Microwave Background

COBE Cosmic Background Explorer

DASI Degree Angular Scale Interferometer

DIRBE Diffuse Infrared Background Experiment

DMR Differential Microwave Radiometer

ELD Extended Low-Density

EM Emission Measure

FIRAS Far Infra-Red Absolute Spectrometer

FWHM Full Width Half Maximum

HIPASS H Parkes All-Sky Survey

HVC High Velocity Cloud

IDL Iterative Data Language

ILC Internal Linear Combination

IRAS *Infrared Astronomical Satellite*

IRIS Improved Reprocessing of the IRAS Survey

ISM Interstellar Medium

ISRF Interstellar Radiation Field

LSR Local Standard of Rest

LSRK Kinematic Local Standard of Rest

LTE Local Thermodynamic Equilibrium

MEM Maximum Entropy Model

NRAO National Radio Astronomy Observatory

NVSS NRAO VLA Sky Survey

PAH Polycyclic Aromatic Hydrocarbons

PDR Photodissociation Region

rms Root Mean Square

RRL Radio Recombination Line

SHASSA Southern H Alpha All-Sky Survey

SNR Supernova Remnant

SZ Sunyaev-Zeldovich

UC Ultracompact

UV Ultraviolet

VGPS VLA Galactic Plane Survey

VLA Very Large Array

VLSS VLA Low-Frequency Sky Survey

VSGs Very Small Grains

WHAM Wisconsin H Alpha Mapper

WIM Warm Ionised Medium

WMAP *Wilkinson Microwave Anisotropy Probe*

ZOA Zone Of Avoidance

The University of Manchester

ABSTRACT OF THESIS submitted by Marta Isabel Rocha Alves
for the Degree of Doctor of Philosophy and entitled
Diffuse Radio Recombination Line Emission on the Galactic plane. March 2011

A full-sky free-free template is increasingly important for the high-sensitivity Cosmic Microwave Background (CMB) experiments, such as *Planck*. On the Galactic plane, where free-free estimations from Hα measurements become unreliable, Radio Recombination Lines (RRLs) can be used to determine the thermal brightness temperature unambiguously with no dust contamination. RRLs are a powerful tool for the diagnostic of the interstellar medium, tracing the ionised component, its electron temperature, velocity and radial distributions.

This thesis describes the investigation of the ionised emission from H regions and diffuse gas along the Galactic plane using RRLs, with the aim of providing a map of the free-free emission to complement the high latitude Hα observations. Measuring the free-free emission on the Galactic plane is of great importance to understand and characterise other Galactic emission components: synchrotron, anomalous dust and thermal dust emission.

The fully-sampled H Parkes All-Sky Survey and associated deep Zone of Avoidance Survey are re-analysed to recover extended RRL emission. They include three RRLs (H166α, H167α and H168α) at frequencies near 1.4 GHz. A data cube covering $\ell = 20^\circ$ to 44° and $|b| \leq 4^\circ$ is constructed of RRL spectra with velocity and spatial resolution of 20 km s^{-1} and 14.8 arcmin, respectively. Well-known H regions are identified as well as the diffuse RRL emission on the Galactic plane.

In order to convert the integrated RRL emission into a free-free brightness temperature a value of the electron temperature (T_e) of the ionised gas is needed. Using the continuum and line data from the present survey, the variation of T_e with Galactocen-

tric radius was derived for the longitude range $\ell = 20^\circ$ to 44°, with a mean T_e on the Galactic plane of 6000 K. The derived T_e variation was used to obtain the first direct measure of the free-free brightness in this region of the Galactic plane. Subtraction of this thermal emission from the total continuum at 1.4 GHz leaves the first direct measurement of the synchrotron emission. A narrow component of width 2° is identified in the synchrotron latitude distribution. Determining the free-free and synchrotron emission in this region of the Galactic plane identifies the anomalous microwave component, when combined with *WMAP* and *IRIS* data. The results are in agreement with models of small spinning dust grains.

Declaration

I declare that no portion of the work referred to in the thesis has been submitted in support of an application for another degree or qualification of this or any other university or other institute of learning.

Copyright Statement

(i) The author of this thesis (including any appendices and/or schedules to this thesis) owns any copyright in it (the "Copyright") and s/he has given The University of Manchester the right to use such Copyright for any administrative, promotional, educational and/or teaching purposes.

(ii) Copies of this thesis, either in full or in extracts, may be made **only** in accordance with the regulations of the John Rylands University Library of Manchester. Details of these regulations may be obtained from the Librarian. This page must form part of any such copies made.

(iii) The ownership of any patents, designs, trade marks and any and all other intellectual property rights except for the Copyright (the "Intellectual Property Rights") and any reproductions of copyright works, for example graphs and tables ("Reproductions"), which may be described in this thesis, may not be owned by the author and may be owned by third parties. Such Intellectual Property Rights and Reproductions cannot and must not be made available for use without the prior written permission of the owner(s) of the relevant Intellectual Property Rights and/or Reproductions.

(iv) Further information on the conditions under which disclosure, publication and commercialisation of this thesis, the Copyright and any Intellectual Property and/or Reproductions described in it may take place is available in the University IP Policy (see http://www.campus.manchester.ac.uk/medialibrary/policies/intellectual-property.pdf), in any relevant Thesis restriction declarations deposited in the University Library, The University Librarys regulations (see http://www.manchester.ac.uk/library/aboutus/ regulations) and in The Universitys policy on presentation of Theses.

Dedication

Para a minha família. Pai, mãe, irmã, cunhado, e por último mas não menos importante, namorado.

Acknowledgements

First of all I want thank the three most important people that guided me through my work: Professor Richard Davis, who was always there since the very beginning; Professor Rod Davies, for his never ending knowledge and indescribable help; Dr. Clive Dickinson, who always had time and solutions for all my questions. With them and at JBCA I had the best possible introduction to radio astronomy. I also want to thank Professor Lister Staveley-Smith, who hosted me for three lovely periods at the International Centre for Radio Astronomy Research where I have always made major progress on my work. These visits to Perth would not have been so profitable without the help of Dr. Mark Calabretta, for his detailed knowledge of the observing system and reduction software.

Secondly, I want to thank all the people I have met at JBCA that helped me to survive the PhD and mancunian life. I start with Ana Cabral, the best friend I have had for the last few years who was always there to help me in every possible way. Thank you Claire, Bruno, Czarek, Nicolas, Giampaolo, Cormarc, Matias and Mel for all the good moments, the help, the company. I also want to thank all the lovely people I met outside JBCA that made my life here much better. To Gatty, Ana Silva, Marta, Kate, Mário, Sophia, George and Alexis.

Finally, to my family. Even though they only have a rough idea of what I am doing for a living, they have always supported me. I want to thank my dad, who has been telling me to look ahead and think about my future since my first day at school. My mum, for learning how to skype to talk to me and see me every single day. My sister, for her interest and fascination by what I do and for always being there. My lovely brother-in-law who was always so happy to see me. And to my beloved boyfriend who has been with me ever since we met, through everything. I love you all. Thank you for the never ending love and support.

I acknowledge the Portuguese foundation, Fundação para a Ciência e Tecnologia, for sponsoring my PhD. This thesis was typeset with TEX/LATEX.

The Author

The author obtained a degree (“*Licenciatura*”) in Physics and Applied Mathematics (Astronomy) at the University of Porto, Portugal, graduating in 2007. In September of the same year, being awarded a scholarship by the Fundação para a Ciência e Tecnologia of Portugal, she began studying for a PhD at the Jodrell Bank Centre for Astrophysics, University of Manchester, the results of which are presented in this thesis.

Supporting Publications

Alves M. I. R., Davies R. D., Dickinson C., Davis R. J., Auld R. R., Calabretta M., Staveley-Smith L., *Diffuse Radio Recombination Line emission on the Galactic plane between* $\ell = 36°$ *and* $44°$, 2010, MNRAS, 405, 1654

Alves M. I. R., Davies R. D., Dickinson C., Calabretta M., Davis R. J., Staveley-Smith L., *A definitive derivation of the free-free emission on the Galactic plane between* $\ell = 20°$ *and* $44°$, in prep.

1

Introduction

This Chapter provides the background and introduction to the work in this thesis. Section 1.1 summarises the observations of the Cosmic Microwave Background and explains the relevance of this work in the study and modelling of its Galactic foregrounds. Section 1.2 introduces Radio Recombination Lines (RRLs) and their applications to Galactic astrophysics, in particular to the study of the free-free emission. Finally, Section 1.3 gives the goals and outline of this thesis.

1.1 Observations of the Cosmic Microwave Background

The Cosmic Microwave Background (CMB) radiation was first discovered in 1965 by Penzias & Wilson (Penzias & Wilson 1965), as a temperature excess of 3.5 K in their measurements of the sky background. This is explained in terms of an expanding Universe. The temperature decreases as $T(z) = T_0(1 + z)$, where z is the redshift and T_0 is the temperature at $z = 0$. By the time of recombination, about 400,000 years after the Big Bang or $z \sim 1000$, the Universe had cooled to a temperature of ~3000 K. At this temperature, matter can no longer remain ionised and so the electrons combine with protons to form neutral hydrogen atoms. The CMB is formed at the surface of last scattering at $z \sim 1000$ when the photons last interact with free electrons and the Universe becomes transparent.

The CMB radiation has a spectrum that fits a blackbody curve with great precision, showing that the Universe was in perfect thermal equilibrium when recombination occurred. The Far Infra-Red Absolute Spectrometer (FIRAS) instrument aboard COBE (Cosmic Background Explorer, Smoot et al. 1992), was the first to compare the CMB radiation spectrum to a Planck curve, and found a temperature of 2.725±0.002 K (Mather et al. 1999).

In order for structures to form and evolve to what we see today, there had to be density fluctuations in the Universe at those early stages and thus, those inhomogeneities should be imprinted in the CMB. The first detection of CMB fluctuations was announced by the COBE team. The Differential Microwave Radiometers (DMR) instrument measured a characteristic anisotropy of $\Delta T/T \approx 6 \times 10^{-6}$ in its maps (Smoot et al. 1992), on large angular scales. The CMB temperature fluctuations are studied as a function of angular scale, known as the angular power spectrum. A scalar field on a sphere can be expressed as a series of spherical harmonics,

$$\frac{\Delta T}{T}(\theta, \phi) = \sum_{\ell m} a_{\ell m} Y_{\ell m}(\theta, \phi) \tag{1.1}$$

where θ and ϕ are the usual spherical angles. Each value of ℓ corresponds to a particular size scale of $\simeq 180^\circ/\ell$. For a given ℓ the power is $(2\ell + 1)C_\ell/4\pi$, where $C_\ell = \langle |a_{\ell m}|^2 \rangle$. The CMB angular power spectrum, in temperature TT, is usually given as the power per logarithmic scale defined by

$$\left(\frac{\Delta T}{T}\right)^2_{rms} = \frac{\ell(\ell + 1)C_\ell}{2\pi}. \tag{1.2}$$

$\ell = 0$ corresponds to the mean CMB temperature and $\ell = 1$, the dipole, is dominated by the motion of the Earth relative to the CMB. The polarisation of the microwave radiation is due to the scattering by electrons of the quadrupole $\ell = 2$ component of the CMB anisotropies. The linear polarisation of the CMB is decomposed in two components: a gradient (E) and a curl (B) modes. The E mode was discovered by the Degree Angular Scale Interferometer (DASI, Kovac et al. 2002) with a spectrum consistent with theoretical predictions based on primordial scalar adiabatic fluctuations.

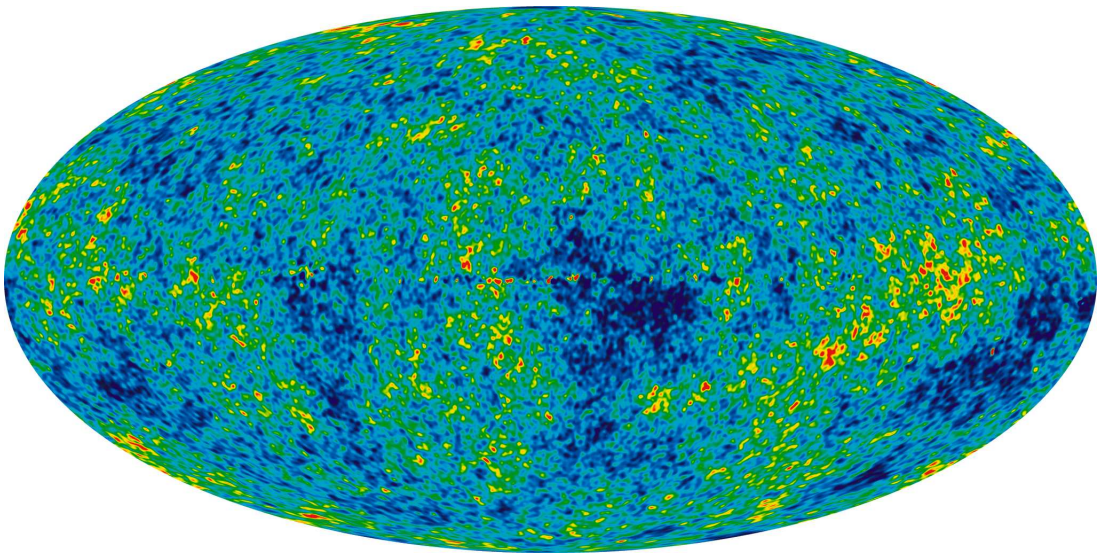

Figure 1.1: The WMAP 7-year Internal Linear Combination (ILC) map of the CMB anisotropies. The linear scale is from -200 to 200 μK. Credit: NASA/WMAP Science Team.

B modes are expected to arise from gravity waves from the time of inflation, therefore their detection would be the next major discovery in cosmology. Their intensity is usually described in the form of a ratio r, the ratio between the tensor and scalar perturbations. The BB mode power spectrum obtained by the *Wilkinson Microwave Anisotropy Probe* (WMAP, Bennett et al. 2003) data is consistent with zero, with an upper limit on r of 0.36 (Larson et al. 2011). The *Planck* satellite should be able to detect a tensor-to-scalar ratio of $\gtrsim 0.1$.

The best current map of the CMB anisotropies is provided by the WMAP satellite after surveying the entire sky for 7 years and its shown in Fig. 1.1. The resulting power spectrum in Fig. 1.2 shows a main peak at $\ell \sim 200$. This corresponds to angular scales of $\vartheta \simeq 180^\circ/200 \simeq 0^\circ.9$, where the CMB anisotropies are seen to dominate in Fig. 1.1. The CMB is a powerful tool in constraining cosmological constants and theories about the evolution of the Universe. The best fit to the CMB power spectra is given by a ΛCDM model (Hinshaw et al. 2009; Reichardt et al. 2009; Brown et al. 2009) of a flat universe dominated by a cosmological constant with adiabatic and nearly scale-invariant Gaussian fluctuations.

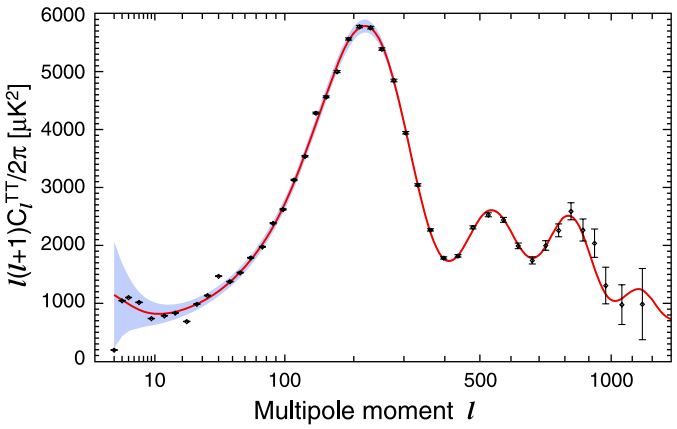

Figure 1.2: The WMAP 7-year power spectrum of the CMB temperature anisotropies. Credit: NASA/WMAP Science Team.

However, measurements of the CMB have to be corrected for foreground emission if the true cosmological information is the be extracted. CMB foregrounds, all the emission between us and the surface of last scattering, are usually categorised as extra-galactic and Galactic foregrounds.

1.1.1 Extra-Galactic CMB foregrounds

Extra-galactic foregrounds to the CMB are separated into point sources and the Sunyaev-Zeldovich effect.

Point sources are a dominant contamination of CMB observations at small angular scales, $\ell \gtrsim 400$. Once they are resolved by the telescope beam they need to be accurately subtracted. At larger angular scales, the background of faint radio sources can also be an important contributor to the measured sky brightness. Radio source counts at mm wavelengths down to the rms in CMB observations (hundreds of mJy) are needed to account for the fluctuations in the number of weak sources. The WMAP survey generated a source catalogue complete to a 1 Jy limit, whereas recent observations by Massardi et al. (2011) using the Australia Telescope Compact Array (ATCA) at 20 GHz detect 5808 extragalactic sources with a flux limit of 40 mJy. At frequencies below $\sim$ 150 – 200 GHz Active Galactic Nuclei dominate the point source population,

whereas at higher frequencies, where dust emission becomes important, dusty galaxies are the main sources (Planck Collaboration et al. 2011c).

The Sunyaev-Zeldovich (SZ) effect (Sunyaev & Zeldovich 1970) is the distortion of the CMB spectrum due to the interaction of the CMB photons with relativistic electrons. The intra-cluster medium of dense clusters of galaxies is highly ionised and has temperatures as high as 10^8 K. The interaction of this gas with the much colder CMB photons is through inverse Compton scattering, which produces a difference in the incoming and scattered radiation, distorting the spectrum. This difference is small, of about 100 – 1000 μK, and is seen as a cool region at frequencies smaller than $\sim$ 220 GHz and a hot region at higher frequencies. At a frequency of about 220 GHz, or $\lambda \sim 1$ mm, the distorted and undistorted spectra have the same intensity. The SZ effect is proportional to the integral $\int n_e T_e dl$ along the line of sight, where n_e and T_e are the electron density and temperature of the intra-cluster gas. A further contribution to the SZ effect, is from the bulk motion of the cluster with respect to the CMB. This is called the kinetic SZ effect, as opposed to the thermal SZ effect described before. The SZ contribution to the CMB fluctuations increases with multipole moment l.

1.1.2 Diffuse Galactic foregrounds

The Galactic foregrounds are the most difficult to account for. They are usually characterised in terms of a temperature spectral index β, $T \propto \nu^\beta$, which can vary with frequency and sky position. Since they originate from different processes in the Galaxy, one needs to map them across the whole sky.

Free-free emission

The free-free radio continuum emission, or thermal bremsstrahlung, arises from the acceleration of unbound charged particles in the ionzed gas and is described by the radiation transfer equation. The interaction between two charged particles involves a change in their direction, meaning acceleration and therefore they radiate. Radiation

in the radio is produced by distant encounters between the particles, where Coulomb forces are small and the particles are considered to continue travelling in a straight line. A full calculation requires a sum over all directions, impact parameters and velocities and it is well described by Oster (1961). Since this is the Galactic emission under study in this thesis, it will be described in more detail in the next Chapter.

The free-free emission is a principal foreground contaminant of the CMB at frequencies between 10 and 100 GHz. It becomes a major component near the Galactic plane where it is produced in the gas layer ionised by radiation from recently formed stars. A true all-sky foreground template needs to include this low Galactic latitude component if the CMB power spectrum is to be correctly evaluated at low values of angular scale ℓ.

The spectral index β of the free-free emission is a slowly varying function of frequency and electron temperature (Bennett et al. 1992; Dickinson et al. 2003). It can lead to significant discrepancies in the predicted radio emission over a wide range of frequencies if not accounted for. With a typical value of 7000 K for the electron temperature of the gas, at 1.4 GHz $\beta \simeq -2.10$ and at 33 GHz $\beta \simeq -2.13$.

Synchrotron emission

Synchrotron emission is the radiation produced when relativistic electrons are accelerated in magnetic fields. Their energy distribution is given by $\mathrm{dN}(E) \propto E^{-p}$, where p is the spectral index (Longair 1994). Diffuse synchrotron emission originates from the interaction of cosmic rays with the Galactic magnetic field, but localised regions of synchrotron emission are also observed. These are mainly Supernova Remnants (SNRs) whose progenitors, Supernovae, are sources of cosmic ray electrons.

The surface brightness I_ν of the synchrotron radiation depends on the energy power spectrum of the electrons and on the magnetic field intensity B as follows:

$$I_\nu \propto B^{(p+1)/2} \nu^{-(p-1)/2} \tag{1.3}$$

(Longair 1994). The power law in the cosmic ray distribution results in a power law in

the synchrotron emission, with a temperature spectral index of $\beta = -(p + 3)/2$. For a typical spectral index p of 2.5, β is -2.75.

The synchrotron emission is linearly polarised on a plane perpendicular to the magnetic field, with a polarisation fraction given by $\Pi = (p + 1)/(p + 7/3)$. For $p = 2.5$, $\Pi = 0.72$ (Longair 1994). However, the measured polarisation of the synchrotron emission is not usually as high as the intrinsic polarisation of 72 per cent. This is due to several factors: the presence of a random component of the magnetic field, different field alignments along the line of sight, depolarisation in the observing beam and Faraday rotation. Faraday rotation is the process by which the polarisation angle of radiation changes when passing through the partially ionised interstellar gas that is permeated by the Galactic magnetic field (Spitzer 1998). The rotation angle θ between the direction of the incident radiation and the magnetic field direction is given by $\lambda^2 R$, where λ is in m and R, the Rotation Measure, is in rad m^{-2}. Faraday rotation increases with decreasing frequency.

The synchrotron emission is well traced at low frequencies and is the dominant CMB foreground for $\nu < 1$ GHz, with a spectral index of $-2.7 > \beta > -3.2$ (Davies et al. 1996). It is stronger on the Galactic plane, with a large contribution from SNRs.

Thermal Vibrational Dust emission

Dust grains in the Galaxy are heated by the interstellar radiation field (ISRF) absorbing ultraviolet and optical radiation which is re-emitted in the infrared via vibration of the grains. The dust population is thought to be composed by Big Grains (BGs), Very Small grains (VSGs) and Polycyclic Aromatic Hydrocarbons (PAHs). These three populations are needed to fit the observed infrared emission (Mathis et al. 1977; Desert et al. 1990; Draine & Li 2001; Zubko et al. 2004).

The BGs, about 1 μm in size, are in equilibrium with the ISRF and therefore a temperature $T_{\rm D}$ is usually defined, associated with a modified blackbody spectrum of the form $I(\nu) \propto B_\nu(T_{\rm D})\nu^\beta$. Schlegel, Finkbeiner, & Davis (1998) use the COBE Diffuse Infrared Background Experiment (DIRBE) data to find dust temperatures in

the range 17 to 21 K, fitting the spectrum for the diffuse interstellar medium (ISM) at high latitude with $\beta = 2$. Recent results from the *Planck* satellite favour a spectral index of $\beta = 1.8$ with a mean temperature $T_{\rm D} = 17.9$ for the local ISM (Planck Collaboration et al. 2011a). The spectrum peaks at around 100 μm and so BGs are the main CMB foreground contributor from 100 GHz to 800 GHz.

Emission from VSGs and PAHs is dominant at even higher frequencies, $\nu > 3000$ GHz. The VSGs spend most of the time at a low temperature, emitting strongly when they absorb one single ultraviolet (UV) photon and are heated temporarily to several hundreds of degrees Kelvin. PAHs, first discovered by Gillett et al. (1973), are a combination of multiple aromatic hydrocarbons and their emission is concentrated in bands, from 3.3 to 11.3 μm.

Anomalous microwave emission

Recent observations have revealed an extra emission component at $10 - 60$ GHz. The first observation of this excess emission was made by Kogut et al. (1996) using COBE data and explained as free-free emission and thermal dust. Subsquent observations by Leitch et al. (1997) ruled out the free-free origin due to the lack of Hα associated with it and showed a correlation between the excess emission at 14.5 GHz and infrared data from the *Infrared Astronomical Satellite* (IRAS) at 100 μm. Possible explanations have been suggested for the origin of this emission (Bennett et al. 2003; Draine & Lazarian 1999; Jones 2009) and the strong candidate is electric dipole emission from spinning dust grains (Draine & Lazarian 1998; Ali-Haïmoud et al. 2009) which is expected to be correlated with far infra-red dust emission.

This electric dipole emission is due to the rapid rotation of VSGs. It is expected to have a steep rise with frequency, $\beta \simeq 3$, peaking at about $20 - 30$ GHz and falling with a cut-off in the grain rotation at $\nu \gtrsim 40$ GHz. Spinning dust models have been successfully used to fit observations both from Galactic objects (Finkbeiner et al. 2002; Watson et al. 2005; Davies et al. 2006; Scaife et al. 2009) and from the external galaxy NGC 6946 (Murphy et al. 2010; Scaife et al. 2010), showing that anomalous emission

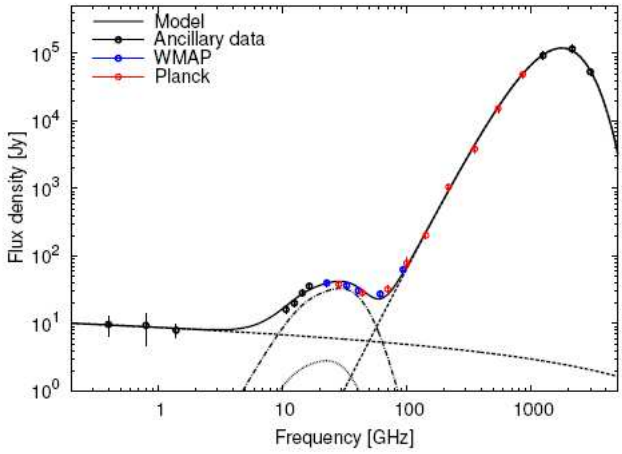

Figure 1.3: Spectrum of G160.26-18.62 in the Perseus molecular cloud, showing the best fit model consisting of free-free, spinning dust and thermal dust emission. The dot-dashed and dotted lines are two components of the spinning dust model (Dickinson et al. 2003).

must be a common mechanism in the ISM. The most precise spinning dust spectra measured to date have been recently obtained with *Planck.* An example, for the Perseus molecular region is given in Fig. 1.3. The higher frequency part of the spinning dust spectrum is clearly measured for the first time, constraining the contributions from the various phases of the ISM (Planck Collaboration et al. 2011d).

1.1.3 Component separation

The determination of the various Galactic foregrounds with higher accuracy is necessary as CMB studies move to higher precision. Foreground component separation is based on template maps, which are maps of Galactic emission at the frequencies where each of the components is known to dominate. From there, a spectral index is derived or assumed to extrapolate the emission to the CMB observing frequencies.

The 408 MHz map from Haslam et al. (1982) is used as the template for synchrotron emission, as it is the only all-sky map with adequate resolution, 51 arcmin, at a sufficiently low frequency. The synchrotron spectral index is known to vary with frequency and sky position and a value of $\beta \sim -3.0$ is usually assumed to extrapolate

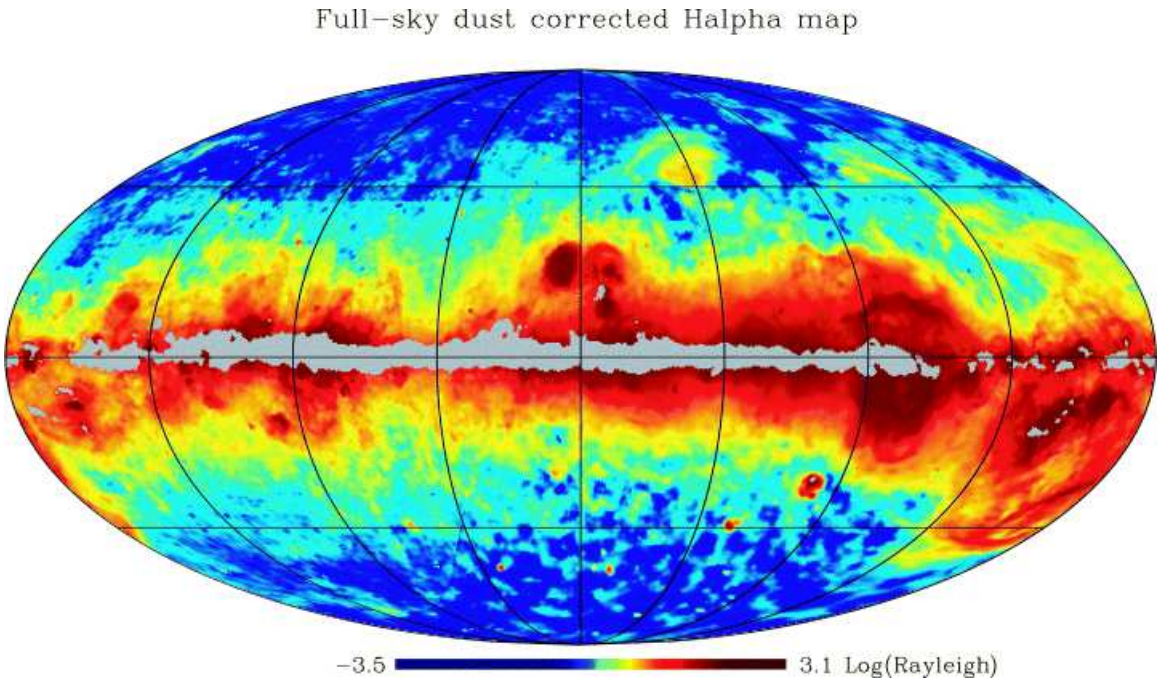

Figure 1.4: Full-sky Hα map corrected for dust absorption, at 1° resolution. Grey regions correspond to absorption greater than 1 magnitude (Dickinson et al. 2003).

the 408 MHz map to frequencies up to 90 GHz.

Thermal dust emission is well traced by the most sensitive full-sky map at 100 μm from *IRAS*, the Infrared Astronomical Satellite, at a resolution of 6 arcmin. Using *IRAS* and COBE data Finkbeiner et al. (1999) derived a two-component model for dust emission from 200 to 2100 GHz that is described by an emissivity spectral index of $\beta = +1.7$ at frequencies below 500 GHz. It takes account of the variation of dust temperature in the sky, by using the 100 μm/240 μm COBE/DIRBE colour ratio. The mean temperature of the low frequency component is 9.4 K. The Finkbeiner et al. (1999) model is commonly used as the template for thermal dust emission.

The free-free template is derived from Hα observations, which trace the same ionised hydrogen gas as the RRLs and the underlying free-free continuum (Chapter 2). A full-sky Hα map can be obtained from the combination of the northern Wisconsin H Alpha Mapper (WHAM, Haffner et al. 2003) and the Southern H Alpha All-Sky Survey (SHASSA, Gaustad et al. 2001) Hα surveys. However, in order to convert the

Hα line intensity into free-free brightness temperature, the absorption by interstellar dust must be taken into account. This correction is significant at intermediate and low latitudes, where the dust concentration is higher. Dickinson et al. (2003) have used the Schlegel, Finkbeiner, & Davis (1998) $D_{\rm T}$ dust map, derived from the *IRAS* and DIRBE 100 μm all-sky surveys for a fixed temperature of 18.2 K, to correct the Hα intensities from the combination of the WHAM and SHASSA surveys. The result is shown in Fig. 1.4. At $|b| \lesssim 5^\circ$ the correction breaks down and accordingly the derived Hα intensity is unreliable. In this region RRLs provide an alternative to the optical Hα recombination line, since their intensity is not affected by the heavy dust absorption along the Galactic plane.

A free-free template that includes the Galactic plane is crucial for CMB observations of the whole sky. It helps to understand the other Galactic foregrounds, the anomalous dust emission and the synchrotron. It is somewhat difficult to observe the anomalous dust emission since its associated continuum emission is mixed in with the synchrotron and the free-free. Even so constraints can be put on the different models for anomalous dust emission. Davies et al. (2006) use the templates described above to derive a spectral index of $\beta = -2.85$ for the favoured spinning dust model of the anomalous dust emission in regions of high Galactic latitude, from 23 to 41 GHz. The relative contribution of the foreground components in such regions is shown in Fig. 1.5. It is seen that the minimum foreground contamination is at $\nu \sim 60$ GHz, where the free-free emission is a major contributor.

1.2 The Galaxy in Recombination Lines

RRLs are used in this work to estimate the free-free CMB foreground on the Galactic plane, where Hα observations are of no use (Chapter 2). In this Section I introduce RRLs and how they are used to observe and study the ionised gas in the Galaxy. I start from H regions which are the strongest free-free emitting sources on the Galactic plane and lead on to the diffuse gas.

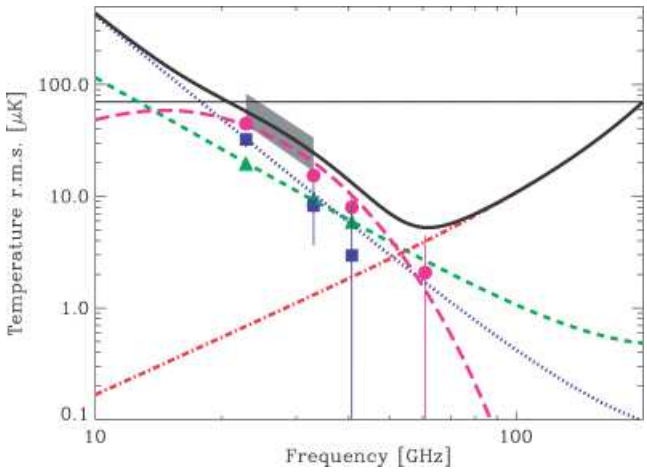

Figure 1.5: Galactic foreground temperature as a function of frequency. Blue represents synchrotron ($\beta = -3.1$); green is the free-free ($\beta = -2.14$); red is the vibrational dust ($\beta = +1.7$) and magenta is spinning dust emission. The thick black line is the combination of all the foregrounds and the thin black line represents the CMB black-body fluctuations (Davies et al. 2006).

1.2.1 Radio Recombination Lines from H regions

The possibility of detecting radio line transitions between highly excited levels of atoms in the ISM was first noted by van de Hulst (1945). However, he overestimated the broadening of the lines, concluding that they would be too weak to be detected. The opposite conclusion was reached by Kardashev (1959), who predicted that excited hydrogen radio lines should be detectable in H regions. This stimulated subsequent experiments and theoretical investigations and the discovery of such lines was reported a few years after (Dravskikh & Dravskikh 1964; Sorochenko & Borozich 1965). The first RRL detection by Sorochenko & Borozich (1965) was towards the Omega nebula, at 8872.5 MHz, the frequency of the hydrogen transition from $n = 91$ to 90.

RRLs have been widely used in astrophysics, especially as probes of the physical conditions of the line emitting plasma and H regions. From the observation of a single transition, the electron temperature can be determined by comparing the energy radiated in the line to that in the underlying free-free continuum. This is one of the most accurate methods to determine the electron temperature (T_e). The central velocity

of the line and its width give information about systematic motions of the gas and turbulence, and can be used to derive the distance and location of the region under study in the Galaxy. By comparing H and He lines, one can investigate the abundance of single ionised helium from interstellar enrichment. Moreover, RRLs trace the sites of current star formation.

The radio recombination line-to-continuum ratio has been used to obtain the variation of T_e with Galactocentric radius (Downes et al. 1980; Shaver et al. 1983; Wink et al. 1983; Paladini et al. 2004). T_e increases with increasing Galactocentric radius due to a gradient of metallic elements in the Galaxy. Metals cool H regions through radiation in spectral lines because they are excited by collisions with free electrons. Thus, higher metallicity H regions are at a lower electron temperature. Since the star formation rate is higher in the inner parts of the Galaxy, the metallicity decreases with Galactocentric radius, meaning that the electron temperature increases. High angular resolution RRL observations have also been used to study T_e variations within H regions. The T_e of an H region depends on the UV field of the ionising star and the distribution of gas around it, which determines the fraction of UV light that escapes the compact region to ionise the surrounding diffuse gas.

H regions are usually classified according to their physical properties. Table 1.1 lists the typical values of the physical parameters of H regions and their classification (Kurtz 2005). Several low angular resolution observations have shown that compact and ultracompact H regions (UCH) are surrounded by low-density ionised gas (Mezger et al. 1967; Koo et al. 1996; Kurtz et al. 1999). The physical relationship between the compact and extended components is still unclear. Two possible explanations are an intrinsically density-structured medium or a dynamical evolution of the ionised gas, or even the combination of the two. The smaller and denser regions are generally still embedded in the natal molecular cloud, thus only observable at infrared and radio frequencies (Wood & Churchwell 1989; Walsh et al. 1998; Hanson et al. 2002).

At the spatial resolution of $\sim$ 15 arcmin of the present study, the free-free emission

Table 1.1: Physical parameters of H regions (Kurtz 2005).

Class of Region	Size (pc)	Density (cm^{-3})	Emis. Meas. ($pc\ cm^{-6}$)	Ionized Mass ($M_\odot$)
Hypercompact	$\lesssim 0.03$	$\gtrsim 10^6$	$\gtrsim 10^{10}$	$\sim 10^{-3}$
Ultracompact	$\lesssim 0.1$	$\gtrsim 10^4$	$\gtrsim 10^7$	$\sim 10^{-2}$
Compact	$\lesssim 0.5$	$\gtrsim 5 \times 10^3$	$\gtrsim 10^7$	~ 1
Classical	~ 10	~ 100	$\sim 10^2$	$\sim 10^5$
Giant	~ 100	~ 30	$\sim 5 \times 10^5$	$10^3 - 10^6$
Supergiant	> 100	~ 10	$\sim 10^5$	$10^6 - 10^8$

is mostly dominated by low density, extended H regions, thus the emission is optically thin at 1.4 GHz (Chapter 2). However, this may not apply to the brightest H regions, that usually have UCH counterparts.

1.2.2 Observations of the Extended Ionised Medium in the Galactic plane

RRLs have been detected not only in individual H regions but also towards positions away from H regions. The first observations of this diffuse ionised gas by Gottesman & Gordon (1970) detected a distinct H157α signal from three directions in the first quadrant of the Galactic plane. In the subsequent years, further observations indicated that the physical conditions of this diffuse RRL emitting gas are the same as expected from extended, low-density H regions rather than from cold (< 800 K), partially ionised gas, as originally suggested by Cesarsky & Cesarsky (1971). Analysis of the H110α line away from discrete H regions by Shaver (1976) gave average electron densities between 5 and 10 cm^{-3}, in agreement with the results from Matthews et al. (1973), that gave $< N_e >= 2$ to 10 cm^{-3} and $< T_e >= 6000 \pm 1000$ K.

Supporting evidence of these results came from locating the diffuse RRL emission in the Galaxy. Observations of the H157α line along the Galactic plane from $\ell = 9°.4$ to $80°.6$ by Gordon & Cato (1972), along with H166α line measurements by Hart & Pedlar (1976) and Lockman (1976) covering the longitude range $358° \leq \ell \leq 50°$, showed

a spatial correlation between the diffuse gas and the discrete H regions. Furthermore, they showed that the diffuse RRL emitting gas is not connected with the HI, suggesting that this emission arises from the vicinity of H regions rather than in a cold, partially ionised component of the ISM.

Mezger (1978) suggested that the 80% of the O stars that Mezger & Smith (1976) found not to be located within H regions could form extended regions of what he called "extended, low-density" (ELD) fully ionised gas. He estimated typical values of 7000 K and 3 cm^{-3} for electron temperature and density, respectively. This was confirmed by H272α line observations by Anantharamaiah (1985a,b) at 325 MHz. These low frequency line measurements showed that the main part of the detected diffuse emission comes from the low-density, outer envelopes of H regions. Fig. 1.6 is a longitude-velocity diagram that illustrates the results, showing that the locations of the discrete H regions (points) are in general the same as those of the ionised diffuse gas (contours and lines). The observations gave electron densities of 1 to 10 cm^{-3}, electron temperatures between 3000 and 8000 K, emission measures in the range 500 to 3000 cm^{-3}pc and sizes of 30 to 300 pc. Heiles, Reach, & Koo (1996b) detected RRL emission from 418 positions along the Galactic plane ($\ell = 0°$ to 60°) and confirmed that emission coming from the extended low-density warm ionised medium (ELDWIM, following Petuchowski & Bennett 1993) located in the Galactic arms has an average T_e of 7000 K and N_e of 5 cm^{-3} and occupies $\sim$ 1% of the volume.

The origin of H regions with low densities and surface brightness is probably the combination of a few possible mechanisms. The expansion of compact H regions can lead to lower electron densities and emission measures (Anantharamaiah 1986; Lockman et al. 1996). The evolution of H regions from the giant molecular clouds by means of stellar winds from the hot star, can disperse the cocoons around it or isolated H regions, leaving UV radiation available to ionise larger areas of the ISM (Churchwell & Walmsley 1975). Cosmic rays from supernovae, originally thought to be the only source of large-scale ionisation (Pikelner 1967; Spitzer & Tomasko 1968; Field et al. 1969; Hjellming et al. 1969), are also a possible contributor.

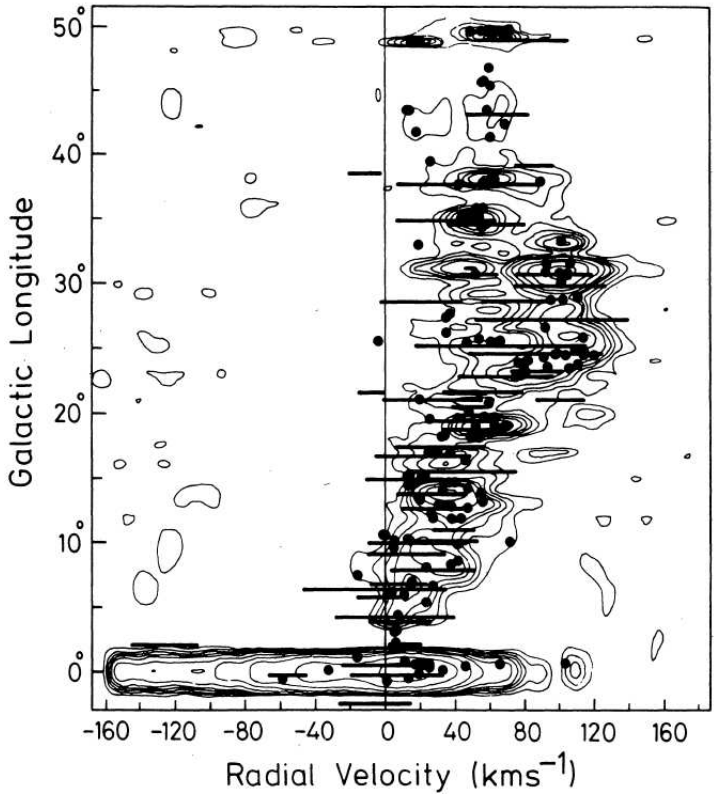

Figure 1.6: Longitude-velocity diagram of the 272α (horizontal lines), H166α (contours) and H110α (points) RRLs. The horizontal lines, that represent the half-power width of the 272α lines and the dots, that locate the H regions observed by Downes et al. (1980), are superposed on the $\ell-$v diagram from Lockman (1976). From Anantharamaiah (1986).

1.2.3 The large-scale ionised gas in the Galaxy

The diffuse ionised gas is only observed in RRLs at low Galactic latitudes, which give a thin layer of diffuse gas with a scale height ranging from 36 pc (Gordon et al. 1972) to 100 pc (Hart & Pedlar 1976; Mezger 1978; Anantharamaiah 1986), whereas the optical recombination line Hα has detected the ionised component up to much higher latitudes. On the plane and in some high latitude regions, such as the Gould's Belt system, strong interstellar absorption makes it difficult to interpret the Hα data.

The WHAM survey, the most sensitive Hα survey to date, reveals that the Hα line detected in nearly all directions of the sky with a pervasive faint background $I_{\mathrm{H}\alpha}$ >

0.1 R (1 R or Rayleigh is defined as $10^6/4\pi$ photons $s^{-1}cm^{-2}sr^{-1} \equiv 2.41 \times 10^7$ erg $s^{-1}cm^{-2}sr^{-1} \equiv 2.25$ $cm^{-6}pc$ for $T_e = 8000$ K). This diffuse ionised gas is thought to extend to heights above the Galactic plane considerably higher than the ionised gas along the plane observed with RRLs. It consists of regions of warm (10^4 K), low-density (0.1 cm^{-3}), nearly fully ionised hydrogen that occupy approximately 20% of the volume within a 2 kpc thick layer about the Galactic midplane (Reynolds 1991; Nordgren et al. 1992; Taylor & Cordes 1993; Haffner et al. 1999). There is a considerable interest in the relationship between the narrow diffuse ionised distribution with a scale height of $z \sim 100$ pc with the thick component with $z \sim 1000$ pc (Gaensler et al. 2008). Issues of concern are the clumpiness (filling factor), the scale height and the electron temperature as well as the transport of ionising radiation from the hot stars in the narrow to the broad distribution.

1.3 Thesis goals

In this Chapter I have discussed the importance of obtaining a full-sky free-free template for CMB foreground subtraction and discuss how RRLs can be used for this purpose. The main goal of this thesis is to provide a map of the free-free emission on the Galactic plane using RRLs to complement the high latitude Hα observations. This map is derived in the present work for the region $\ell = 20°$ to $44°$ and $|b| \leq 4°$, at 1.4 GHz and 14.8 arcmin resolution, using the H Parkes All-Sky Survey (HIPASS) and associated Zone of Avoidance (ZOA) Survey. This is the first fully sampled measurement of the free-free emission along the Galactic plane uncontaminated by synchrotron emission. The fact that line and continuum data are available from the HIPASS/ZOA survey make this a unique dataset for which the electron temperature of the diffuse ionised gas and H regions can be determined as a function of Galactocentric radius. It also allows a synchrotron map to be derived from the difference between the total continuum and the free-free for the first time. The velocity information of the RRLs is used to map the distribution of the diffuse ionised emission in the $\ell - V$ plane and hence a distribution

in the Galactic disk.

The outline of the thesis is as follows: in Chapter 2 I present the theory of radio continuum and line emission from ionised regions. Chapter 3 gives a description of the HIPASS data. Chapter 4 presents the first results from the initial analysis of the datacube centred at $\ell = 40°$, which was a major part of this work. In Chapter 5 the improved RRL data analysis pipeline is introduced along with the final maps of RRL integrated emission for the three zones under study, centred at $\ell = 40°$, $\ell = 32°$ and $\ell = 20°$. It also compares the results from the upgraded pipeline with the initial pipeline used in Chapter 4. The final free-free map is presented in Chapter 6 along with its applications for Galactic and CMB science. Finally, Chapter 7 gives the conclusions of this work and a look towards the future of this project.

2

Radio Continuum and Line Emission from H regions

Radio recombination lines are used to identify H regions because they occur in ionised plasmas, when the electrons combine with protons and become bound. The electron is in a high state of energy and it can immediately jump to a lower level (giving rise to a resonance line) or it can cascade downwards level to level emitting energy in a series of lines, known as recombination lines. Well known hydrogen recombination lines are Hα and Hβ, transitions from principal quantum numbers $n = 3$ to 2 and $n = 4$ to 2, respectively, both in the optical. For higher level transitions, $n \geq 40$, the line will be in the radio domain. At such high energy levels, the radius of the electron's orbit becomes large and thus the electron "sees" the nucleus as a point mass. Therefore, for all atomic species, the recombination line spectrum is hydrogenic, with the frequency of the transitions given by:

$$\nu = Z^2 R_X c \left(\frac{1}{n^2} - \frac{1}{(n + \Delta n)^2} \right) \tag{2.1}$$

where ν is in GHz, Z is the nuclear charge of the ion of species X, R_X is the Rydberg constant for species X and c is the speed of light. R_X is given by $R_X = 10.97373(1 + m_e/M_X)^{-1}$, for a nucleus mass M_X and electron mass m_e. A transition for a given species X from level $n + \Delta n$ to level n is denoted $Xn\Delta n$. $\Delta n = 1$ transitions are called α

Table 2.1: Properties of other atomic species relevant to RRL observations. The velocity offsets from hydrogen are listed in the last column (Roelfsema & Goss 1992).

Species	Mass (amu)	First ionisation potential (eV)	Abundance[a]	$V_X - V_H$ km s^{-1}
H	1.0078	13.6	1	0
He	4.0026	24.6	0.1	122.1
C	12.0000	11.4	3×10^{-4}	149.5
Mg	23.9850	7.6	3×10^{-5}	156.3
Si	27.9769	8.2	3×10^{-5}	157.3
S	37.9721	10.3	2×10^{-5}	158.0
Z [b]	∞			163.2

[a] solar abundance by number, relative to H (Lang 1974)
[b] Z is used for all elements heavier than Sulfur

lines, $\Delta n = 2$ are β lines, $\Delta n = 3$ are γ lines, etc. For example, H166α is the hydrogen transition from level 167 to 166. From equation (2.1) it follows that the separation of the lines of different atomic species are independent of the quantum level n, when expressed in terms of radial velocity. Table 2.1 shows a table of the velocity shifts relative to hydrogen, for a number of ions (from Roelfsema & Goss 1992).

The first detection of helium RRLs, He156α, He158α and He159α, was reported by Lilley et al. (1966b) towards the Omega nebula. A year later, Goldberg & Dupree (1967) identified a line, which had been detected by Palmer et al. (1967) at a frequency slightly higher than the He109α, as radiation coming from the excited carbon C109α line. There are other elements, apart from those in Table 2.1, with an ionisation potential below 13.6 eV, but they are even less abundant than C, Mg, Si and S, thus they are expected to produce very weak RRL emission. Also, the decreasing separation of the lines in velocity space, makes it impossible to distinguish between the lines from different high mass species. Figure 2.1 shows the 168α spectrum of NRAO 608 where the carbon RRL appears to be blended with emission from heavier elements (Onello & Phillips 1995).

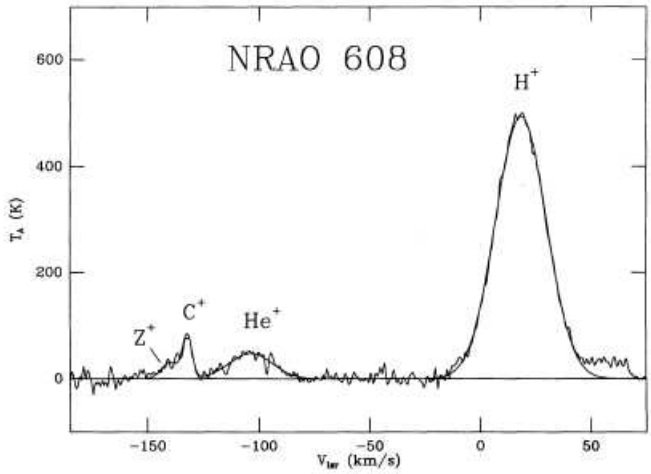

Figure 2.1: 168α recombination line spectrum of NRAO 608 (G48.6+0.0) showing emission from H, He, C and heavier elements (Onello & Phillips 1995).

2.1 Transfer Equation, Continuum radiation and the Hα Line

2.1.1 Transfer equation

In order to quantitatively understand how radiation travels through a medium, we first consider loss and gain mechanisms disregarding the atomic processes. The macroscopic theory that describes the propagation of radiation through a gas cloud is given by the Equation of Transfer:

$$\frac{dI_\nu}{ds} = -\kappa_\nu I_\nu + j_\nu \tag{2.2}$$

which shows that the change in specific intensity I_ν in a slab of material of thickness ds will change along the line of sight if radiation is absorbed or emitted. κ_ν and j_ν, the absorption and emission coefficients, respectively, describe the physical processes occurring in the medium. The optical depth is defined as

$$\tau_\nu(s) = \int_{s_0}^{s} \kappa_\nu ds \tag{2.3}$$

where s is the distance that the radiation travels toward the observer from the most distant part of the cloud, s_0. In Local Thermodynamic Equilibrium (LTE), when the ra-

diation is in equilibrium with its surroundings, the brightness distribution is described by the Planck function, $B_\nu(T_e)$. Hence, when $dI_\nu/ds = 0$

$$I_\nu = B_\nu(T_e) = j_\nu/\kappa_\nu \tag{2.4}$$

where the ratio j_ν/κ_ν is called the "source function", usually symbolised by S. $j_\nu = \kappa_\nu B_\nu(T_e)$ and is called the Kirchhoff's law.

Using equations (2.3) and (2.4) in the integration of the transfer equation (2.2), $I_\nu(s)$ then becomes

$$I_\nu(s) = I_\nu(0)e^{-\tau_\nu(s)} + \int_0^{\tau_\nu(s)} B_\nu(T_e)e^{-\tau}d\tau \tag{2.5}$$

where $I_\nu(0)$ is the background emission being attenuated by the gas cloud. If the medium is isothermal this equation can be computed explicitly, resulting in

$$I_\nu(s) = I_\nu(0)e^{-\tau_\nu(s)} + B_\nu(T_e)(1 - e^{-\tau_\nu(s)}). \tag{2.6}$$

In the radio regime, $h\nu \ll kT$, the Planck function can be approximated by $B_\nu(T_e) = 2kT_e\nu^2/c^2$, the Rayleigh-Jeans approximation. In practice in radio astronomy, the intensity of radiation is measured in units of temperature, the *brightness temperature* T_b. This is the temperature which would result in the given intensity if inserted into the Rayleigh-Jeans law, $I_\nu = 2kT_b/c^2$. Therefore, equation (2.5) can be computed as follows

$$T_b(s) = T_b(0)e^{-\tau_\nu(s)} + T_e(1 - e^{-\tau_\nu(s)}) \tag{2.7}$$

again, for an isothermal medium. This result can be even further simplified if the background radiation is ignored. Two limiting cases are often considered:

optically thin, $\tau \ll 1$,

$$T_b = T_e\tau_\nu \tag{2.8}$$

and optically thick, $\tau \gg 1$,

$$T_b = T_e. \tag{2.9}$$

2.1.2 Continuum Thermal radiation

The continuum radiation underlying RRLs in H regions is the free-free emission, from unbound charged particles. The absorption coefficient for continuum radiation is difficult to calculate, as noted by Oster (1961), who derives an expression valid for the Rayleigh-Jeans domain as follows

$$\kappa_{\rm C} = \left(\frac{N_{\rm e}N_{\rm i}}{\nu^2}\right)\left(\frac{8Z^2e^6}{3\sqrt{3}m^3c}\right)\left(\frac{\pi^{1/2}}{2}\right)\left(\frac{m^{3/2}}{kT}\right) < g > \tag{2.10}$$

where $N_{\rm e}$ and $N_{\rm i}$ are the densities of electrons and ions, respectively. $< g >$ is the velocity-averaged Gaunt factor, that comprises all the terms by which the quantum mechanical expressions differ from the classical ones. The evaluation of the Gaunt factor has been refined over the years. Hummer (1988) gives accurate Gaunt factors (to 0.7 per cent), for a range of frequencies and temperatures.

Altenhoff et al. (1960) suggested a simple approximation for the absorption coefficient, given by

$$\kappa_{\rm C} \approx \frac{0.08235N_{\rm e}N_{\rm i}}{\nu^{2.1}T_{\rm e}^{1.35}} \tag{2.11}$$

where ν is in units of GHz, $N_{\rm e}$ in cm^{-3}, $T_{\rm e}$ in K and $\kappa_{\rm C}$ in pc^{-1}. The error in this approximation is of the order a few per cent at low frequencies, but it increases to $5-20$ per cent for frequencies above 10 GHz.

It is common to use the formalism introduced by Mezger & Henderson (1967), that relates the optical depths derived by Oster (1961) and Altenhoff et al. (1960). They introduce the factor $a(T,\nu)$ as follows

$$a = \frac{\tau_{\rm C}({\rm Oster})}{\tau_{\rm C}({\rm AMWW})} = 0.366\nu_{\rm GHz}^{0.1}T_{\rm e}^{-0.15} \times [\ln(4.995\times10^{-2}\nu_{\rm GHz}^{-1}) + 1.5\ln(T_{\rm e})]. \tag{2.12}$$

This factor can be computed for relevant frequencies and temperatures, it is of the order unity, and is convenient because it produces a simple formula for the free-free optical depth,

$$\tau_{\rm C} = 8.235\times10^{-2}aT_{\rm e}^{-1.35}\nu_{\rm GHz}^{-2.1}({\rm EM}) \tag{2.13}$$

where EM is the emission measure, defined as

$${\rm EM} = \int {\rm N_e(s)N_i(s)ds} = \int \left(\frac{\rm N_e(s)}{\rm cm^{-3}}\right)^2 {\rm d}\left(\frac{\rm s}{\rm pc}\right) \tag{2.14}$$

where it was assumed that $N_i(s) = N_e(s)$, which should be reasonable due to the large abundance of hydrogen and helium.

Finally, following the result in equation (2.8), the free-free continuum brightness temperature in LTE for an optically thin medium can be written as

$$T_C = 8.235 \times 10^{-2} a T_e^{-0.35} \nu_{GHz}^{-2.1} (1 + 0.08)(\mathrm{EM}). \quad (2.15)$$

The factor (1 + 0.08), where 0.08 is a typical value for the ratio $N(He^+)/N(H^+)$, accounts for the contribution from the fraction of helium atoms, all of which are assumed to be singly ionised.

2.1.3 Hα emission from ionised hydrogen

EM is an important quantity to obtain in order to determine the free-free emission via equation (2.15). The same ionised hydrogen that produces the radio continuum also generates Hα emission. Both optical and radio emission are functions of the electron temperature T_e and depend on EM. The intensity of the Hα recombination line depends on whether the emitting medium is optically thin in all lines (case A) or if it is optically thick to the Lyman continuum photons (case B). In H regions and nebulae studied using Hα, it is believed that case B applies (Osterbrock 1989). Based on Hα data from Hummer & Storey (1987), Valls-Gabaud (1998) gives an accurate expression for the Hα intensity in units of erg s^{-1}cm^{-2}sr^{-1}, for case B:

$$I(H\alpha) = 9.41 \times 10^{-8} T_4^{-1.017} 10^{-0.029/T_4} (\mathrm{EM}) \quad (2.16)$$

where T_4 is the electron temperature in units of 10^4 K and EM is in cm^{-6}pc. Using the previous expression for the Hα line intensity along with equation (2.15), Dickinson et al. (2003) obtained the relationship between free-free and Hα emission as follows

$$\frac{T_C}{I_{H\alpha}} = 8.396 \times 10^3 a \nu_{GHz}^{-2.1} T_4^{0.667} 10^{0.029/T_4} (1 + 0.08) \quad (2.17)$$

where T_C is in μK and $I_{H\alpha}$ is in Rayleighs (R). Dickinson et al. (2003) also correct the equation for the Gaunt factor (Oster 1961) in Valls-Gabaud (1998) to explain the

difference between their results on the $T_C/I_{H\alpha}$ relation. Assuming an electron temperature of 7000 K, it follows that the free-free brightness temperature per unit Rayleigh at 1.4 GHz is 3.87 mK.

RRLs are emitted under the same conditions as the optical Hα line, thus provide an independent measure of EM. They will be treated in more detail in the next sections.

2.2 The intensity of radio recombination lines

When line radiation is considered, the macroscopic parameters κ_ν and j_ν presented in Section 2.1.1 must be related to the atomic properties of matter. According to Einstein (1916), there are three different processes occurring in the formation of an atomic spectral line that contribute to the intensity I_ν passing through a slab of material. These are spontaneous emission, stimulated emission and absorption, each of which with an associated probability of occurring given by the Einstein coefficients A_{21}, B_{21} and B_{12}, respectively. Each system making a transition from level E_2 to E_1 contributes the energy $h\nu_0$ distributed over the full solid angle 4π. The absorption and emission coefficients are then given by:

$$\kappa_\nu = \frac{h\nu_0}{c}(N_1 B_{12} - N_2 B_{21})\varphi(\nu) \tag{2.18}$$

and

$$j_\nu = \frac{h\nu_0}{4\pi} N_2 A_{21} \varphi(\nu) \tag{2.19}$$

where N_n is the number of atoms having the electron in the principal quantum state n and $\varphi(\nu)$ is the line profile function. N_n is given by the Boltzmann distribution

$$\frac{N_2}{N_1} = \frac{b_2}{b_1}\frac{g_2}{g_1} e^{-h\nu_0/kT_e} \tag{2.20}$$

where g_n is the statistical weight of the quantum state n. b_n, the departure coefficient from LTE, is the ratio of the actual number of atoms having the electrons in level n to the number which would be there if the population were in LTE. Thus, by definition, in LTE the departure coefficient is equal to 1.

The three Einstein coefficients are related by the equations

$$g_1 B_{12} = g_2 B_{21} \tag{2.21}$$

and

$$A_{21} = \frac{8\pi h\nu_0^3}{c^3} B_{21}. \tag{2.22}$$

Replacing these two expressions in equation (2.18), results in

$$\kappa_\nu = \frac{c^2}{8\pi\nu_0^2}\frac{g_2}{g_1} N_1 A_{21}\left[1 - \frac{b_2}{b_1}\exp\left(-\frac{h\nu_0}{kT_\mathrm{e}}\right)\right]\varphi(\nu). \tag{2.23}$$

The Einstein coefficients can also be related to the oscillator strength, a measure of the transition's strength, by

$$f_{12} = \frac{m_\mathrm{e} c^3}{8\nu_0^2\pi^2 e^2}\frac{g_2}{g_1} A_{21} \tag{2.24}$$

where f_{12} is the absorption oscillator strength, and $f_{21} = -f_{12} g_1/g_2$ is the emission oscillator strength. Oscillator strengths for quantum levels appropriate to hydrogen RRLs have been tabulated by Goldwire (1968) and by Menzel (1969). Menzel (1968) gives the useful approximation

$$f_{12} \approx n_1 M_{\Delta n}\left(1 + 1.5\frac{\Delta n}{n_1}\right) \tag{2.25}$$

where $M_{\Delta n} = 0.190775, 0.026332, 0.0081056$ for $\Delta n = 1, 2$ and 3, respectively.

2.2.1 RRL intensity under LTE conditions

Some considerations can be made to compute the absorption coefficient for a given hydrogen recombination line in LTE. The Einstein coefficient A_{nm} for hydrogen has been determined by many different authors. The correspondence principle states that the theory of quantum mechanics reproduces classical physics in the limit of large quantum numbers. It is therefore possible to use the classical electric dipole oscillator, one of the simplest sources for electromagnetic radiation, to calculate the transition probability. The result, for a hydrogen α line and for the limit at large n, is given by

$$A_{n+1,n} = \frac{128\pi^6 m e^{10}}{3h^6 c^3}\frac{1}{n^5} = \frac{5.36\times10^9}{n^5} s^{-1}. \tag{2.26}$$

The Saha-Boltzmann equation gives the number of atoms with electrons in the principal quantum state n as follows

$$N_n = n^2 \left(\frac{h^2}{2\pi m k T_\mathrm{e}} \right)^{3/2} e^{\frac{X_n}{kT_\mathrm{e}}} N_\mathrm{i} N_\mathrm{e} \tag{2.27}$$

where

$$X_n = h\nu_0 - \chi_n = \frac{h\nu_0}{n^2}. \tag{2.28}$$

Finally, a Gaussian line profile, of width $\Delta\nu$, is assumed for $\varphi(\nu)$. Noting that in the radio range $\exp(X_n/kT_\mathrm{e}) \cong 1$ and $1 - \exp(-h\nu_{n+1,n}/kT_\mathrm{e}) \cong h\nu_{n+1,n}/kT_\mathrm{e}$, using equations (2.23) and (2.3) results in the following expression for the optical depth in the centre of the line

$$\tau_\mathrm{L} = 1.92 \times 10^3 T_\mathrm{e}^{-5/2} (\Delta\nu)^{-1} (\mathrm{EM}) \tag{2.29}$$

for an α transition. T_e is in K, $\Delta\nu$ in KHz and EM, as defined in (2.14), is in pc cm^{-6}.

Therefore, if $\tau_\mathrm{L} \ll 1$, the peak line brightness temperature is obtained by substituting equation (2.29) into equation (2.8) which becomes

$$T_\mathrm{L} = 1.92 \times 10^3 T_\mathrm{e}^{-3/2} (\Delta\nu)^{-1} (\mathrm{EM}) \tag{2.30}$$

(Rohlfs & Wilson 2000).

2.2.2 RRL intensity when LTE conditions do not apply

The term LTE describes a situation in which the energy exchange between the radiative and kinetic energy domains of the gas is so efficient that a single parameter, temperature, describes exactly the characteristics of both domains. The departure coefficients were introduced by Goldberg (1968) after noting that the excitation temperature T_{ex} that describes the relative population of the bound quantum levels was not the same as the temperature of the ionised gas in the nebula T_e. The correct form of the Boltzmann distribution in equation (2.20) is the result of

$$e^{-h\nu/kT_{ex}} = \frac{b_n}{b_{n-1}} e^{-h\nu/kT_\mathrm{e}}. \tag{2.31}$$

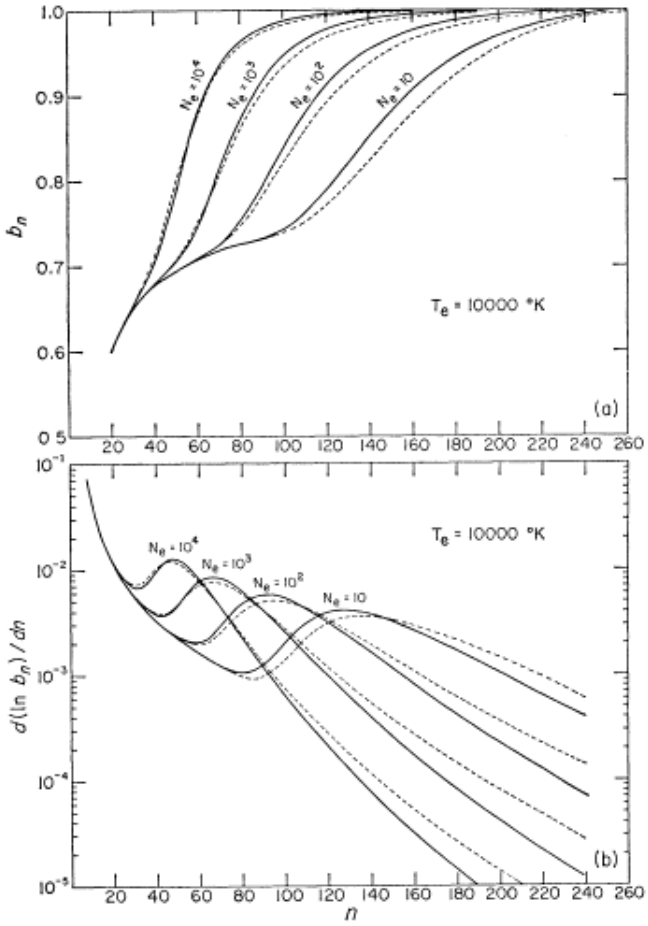

Figure 2.2: The population factor b_n and the slope function $\frac{d \ln b_b}{dE_n}$, for a $\Delta n = 1$ transition, plotted against the quantum number n for hydrogen gas with different electron densities N_e at the fixed electron temperature of 10^4 K (Sejnowski & Hjellming 1969). The full and dotted lines represent the exact and the approximate solutions for the collisional-transition probabilities, respectively.

Equation 2.23 can be written as

$$\kappa_\nu = \kappa_\nu^* b_n \beta \tag{2.32}$$

where

$$\beta = \left(1 - \frac{kT_e}{h\nu} \frac{d \ln b_n}{dn}\right) \tag{2.33}$$

is the departure coefficient β for a $\Delta n = 1$ transition (Brocklehurst & Seaton 1972) and κ_ν^* is the absorption coefficient for LTE.

The departure coefficients b_n and β_n have been calculated for a broad range of densities and temperatures, as found in H regions and also in the cold partially ionised gas, by many authors (Seaton 1964; Sejnowski & Hjellming 1969; Brocklehurst & Salem 1977; Salem & Brocklehurst 1979; Walmsley 1990; Storey & Hummer 1995). Fig. 2.2 illustrates the behaviour of b_n and β_n as a function of principal quantum number for various densities (Sejnowski & Hjellming 1969). b_n represents a weakening factor due to the depletion of the level population available for absorption and β describes the enhancement of the stimulated emission because of the enhanced population gradient across the principal quantum levels. Fig. 2.2 shows that in a dense medium, where collision rates dominate the level populations, the departure coefficients will be close to unity. On the other hand, in a tenuous medium, the radiative processes dominate, thus T_e no longer accurately characterises the relative populations of the bound levels and the departure coefficients are below 1.

The departure coefficient b_n can only have values between 0 and 1, but β can differ from 1 and even become negative. This means the absorption coefficient is negative, thus maser amplification occurs. From equation (2.19), the emission coefficient can be written in non-LTE as $j_\nu = j^*_\nu b_n$, since $N_n = b_n N^*_n$. And, according to Kirchhoff's law, $j^*_\nu = \kappa^*_\nu B_\nu(T_\mathrm{e})$. Therefore, the emission coefficient becomes

$$j_\nu = \kappa^*_\nu b_n B_\nu(T_\mathrm{e}). \tag{2.34}$$

The intensity at some frequency within the RRL is the sum of that in the underlying continuum (I_C) and that from the line (I_L) and can be written as $I = I_\mathrm{L} + I_\mathrm{C} = S(1 - e^{-\tau_\mathrm{C}-\tau_\mathrm{L}})$. The source function S is given by $S = \eta B_\nu(T_\mathrm{e})$, with

$$\eta = \frac{\kappa_\mathrm{C} + \kappa^*_\mathrm{L} b_n}{\kappa_\mathrm{C} + \kappa^*_\mathrm{L} b_n \beta} \tag{2.35}$$

using the line absorption and emission coefficients from equations (2.32) and (2.34). For an isothermal and homogeneous slab of material this can be written in terms of the brightness temperature as follows,

$$T_\mathrm{L} + T_\mathrm{C} = \eta T_\mathrm{e}(1 - e^{-\tau_\mathrm{C}-\tau_\mathrm{L}}) \tag{2.36}$$

and the ratio T_L/T_C is found to be

$$\frac{T_L}{T_C} = \eta \frac{\tau_L(1 - \tau_L/2 - \tau_C/2)}{\tau_C(1 - \tau_C/2)} - 1 \tag{2.37}$$

expanding the exponential and retaining the quadratic terms in τ_C and τ_L. Noting that under LTE conditions $b_n = 1$, $\beta = 1$, thus $\eta = 1$, the influence of non-LTE effects on the line intensity can be written as

$$\frac{T_L}{T_L^*} = b\left(1 - \frac{1}{2}\tau_C\beta\right). \tag{2.38}$$

The first term of the last expression accounts for non-LTE line formation effects, while the second term describes non-LTE transfer effects, that is, maser amplification in the line intensity.

2.2.3 Line-to-continuum ratio

Equations (2.30) and (2.15) can be used to obtain the line-to-continuum ratio under the following conditions: the H region is homogeneous and isothermal; the medium is optically thin $|\tau_L + \tau_C| \ll 1$; the lines can be treated as formed and transferred in LTE. This results in

$$\frac{T_L}{T_C}\Delta V = \frac{6.985 \times 10^3}{a(T_e, \nu)} \nu_{\rm GHz}^{1.1} T_e^{-1.15} \frac{1}{1 + 0.08} \tag{2.39}$$

where ΔV is the line width in km s^{-1} and T_e in K. The factors a and $(1 + 0.08)$ are defined in equations (2.12) and (2.15), respectively. It follows that, under these special conditions, $T_L/T_C \propto \nu^{1.1}$. From the line temperature equation (2.30), $T_L \propto \nu^{-1}$, so the amplitude of the RRL decreases with frequency. Therefore, extended diffuse objects should be observed at low frequencies in order to maximise T_L. However, it must be at a frequency above the turnover frequency, the frequency at which $\tau_C = 1$, otherwise the source becomes optically thick and no line is detected. This last condition comes from the fact that if $\tau_C \gg 1$, optically thick thermal radiation approaches black body radiation where no lines are emitted. On the other hand, to observe compact H regions that are optically thick even at a few GHz and are unresolved by the telescope, the highest possible frequency maximises T_L leaving T_L/T_C unchanged.

At frequencies near 1 GHz, and for a typical RRL width of 25 km s^{-1} and electron temperature of 10^4 K, the line temperature is approximately 1 per cent of the underlying free-free continuum. For a nominal brightness temperature of 5 – 10 K for the thermal ridge on the Galactic plane at this frequency, the peak RRL temperature will be 50 – 100 mK and correspondingly less if the emission is spread over a larger velocity range due to Galactic differential rotation, for example.

The above equation for the line-to-continuum ratio shows that if the RRL temperature and width are measured, then the corresponding continuum brightness temperature can be determined. Equation (2.39) can be written in the form

$$T_C = 4.289 \times 10^{-5} a(T_\mathrm{e}, \nu) T_\mathrm{e}^{1.15} \nu_\mathrm{GHz}^{-2.1} (1 + 0.08) \int T_\mathrm{L} d\nu \tag{2.40}$$

to give the free-free brightness temperature at a given frequency, using an appropriate value for the electron temperature.

If, on the other hand, the continuum emission T_C coming from a source is known, equation (2.39) can be used to calculate the electron temperature. If the source is optically thin, homogeneous and isothermal and under LTE conditions

$$T_\mathrm{e}^* = \left[\frac{6.985 \times 10^3}{a(T, \nu)} \nu_\mathrm{GHz}^{1.1} \frac{1}{1 + 0.08} (\Delta\nu)^{-1} \left(\frac{T_\mathrm{C}}{T_\mathrm{L}} \right) \right]^{1/1.15} . \tag{2.41}$$

Non-LTE effects are accounted for using equation (2.38), resulting in

$$T_\mathrm{e} = T_\mathrm{e}^* \left[b \left(1 - \frac{1}{2} \beta \tau_\mathrm{C} \right) \right]^{1/1.15} . \tag{2.42}$$

2.3 The profile of radio recombination lines

In the Section (2.2.1) a Gaussian was adopted to describe the line shape. This is because the basic line profile for a homogeneous clump of gas is given by the Doppler broadening caused by thermal motions, which is Gaussian. The lines have an intrinsic width due to the finite length of the emitted wave train and the variation of its amplitude over the emission time, but this is found to be very small, order of 10^{-4} km s^{-1}, compared to other types of broadening as described below.

2.3.1 Doppler broadening

Doppler broadening is caused by the thermal motions in the gas which is described by the Maxwell-Boltzmann velocity distribution. This gives the number of atoms with velocity components between V_x and $V_x + dV_x$ along the line of sight, as

$$N(V_x)dV_x = N\sqrt{\frac{M}{2\pi kT}}e^{-MV_x^2/2kT}dV_x \tag{2.43}$$

where N is the total number of atoms contributing photons to the line and M is the mass of the atoms of that species. Using the classical Doppler formula, $\nu = \nu_0(1-V_x/c)$, and assuming that the total intensity I of the line is proportional to the number of emitters N, the Doppler-broadened line profile is then

$$\varphi(\nu) = \frac{2}{\Delta\nu}\sqrt{\frac{\ln(2)}{\pi}}e^{-4\ln(2)(\nu-\nu_0)^2/\Delta\nu^2} \tag{2.44}$$

where ν_0 is the rest frequency of the line and $\Delta\nu$ the Doppler Full-Width at Half Maximum (FWHM) in Hz. $\Delta\nu$ is obtained by equating the exponential arguments of equations (2.43) and (2.44), resulting in

$$\Delta_\nu = \left(4\ln(2)\frac{2kT}{Mc^2}\right)^{1/2}\nu_0 \tag{2.45}$$

where the mass M is in units of amu and T is in K (Gordon & Sorochenko 2009). For a typical H region of temperature 8000 K, equation (2.45) gives a line width of 19 km s^{-1}, which is a constant in units of velocity because $\Delta V = (c/\nu)\Delta\nu$.

2.3.2 Turbulence broadening

Turbulence broadening is caused by cells of gas moving and colliding with each other, within the radio telescope beam. The velocity distribution of these packets of gas is also Gaussian, so the observed width of the RRL is the convolution of two Gaussian profiles and is given by

$$\Delta_V = \left[4\ln(2)\left(\frac{2kT}{M} + V_t^2\right)\right]^{1/2} \tag{2.46}$$

where V_t, in km s^{-1}, is also called microturbulence velocity (Gordon & Sorochenko 2009).

2.3.3 Stark broadening

The most important mechanism for broadening RRLs is the Stark effect, also known as pressure broadening, because of its strong dependence on the electron density. The electrons in the high level orbits of atoms collide with ions and other electrons which makes the energy levels become smeared and less discrete.

The first observations of RRLs did not show the broadening expected from the theory (Hoglund & Mezger 1965; Lilley et al. 1966a; Griem 1967) and even after new theoretical considerations the agreement with experiments only arose when it was shown that density inhomogeneities within a nebula decrease the Stark effect (Brocklehurst & Seaton 1972; Lockman & Brown 1975).

Stark broadening redistributes the energy in the line over a larger frequency interval, resulting in a Voigt profile, which is the combination of Gaussian and Lorentzian profiles. Therefore, the Stark broadening effect in a line can be characterised by the ratio between the Lorentz and Gaussian portion of the spectrum. Brocklehurst & Seaton (1972) derive this ratio, for an α line, as

$$\frac{\Delta\nu_I}{\Delta\nu} = 0.14\left(\frac{n}{100}\right)^{7.4}\left(\frac{N_\mathrm{e}}{10^4}\right)\left(\frac{T_\mathrm{e}}{10^4}\right)^{-0.1}\left(\frac{M}{M_H}\frac{2\times10^4}{T_D}\right)^{1.2} \tag{2.47}$$

where, $\Delta\nu_I$ and $\Delta\nu$ are the widths of the Lorentzian and Gaussian profiles, respectively, T_D is the Doppler temperature (responsible for the Gaussian profile including microturbulence) and M is the mass of the species. Equation (2.47) shows the importance of Stark broadening with principal quantum number, or frequency. For $T_\mathrm{e} = 10^4$ K, $T_D = 2\times10^4$ K and $N_\mathrm{e} = 10^4$ cm $^{-3}$, the previous result gives $\Delta\nu_I/\Delta\nu = 0.14$ if $n = 100$ and $\Delta\nu_I/\Delta\nu = 20$ if $n = 150$. So, for a given density N_e there is a maximum quantum number n_{max} for which an RRL is detectable, which means that for a high density cloud, lines with $n > n_{max}$ will be broadened. Therefore, lines of high n indicate gas of low density, whereas high density gas can only be detected by low n lines.

2.4 Observations of H Regions

2.4.1 Distribution of H Regions in the Galaxy

The rotational velocity of the Galaxy changes as a function of Galactocentric radius, creating a variation of radial velocity with distance along the line of sight through the Galactic plane. This makes it possible to locate an H region based upon the radial velocity from its RRL. The measured velocity is usually expressed in the Local Standard of Rest (LSR) frame which is based on the mean motion of stars in the vicinity of the Sun. There is however, a distance ambiguity for sightlines within $|\ell| < 90°$. This is because an arbitrary line of sight through the plane of the Galaxy for $|\ell| < 90°$ crosses two points that lie at the same distance from the Galactic centre and, hence, have the same radial velocity. These two points lie at different distances from the Sun, usually called near and far distances. The only positions with a unique location at a given velocity are the so called ”tangent” points, the points where the line of sight is tangent to a Galactocentric circle. The distance ambiguity can be overcome by using additional information such as absorption lines, elevation above the plane, etc.

Many RRL surveys have been carried out to map the distribution of H regions in the Galaxy. Reifenstein et al. (1970) and Wilson et al. (1970) found 82 and 130 H regions in the H109α line, in the northern and southern hemisphere, respectively, resolving the distance ambiguity for some of the sources. However, the spiral structure of the Galaxy was not entirely mapped because most of the objects were located in the inner Galaxy. Georgelin & Georgelin (1976) used the velocity from both surveys along with Hα radial velocities (Georgelin 1975) to construct a spiral model of the Galaxy. Later, Taylor & Cordes (1993) used this model and included the results from the surveys of H regions by Downes et al. (1980) and Caswell & Haynes (1987). A revised version of the 2D distribution of H regions in the Galaxy is given by Paladini et al. (2004), based on the Paladini et al. (2003) catalogue compiled from several RRL surveys, and it is shown in Fig. 2.3. The figure shows that the H regions are located along the asymmetrical spiral arms.

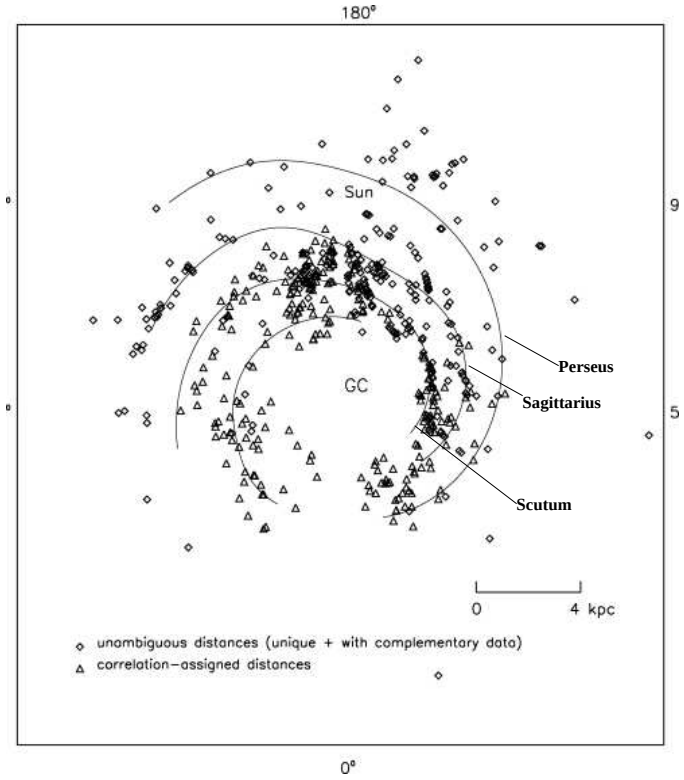

Figure 2.3: Galactic spiral arms outlined in H regions (Paladini et al. 2004). The Perseus, Sagittarius and Scutum arms are labelled in the map. 550 H regions from the Paladini et al. (2003) catalogue are shown based on the spiral arm model by Taylor & Cordes (1993).

The two extensive surveys by Lockman (1989) in the northern sky and Caswell & Haynes (1987) in the south, detected 462 and 316 H regions, respectively, at wavelengths from 3 to 9 cm. Lockman (1990) used these results to derive H region surface brightness density as a function of Galactocentric radius, to compare with the CO emissivity expressed as an equivalent surface density of molecular hydrogen (Bronfman et al. 1988). He found that the radial distribution of the surface density of H regions is double peaked in the range $4 < R < 6$ kpc, increasing from the centre to a maximum and then decreasing toward the outer boundary of the Galaxy, as well as that it follows very closely the distribution of molecular hydrogen, which was expected as both components are related to star-formation activity.

2.4.2 Helium and Carbon RRLs

Figure 2.4 shows a simplified picture of the main components of an H region and the possible locations of the different RRL emitting regions. A basic H region is the result of the ionisation of the gas surrounding a young star. Its size, the Strömgren radius R_H, depends on the ionising radiation and the density of the gas. If the ionising radiation has photons with wavelengths shorter than 504Å, then a He region is formed with a radius R_{He}, which can be smaller or larger than R_H, depending primarily upon the ionising spectrum of the central star. Photons that are incapable of ionising hydrogen ($\lambda > 912$Å), will escape the H region and ionise other atomic species in the neutral gas, such as carbon, magnesium or sulfur (creating a photodissociation region, PDR). These regions are located outside the H region and can also be ionised by the interstellar radiation field (IRF). They form an interface between the H region and the surrounding molecular cloud, thus have temperatures of a few hundred degrees K. Also illustrated in Fig. 2.4 is the H^0 region, where the hydrogen is only partially ionised. This is thought to be caused by the leakage of soft X-ray photons from the H region (Pankonin et al. 1977; Krugel & Tenorio-Tagle 1978) or by the interaction of a weak shock front with the neutral material (Hill 1977). H^0 line emission was first detected by Ball et al. (1970).

The first helium RRL detection was towards the Omega Nebula by Lilley et al. (1966b). The velocity separation of the H and He lines was that predicted by theory (see Table 2.1) and the integrated intensity ratio I_{He}/I_H was found to be 0.10 ± 0.05. Since then, He RRLs have been used to determine the abundance of ionised helium in the Galaxy, which can in principle be used to separate the primordial helium abundance from the interstellar enrichment due to galactic evolution. In an H region the "true" helium abundance is given by $y = y^0 + y^+ + y^{++}$, the sum of the relative number densities of neutral, singly and doubly ionised helium. Churchwell et al. (1974) found for 39 Galactic H regions $0.06 \leq y^+ \leq 0.10$ and derive an upper limit for y^{++} of 0.008, thus this contribution is usually ignored. They also suggest the true relative abundance of

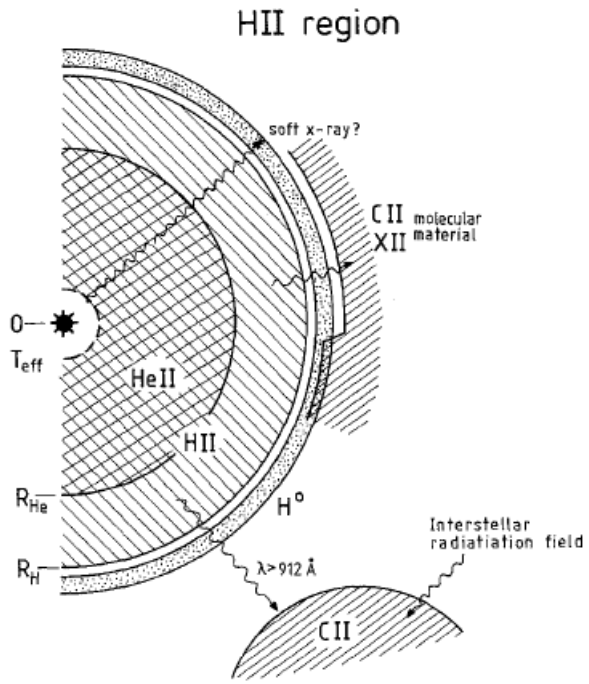

Figure 2.4: A schematic representation of an H region and its main components (Roelfsema & Goss 1992). The H and He ionised regions are surrounded by a partially ionised medium of hydrogen, carbon and heavier elements, that form an interface between the H region and the molecular cloud.

helium in the Galaxy to be $y = 0.1$. Shaver et al. (1983) combined radio and optical observations of H regions to derive $y^+ = 0.074 \pm 0.003$. The difference between y and y^+, which is what RRL measurements provide, is attributed to the non-coincidence of the He^+ and H^+ zones in the H region. Correcting for that effect, Osterbrock (1989) found the results of Shaver et al. (1983) to be consistent with the helium abundance of 0.1. Heiles et al. (1996a) derives, for 3 H regions, slightly lower values for the ionised helium abundance as compared to previous results. This can be explained by "geometric effects" (Mezger & Smith 1976): larger beam sizes weight the outer less dense parts of the H region, where the He^+ zone has disappeared. Heiles et al. (1996a) also find an upper limit for the y^+ in the diffuse ionised medium of 0.013.

Lines at roughly the expected velocity of carbon RRLs were first detected by Palmer et al. (1967) towards the H regions Orion B and W3, in the 109α transition.

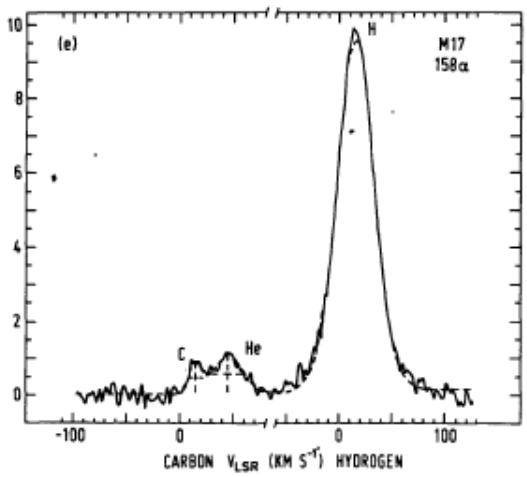

Figure 2.5: The 158α spectrum of the H region M17 (Omega nebula), where the hydrogen, helium and carbon lines are visible (Pankonin et al. 1977).

Even though the line intensities were greater than predicted by carbon abundance, Goldberg & Dupree (1967) confirmed the detection as C109α lines. Additional observations suggested that the carbon lines originated in the outer layers of molecular clouds at the boundaries of H regions (Balick et al. 1974; Zuckerman & Ball 1974; Dupree 1974) (Fig. 2.4). The measured narrow line widths (4 km s^{-1} from NGC2024, Ball et al. 1970) required lower gas temperature and also the radial velocities of C$n\alpha$ lines agreed well with lines from the cold ISM rather than from the H$n\alpha$. The observable characteristics of a C region depend on a combination of: the spectral type of the star; the relative location of the H region, the C and the observer; the distance of the source from the observer; the abundance of the atomic carbon; the density of the neutral cloud (Pankonin et al. 1977). The combination of all these factors makes it difficult to predict the carbon RRL intensity or even its velocity shift relative to the H line. A typical width for a carbon line from a C region which is associated with an H region is $\sim$ 6 km s^{-1} (Pankonin et al. 1977) and typical values of electron temperature and density in the C region are $T_e \approx 100$ K and $N_e \approx 3$ to 30 cm^{-3} (Gordon & Sorochenko 2009). Fig. 2.5 shows the spectrum of M17 with the H158α, He158α and C158α lines.

2.5 Derived physical parameters of the ionised medium

2.5.1 Electron temperature

RRLs provide the simplest and most precise method of determining the electron temperature of an H region, by means of the line-to-continuum ratio. Early observations of α line transitions from H regions, gave low T_e values with an average of 5800 K (Mezger & Henderson 1967), compared to the results from optical line measurements which gave an average of 10000 K. Soon it was noted that the electron temperature calculation is subject to complications, namely due to non-LTE conditions and the Stark effect (see Sections 2.2.3 and 2.3.3).

From equation (2.42) it follows that, ignoring the maser effect, if the RRL is formed under non-LTE conditions the derived electron temperature using equation (2.41) for the LTE formalism is an underestimation of the true temperature, as found in the early RRL measurements. However, there are frequencies where the derived temperature using equation (2.41) is correct. Shaver (1980a) examined the ratio T_e^*/T_e, where T_e^* is the electron temperature in LTE (Section 2.2.3), as a function of frequency and emission measure EM. The calculations assumed an excitation parameter for the central star $U = 100$ pc cm^{-2}, which corresponds to an early O-star, and a typical filling factor f of 0.1. The electron density is related to EM and f by EM $= 2UN_e^{4/3} f^{2/3}$. The results show that there is a unique frequency at which $T_e^* = T_e$, given by

$$\nu \sim 0.081 \mathrm{EM}^{0.36}. \tag{2.48}$$

The accuracy of the electron temperature calculated from RRL measurements at this optimal frequency is claimed to be 2 – 3 per cent (Shaver 1980a). The reason for T_e^* to be very close to T_e is that, in general, there is a frequency at which in an H region the collision rates populating the levels become dominant over the radiative rates, where the line amplification is just offset by the line weakening due to the underpopulation of the quantum levels themselves, thus eliminating the effects of the departures from LTE. Using equation (2.48), it follows that at a frequency of 1 GHz, the derived electron

temperature is essentially equal to its LTE value, for EM $\sim 10^3$ pc cm^{-6}. This value of EM is representative of classical H regions, which is what we expect to observe in this survey.

The calculation of electron temperature of H regions using RRL observations enabled the detection of a gradient in T_e as a function of Galactocentric radius (R_G) by Churchwell & Walmsley (1975). The Galactocentric radius of an H region is calculated using the rotation curve $\Theta(R_G)$, assuming that the object moves around the Galactic centre in a circular orbit with radial velocity V. An object at longitude ℓ has rotation velocity given by:

$$\Theta = (R_G/R_0)(\Theta_0 + V/\sin(\ell)) \tag{2.49}$$

where R_0 and Θ_0 are the Galactocentric distance and radius of the Sun, respectively (Verschuur & Kellermann 1988). The Galactic rotation curve used in this work is from Fich et al. (1989):

$$\Theta = (221.6 - 0.44R_G)\ \mathrm{km\,s^{-1}} \tag{2.50}$$

with $R_0 = 8.5$ kpc and $\Theta_0 = 220$ km s^{-1}, the IAU-recommended values for the Galactocentric distance and rotation velocity of the Sun, respectively (Kerr & Lynden-Bell 1986).

Using a sample of 67 H regions Shaver et al. (1983) obtained the following relation between T_e and R_G

$$T_e = (3150 \pm 110) + (433 \pm 40)R_G \tag{2.51}$$

where T_e is in K, R_G in kpc. Shaver et al. (1983) used the Schmidt (1965) rotation curve with the local radius $R_0 = 10$ kpc. The temperature gradient is shown in Fig. 2.6. Shaver et al. (1983) suggested the gradient to be caused by a corresponding gradient of metallic elements, as described in Section 1.2.1, based on a similar trend observed in the normalised abundances of oxygen and nitrogen, O/H and N/H. The scatter at a fixed distance from the Galactic centre is due to real differences in the electron temperature

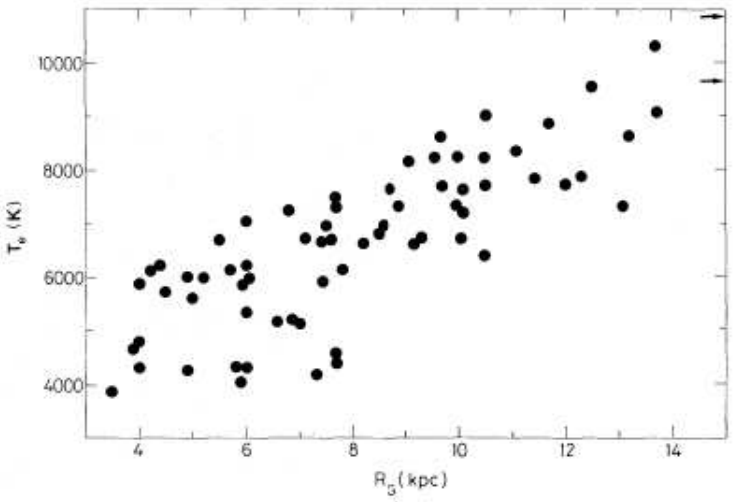

Figure 2.6: Electron temperatures of H regions against Galactocentric radius. The horizontal arrows at the upper right represent N66 and 30 Doradus in the Magellanic Cloud (Shaver et al. 1983).

of each region, in addition to measurement errors, as H regions differ in density and radiation field from the exciting star.

Paladini et al. (2004) used the published data for 404 H regions with reliable Galactocentric distances and found

$$T_e = (4166 \pm 124) + (314 \pm 20)R_G \tag{2.52}$$

using equation (2.50) and $R_0 = 8.5$ kpc. This result is in general agreement with the result from Shaver et al., any differences may be due to the larger number of fainter H regions in the Paladini et al. sample.

The above relationships can be applied to derive likely values of the electron temperature for the Galactic spiral arms in the first quadrant. Table 2.2 summarises the T_e values from equations (2.51) and (2.52) for the near and far Galactocentric radii of the Local, Sagittarius and Scutum spiral arms. These radii are derived from the spiral pattern for H regions given in Paladini et al. (2004). T_e ranges from 6700 K for the Local arm to 5500 K for the Scutum arm.

The metal abundance responsible for cooling of the H regions and the diffuse gas

Table 2.2: Electron temperatures from equations (2.51) and (2.52) for the mean, near and far galactocentric radii of the line of sight intersection with the Local, Sagittarius and Scutum arms.

Arm	$R_{\rm near}$ (kpc)	$R_{\rm far}$ (kpc)	$R_{\rm mean}$ (kpc)	$T_{\rm e}$ (K) (Shaver)	$T_{\rm e}$ (K) (Paladini)
Local	8.5	7.5	8.0	6610	6680
Sagittarius	6.5	6.0	6.25	5860	6130
Scutum	5.0	5.0	5.0	5310	5740

is expected to be the same, since both components are correlated spatially (Section 1.2.2). The main difference would be the effective temperature of the radiation field which would be lower for the diffuse gas, arguing for a lower $T_{\rm e}$. However the diffuse warm ionised medium (WIM) is found to be $\sim$ 2000 K warmer than traditional H regions (Reynolds et al. 2001). Direct measurements of emission lines of intermediate latitude by Reynolds (1985) gave the first estimate of the electron temperature for the WIM, with a mean of $\sim$ 8000 K. More recently, Madsen et al. (2006) using Hα data from WHAM reinforce the general assertion that the WIM is warmer and less ionised compared to classical H regions. They find temperatures between 7000 and 10000 K. This difference in electron temperature between the diffuse gas and the individual H regions may require spectral processing of the stellar radiation (e.g. hardening of the radiation field, Wood & Mathis 2004) and/or an additional heating beyond photoionisation (e.g. magnetic reconnection, cosmic rays, photoelectric emission from small grains, Reynolds et al. 1999).

2.5.2 Line Widths

The measured RRL width is usually made up of major contributions from the thermal Doppler broadening and turbulent motions: $\Delta V_{tot}^2 = \Delta V_D^2 + \Delta V_t^2$. A narrow RRL is evidence that the H region has a lower electron temperature. Lockman (1989) detected 11 H regions with $\Delta V \leq 14.7$ km s^{-1}, which corresponds to $T_{\rm e} \leq 4600$ K. "Cool" nebulae are not very commonly detected, so Shaver (1979) suggested that along

with low emission measures, making these sources faint in the Galactic continuum, they must have higher metal abundances to explain the low electron temperature. A very broad line can be either explained by broadening due to Stark effects, but also by the contribution of emission from unrelated regions of different velocities, within the beam. The Stark effect becomes important for high density gas observed at high n transitions, and can be identified by the non-Gaussian shape of the line.

Lockman et al. (1996) detected 130 diffuse Galactic H regions, with an antenna beam size of 9 arcmin, for which the typical line width was found to be 25 km s^{-1}, with most of the nebulae having $18 < \Delta V < 35$ km s^{-1}. These results are similar to those found by Lockman (1989) and Caswell & Haynes (1987) for discrete H regions. The fact that the expected Doppler line width for a gas at a temperature of 8000 K is $\sim$ 19 km s^{-1} (Section 2.3.1) means that turbulence, with a typical velocity $V_t \sim 16$ km s^{-1}, is a significant broadening effect, comparable to the thermal broadening. Caswell & Haynes (1987) derive $V_t = 18.6$ km s^{-1}, with no dependence on Galactocentric radius, in contrast to V_D, which can depend on $R_{\rm G}$ since it is proportional to the electron temperature.

2.5.3 Observations of non-LTE effects at 1.4 GHz

Non-LTE effects are highly dependent on the density of the region (Section 2.2.2), as well as the Stark effect (Section 2.3.3). Shaver (1980b) pointed out that the presence of density variations explains not only the absence of significant observable pressure broadening, but also the attenuation of the stimulated emission. Therefore, the RRL observations can be treated using the LTE formalism.

Cersosimo & Magnani (1990) measured the ratio β/α for 13 H regions, using the H159α and H200β RRLs, at 1.62 GHz with a telescope beam size of 2.9 arcmin. The ratio allows the investigation of non-LTE effects with ~ 0.28 as the expected value in LTE. Even though observing at the optimal frequency prescribed by Shaver (1980a), the observed ratios vary from source to source, indicating that the generalised interpre-

tation of the non-dependence on the electron density and temperature is not adequate. For 5 sources the measured ratio is lower than the LTE value and no pressure broadening is observed, meaning that non-LTE effects are responsible for the line intensities and no clumping of the H region can explain the low ratios caused by stimulated emission. This shows how uncertain non-LTE effects are at these frequencies.

Nevertheless, the same β/α ratio study at 1.62 GHz of two diffuse ionised regions with a 18 arcmin beam, led Cersosimo & Onello (1991) to conclude that the observed LTE intensity ratio of the lines can arise from an inhomogeneous ionised nebula with a low-density component. The model that explains the LTE ratios is composed of a classical H region of electron density 100 cm^{-3} and 5 pc diameter, embedded in a low-density (N_e < 1 cm^{-3}) envelope 40 times bigger. This is likely to be the case of our observations, with a beam of $\sim$ 15 arcmin, thus the bulk of what is observed is close to LTE.

3

H Parkes All-Sky Survey Data

3.1 The H Parkes All-Sky Survey and the H Zone of Avoidance Survey

The sensitive multibeam survey for RRL emission described in this work is a by-product of the HIPASS survey (Staveley-Smith et al. 1996). The aim was to detect H -emitting galaxies in the local Universe using a bandwidth of 64 MHz centred on 1394.5 MHz corresponding to redshifted velocities of -1280 and 12700 km s^{-1}. Within this velocity range there is also Galactic H and high-velocity cloud (HVC) emission at near-Galactic velocities. In addition, there are three Galactic RRLs, H166α, H167α and H168α.

HIPASS is the largest blind H survey[1], covering 71% of the sky south of declination +25°.5. This survey enabled the investigation of the H mass function of galaxies (Kilborn et al. 1999; Zwaan et al. 2003), the discovery of new galaxies and generation of catalogues (Meyer et al. 2004; Wong et al. 2006) as well as the discovery of a leading arm to the Magellanic stream (Putman et al. 1998). HIPASS has also provided a new view of the Galactic HVC distribution in the southern sky (Putman et al. 2002). Its resolution, full spatial sampling and sensitivity revealed a large population of com-

[1]Excluding surveys of local H in our Galaxy.

pact high-velocity cloud (CHVC) and provided clues to the clouds' origins (Putman & Gibson 1999; Putman et al. 2002).

Of particular interest for the study of the necessarily weak RRL emission from the Galactic plane is the ZOA survey associated with HIPASS (Staveley-Smith et al. 1998). This searched for galaxies behind the Galactic plane with a factor of 5 longer integration time than HIPASS, therefore resulting in a more sensitive survey, with an rms noise of 6 mJy/beam compared with 13 mJy/beam for HIPASS. The ZOA survey covers the Galactic plane accessible from Parkes, $\ell = 196^\circ - 0^\circ - 52^\circ$ and $|b| < 5^\circ$. An analysis of the shallow survey data for the southern ZOA ($\ell = 212^\circ - 36^\circ$) led to the detection of 110 galaxies, 67 of which were previously unknown (Henning et al. 2000). Using the northern extension data ($\ell = 36^\circ - 52^\circ$ and $\ell = 196^\circ - 212^\circ$) at the full survey sensitivity, Donley et al. (2005) detected 77 galaxies, only 20 of which have been previously detected in H .

Both HIPASS and ZOA surveys use the 21-cm multibeam receiver system installed on the Parkes 64-m telescope. The multibeam specifications and survey parameters are described in the following sections.

3.1.1 The multibeam receiver

The Parkes multibeam system consists of a 13 beam receiver and a digital correlator. The circular beams are set on a hexagonal grid as shown in Fig. 3.1. The 26 receivers (two per feed horn) are sensitive to orthogonal linear polarisations in the frequency range 1.27−1.47 GHz. The correlator (Canaris 1993) uses a 1024-lag chip and provides 128×10^6 samples per second from an input signal within the 64 MHz bandwidth, for all 26 receivers. For HIPASS/ZOA the frequency coverage is from 1362.5 to 1426.5 MHz centred on 1394.5 MHz in 1024 channels spaced by 62.5 KHz or 13.2 km s^{-1} for the H line (Staveley-Smith et al. 1996).

A radio telescope beam solid angle is usually divided into main beam and side-lobes. The quality of the antenna as a direction measuring device depends on how well

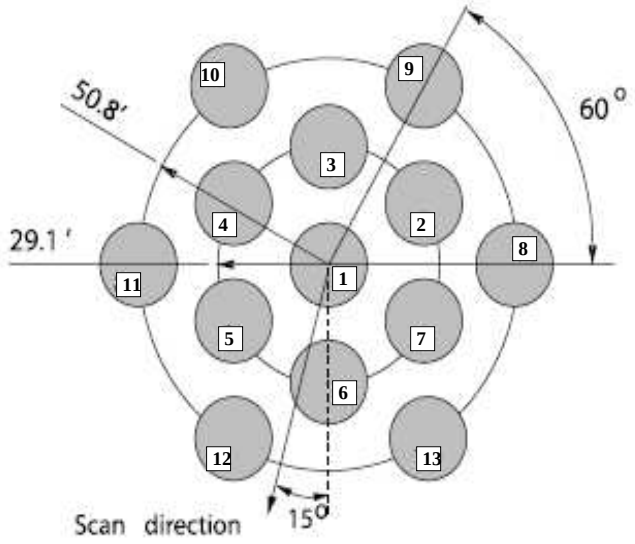

Figure 3.1: The multibeam receiver configuration on the sky. The radii of the inner and outer rings of beams is 29.1 and 50.8 arcmin, respectively (Barnes et al. 2001).

the power pattern is concentrated in the main beam and is given by the main beam efficiency, or simply beam efficiency, η_B, defined as

$$\eta_B = \frac{\Omega_{MB}}{\Omega_A} \tag{3.1}$$

where Ω_{MB} and Ω_A are the main beam solid angle and beam solid angle, respectively. A typical parabolic reflector antenna, like the Parkes 64-m, has a main beam efficiency of 70%, so a sidelobe contribution of 30%. It can be modified for parabolic antennas by a choice of feed systems which provide the appropriate illumination of the dish. For unblocked apertures the main beam efficiency improves to 90%, so the sidelobe contribution decreases to 10%. Consequently, the observed signal may originate from the main beam or may be picked up by the sidelobes of the antenna. The main sidelobes are the result of reflections from the feed legs that carry the prime focus cabin and reflections at the rim of the telescope.

Figures 3.2 and 3.3 show the computed and measured radiation pattern of beams 1 and 9 and beams 1, 2 and 8, respectively. Fig. 3.2 (b) shows the radial elongation, or coma distortion, of beam 9, 14 dB below the peak value. This causes the efficiency

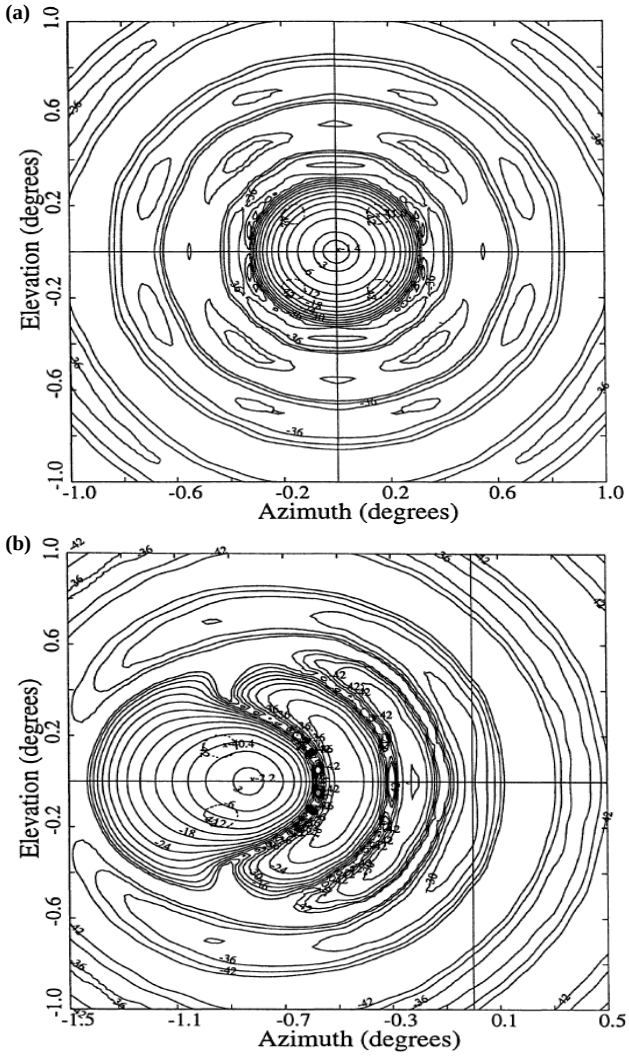

Figure 3.2: Theoretical radiation pattern of beams (a) 1 and (b) 9. Contours are every 3 dB and the peak values of −1.59 and −2.23 dB, respectively, are relative to a uniformly illuminated aperture (Staveley-Smith et al. 1996).

of the outer beams to go down by ∼ 10% in relation to the central beam, shown in Fig. 3.2 (a) (Staveley-Smith et al. 1996). Fig. 3.3 displays the antenna response pattern within a radius of 6° for beams 1, 2 and 8 (Kalberla et al. 2010), where the resulting six-fold symmetry from the three feed legs is visible. Fig. 3.3 also shows that the coma lobe increases in strength with feed offset and that sidelobe structure becomes more asymmetric and has a more pronounced ringing with increasing feed offset. Furthermore, azimuthal asymmetries in the antenna pattern due to the feed

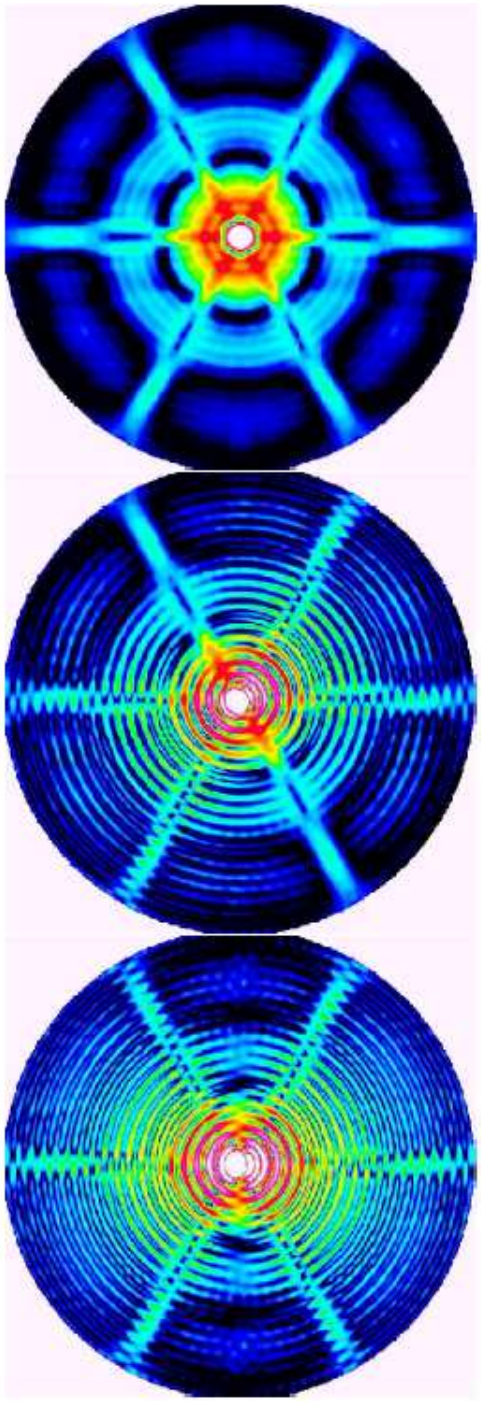

Figure 3.3: Measured antenna patterns within a radius of 6° for beam 1, 2 and 8, from top to bottom. The levels are between −20 dB (white) and −50 dB (black) (Kalberla et al. 2010).

Table 3.1: The HIPASS multibeam receiver specifications.

Parameter	Beam 1	Beams 2 to 7	Beams 8 to 13
Average system temperature(K)[a]	21	21	21
FWHM beamwidth (arcmin)	14.0	14.1	14.5
FWHM ellipticity (radial)	0.00	0.03	0.06
Efficiency (Jy K^{-1})	1.36	1.45	1.72
Average system temperature (Jy)	29	30	36
Average Cal temperature (Jy)	1.6	1.8	2.0
Coma lobe	none	−17 dB	−14 dB

[a]System temperature at an elevation of 55°, where it reaches a minimum. At extreme elevations (30° and 90°) temperatures are about 2 K higher. Temperatures measured at a frequency of 1394.5 MHz over a bandwith of 64 MHz.

offsets decrease on average with increasing distance from the main beam.

Measurements of the widths of the beams give full widths at half power of 14.0 arcmin for the central beam, 14.1 arcmin for the beams in the inner ring with an ellipticity of 0.03 and 14.5 arcmin for the beams in the outer ring with an ellipticity of 0.06. The mean observing beamwidth is 14.4 arcmin and the typical separation of the beams projected on the sky is 30 arcmin, just over two beamwidths. Table 3.1 summarises the receiver specifications[1].

3.1.2 Scanning strategy and data acquisition

HIPASS scanning

HIPASS observations are taken by scanning the telescope in declination strips of 8° length. As a result of data being acquired while the telescope is scanning, the beam is slightly extended in the scan direction to 14′.7. The footprint of the receiver on the sky is $\sim 1^{\circ}.7$, thus each scan maps an area of $8^{\circ} \times 1^{\circ}.7$. Prior to each scan, the feed is rotated by the parallactic angle at the scan mid-point, plus another 15°, to obtain approximately uniform coverage of the sky. To obtain full coverage at full sensitivity the scans are made in sets of 5 (also known as the 'a' through 'e' scans) separated by 7 arcmin in right

[1]Available on the Multibeam website http://www.atnf.csiro.au/research/multibeam/.overview.html

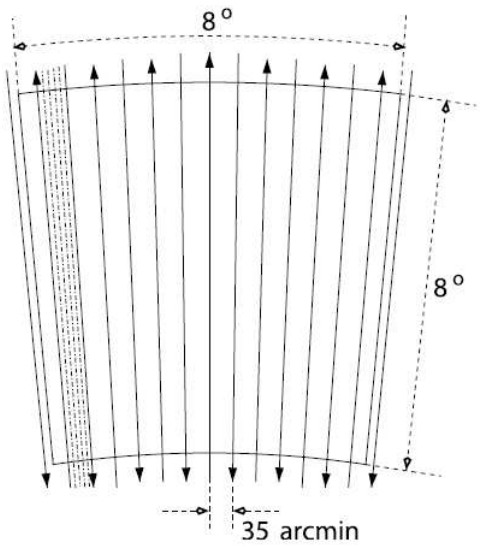

Figure 3.4: HIPASS scan pattern on the sky, for an $8^\circ \times 8^\circ$ field, as described in the text. The arrows indicate the direction of each scan and the final scan density for a single beam is shown by the dot-dashed lines (Barnes et al. 2001).

ascension, which ensures that the sky is mapped at close to the Nyquist rate (Section 3.2.2), $\lambda/2D = 5.7$ arcmin, by *each* of the 13 beams. A total of 15 sets covers an $8^\circ \times 8^\circ$ field, as shown in Fig. 3.4.

Observations of a given part of the sky were made at well-separated times so that interference, if present, did not corrupt all data for that direction. The scan rate is 1° per minute and the integration time is 450 s per beam, which results in a noise per channel of $\sim$ 13 mJy/beam.

ZOA scanning

The ZOA survey was scanned in Galactic coordinates, along 8° strips of constant Galactic latitude, separated by 1.4 arcmin. Similarly to HIPASS, the 25 scans within a 35 arcmin set are know as the 'a' through 'y' scans. At the midpoint of each scan, the feed is rotated by 15° with respect to the scan direction. Each field is scanned 425 times, corresponding to 17 sets of scans, thus the latitude coverage of the ZOA survey is $|b| < 5^\circ$. The total integration time is 2100 s per beam for rms per channel

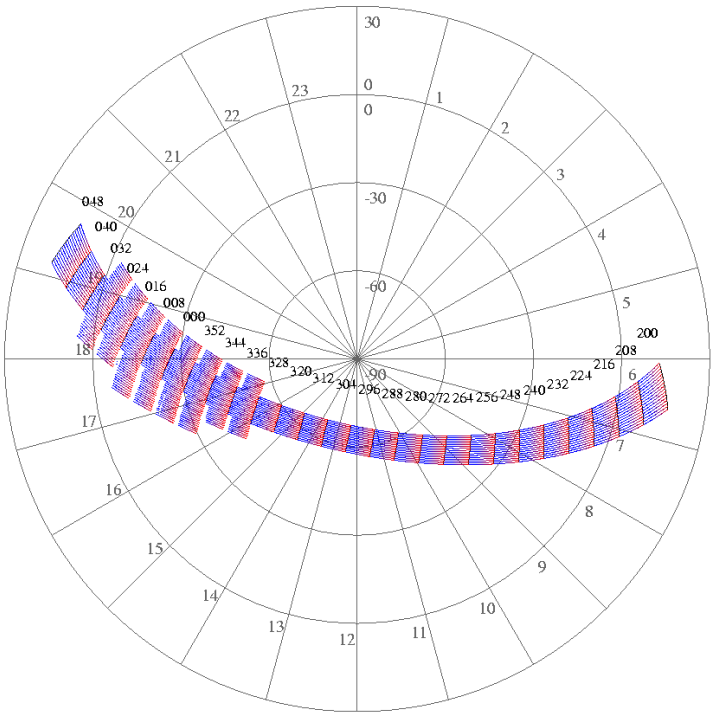

Figure 3.5: The ZOA scans projected on the southern celestial sky. Each cube is numbered with its central Galactic longitude and the red and blue lines represent the scans. Image available at http://www.atnf.csiro.au/research/multibeam/release/.

of 6 mJy/beam. The ZOA survey resulted in 27 8° (ℓ) × 10° (b) × 1024 channel datacubes, shown in Fig. 3.5, projected on the southern celestial sky. From this figure it is evident that the HIPASS scans in declination will cross the Galactic plane, and thus the ZOA scans at a different angle in each ZOA field. Fig. 3.6 shows one HIPASS and one ZOA scan for the fields ZOA-040 and ZOA-304, respectively. HIPASS scans, in red, change from being $< 45°$ inclined in relation to the Galactic plane for the ZOA-040 zone, to almost perpendicular at $\ell = 340°$. The significance of this will be discussed in Section 5.1.4.

The multibeam correlator cycle is 5 s and spectra are written for each beam and polarisation at the end of each cycle. There are two polarisations per beam (A and B), so a total of 26 spectra are written each cycle, each with 1024 channels. With a scan rate of 1° per minute, the 8° scan length is $\sim$ 100 cycles, thus a single scan contains

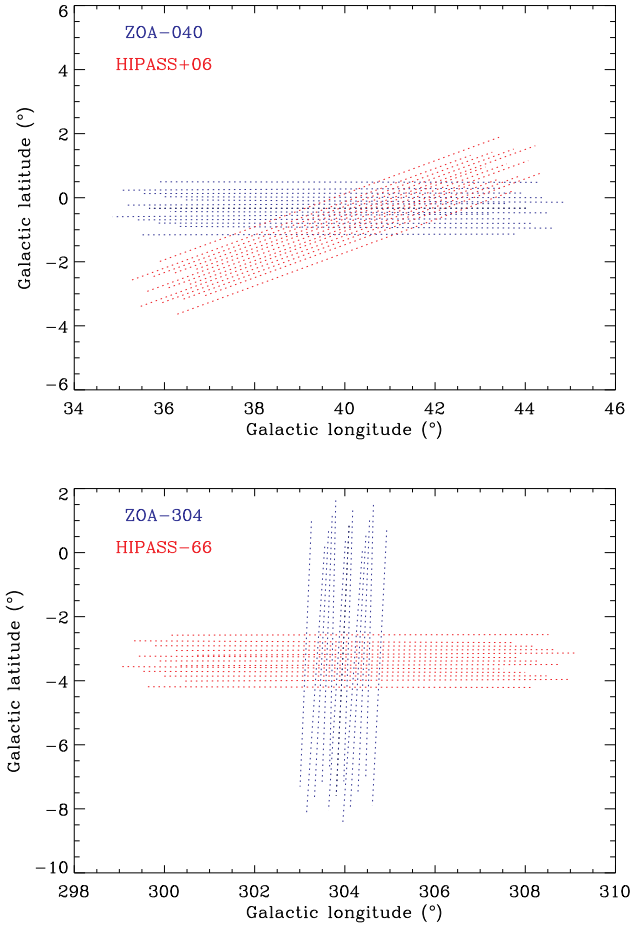

Figure 3.6: Comparison between ZOA and HIPASS scans, for two fields on the Galactic plane. Each line represents the track of one individual beam in that scan and each dot represents one integration from that beam. The change in angle between ZOA and HIPASS scans, due to the inclination of the Galactic plane, is evident.

$\sim$ 2600 spectra. Each scan is written as one file and files are named according to their date and time of acquisition, as well as their position on the sky. HIPASS file names contain the right ascension and declination of the middle of the scan, whereas ZOA file names have the central Galactic longitude and latitude and are of the form year−month−day_time_ℓ_{central}−b$_{\text{central}}$_number&repetition.hpf. For example the ZOA file 2000−10−15_0757_040−021629_05p.hpf is the scan that covers $36^\circ < \ell < 44^\circ$ centred at $b = 2^\circ.1629$.

3.2 HIPASS data reduction

Spectra generated by the multibeam correlator are dominated by the system bandpass spectrum, plus noise whose amplitude depends inversely on the square root of the integration time and channel bandwidth. Other effects such as baseline ripple, non-linearities in the receiver and amplifier system, as well as spectral ringing due to strong H Galactic emission, can also contaminate the spectra.

The bandpass spectrum reflects the system temperature, which is a sum of the sky, ground and receiver temperatures, multiplied by the product of the filters in the receiver chain. The bandpass differs for all 26 feeds of the multibeam, since there are 26 separate pathways through independent receivers, amplifiers, down converters and correlators, and also varies in time because of external influences such as atmospheric conditions. Therefore, one of the main tasks of the data reduction is the bandpass removal.

Baseline ripple may be reduced but is not eliminated by the bandpass correction. It is caused by single or multiple reflections of radiation from strong continuum sources, such as the Galactic plane and the Sun, spillover radiation from the ground as well as from stray radiation off the telescope structure, including the focus cabin, its support legs and the imperfections in the dish. Standing waves develop from reflections between the various parts of the telescope structure and manifest themselves as a sinusoidal ripple in the spectral baseline. Their behaviour and different contributions will be characterised in the next chapter (Section 4.1.4). The main reflection path in the Parkes telescope, from the receiver to the dish centre and back to the receiver, is 52 m, or twice the focal length. This corresponds a sine wave of period 5.7 MHz in the spectrum. The Sun is the most common cause of ripple, affecting a large fraction of day-time acquired data. The other predominant cause of non-flat baselines after bandpass removal is spectral ringing associated with Galactic H emission. It is, nevertheless, possible to suppress the ringing or at least reduce it by spectrally smoothing the data. Another baseline distortion seen in the spectra is due to bandedge effects.

Spectra taken near strong continuum sources show a gradual rise in flux towards the lower frequency end of the band, that depends on the strength of the source. This means that the Multibeam receiver response to strong continuum sources is a noise spectrum whose amplitude is increased at lower frequencies.

The Multibeam data reduction software, originally designed to perform real time data manipulation, consists of two packages: and . The first was designed to remove the system bandpass spectrum, to calibrate the residual spectrum and remove any remaining baseline offset, to suppress strong ringing effects, shift the resultant spectrum from the observing topocentric frame to a fixed frame of reference and finally, grids the spectra into datacubes. The actual algorithms used in this work differ from what was used to reduce HIPASS H data, whose detailed explanation is given in Barnes et al. (2001). The following sections describe some aspects of the standard HIPASS spectral processing that are relevant for the present work.

3.2.1 Bandpass removal and data calibration

The bandpass estimation and removal for the standard HIPASS reduction, which was designed to image discrete H sources, is optimised for compact sources. Due to the active scanning of the telescope, the traditional signal/reference bandpass removal is not possible. In this mode, a reference spectrum towards a position free of line or continuum emission is acquired and removed from the target position spectrum by division. For HIPASS spectra bandpass correction is done by dividing the target spectrum by an estimate of the bandpass, which consists of a set of earlier and/or later spectra observed by the same feed of the multibeam. The bandpass estimate must represent the underlying spectral shape as well as the spectral shape of the receivers, ground pick-up and sky radiation and is generated channel-by-channel, for each beam and polarisation.

Data calibration is done simultaneously with bandpass removal and uses the system temperature recorded for every spectrum written by the correlator. The system

temperature, in Jy, indicates the total power measured by the correlator for each cycle and is calibrated against a calibrator diode, which is constantly switched in and out of the signal path. The calibration diode is occasionally calibrated against an extragalactic radio source of known amplitude, e.g., 1934-638 (14.9 Jy at 1420 MHz) or Hydra A (40.6 Jy at 1395 MHz).

Figure 3.7 shows the raw and the bandpass-corrected and calibrated spectra for two different positions on the sky, from one HIPASS $\delta = +6°$ scan, at RA= $19^{h}7^{m}41.52^{s}$. Fig. 3.7 (a) shows the system temperature (T_{sys}, in Jy) across the scan for the central beam and polarisation A. The total power measured by the correlator increases from 35 to almost 60 Jy as the beam passes through the Galactic plane and through a continuum source at $\ell = 41°$. The raw spectrum for that position, $(\ell, b) = (41°.0, -0°.4)$, is shown in Fig. 3.7 (b). Fig. 3.7 (c), on the other hand, shows the spectrum for the first integration of beam 1, at the beginning of the scan, where T_{sys} is at its minimum. Both spectra illustrate the system's bandpass shape and response, at each position, as well as the strong Galactic H line (channel $\sim$ 100). Figs. 3.7 (d) and (e) are the spectra for the same positions after bandpass correction and calibration. Residual baseline effects are still present in the spectra. Spectrum (d) from a strong continuum source G41.1-0.4, shows a gradual rise in flux towards higher channel numbers (lower frequencies) as well as sinusoidal ripple and ringing, as opposed to spectrum (e), that shows a flat baseline only contaminated by H ringing.

Brightness temperature conversion

The data are calibrated in Jy and presented in Jy/beam in the final datacube. Staveley-Smith et al. (2003) established the conversion factor 0.80 K/Jy by observations of S9 (T_b = 85 K, Williams 1973), a standard line calibration region. This is the result obtained using the Rayleigh-Jeans relation:

$$S = \frac{2kT_b\Omega}{\lambda^2} \tag{3.2}$$

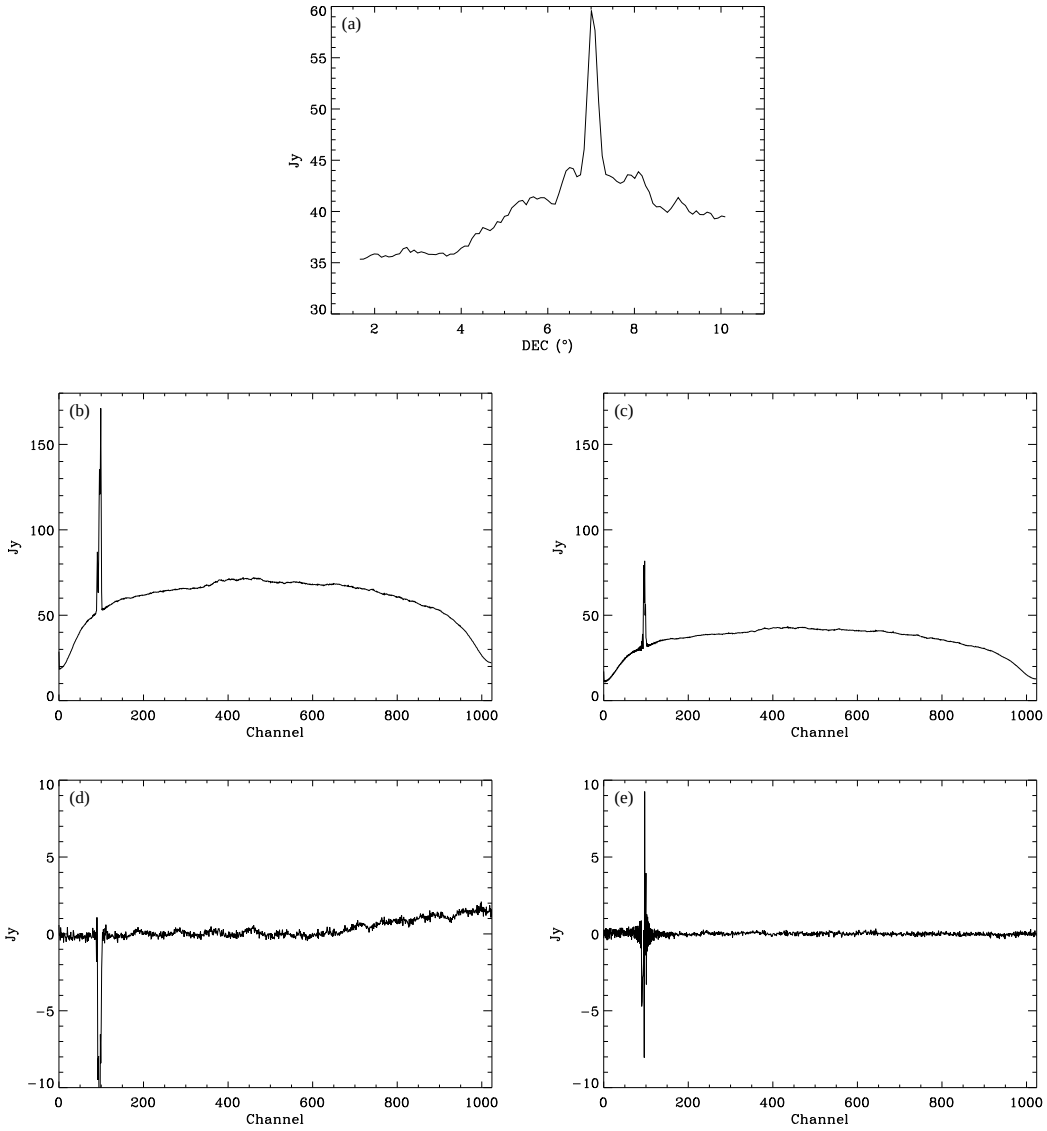

Figure 3.7: System temperature (a) and spectra from the $\delta = +6°$ HIPASS scan at RA= $19^h7^m41.52^s$, for beam 1 and polarisation A. The rise in T_{sys} at $\delta \approx 7°$ is caused by the continuum source at $(\ell, b) = (41°.0, -0°.4)$. The two middle figures show the raw spectra for integrations 65 (b) and 1 (c), or declinations 7°.01 and 1°.66, respectively. The lower figures show the corresponding spectra after bandpass correction and calibration.

where Ω is the solid angle for a gaussian beam of FWHM 14.4 arcmin at the frequency of the H line. At the frequency of the central RRL in the band, H167α, the conversion factor for the same beam size is 0.84 K/Jy. This is the main beam scale, appropriate for point sources and it will be further discussed in Chapter 5.

3.2.2 Spectral smoothing

Spectral ringing due to the strong Galactic H line is probably the easiest cause of non-flat baselines to correct, by smoothing the spectrum. This is done prior to bandpass correction. Spectral ringing is caused by the sidelobes in the spectral response of the system, which spreads strong Galactic emission and strong narrow band interference thoughout the nearby spectrum. The spectral response of a digital correlator is the result of multiplying the autocorrelation function of the input signal by a lag window. In the Fourier domain, the lag window of the multibeam correlator is nearly constant, thus it can be described, to a first order, by the rectangular function

$$w(\tau) = \begin{cases} 1 & \text{for } |\tau| \leq \tau_m \\ 0 & \text{otherwise} \end{cases} \tag{3.3}$$

with a frequency response given by

$$W(\nu) = 2\tau_m \text{sinc}(2\nu\tau_m) \tag{3.4}$$

where τ_m is the width of the lag window. The spectral resolution of the autocorrelation spectrometer, $\Delta\nu$, can be defined as the half-width of $W(\nu)$:

$$\Delta\nu = \frac{0.605}{\tau_m}. \tag{3.5}$$

From the Nyquist's sampling theorem, the width of the lag window is

$$\tau_m = \frac{N_0}{2\Delta B} \tag{3.6}$$

where N_0 is the number of lags, 1024, andΔB is the bandwidth, 64 MHz (Rohlfs & Wilson 2000). Therefore, the spectral resolution is found to be

$$\Delta\nu = 1.21\frac{\Delta B}{N_0} \tag{3.7}$$

or 1.21 times the channel width, 13.2 km s^{-1}, which means that the unsmoothed spectra have a resolution of 16 km s^{-1}.

In the presence of strong narrow lines, this spectral response causes strong ringing that decays roughly as n^{-1} (or $1/2\tau_m$), where n is the number of channels away from the narrow line. A standard procedure to suppress the ringing effect is to apply a different filter, of the form

$$w(\tau) = \begin{cases} 1 + \frac{1}{2}\cos\left(\pi\frac{|\tau| - f\tau_m}{\tau_m(1-f)}\right) & \text{for } f\tau_m \leq |\tau| \leq \tau_m \\ 1 & \text{for } |\tau| < f\tau_m \end{cases} \tag{3.8}$$

where $1 - f$ is the fraction of the lag spectrum that is tapered, or the ratio of the tapered section to the constant section. For $f = 1$, the rectangular window is recovered from equation (3.8) and for $f = 0$ it becomes the Hanning filter

$$w_H(\tau) = \begin{cases} \cos^2\left(\frac{\pi\tau}{2\tau_m}\right) & \text{for } |\tau| \leq \tau_m \\ 0 & \text{otherwise} \end{cases} \tag{3.9}$$

for which the frequency response is

$$W_H(\nu) = \tau_m\left[\text{sinc}(2\nu\tau_m) + \frac{2\nu\tau_m}{\pi[1-(2\nu\tau_m)^2]}\text{sinc}(2\pi\nu\tau_m)\right]. \tag{3.10}$$

and the corresponding frequency resolution is

$$\Delta\nu_H = \frac{1}{\tau_m} = 2\frac{\Delta B}{N_0}. \tag{3.11}$$

Therefore, the frequency resolution of Hanning smoothed spectra is 26.4 km s^{-1} or 40% less than using the window given by equation (3.3). Nevertheless, the sidelobes are effectively suppressed, decaying as n^{-3}, with the first sidelobe at 2.6% of the peak, whereas for (3.3) it is at 22% (Rohlfs & Wilson 2000).

If only a part of the lag spectrum is tapered, controlled by the parameter f, the sidelobe level is higher but the frequency resolution is less degraded compared to the Hanning window. HIPASS spectra are smoothed using the Tukey 25% filter, for which $1 - f = 0.25$. The Tukey filter can be regarded as a convolution of a cosine lobe of width $fN_0/2$ with a rectangle window of width $(1 - f/2)N_0$. The sidelobes still decay

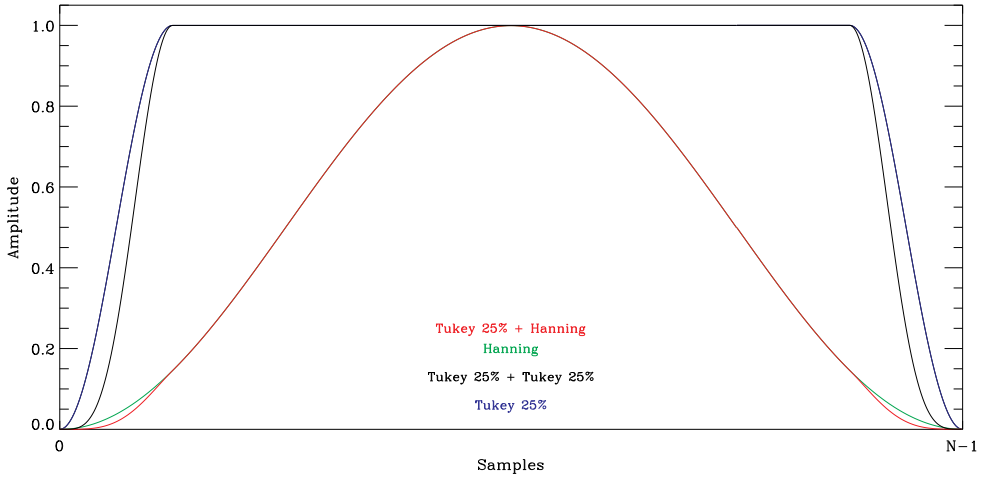

Figure 3.8: Filter functions in the lag domain. Note the minimal difference between the Hanning and Tukey+Hanning filters.

as n^{-3}, but the first sidelobe is at 20% of the peak. However, the spectral resolution is only degraded by 15% compared to the rectangular window. Therefore, the resolution of the Tukey smoothed spectra is 18 km s^{-1}, or 1.36 times the channel spacing.

The Tukey and Hanning filter functions can be combined, multiplied in the lag domain, to produce Tukey+Hanning smoothed spectra. The corresponding frequency resolution is 2.05 times the channel spacing, thus 27 km s^{-1} for the HIPASS 13.2 km s^{-1} channel width. The combination of the two filters is dominated by the Hanning window, therefore the resolution is not much different from Δv_H (3.11). If, on the other hand, the Tukey filter is combined with itself, then the final spectral resolution is 20 km s^{-1}.

Figures 3.8 and 3.9 show the different window functions in the lag domain and how the ringing caused by the Galactic H line is suppressed by applying each filter. Spectral smoothing of the data is important due to the proximity of one of the RRLs, H166α, to the H line.

3.2.3 Velocity tracking and residual baseline removal

After spectral smoothing and bandpass removal, performs the velocity frame conversion. HIPASS observations are made in topocentric mode, thus the observing

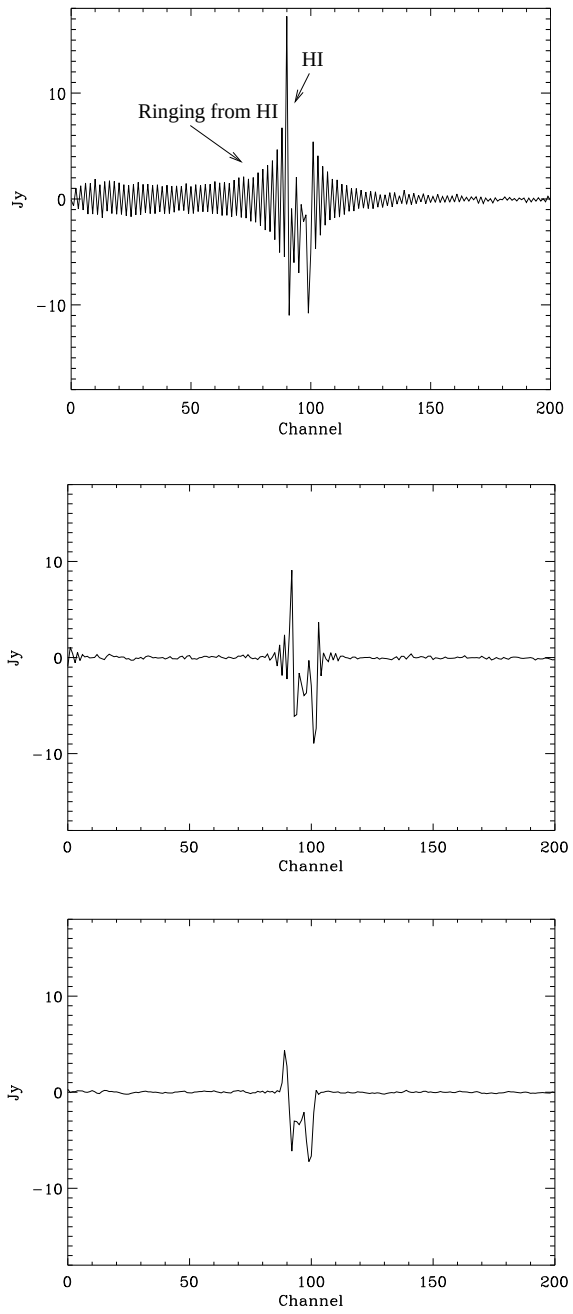

Figure 3.9: Suppression of the ringing in the unsmoothed spectrum (top), caused by Galactic H emission, by spectral smoothing using the Tukey (middle) and Hanning filters (bottom).

frequencies for each channel are fixed throughout the survey. currently applies the correction by scaling the reference frequency and channel increment by the Doppler factor and then shifting the spectra by a fraction of a channel to make the reference frequency an integral multiple of the original channel spacing. Apart from the Barycentric frame conversion, used for extragalactic studies, also converts to the Kinematic Local Standard of Rest (LSRK) frame. This is the preferred frame for Galactic studies, since the resulting radial velocities are in a system such that the gas in the Solar neighbourhood is at rest. This reference frame is based upon the average velocity of stellar spectral type $A - G$ in the vicinity of the Sun without regard to luminosity class (Delhaye 1965; Gordon 1976), in which the Solar system is moving at 20 km s^{-1} towards $\alpha_{1900} = 18$ hours and $\delta_{1900} = +30°$. Therefore, the measurement of LSR velocities from Galactic spectral lines, is a direct measurement of their radial velocity due to Galactic rotation.

Residual baseline removal can be applied to the resulting spectra by , in the form of polynomial fitting. The ripple caused by strong continuum sources and by the Sun as well as the flux rise towards the high velocity end of the band due to nonlinearities of the receivers in the presence of a strong source, yield curved baselines that are not straightforward to correct. At this point, a DC level offset is removed from the HIPASS spectra using a robust first order polynomial fit. In order to ensure a fit that is robust to a high fraction of outlying data points such as strong Galactic H emission and strong narrow band interference, instead of minimising the mean of the squared differences between the data points and the fitted line, the median of the squared differences is minimised. This correction is satisfactory for most of the sky, since most parts of the spectra are away from the Galactic plane, thus free of continuum ripple, of baseline curvature and residual bandpass effects. Furthermore, most parts of the spectra are free of H line emission as well, due to the sparsity of galaxies on the sky. Nevertheless, where present, baseline ripple degrades the spectra and must be removed. Such a correction is only performed after the spectra are gridded and will be discussed in Section 3.2.5.

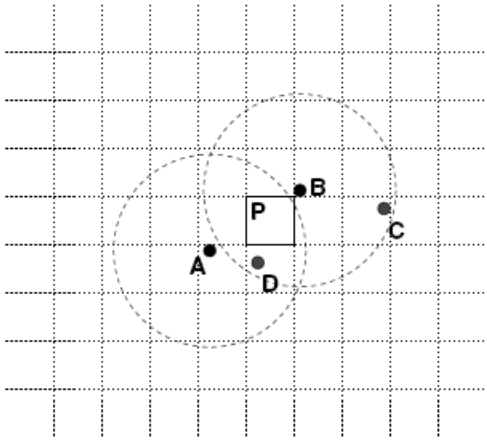

Figure 3.10: Diagram showing the positions of two observations A and B near a target pixel P with two sources C and D in the field. The dashed circles show the half-power radii of each observation (Barnes et al. 2001).

3.2.4 Gridding

At this stage, each individual spectrum for a unique position on the sky has been bandpass-corrected and calibrated and is now ready to be placed on a regular grid. is responsible for reconstructing the flux at a certain pixel given a number of single beam spectra measured at irregularly distributed positions near the target pixel.

The gridding algorithm used in the standard HIPASS reduction is optimised for point sources, since the aim is to detect galaxies that are expected to be smaller in angular size than the multibeam resolution, and is fully described in Barnes et al. (2001). Spectra that go into a given pixel are selected based on their distance from the centre of that pixel which is given by the smoothing radius $r_{\max}$, set to $6'$. The corresponding width of the top-hat smoothing kernel function is $12'$. Fig. 3.10 shows a schematic representation of the gridding process.

A simple estimate of the flux, F_e, to be assigned to the target pixel, can be estimated as the weighted mean of F_A and F_B, where $F_A = F'_A/w(r_A)$ and $F_B = F'_B/w(r_B)$ are the reconstructed fluxes of sources C and D. The weights $w(r_A)$ and $w(r_B)$ should only depend on the distance from the beam centre r and are given by the beam weighting

function $w(r)$, which can be written in the form

$$w(r) = \begin{cases} \exp\left[-\left(\frac{r}{\sigma}\right)^2 /2 \right] & \text{for } r \leq r_{\max} \\ 0 & \text{for } r > r_{\max} \end{cases} \tag{3.12}$$

assuming the telescope beam is a two-dimensional Gaussian function of width 14.4′, corresponding to $\sigma = 6.1'$. The median estimator is preferred over the mean estimator, for its robustness to corrupt data arising from externally generated interference or an observing system failure. Therefore, the flux value assigned to pixel P is

$$F_e = \frac{\text{median}(F')}{\text{median}(w)} \tag{3.13}$$

defined as median gridding. This included both polarisations, which is essentially as having twice the information for the same position. The term median(w) in equation (3.13) ensures that a source like D, near pixel P and thus likely to be detected by most observations around it, is reconstructed at a modest fraction of its intrinsic flux in pixel P. It also ensures that for a sky containing a single point source centred on pixel P, its reconstructed flux is exactly that of the point source. For a random distribution of observations and a smoothing radius $r_{\max} = 6'$, the median of the weights is simply the beam weighting function (3.12) evaluated at the radius which divides the smoothing area equally in two, meaning

$$\text{median}(w) = w(r_{\max}/\sqrt{2}) = 0.78. \tag{3.14}$$

As a consequence, the term median(w) over-corrects the fluxes of extended sources. For an infinitely extended source (in this case any source larger than say 60 arcmin), the over-correction is exactly the factor $1/\text{median}(w)$ of equation (3.13), which is $1/0.78 = 1.28$ (Barnes et al. 2001).

The resulting HIPASS datacubes from the gridding process are 8° RA × 8° δ with 4×4 arcmin^2 pixels and extend over the full frequency range. The ZOA datacubes are gridded in Galactic coordinates using the same paremeters. The final HIPASS image beam can only be estimated using simulations. The average beam of width

14.4′ is elongated in the scan direction to 14.7′ due to the telescope active scanning and then convolved with the gridding kernel, which is a 12 arcmin top-hat function. However, due to the non-linearity of the median estimator, the exact final beam is not well defined. It also depends on the sky sampling, source strength and source shape. Measurements of unresolved sources inserted into the data prior to gridding show that the resulting resolution is ∼ 15.5′ (Meyer et al. 2004; Donley et al. 2005).

3.2.5 Continuum ripple removal

In order to correct for the remaining baseline distortion that affects spectra in HIPASS images, an algorithm was designed to compute a template for the baseline ripple and remove it from each spectrum across the datacube. The *scaled template method* (Barnes et al. 2001) also called , computes a canonical baseline, $S_c = \sum_{i=1}^{M} w_i S_i$, using continuum source spectra and then removes it from all the spectra in the datacube. The selected S_i spectra are those that have the largest positive flux at the higher velocity end of the band, thus the canonical baseline is the weighted average of the spectra that better represent the shape of the bandpass curvature and continuum ripple. The weights are proportional to the increased system temperature (compared to the average system temperature) of the ungridded spectra which were combined to compute that part of the image. An iterative process is introduced to flag H signals that appear, for a given channel, in one spectrum but not in the others, which does not apply in the case of Galactic H emission. The final canonical baseline is then subtracted from all spectra across the datacube, scaled by a coefficient which is given by the slope of a linear regression to each spectrum S_i against S_c. Fig. 3.11 shows the canonical baseline generated by when applied to the HIPASS datacube covering the region $36° < \ell < 44°$, $|b| \leq 4°$.

This method was applied to the HIPASS and ZOA datacubes, in order to run the automatic and iterative processes of galaxy search (Meyer et al. 2004; Wong et al. 2006; Donley et al. 2005). It is only described here to present the maps in the next

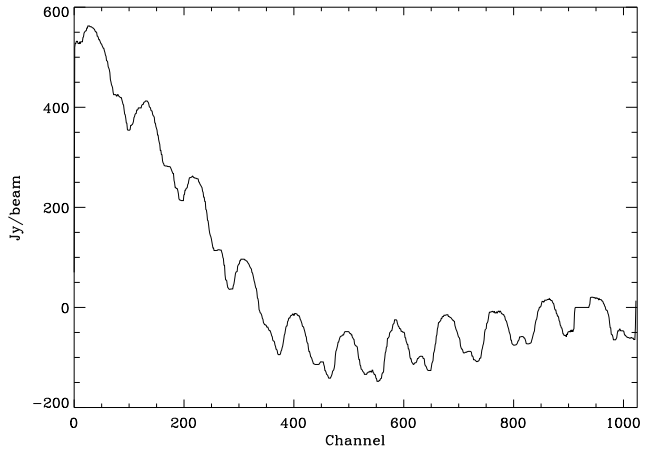

Figure 3.11: The baseline template resulting from the algorithm when applied to the HIPASS datacube that covers the region $36^\circ < \ell < 44^\circ$, $|b| \leq 4^\circ$.

Table 3.2: Frequency and velocity relative to the H line, for the three HIPASS hydrogen α lines.

Line	ν (MHz)	V (km s^{-1})
H168α	1374.601	+9667.6
H167α	1399.368	+4440.2
H166α	1424.734	−913.5

Section and it will not be further used in this work.

3.3 RRL data in HIPASS

Although HIPASS and ZOA surveys were designed to detect H emitting galaxies in the Local Universe, the 64 MHz bandwidth contains several hydrogen RRLs (Meyer et al. 2004). Since the α RRL transitions, for a given quantum number, are the most intense (equation (2.25)), only the following three RRLs are used in this study: H166α, H167α and H168α. Table 3.2 lists their rest frequencies and velocities relative to the Galactic H line, calculated using the classical Doppler formula.

The data reduction techniques described above are aimed at detecting extragalactic point sources. Thus H emission from extended H sources, including the Galaxy,

HVCs, the Magellanic Clouds and Stream, is corrupted in the standard HIPASS reduced data. Therefore, RRL emission in the HIPASS cubes will be restricted to individual H regions, since extended emission is truncated by the bandpass removal algorithm.

Figure 3.12 shows two HIPASS spectra, towards the bright H regions W49 and W47, where the three RRLs can be identified at their rest frequencies. The spectra are from a HIPASS datacube covering the ZOA-040 zone, reduced using the standard procedure described in the previous sections. The continuum ripple removal algorithm, , has produced a flatter baseline for W47 than for the stronger H region W49, where oscillations in the spectrum are still noticeable. The fact that uses spectra from strong continuum sources means that the RRLs are likely to be included in the canonical baseline. Indeed, Fig. 3.11 shows a small signal at the frequency of the H167α line. As a result, the RRLs or a fraction of their signal, are subtracted from the spectra across the cube as well as shifted in frequency due to the different LSR velocities of the lines for each H region.

Figure 3.13 shows the H167α peak line temperature maps, covering the Galactic plane between $\ell = 300^\circ \rightarrow 52^\circ$ and $|b| < 5^\circ$, obtained using HIPASS datacubes reduced as described in this Chapter. The maps confirm that no large structure is recovered with the standard reduction process, only individual H regions and some diffuse emission around them. Therefore, the data need to be reprocessed using different algorithms that preserve spatially extended emission. That will be treated in the next chapter.

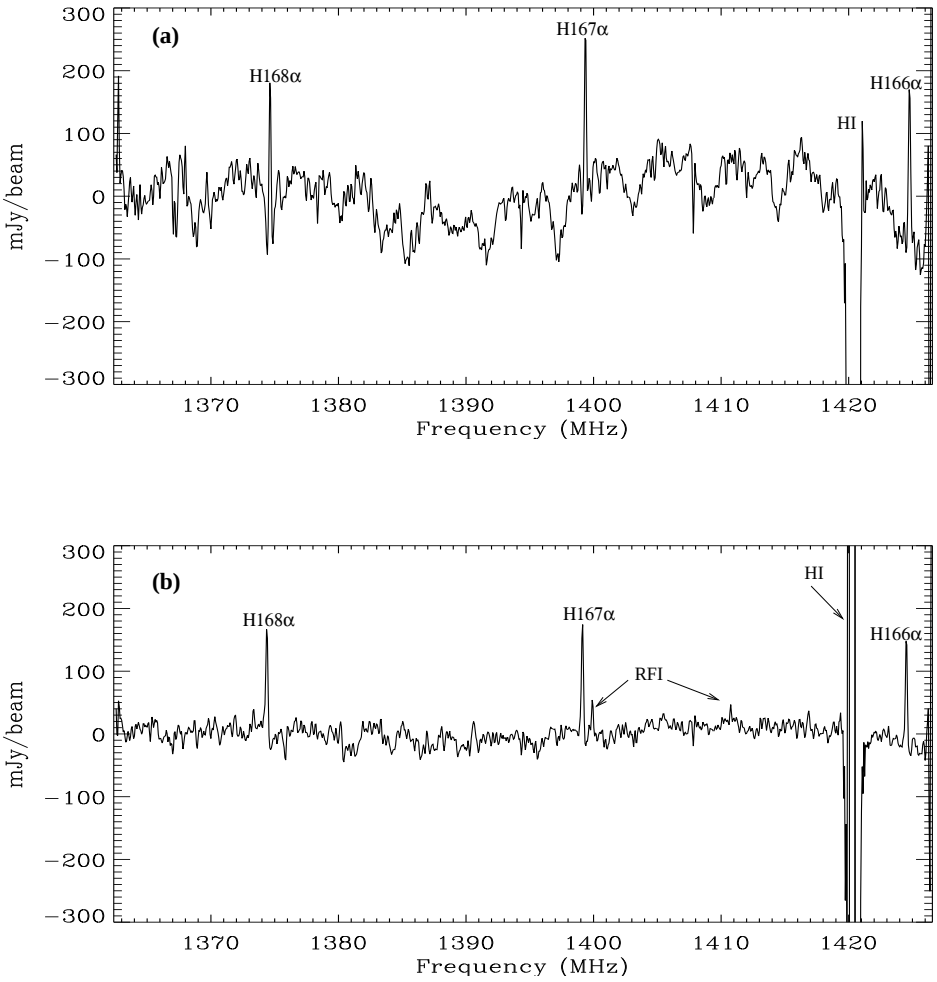

Figure 3.12: HIPASS spectra for two H regions, W49 G43.2+0.0 (a) and W47 G38.0-0.3 (b). The three RRLs can be clearly seen as narrow lines at their rest velocities and are distinguishable from the ripple.

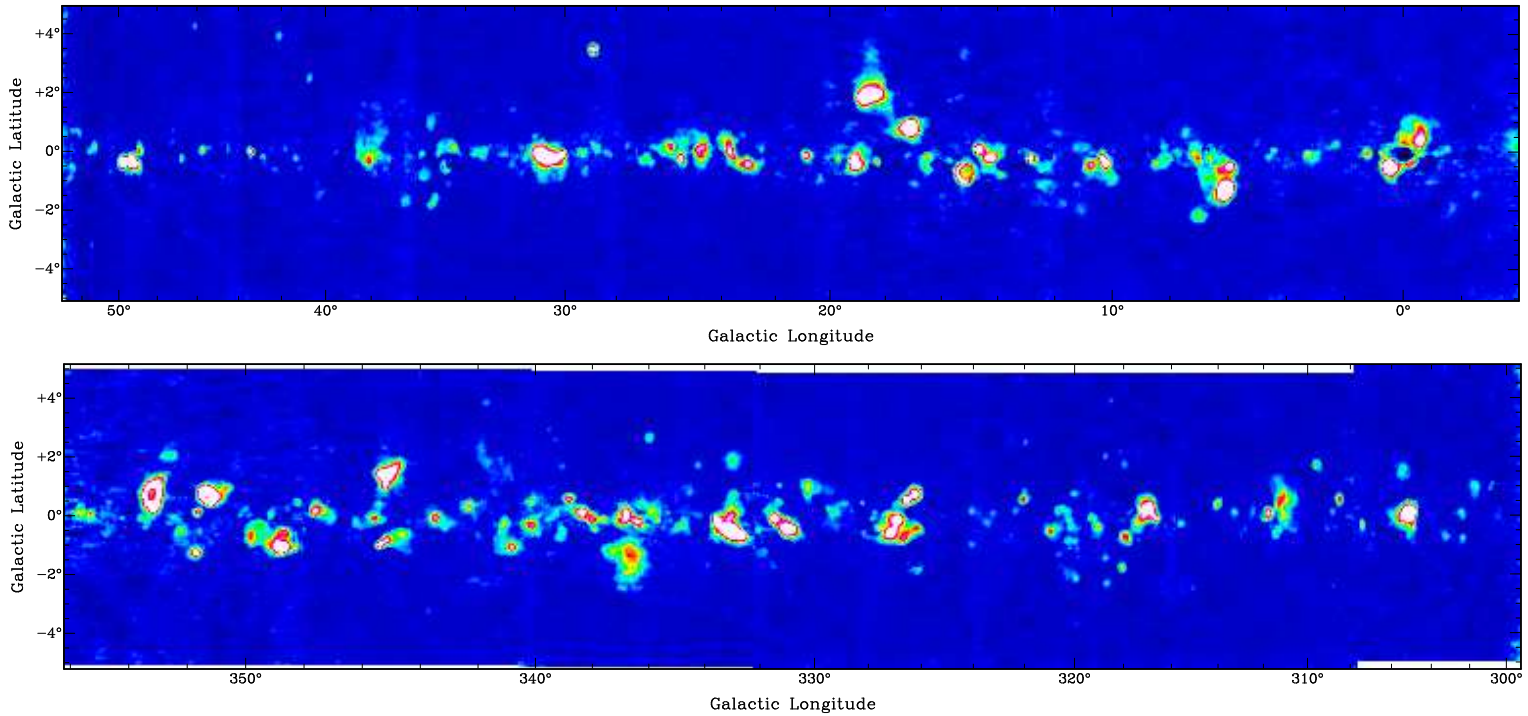

Figure 3.13: H167α peak line temperature maps on a linear colour scale from −0.04 Jy/beam to 0.22 Jy/beam. The maps are obtained from the HIPASS cubes covering the Galactic plane between $\ell = 300^\circ \rightarrow 52^\circ$ and $|b| < 5^\circ$, reduced using the standard HIPASS reduction as described in Barnes et al. (2001).

4

RRL emission in the ZOA-040 data cube

For the initial analysis, the datacube covering the longitude range $\ell = 36^\circ$ to 44° was chosen. This includes emission from the Local, Sagittarius and Scutum spiral arms. The intersection of the survey area with the three arms can be seen in Fig. 2.3. Clearly the major contribution to the RRL emission will be from the Sagittarius arm which is sampled at distances of 3 to 7 kpc. The line of sight is tangent to the Scutum arm at $\sim$ 6 kpc. Significant RRL emission from the inner Galaxy is expected in this longitude range, which is also covered by other surveys such as the Effelsberg (Reich et al. 1984, 1990b) and Very Small Array (Todorović et al. 2010) surveys of the Galactic plane.

An examination of RRL surveys, such as Gordon & Cato (1972), Hart & Pedlar (1976), Lockman (1976), Heiles et al. (1996b) and Lockman et al. (1996), shows line brightness temperatures of $\sim$ 50 – 100 mK in areas away from strong H regions. The ZOA survey, with an rms sensitivity per beam per channel of 6 mJy, provides the required level to map the Galactic ridge RRL emission. The challenge though, is to achieve this sensitivity in the presence of baseline effects and interference as the following sections will describe. Therefore, the deeper ZOA data for this region is used in preference to HIPASS data. This corresponds to the cube ZOA-040, centred

at (ℓ, b)=(40°,0°). Some of the results presented in this Chapter have been published in the Monthly Notices of the Royal Astronomical Society (Alves et al. 2010) and are based on the data analysis described here.

4.1 RRL Data reduction

Since the diffuse Galactic RRL emission is a narrow-band extended along the Galactic plane, a modified version of the bandpass removal technique is required. The gridding algorithm also needs to be adjusted for the treatment of extended emission. The ZOA RRL data processing can be summarised as follows:

- The bandpass correction is performed using the 5 algorithm.
- Spectra are shifted to the LSR frame and Tukey+Hanning smoothed.
- The gridding is done using a median with no beam normalisation of the data.
- Each RRL is extracted from the spectra in the final cube and corrected for baselines.
- The three RRLs are stacked at each position and the final line is corrected for any remaining baseline.

These steps are described in detail in the next sections.

4.1.1 Bandpass correction - The 5 method

is the bandpass reduction algorithm developed to recover extended emission from HIPASS data. While the standard reduction calculates the bandpass correction through a median of the reference spectra taken ±2° from the target spectrum, filtering out emission that extends over angular scales greater than 2° in the scan direction, uses the entire 8° scan to recover large-scale emission. For each channel, beam and polarisation, $_n$ breaks the scan into n sections, finds the median value for

each section and uses the minimum of the median values to form the bandpass template for the entire 8° scan.

5 has been successfully implemented to image the Magellanic Stream (Putman et al. 1998) as well as HVCs in the southern sky (Putman et al. 2002). This method greatly increases the sensitivity of the data to large-scale structure without substantial loss of flux density, except when the emission fills the entire 8° scan. The possible time variation of the bandpass makes 5 less stable than the standard HIPASS method due to the difference in the value chosen for adjacent scans. However, the only effect is small residual striation in the final cube (Putman et al. 2002, 2003).

Figure 4.1 shows the difference in channels maps of the H167α line from the ZOA-040 datacube reduced using 5 and the standard median procedure. The standard method clearly filters out emission resulting in negative sidelobes, that are reduced using the 5 method. The biggest negative in the map reduced using the standard procedure is -28.8 mJy/beam, whereas in the map reduced using 5 is -13.8 mJy/beam. There are, however, still sidelobe artifacts and flux loss due to the emission filling the entire 8° scan. Because the ZOA scans are taken at constant Galactic latitude, this affects the Galactic plane where RRL emission is expected along the whole longitude scan. In that case, the minimum of the medians contains real emission and so the bandpass correction lowers the flux, or even generates negatives in the spectra (see section 4.1.6). The striping along the scanning direction is also visible in the 5 channel map at a 1.5σ level, thus it only affects the low flux density regions. In terms of emission recovered per channel, Fig. 4.2 shows the spectra, H167α line, of the H region W47 at (ℓ, b)=(37°.0,$-$0°.2), again reduced with the standard method (dashed line) and with 5 (full line). The emission lost in the individual channels is apparent, as well as the negative sidelobes in the spectrum reduced with the original HIPASS bandpass method.

The 5 greatly improves the quality of the channel maps and the spectra, thus it is clear that a bandpass calibration method that utilises the whole scan is better for recovering extended emission than the standard compact method. Putman et al.

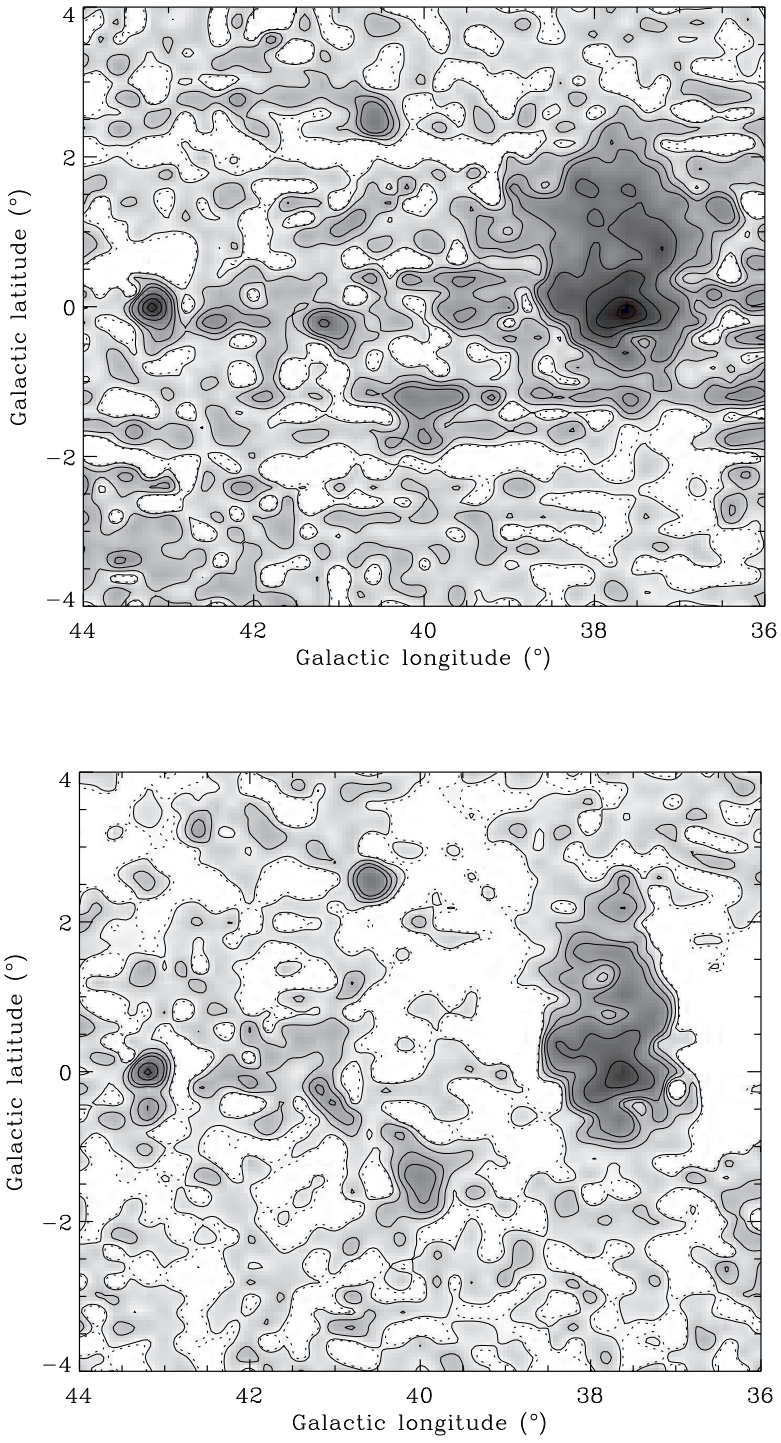

Figure 4.1: Channel maps, $V_{\rm LSR} \approx 30$ km s^{-1}, of the H167α line from the ZOA-040 datacube reduced with the 5 method (top) and with the standard bandpass reduction method (bottom). Contours are shown for ±0.5, 5, 10, 15, 30, 45, 60, 75 and 90 mJy/beam and the logarithmic colour scale ranges from −1 to 80 mJy/beam.

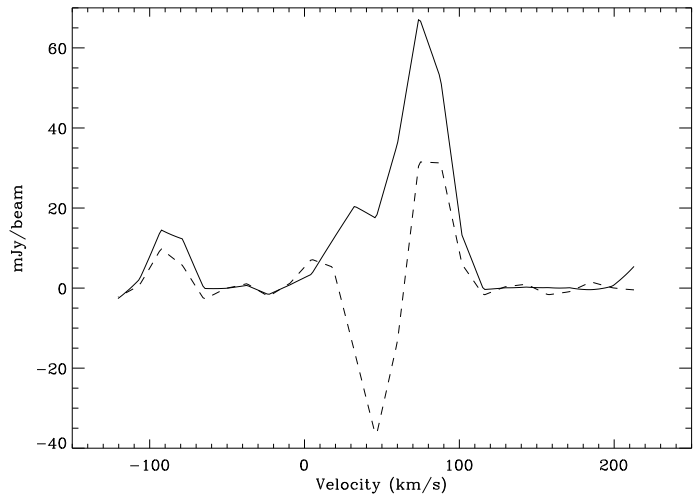

Figure 4.2: H167α line 12 × 12 arcmin^2 average spectra of the H region W47, at (ℓ, b)=(37°.0,−0°.2). This shows the difference between spectra reduced with the standard method (dashed line) and with 5 (full line).

(2002) found that the minimum of a series of medians with 5 sections was the best compromise between recovering as much extended emission as possible and the risk of selecting a value which does not accurately represents the bandpass.

In order to establish 5 as the preferred method for RRL bandpass correction, a different number of sections were tested. Fig. 4.3 shows channels maps of the H167α line reduced using *n* for *n* = 3, 8, 10 and 15 sections. Increasing the number of sections increases the total flux recovered in regions where the emission fills the entire 8° scan. This is noticeable on the Galactic plane, where more flux is recovered with 15 as compared to the other number of sections, further illustrated in the spectra of Fig. 4.4. However, increasing the number of sections also leads to an increased variation in the correction for adjacent scans, resulting in stronger striping residuals. The longitude stripes are visible in all the channel maps of Fig. 4.3, although maps (c) and (d), with a similar rms of ∼ 5.2 mJy/beam, have a more pronounced striping than the 5 map, of rms ∼ 3.2 mJy/beam. Furthermore, the channel maps reduced with 15, 10 and 8 sections result in more negative flux than with 5 sections. The 5 map shows slightly more striping as compared to the 3 map, but also

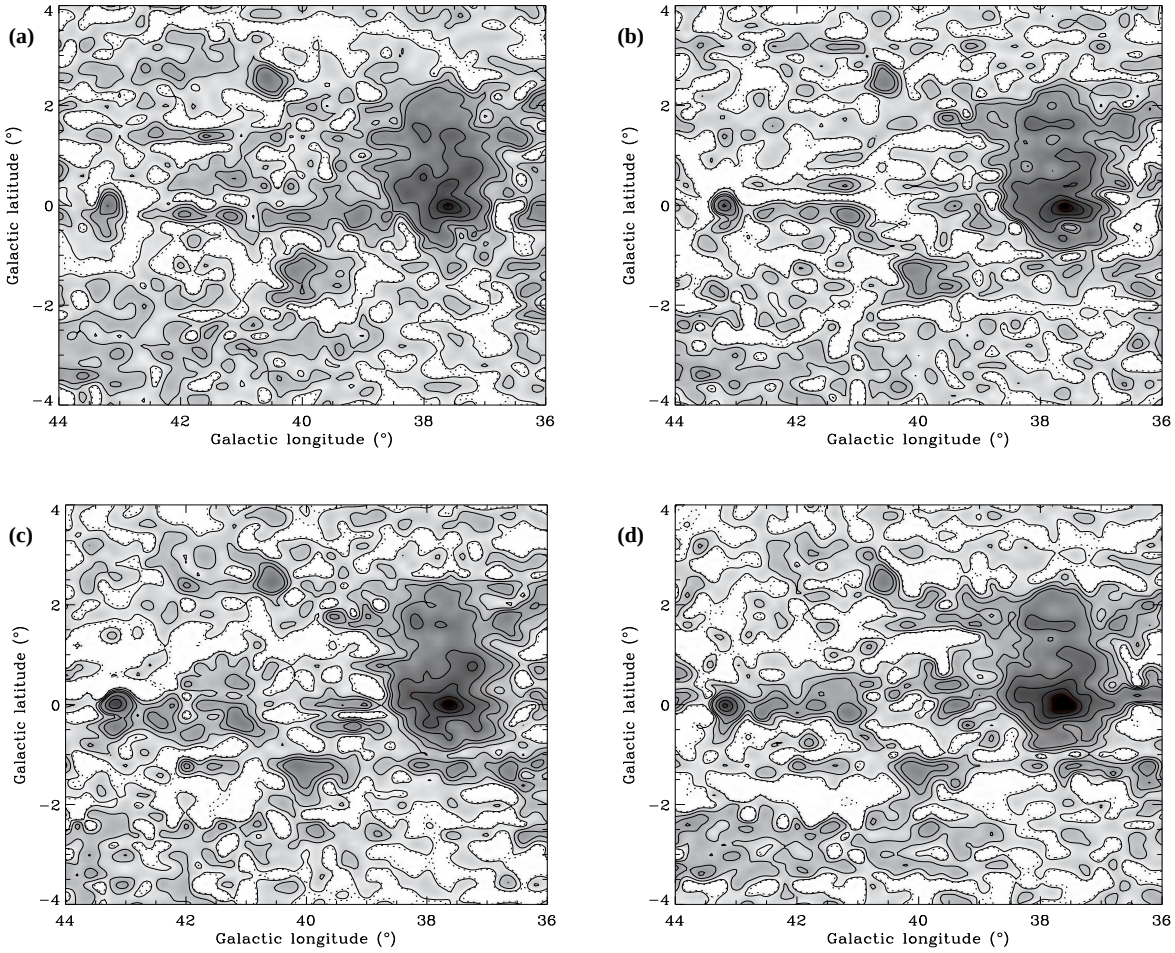

Figure 4.3: Channel maps, $V_{\rm LSR} \approx 30$ km s^{-1}, of the H167α line from the ZOA-040 datacube reduced with the method using 3 (a), 8 (b), 10 (c) and 15 (d) sections. Contours and colour scale are the same as in Fig. 4.1.

more emission is recovered, specially along the Galactic plane.

As a result, 5 was at this stage the favoured method for the bandpass reduction in .

4.1.2 Spectral smoothing

As described in Section 3.2.2, the Hanning filter is more effective in suppressing the ringing caused by the strong Galactic H line than the Tukey 25% window: the price to

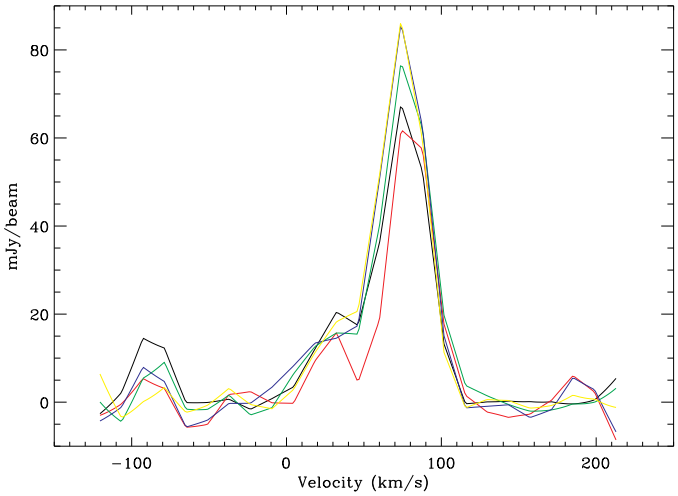

Figure 4.4: The difference in the total flux per channel in the 12×12 arcmin^2 average spectra toward the H region W47, at (ℓ, b)=(37°.0,−0°.2), for the different number of sections in the method. 3 is the red line, 5 is the black line, 8 is the green line, 10 is the blue line and finally 15 is the yellow line.

be paid is a broadening of the spectrum from a half-width of 18 km s^{-1} to 26.4 km s^{-1}. This velocity resolution is still adequate to resolve the emission from the Local (V = 0 km s^{-1}), the Sagittarius (V = 40 km s^{-1}) and the Scutum arms (V = 80 km s^{-1}), that the ℓ = 40° cube covers.

Figure 4.5 shows the RRLs for the H region W45, (ℓ, b)=(40°.5,2°.5), where the effect of the different smoothing functions is visible. It shows that the peak line temperature decreases with the increasing filtering, although the line integral is constant. The H166α line is the closest to the Galactic H signal, 4.3 MHz or 66 channels away from it, therefore is the most affected. Nevertheless, the ringing can be effectively removed by applying the combined Tukey+Hanning filter, which only degrades the velocity resolution to 27 km s^{-1}, as compared to 26 km s^{-1} from the Hanning filter alone. As a result, the three RRLs can be added without propagating the H ringing that contaminates the H166α line, to the stacked spectrum.

Gaussian fits to the H168α line give widths of 28.0±0.6 km s^{-1}, 36.2±0.9 km s^{-1} and 36.4 ± 0.3 km s^{-1} for the Tukey, Hanning and Tukey+Hanning smoothed spectra, re-

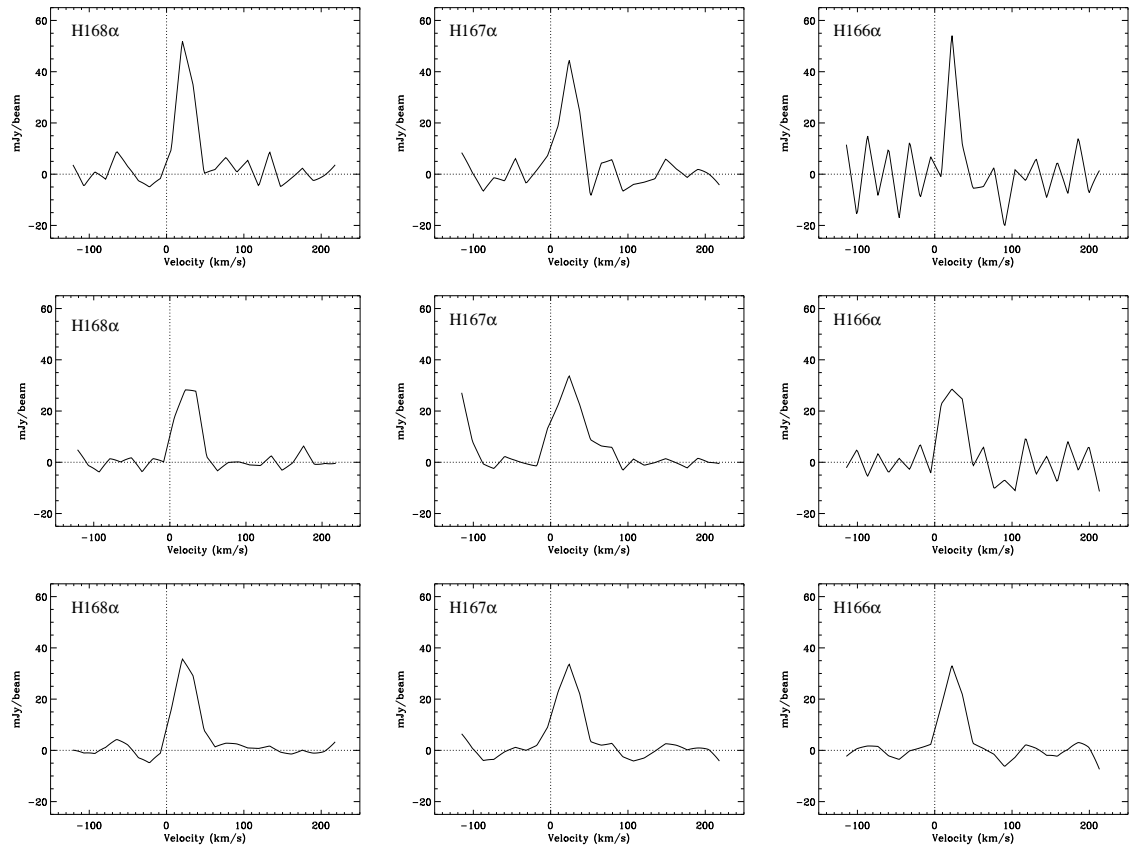

Figure 4.5: RRLs for the H region W45, (ℓ, b)=(40°.5,2°.5), taking a 12×12 arcmin^2 average spectra smoothed with the Tukey (top), Hanning (middle) and Tukey+Hanning (bottom) filters. The residual ringing can be effectively removed by applying an additional process of Hanning smoothing to the Tukey smoothed spectra.

spectively. Taking into account the broadening caused by each of the filters, the results are consistent with a line width of 24 ± 1 km s^{-1} for the H region W45.

4.1.3 Gridding

The standard HIPASS gridding process uses the median of all spectra within a 6′ radius, divided by the median of the corresponding weights (equation 3.13). Since this overcorrects the fluxes of extended sources, the simple median is used. Therefore, the flux value assigned to a given pixel is

$$F_e = \text{median}(F') \tag{4.1}$$

where F' are the measured fluxes within the smoothing radius is of 6 arcmin. Thus, following the discussion of Barnes et al. (2001), the resulting flux density scale is correct for extended sources such as the Galactic plane. The same gridding algorithm was used by Putman et al. (2002) to recover the correct fluxes of HVCs. This process increases the beam width from 14′.4 to 15′.5 (Section 3.2.4).

4.1.4 Standing wave mitigation

The RRL spectra suffer from the effects of standing waves produced when the continuum waves from the target H region interfere with a fraction of the radiation which reaches the focus along separate paths. Although this extra signal is of the order of a few percent of the main signal, it can be comparable with the intensity of the RRL itself, which in the case of the lines at ∼1.4 GHz is ∼1 % (Section 2.2.3). Most of the interfering signal results from standing waves between the focus area (prime focus cabin and supports) and the apex of the antenna, and is also produced by scattered solar radiation. Even during the night, scattered radiation can arise from Galactic structures adjacent to the H region under investigation. This is the case in the present study of a bright section of the Galactic ridge. Similarly, radiation from the ground can find its way into the focus area. All these sources contribute to the standing waves; they will vary with time of day, the azimuth and elevation and the position in the celestial sky.

On the present dataset, the ripple pattern presents two distinct components: one associated with continuum sources and the other caused by off-axis power. Figs. 4.6 and 4.7 show the variation of the standing wave pattern with latitude, at $\ell = 42°.0$ and $\ell = 38°.0$, taking $2° (\ell) \times 1° (b)$ average spectra, at $b = 0°.0, \pm 1°.5$ and $\pm 3°.0$. The ripple pattern on the plane, Figs. 4.6 and 4.7 (c), is associated with the total power going in the main beam of the telescope, or on-source power and has the characteristics described and seen before. The amplitude of the ripple is about 20 mJy/beam at $\ell = 42°.0$ and $\sim$ 120 mJy/beam at $\ell = 38°.0$, a much stronger region of the cube, coincident with the extended group of H regions, W47. For this reason, the spectra at $\ell = 38°.0$ and

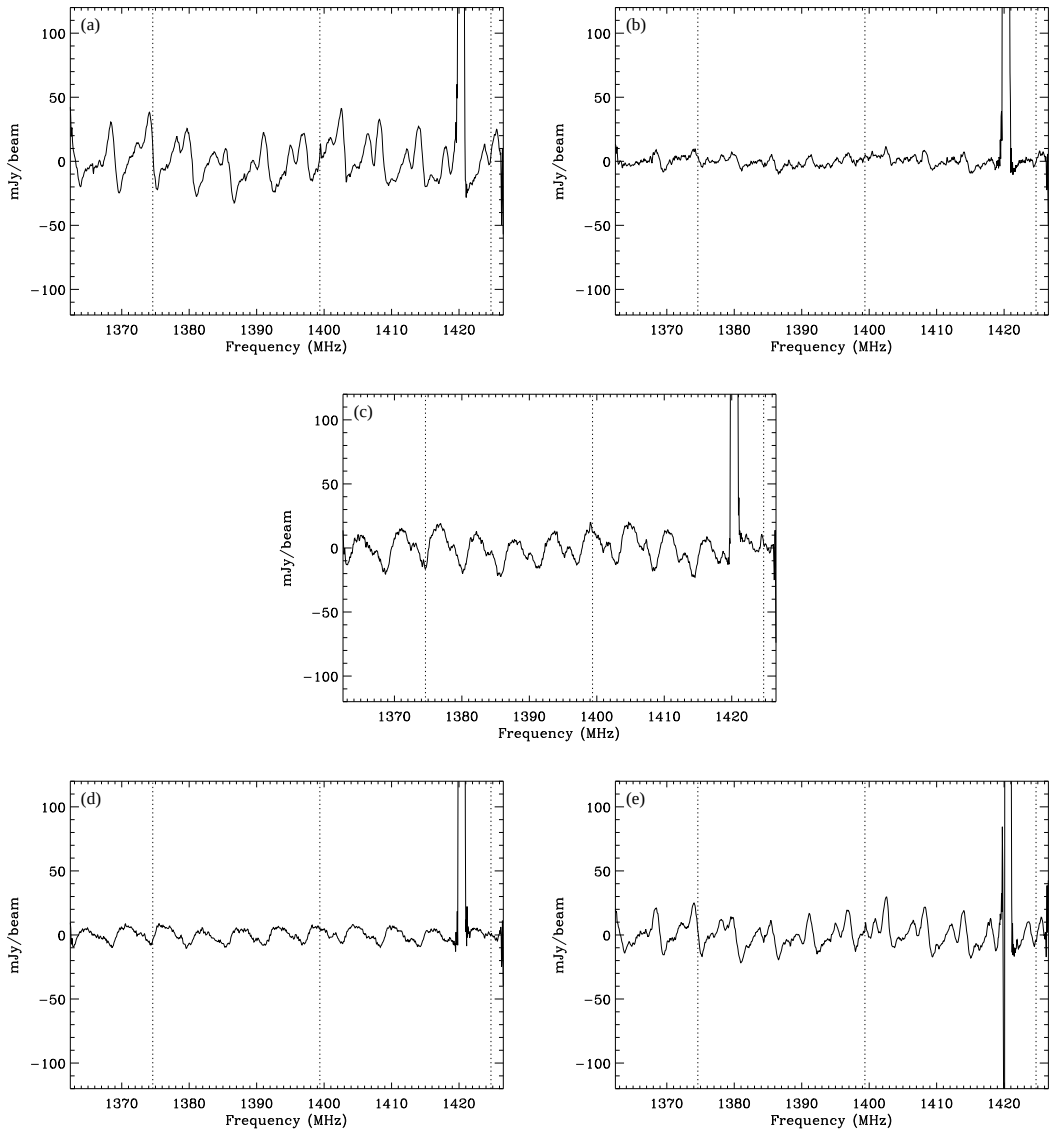

Figure 4.6: The standing wave pattern variation with Galactic latitude and longitude, at $\ell = 42°.0$. Figures (a) to (e) are at $b = -3°.0, -1°.5, 0°.0, 1°.5, 3°.0$, respectively. Each plot shows an average $2° (\ell) \times 1° (b)$ spectrum. The vertical dotted lines indicate the rest frequency of the three RRLs.

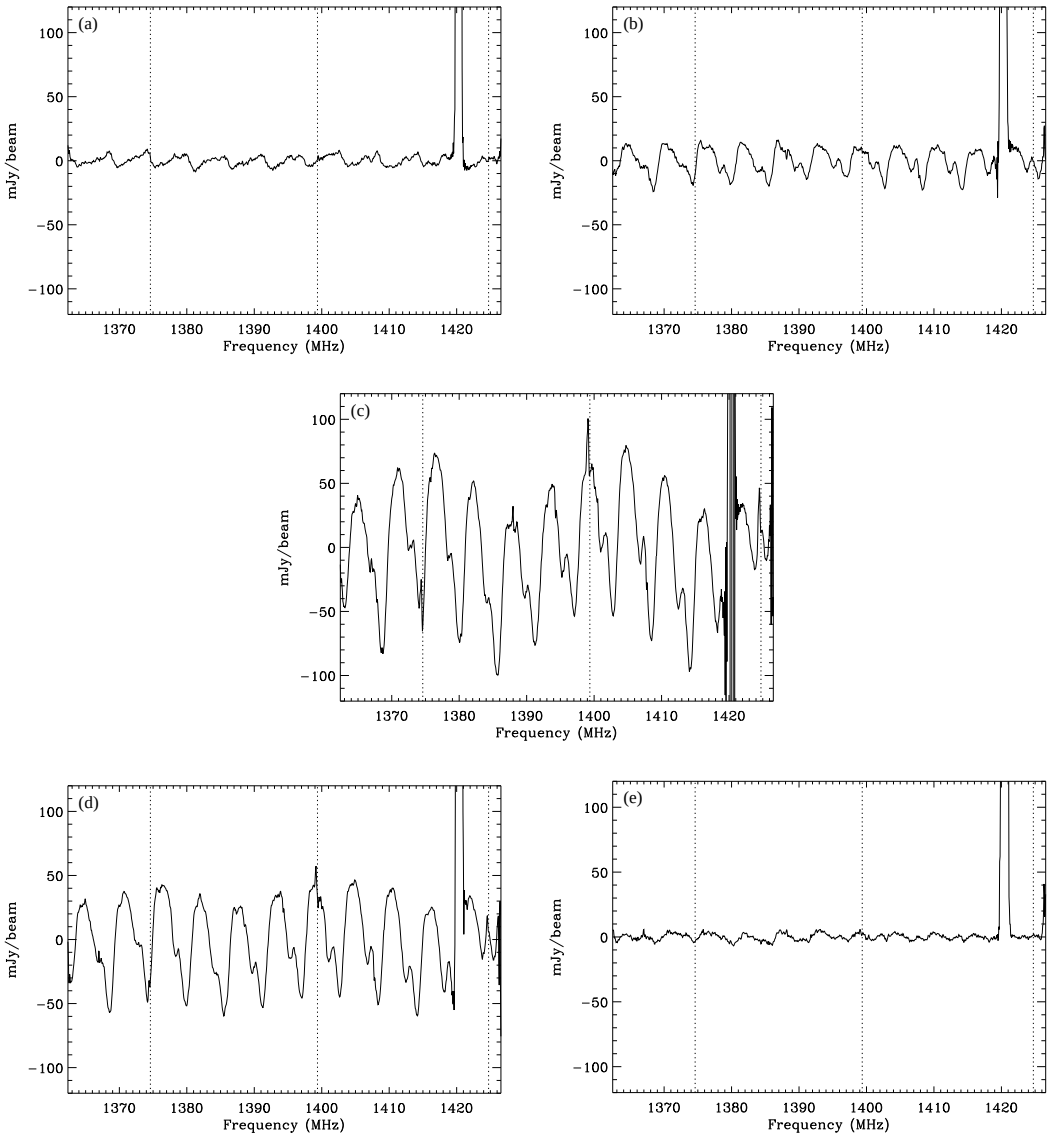

Figure 4.7: The standing wave pattern variation with Galactic latitude and longitude, at $\ell = 38°.0$. Figures (a) to (e) are at $b = -3°.0, -1°.5, 0°.0, 1°.5, 3°.0$, respectively. Each plot shows an average $2° (\ell) \times 1° (b)$ spectrum. The vertical dotted lines indicate the rest frequency of the three RRLs.

$|b| = 1.^{\circ}5$ still have the signature of the continuum source related ripple. Out of the Galactic plane, the spectra show the pattern seen in Figs. 4.6 (a) and (e), with 5.7 MHz still the dominant frequency, but with different fine structure. This pattern is due to the power picked up by the beam sidelobes, either coming from the extended Galactic ridge or the ground. The signal near the rest frequency of the H167α RRL in Figs. 4.6 and 4.7 (a) and (e) is likely to be interference and not a real line, since it is not seen in the other two channels. That is indeed the best way of checking if a signal is in fact an RRL. The same standing wave pattern at $b = \pm 3^{\circ}$ is common to both longitudes, although weaker at $\ell = 38^{\circ}$.

The variation of the continuum ripple with position implies that the baseline around each RRL also varies across the cube. Under these circumstances and given the fact that only a fraction of the 64 MHz spectra is used, corresponding to the three RRLs, it was chosen not to apply a baseline fit to the spectra in nor to use , but to perform local baseline fits around each line. This method is described below. [1] was used to perform all the post-processing analysis of the data.

Baseline fitting

The three RRLs are extracted from the spectra at each position in the gridded datacube, with a given number of channels either side of the line, meaning either side of its rest frequency channel. The RRL spectra are then linearly interpolated to a final grid of 0.1 channels, so that the spectra can be shifted to within a tenth of a channel. The channels containing the rest frequency of each line are given in Table 4.1.

The baseline is estimated and removed by fitting a polynomial to each line, excluding the velocity where the RRL gas is expected to emit in this longitude range, using the outlier-resistant polynomial fit procedure [2], in . From the inspection of Fig. 1.6 as well as the velocity information in the Lockman (1989) survey, it can be seen that the RRL emitting gas for $36^{\circ} < \ell < 44^{\circ}$ is confined to a velocity

[1] Iterative Data Language

[2] From the Astronomy Library

Table 4.1: Rest frequency channels of the three RRLs.

Line	ν (MHz)	Rest frequency channel	Rest frequency channel after interpolation
H168α	1374.601	196	196.0
H167α	1399.368	592	592.3
H166α	1424.734	998	998.2

range of about 0 to 100 km s^{-1} with a major contribution from the Sagittarius arm ($V \sim 40 - 50$ km s^{-1}). This should be the velocity range excluded from the fit in order to preserve the RRL information.

The other two parameters to adjust are the velocity range for the fit, i.e. the number of channels selected either side of the line, and the degree of the polynomial. Fig. 4.8 shows the spectrum from the datacube at the position of W47 (ℓ, b)=(37°.5,−0°.1), or G37.5-0.1, with a peak $T_a \sim 12$ K. This slightly extended H region has a velocity of ~ 53 km s^{-1}, and thus is located in the Sagittarius arm. The Tukey+Hanning smoothed spectrum, Fig. 4.8 (a), shows the baseline curvature and the periodic standing wave pattern with a frequency of 5.7 MHz. This is the frequency expected for standing waves between the focus and the apex of a 64-m antenna with $f/D = 0.4$. There is additional fine structure in the pattern due to longer integration paths. This fine structure does not repeat exactly over the 64 MHz bandwidth, as will be illustrated further in this section. The RRL spectra extracted from the total power spectrum are shown in Figs. 4.8 (b), (c) and (d). The conversion from frequency to LSR velocity is done using the radio convention Doppler formula, $V = c(\nu_0 - \nu)/\nu_0$, where ν is the frequency of each channel of the interpolated spectra and ν_0 the rest frequency of each line. The choice of channels should exclude the edge of the band for the H166α line as well as reduce the number of channels contaminated by the H ringing, which would affect the baseline fitting. The RRL spectra in Fig. 4.8 were extracted with 51 channels, so it results in a velocity range of $\sim \pm 300$ km s^{-1} either side of the RRL range ($0 - 100$ km s^{-1}). More channels give more points for the baseline estimate, but at the same time includes more curvature which requires a higher order polynomial fit. This is illustrated in the

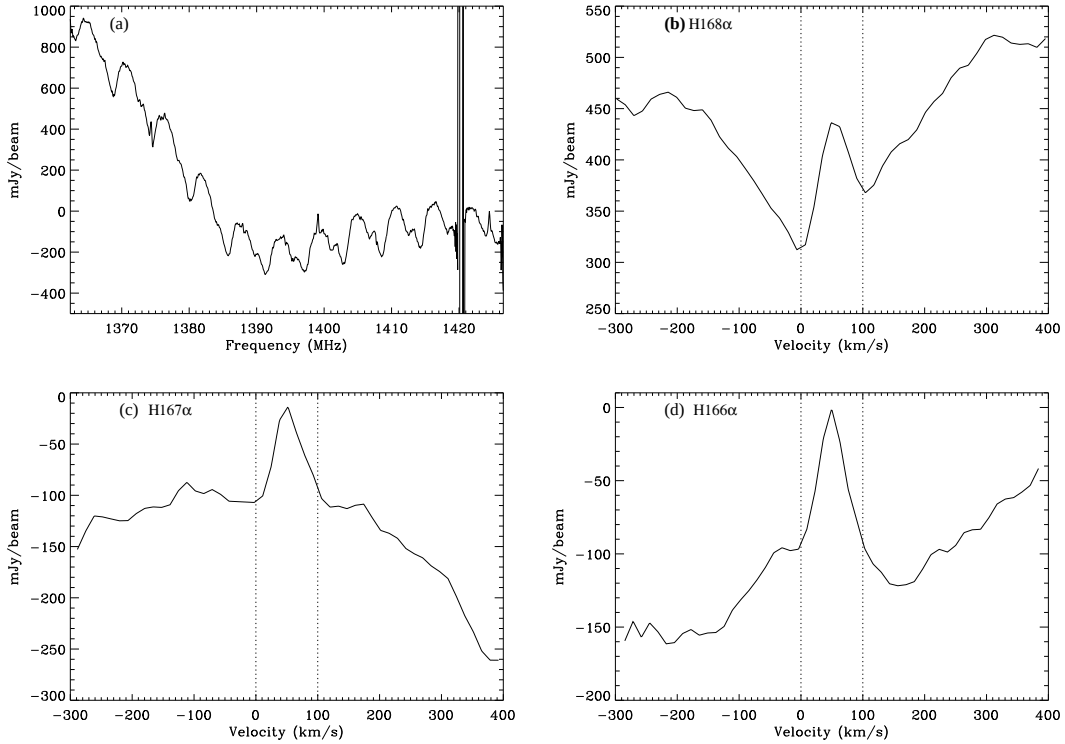

Figure 4.8: Total power spectrum (a) for the H region G37.5-0.1, taking a 12 × 12 arcmin^2 average spectrum Tukey+Hanning smoothed. The three RRLs are in figures (a), (b) and (c). The vertical dotted lines give the velocity range expected for RRL emission. The sinusoidal ripple caused by the continuum source is visible in the spectrum of panel (a).

spectrum of the H168α line in Fig. 4.8 (b), where the concavity of the baseline starts to invert at the edges of the spectrum. Similarly, for the other lines, a slightly narrower velocity range should enable a good baseline fit.

In spite of the above arguments for an RRL range of 0 – 100 km s^{-1}, other velocity ranges were tested. Fig. 4.9 shows the results of different polynomial fits to the H168α line for the H regions W47 (G37.5-0.1) and W49 (G43.2+0.0), excluding the velocity range −30 to 130 km s^{-1}. W49 lies on the far side of the Local spiral arm with a velocity of ∼ 7 km s^{-1}, which motivates the test of an RRL range that extends to negative velocities. Fig. 4.9 indicates that a 4$^{\text{th}}$ order fitting gives the best results, for both regions. However, the final spectra present negative sidelobes and non-flat baselines,

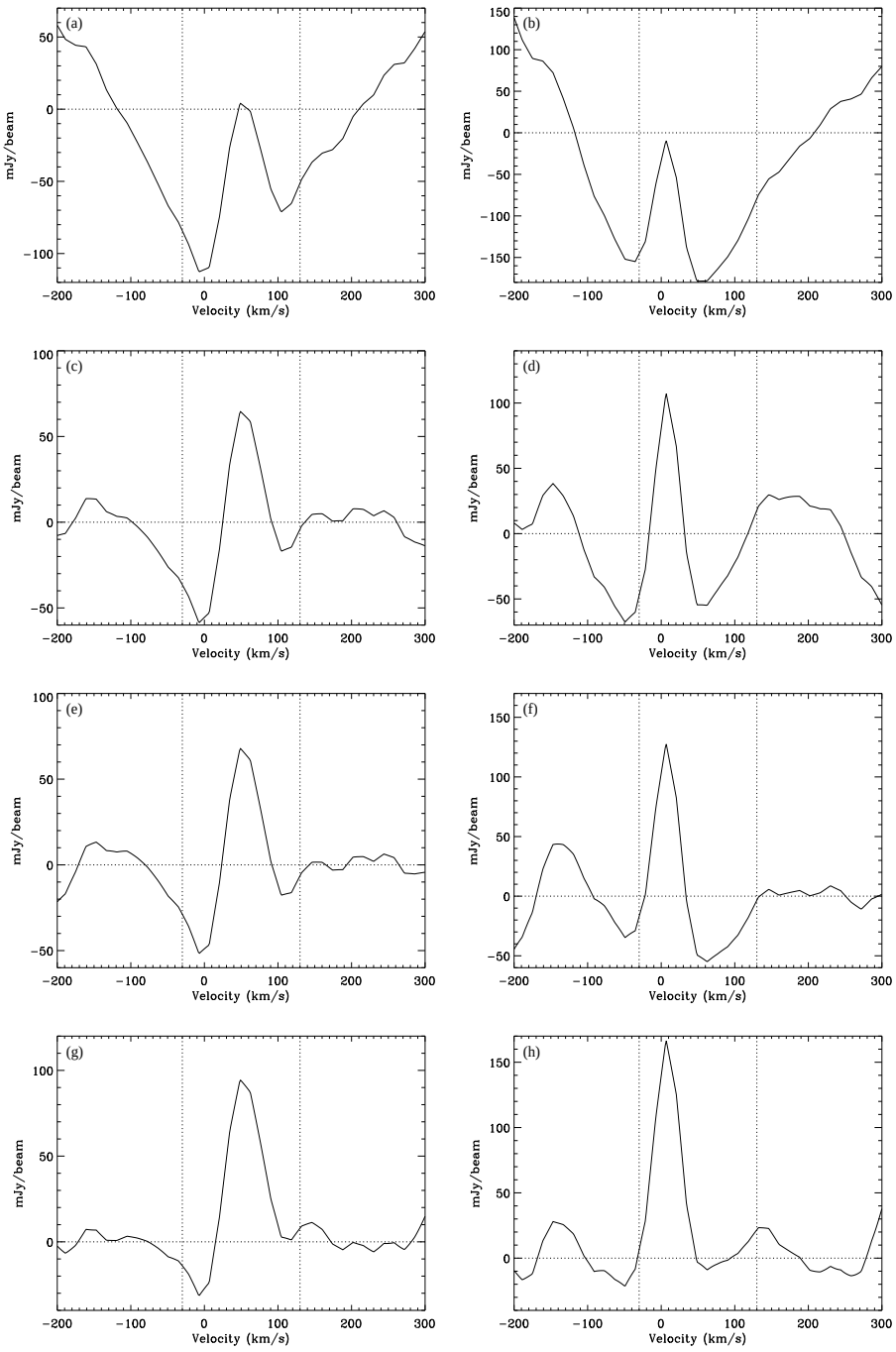

Figure 4.9: Results from different polynomial degree baseline fits to the H168α line, taking a 12×12 arcmin^2 average spectra for the H regions W47 - G37.5-0.1 (left) and W49 (right). The order of the polynomial increases from 1 to 4, from the top to the bottom figures. The velocity range for the fit is $[-200,300]$ km s^{-1}, excluding the range $[-30,130]$ km s^{-1}.

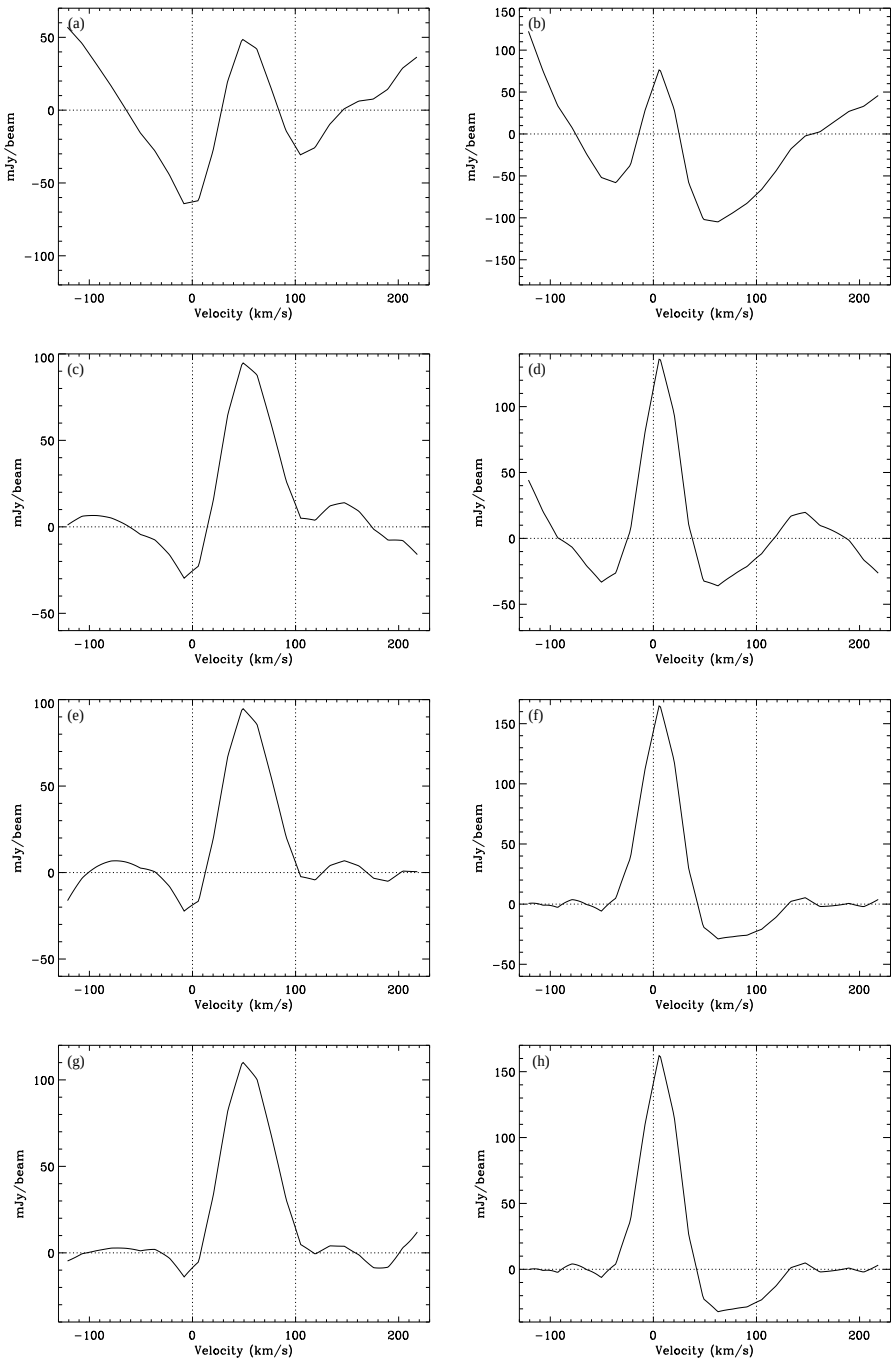

Figure 4.10: Results from different polynomial degree baseline fits to the H168α line, taking a 12 × 12 arcmin^2 average spectra for the H regions W47 - G37.5-0.1 (left) and W49 (right). The order of the polynomial increases from 1 to 4, from the top to the bottom figures. The velocity range for the fit is [−120,220] km s^{-1}, excluding the range [0,100] km s^{-1}.

due to the broad RRL range combined with the small-scale structure present in the spectra. These examples show that the fit should go as close to the line as possible and that at least a 4th degree polynomial is needed. Although this can be partly fitting the noise in some spectra, it is required due to the structure of the bandpass. This situation will be improved in Chapter 5. Therefore, the number of channels extracted should be sufficient to enable a robust 4th order fit and at the same time avoid too much structure in the spectra. Fig. 4.10 shows the baseline-corrected H168α line for the same regions as in Fig. 4.9. The polynomial fit is now performed using the data points between [−120,0] and [100,220] km s^{-1}. The improvement between the spectra in Figs. 4.9 and 4.10 is evident, for all the polynomial degrees in both regions. For this set of fitting parameters, a 3rd or 4th order fit gives similar results. For the H region W47, the negative sidelobe at 0 km s^{-1} decreased from 33 to 12% of the line peak, comparing Figs. 4.9 and 4.10 (g), and resulted in a flat baseline of rms of 5 mJy/beam. For W49, the line in Fig. 4.10 (h) developed a negative sidelobe at $\sim$ 60 km s^{-1}, whereas in Fig. 4.9 (h) it was at $\sim$ −20 km s^{-1} and not as deep. Nevertheless, the 4th order fit from −120 to 0 km s^{-1} and 100 to 220 km s^{-1}, results in a final baseline rms of 11 mJy/beam, as compared to 14 mJy/beam for the previous fit.

Figures 4.9 and 4.10 illustrate the difficulty of finding a baseline fit that takes into account the different standing wave patterns of each RRL spectra, as well as the central velocity shift of the lines. After inspection of the spectra of individual H regions in the datacube, this set of parameters, a 4th order polynomial fit between −120 and 220 km s^{-1} excluding the range 0 to 100 km s^{-1}, was found to be the best method for the baseline correction of each RRL.

A further complication in baseline correction is posed by the negatives generated in the 5 bandpass removal (Section 4.1.1). These are visible in the baseline corrected spectra and are not presented here, but in Section 4.1.6, since they are dealt with after line stacking.

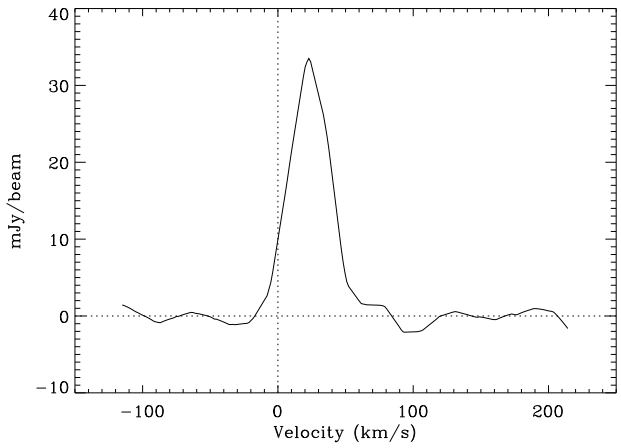

Figure 4.11: The stacked line for the H region W45, taking a 12×12 arcmin^2 average spectrum. The spectrum has been Tukey+Hanning smoothed.

4.1.5 Line Stacking

After correcting each RRL for baselines, the final step is to add them. The three RRLs should come from the same region in the sky, as a result of having the same transition order ($\Delta n = 1$) with similar quantum numbers, the lines should have approximately the same intensity (Section 2.2). Therefore, the three lines can be stacked - aligned and averaged - improving the signal-to-noise ratio by a factor of $\sqrt{3} = 1.73$.

The lines need to be carefully shifted before being stacking otherwise the final line can be easily broadened and consequently give a false indication of the width of the line. In order to do this it is necessary to identify the channel that contains the rest frequency of each line. It is possible to do so to a tenth of a channel after the spectra are interpolated. Fig. 4.11 shows the stacked line for the H region W45, after the three Tukey+Hanning smoothed and baseline-corrected RRLs from Fig. 4.5 are added. It illustrates the improvement in the baseline of the spectrum between the original three spectra and the added spectrum. The different baseline variations in each of the spectra act effectively like noise and are reduced by nearly a factor of two in the addition.

4.1.6 Post-stacking baseline correction

The baseline correction and line stacking described so far, generally yield spectra that are flat and have good signal-to-noise ratios. That is not the case in the presence of negatives, thought to be caused by the incorrect bandpass correction. Figs. 4.12 and 4.13 show the spectra of each RRL plus the stacked lines, for the single pixel centred on the plane at $\ell = 39°.6$ and $\ell = 40°.4$, respectively. These are just two examples that help explaining the adopted method of dealing with the negatives.

In Fig. 4.12, the three RRL spectra have a negative feature at $V \sim 60$ km s^{-1}, which means that there is extended emission along the $\ell = 0°$ scan at that velocity. This is indeed the case, as the extended group of H regions W47 is located on the plane with typical velocities of $50-60$ km s^{-1}. The bandpass correction then depresses the spectra in that channel, creating negatives where the emission is not very strong.

If there is a real signal embedded in the negative, then it should be at roughly the same velocity in the spectra of the three RRLs. The H166α spectrum shows a possible line of ~ 15 mJy/beam at $V \sim 25$ km s^{-1}. Even though the corresponding signal in the H167α and H168α spectra are not as clear, they show an inflection at the same velocity. The polynomial fits to each RRL, shown as dotted lines, are not appropriate to recover this signal, hence the stacked line in Fig. 4.12 (d) (black line) is still strongly affected by the negative. The red curve in Fig. 4.12 (d) shows the result of fitting a 4$^{\text{th}}$ order polynomial from -30 to 100 km s^{-1}, excluding the range [10,60] km s^{-1}, to the stacked line. The result is a line of amplitude 15 ± 1 mJy/beam, at 29 ± 1 km s^{-1} (obtained from a Gaussian fit). If the stacking is done only after this second baseline fit is applied to the original RRL, the resulting final line is that in green, as seen in Fig. 4.12 (d). The consistency between the red and green lines indicates that the correction for the negatives can be done before or after line stacking.

Figure 4.13 shows another region affected by bandpass-generated negatives. It is also a good example of the advantages of line stacking. The H166α spectrum is, in this case, slightly broadened as compared to the other two RRL spectra, which is likely due

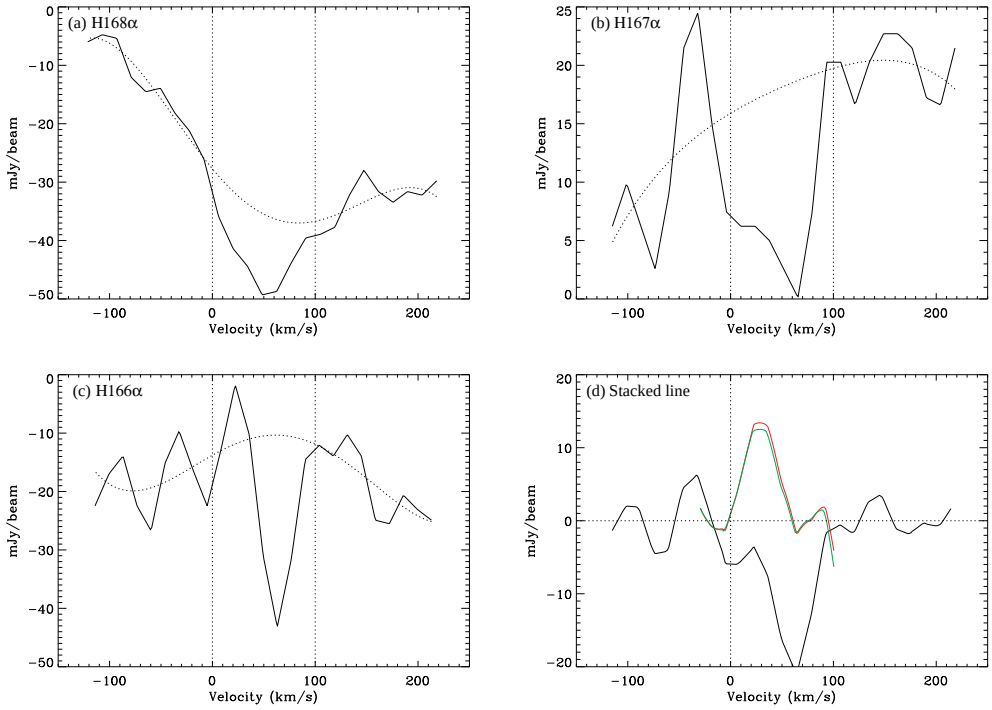

Figure 4.12: The RRL spectra and stacked lines for the pixel centred on (ℓ, b)=(40°.4,0°.0). The dotted curves are the original polynomial fitted to the spectra. The red line is the result of applying the second fit to the stacked line, in black, whereas the green line is the result of applying the second fit to each RRL and then adding them.

to the ringing effect from the H line. Nevertheless, the second fit is able to recover a signal from the stacked line, consistent with that seen in all the three individual spectra.

The reason for applying a fit that is able to recover a line at $V \sim 30$ km s^{-1} but that ignores possible signals at higher velocities, first comes from Galactic rotation arguments. At this longitude, $\ell \sim 40°$, the emitting gas is expected to have velocities between 0 and $\sim$ 50 km s^{-1}, since the line of sight intersects the Local and Sagittarius spiral arms. To confirm this hypothesis, the parameters of the final line recovered in Fig. 4.13 (d) are compared with published results. The line integral is 463 ± 37 mJy/beam km s^{-1}, or 370 ± 30 mK km s^{-1} (Section 3.2.1), which is consistent with the value obtained by Lockman et al. (1996), 395 ± 76 mK km s^{-1}, at the same position. Their observations detected a line at 27.9 ± 1.4 km s^{-1}, also consistent with

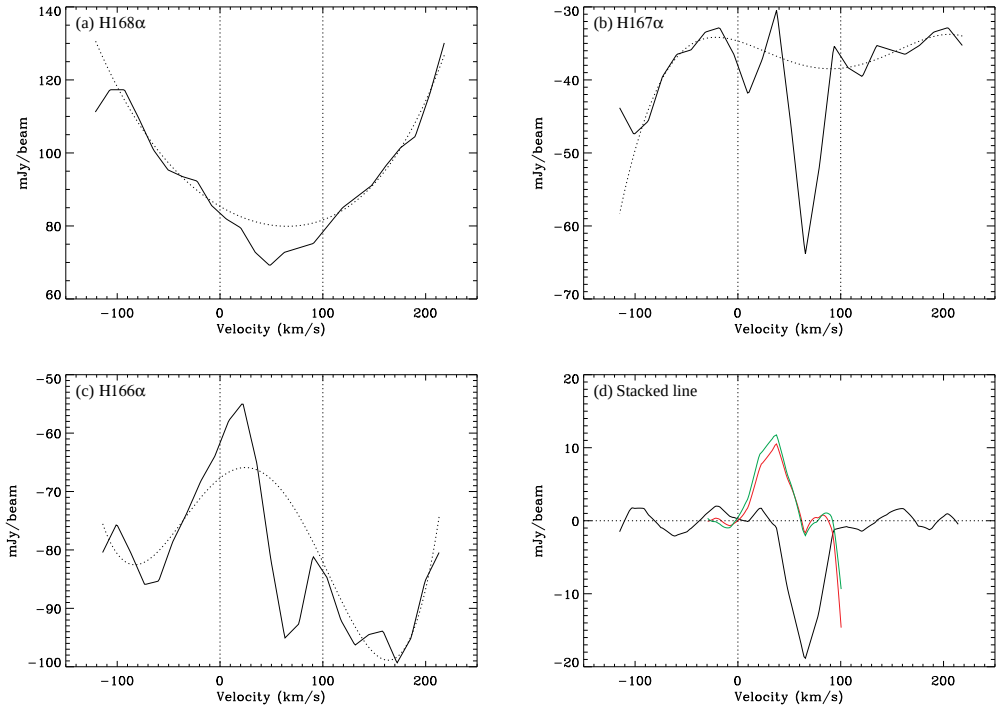

Figure 4.13: The RRL spectra and stacked lines for the pixel centred on (ℓ, b)=(39°.6,0°.0). The labels are the same as in Fig. 4.12.

the present measurement of 31 ± 1 km s^{-1}. The fact that the present beam is broader than the 9 arcmin beam from their observations, is not likely to invalidate this comparison because the direction (ℓ, b)=(39°.6,0°.0) points to an extended ionised region. Lower polynomial orders were tested, since the small number of data points used here does not guarantee a fit as robust as that in the initial wider velocity range. However, a 4$^{\text{th}}$ degree polynomial was found to perform best given the severity of the negatives. It will be shown in Section 5.3.1 that line emission is detected at these two positions in the reprocessed cube, where the line integral recovered at (ℓ, b)=(39°.6,0°.0) is 325 ± 180 mK km s^{-1}. This is consistent with the value of 395 ± 76 mK km s^{-1} found here, whose lower error bar is likely due to an over fit of the noise.

This method was applied anywhere in the datacube where the first stacked line integral was less than zero, as absorption is not expected at these frequencies.

4.2 The distribution of RRL emission at $\ell = 40°$

For the purposes of mapping the diffuse electron gas, the line integral over the emission velocity −20 to 120 km s^{-1} is used, in order to take account of any velocity spread within the spiral arms. The final RRL data cube shows high significance detections of RRL emission from individual H regions and from diffuse gas along the Galactic plane. Fig. 4.14 plots the RRL emission at 6 velocities (0, 20, 40, 60, 80, 100 km s^{-1}), integrated over 20 km s^{-1}. Individual H regions can be identified on the different maps. At the lowest velocities, the emission is broader, since it maps the Local and Sagittarius arms. At the highest velocities (> 60 km s^{-1}) the emission is more confined to the Galactic plane and is stronger at low longitudes where the Scutum arm comes in. W49A, $(\ell, b) = (43°.2, 0°.0)$, is the most prominent H region of the field and is one of the strongest H regions of our Galaxy. It is stronger in the first two panels of Fig. 4.14 because its LSR velocity is 7.7 km s^{-1}, which places it on the far side of our own spiral arm, at ∼ 11.9 kpc from the Sun. W45, $(\ell, b) = (40°.5, 2°.5)$, is also detected at low velocities, $V_{\rm LSR} = 23$ km s^{-1}. It is at a distance of ∼ 1.6 kpc from the Sun, thus in the Local arm. The extended feature on the plane around $\ell = 38°$, W47, is a group of H regions with LSR velocities from 50 to 90 km s^{-1} and is thus in the Scutum arm. The extension to positive latitudes is due to the contribution of some H regions with velocities around 40 km s^{-1}, and therefore belong to the Sagittarius spiral arm.

Figure 4.15 shows two maps of the RRL emission integrated from −20 to 60 km s^{-1} and from 60 to 120 km s^{-1}, and also the corresponding latitude profiles averaged over $\ell = 36°$ to 44°. Comparing Figs. 4.15 (c) and (d), it is seen that low velocity emission has a broader latitude distribution, with a FWHM of 1°.5, whereas the higher velocity emission has a FWHM of about half that value.

Figure 4.16 gives the total RRL emission integrated from −20 to 120 km s^{-1}. This map shows a clear detection of the diffuse ionised gas around the Galactic plane, as well as the individual H regions. The rms noise away from the Galactic plane is 70 mK km s^{-1}. The low-level striping in longitude is apparent, due to the telescope

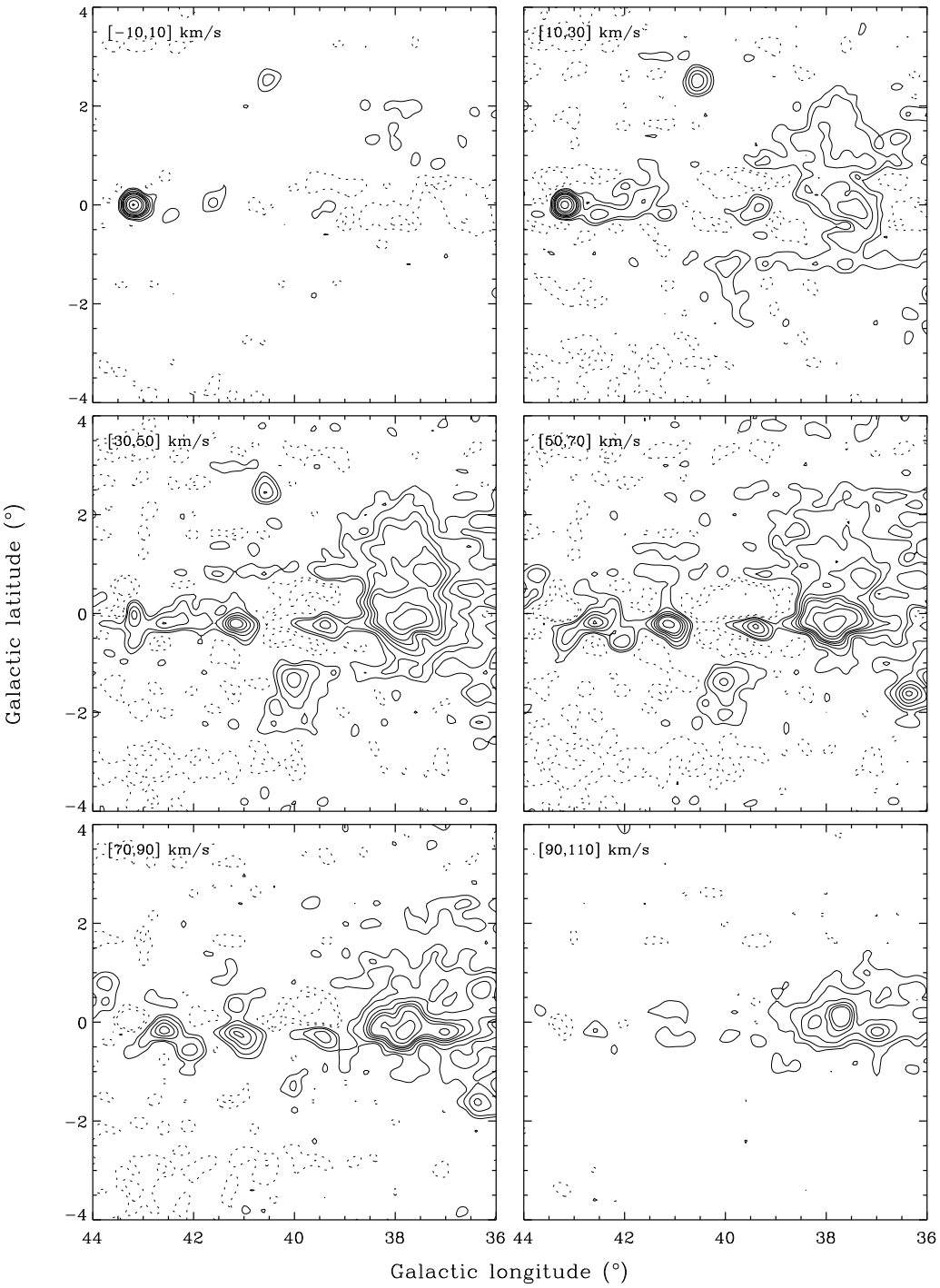

Figure 4.14: Maps of RRL emission centred at 0, 20, 40, 60, 80 and 100 km s^{-1}, integrated over 20 km s^{-1}, at a resolution of 15.5 arcmin. Contours are given at −2, −1, 1, 2, 4, 6, 8, 10, 15, 20, 30, 40, 50, 60, 70, 80 and 90 per cent of 5.29 K km s^{-1}. The two negative contours are dotted.

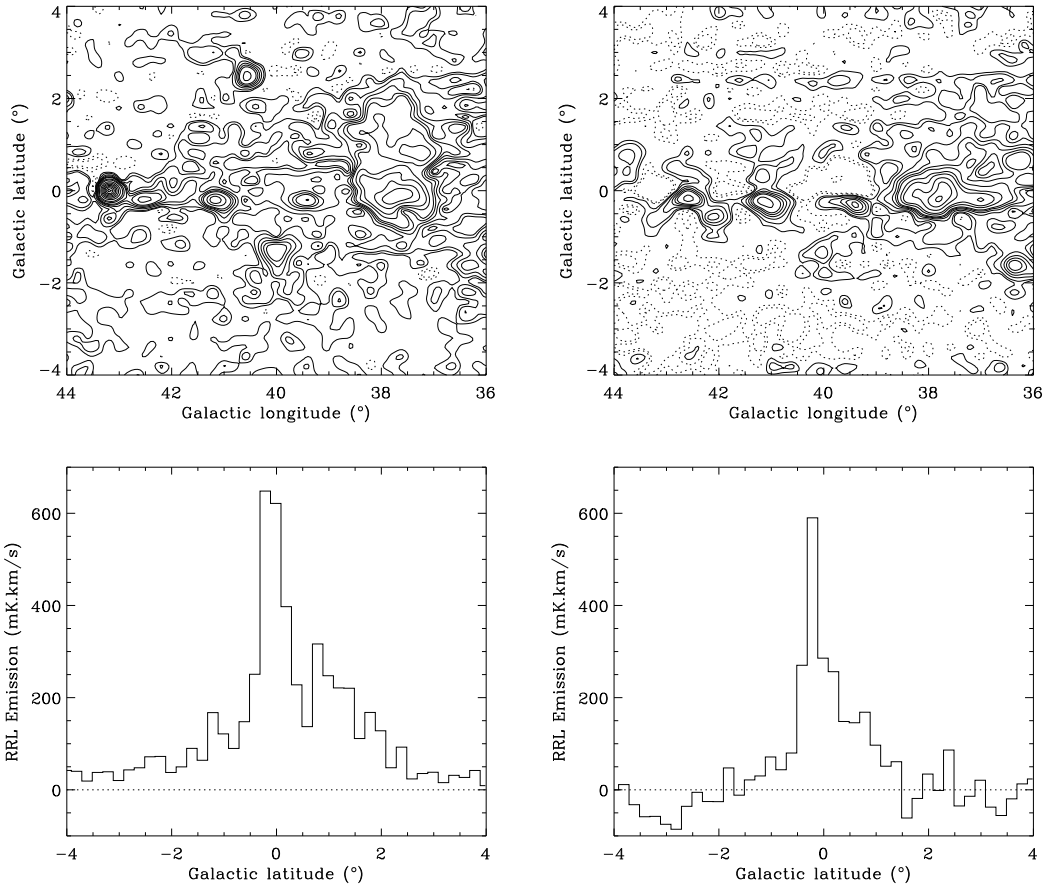

Figure 4.15: Integrated RRL emission for two velocity ranges (top) and the corresponding latitude profiles (bottom). The left- and right-hand side panels correspond to a line integral from -20 to 60 km s^{-1} and from 60 to 120 km s^{-1}, respectively. The contours are the same as in Fig. 4.14.

scanning strategy and the variation of bandpass correction between adjacent scans. The stripes are at the 2.5 σ level, so they only affect the low flux density regions. Some regions near the Galactic plane show sidelobe artifacts due to the emission filling the entire scan (Section 4.1.1). The biggest negative (4 σ) is next to one of the strongest H regions in the map, W49.

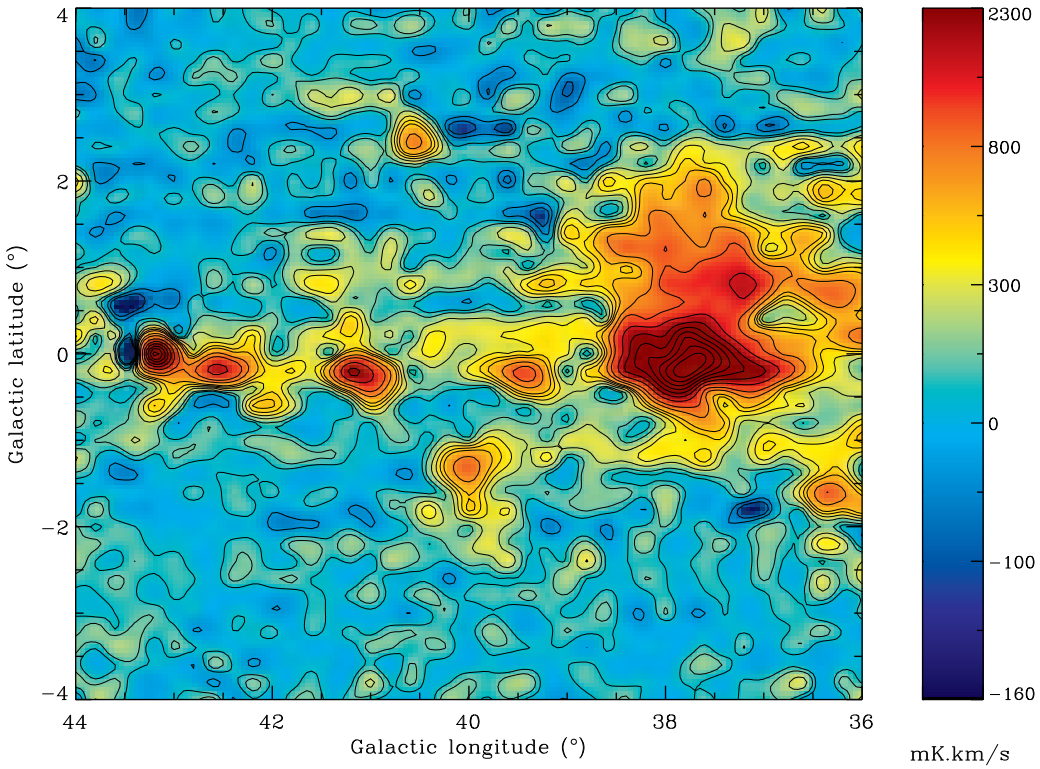

Figure 4.16: Map of the total integrated RRL emission (in mK km s^{-1}) at a resolution of 15.5 arcmin. The integration is made between –20 and 120 km s^{-1}. The contours are the same as in Fig. 4.14, where the value 5.29 K km s^{-1} is the peak of the line integral in this map. Note the non-linear colour scale.

4.3 The distribution of T_b in the $\ell = 40°$ region

4.3.1 Comparison with the 1.4 GHz continuum

In order to obtain a value of the brightness temperature, T_b, from the RRL line integral, equation (2.40) is used. It is necessary to have a reliable estimate of the electron temperature, since equation (2.40) depends on $T_e^{1.15}$. The average electron temperature of H regions, derived from RRL observations, ranges from 6700 K for the Local arm to 5500 K for the Scutum arm whereas T_e for the diffuse gas is slightly higher, ~ 8000 K (Section 2.5.1). As follows, the adopted electron temperature for the $\ell = 40°$ region is 7000 K, thereby 1.0 K km s^{-1} is equivalent to 2.8 K of brightness temperature at 1.4 GHz.

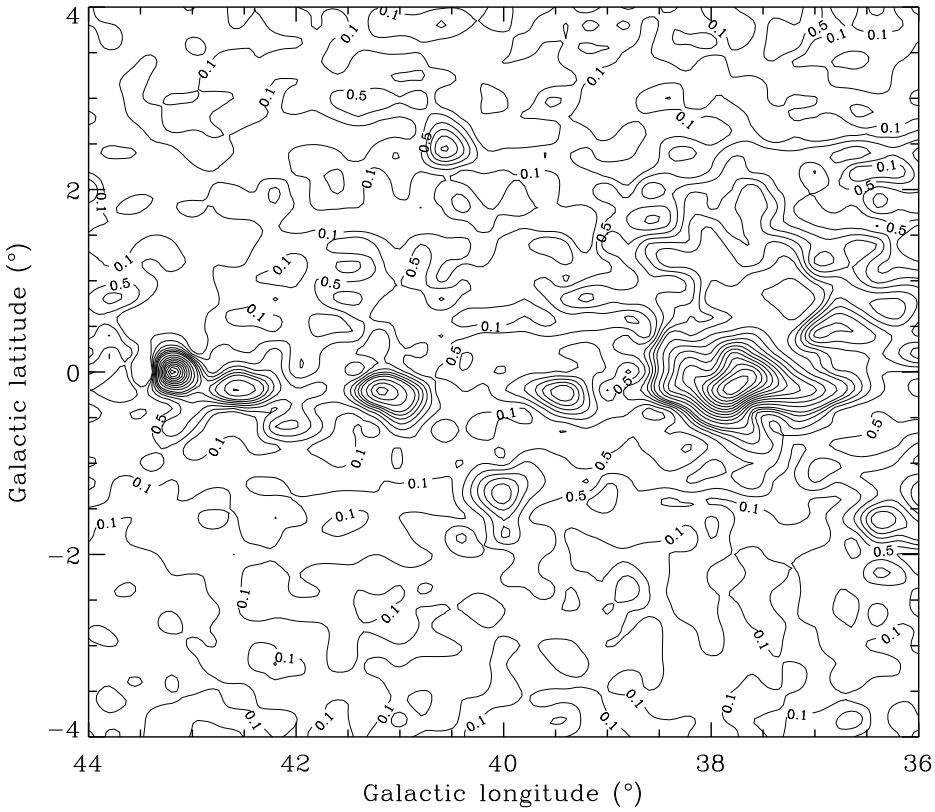

Figure 4.17: Map of thermal brightness temperature at 1.4 GHz estimated from the RRL line integral over the data cube. Contours are given at 0.1 and 0.5 (labelled), 1, 1.5, 2, 2.5, 3 K and then every 1 K until 19 K. The resolution of the map is 15.5 arcmin. Note that 2.8 K (T_b) corresponds to 1.0 K km s^{-1}, for T_e = 7000 K.

Using the adopted value of T_e = 7000 K I can evaluate the T_b from the RRL integral at each pixel in the data cube. Fig. 4.17 shows a contour plot of T_b over the area of the data cube (ℓ = 36° to 44°, b = −4° to 4°). In addition to the compact sources, the diffuse emission can be seen peaking at $b \sim 0°$. Fig. 4.18 plots the total continuum emission for this region. This map is obtained combining ZOA and HIPASS data, using a different set of reduction parameters from the present, and it will be further discussed in the next chapter (Section 5.4). The similarities between the two maps show that the RRLs successfully recover both individual H regions and the diffuse emission.

The extended object at $(\ell, b) = (40°, -2°)$ in Fig. 4.18, W50, appears to have no

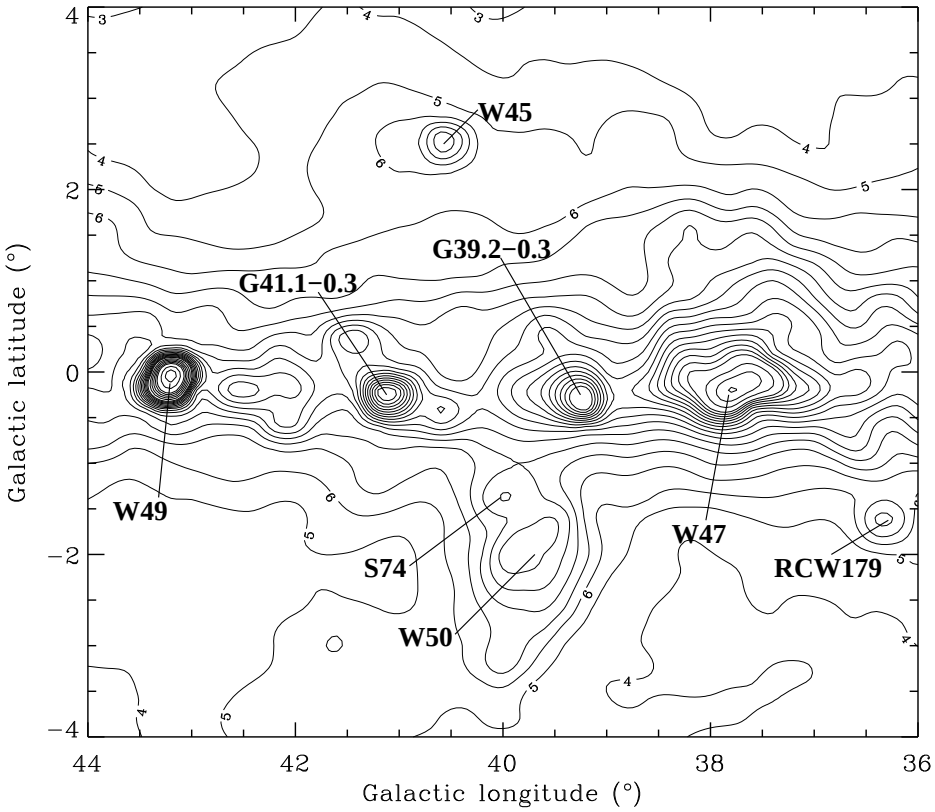

Figure 4.18: Map of the total brightness temperature at 1.4 GHz for the region $\ell = 36° - 44°$, $|b| < 4°$, from the combination of ZOA and HIPASS surveys. The contours are given at every 1 K from 3 to 20 K, every 2 K from 20 to 30 K and at 35, 40, 45, 50 and 55 K. The first four contours are labelled on the map. Some sources are labelled. The resolution is 15.5 arcmin.

RRL emission associated with it, so no evidence for ionised gas. This is a SNR, thought to be powered by the X-ray binary system SS433 which generates two relativistic jets in opposite directions, creating the lobes that elongate the feature. W50 lies at a distance of 6 kpc from the Sun and thus has no association with the H region S74, which is seen in the RRL map at $(\ell, b) = (40°.0, -1°.3)$ (Lockman et al. 2007). S74 is comprised of a compact source embedded in an extended region, also denominated RCW182. I measure a velocity of $V_{\rm LSR} = 44.7$ km s^{-1} for S74, which places it at a distance of ~ 3.0 kpc from the Sun, in the Sagittarius arm.

4.3.2 T_b latitude distribution

In order to make the diffuse emission clearer, latitude cuts integrated over a longitude range are given in Fig. 4.19. Fig. 4.19 (a) is an integral over the full longitude range $\ell = 36°$ to 44° using 0°.2 latitude bands. Fig. 4.19 (b) shows stronger T_b in the ℓ-range 36° to 39° than for $\ell = 39°$ to 44° (Fig. 4.19 (c)). It should be noted that the stronger emission at $\ell = 36°$ to 39° includes the tangent to the Scutum arm which does not extend to $\ell = 39°$ to 44°. Nonetheless, the emission in Fig. 4.19 (c) appears to be low, with the peak of the latitude distribution less than half of that in Fig. 4.19 (b). There is also less extended emission around the plane, so the latitude distribution appears narrow and is mainly accounted for by the few H regions in that longitude range. This suggests that I might be losing some extended diffuse emission in the process, probably due to the bandpass removal associated with the scanning strategy (Sections 4.1.1 and 4.1.6).

The longitude variation of T_b is shown in Fig. 4.19 where 4.19 (d) shows the Galactic ridge emission integrated from $b = -0°.25$ to 0°.25 while (e) is the integral from $b = -0°.5$ to 0°.5; in both plots the longitude step is 4 arcmin. The fall of T_b with longitude as the line of sight passes out of the Scutum arm is visible, leaving only emission from the Sagittarius and Local arms.

4.4 Validity of the RRL data

As a consistency test, I have compared the line integrals with those from the frequency-switched RRL survey by Heiles et al. (1996b). For the pointings between the longitudes of 39° and 44°, where there might be flux loss (Section 4.3.2), I get a ratio of 0.8 with a scatter of 0.2, which shows that the data sets are consistent. The comparison is shown in Fig. 4.20.

The LSR velocity of several lines of sight was also tested against the measurements by Heiles et al. (1996b). Table 4.2 gives a few examples of the present velocities

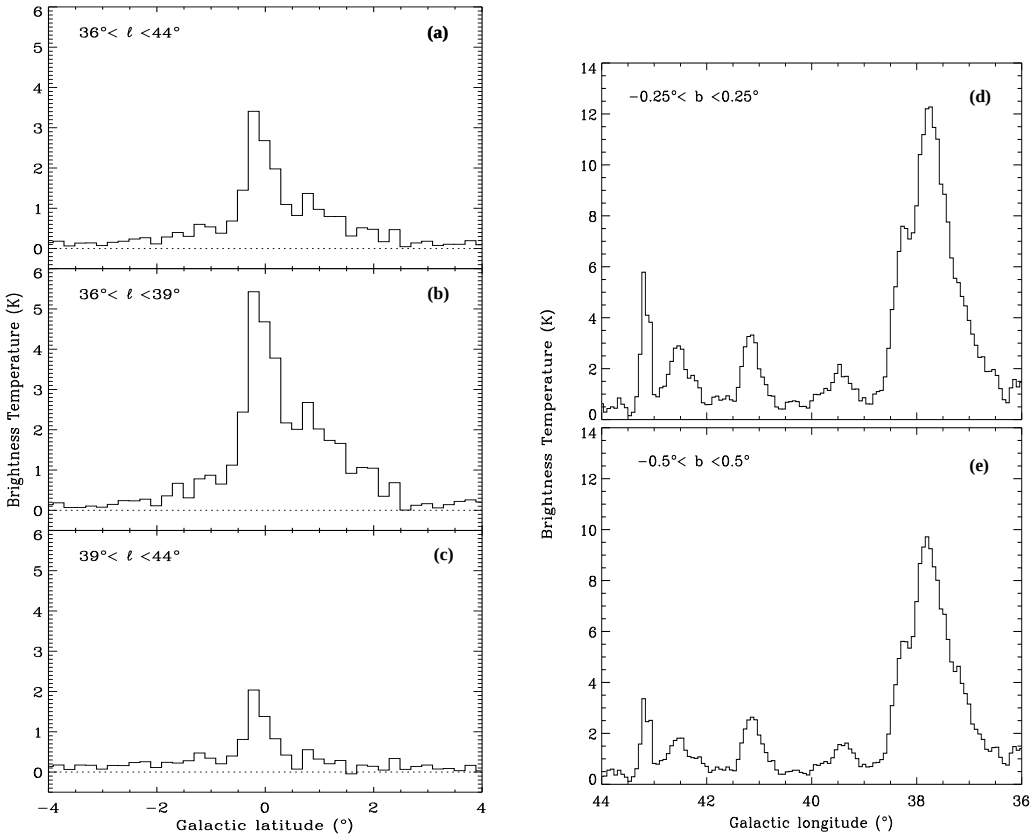

Figure 4.19: Brightness temperature estimated from the ZOA RRLs versus latitude, averaged over three longitude ranges (left) and versus longitude, averaged over two latitude ranges (right).

Table 4.2: Measured LSR velocities compared with published results (Heiles et al. 1996b). The uncertainties in the Heiles et al. (1996b) velocities are of the order of a few per cent (channel spacing is 5 km s^{-1}).

Position	This work	Heiles et al. (1996b)
(ℓ, b)	$V_{\rm LSR}$ (km s^{-1})	$V_{\rm LSR}$ (km s^{-1})
(36°.0,−0°.6)	60.7 ± 0.6	61.0
(36°.6,−1°.7)	63.3 ± 0.2	63.1
(37°.3,1°.0)	45.0 ± 0.4	44.6
(43°.2,0°.0)	7.8 ± 0.2	8.4

obtained from Gaussian fits, compared with the corresponding results from Heiles et al. and indicates that the results are consistent.

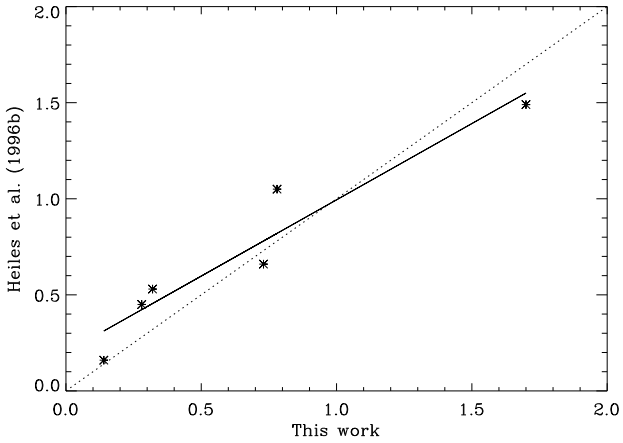

Figure 4.20: Comparison between the integrated intensity of the lines (in K km s^{-1}) from the present work with those from Heiles et al. (1996b), for the pointings in the $\ell-$range 36° to 44°. The solid line gives the linear fit with a slope of 0.8 and the dotted line is the line of slope 1.

5

RRL Data analysis - an improved method

After the study of the ZOA data cube centred at $\ell = 40°$, the two next $8° \times 8°$ regions towards the Galactic centre, $\ell = 32°$and $\ell = 24°$, were analysed. Fig. 2.3 shows that the major contribution to the RRL emission will be from the Scutum spiral arm. Other surveys of the Galactic plane (Reich et al. 1984, 1990b) also show that the continuum emission is much stronger at $\ell = 32°$ than in the previous $\ell = 40°$ region.

This chapter describes the improvement of the RRL reduction pipeline, which includes a new bandpass algorithm exclusively designed for the analysis of RRL spectral line data. It also incorporates some algorithms that were initially developed for the HIPASS continuum data analysis, which is briefly discussed at the end of this chapter (Section 5.4).

5.1 The new RRL pipeline

The ZOA-032 cube was very useful for the development of a new bandpass correction algorithm because it contains a strong and isolated H region, W40 (G28.8+3.5), where the origin of the spectral negatives could be identified. Thus, the following sections on data reduction refer to the $\ell = 32°$ cube.

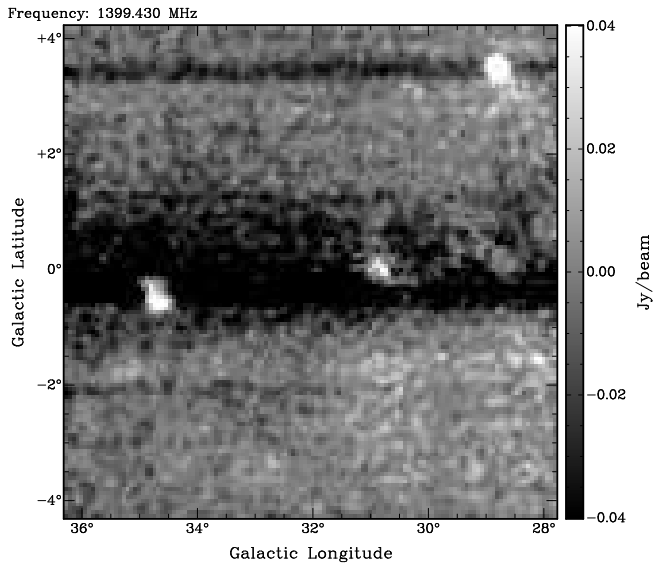

Figure 5.1: Map of the ZOA $\ell = 32^\circ$ cube at 1399.430 MHz (-13.4 km s^{-1}) reduced with the *minmed*$_{10}$ algorithm. The strong source W40 at the right top of the map causes the negative trough along the scan direction through the H region.

5.1.1 Bandpass calibration - the *tsysmin*$_n$ method

At this stage, a refinement of the method (Section 4.1.1) was available for the bandpass correction. This is called the *minmed*$_n$, or the minimum-running-median, because it calculates the median in a sliding box of n integrations along the scan. For a typical 100 integrations scan, 5 breaks it into 5 fixed sections of 20 integrations each, whereas *minmed*$_{10}$ is a box of 10 integrations that runs along the scan, and finds the minimum of all the medians computed. The box $n = 10$ provides a sufficient number of integrations to compute a reliable median without the averaging length being too extended in regions where a large part of the scan may be occupied by extended emission. Fig. 5.1 is a map of the ZOA-032 datacube at 1399.430 MHz, reduced with *minmed*$_{10}$. Besides the negatives on the plane (Section 4.1.1), it shows a negative trough along the scan line through the isolated H region W40. The RRL emission of W40 from the H167α line peaks at about 346 mJy/beam, at 0 km s^{-1}, and the trough varies in depth between about 30 and 70 mJy, or 9 – 20% of the peak.

The cause of the negatives are large-scale distortions of the bandpass response by

very strong sources, such as W40. The bandpass calibration in is based on

$$\mathbf{S}_i = \frac{S_i}{\mathbf{B}(\frac{S_i}{T_{\mathrm{sys_i}}})} - \mathbf{B}(T_{\mathrm{sys_i}}) \tag{5.1}$$

where **B** is the bandpass estimator for extended emission, that is, or the running median *minmed*. The spectrum S_i is first normalised for each integration i by $T_{\mathrm{sys_i}}$, where

$$T_{\mathrm{sys_i}} = \langle S_i \rangle \tag{5.2}$$

is the average of the spectrum S_i taken over all channels. The negative trough is generated by the bandpass quotient $S_i/T_{\mathrm{sys_i}}$ which depresses the channels adjacent to the RRLs but not the channels occupied by the lines themselves. This happens because W40 is a strong continuum source which causes T_{sys} to increase by nearly a factor of two, but the continuum does not contribute equally at all frequencies, either due to instrumental effects or the source's intrinsic spectral index. Fig. 5.2 shows the bandpass quotient $S_i/T_{\mathrm{sys_i}}$ for beam 1, the beam that passes right through W40 for the scan with central latitude +3°.3. Fig. 5.2 (a) shows the trough along the frequency range covering the H167α line (1399.369 MHz) and Fig. 5.2 (b) shows the whole bandpass profile for the integration coincident with W40.

The trough in frequency is then converted into a trough in the scan direction because the bandpass estimator, $\mathbf{B}(S_i/T_{\mathrm{sys_i}})$, locks onto the channels either side of the RRL which causes the baselevel for those channels to be underestimated. As a result, the term $S_i/\mathbf{B}(S_i/T_{\mathrm{sys_i}})$ is inflated. Then, either when $\mathbf{B}(T_{\mathrm{sys_i}})$ is subtracted in equation 5.1, or later when the post-bandpass baseline fit is performed, the whole scan line through W40 for the channels containing the H167α RRL are pushed to negative values. One way to avoid the bandpass estimator locking onto the trough is to find and exclude the integrations where T_{sys} is high. That is, the bandpass must be estimated using the integrations where T_{sys}, and therefore the continuum, is lowest. This, in principle, implies that the RRL signal in those channels is low as well. The solution is then to find the 10, or in general n, integrations for which $\mathbf{B}(T_{\mathrm{sys}})$ is lowest and use those integrations to compute $\mathbf{B}(S/T_{\mathrm{sys}})$. This bandpass estimator is called $tsysmin_n$. Fig.

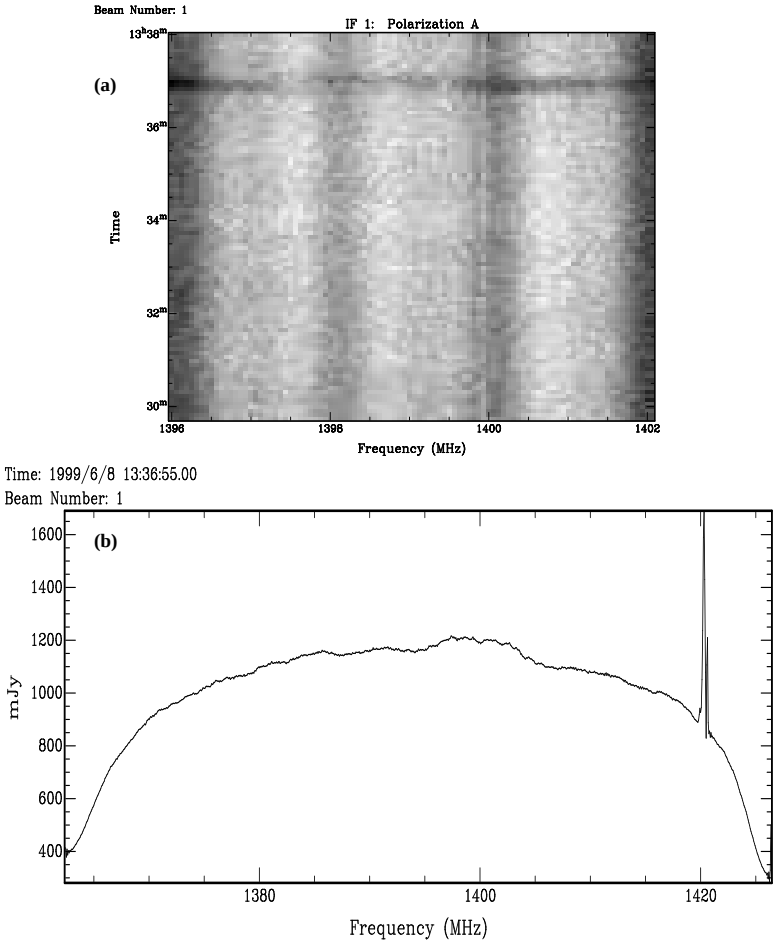

Figure 5.2: (a) The quotient $S_i/T_{\mathrm{sys_i}}$ for beam 1 and polarisation A, of the scan that passes through W40 (near the top). The vertical axis, the scan time, is equivalent to the Galactic longitude. (b) The whole bandpass profile for the integration at $13^{\mathrm{h}}36^{\mathrm{m}}55^{\mathrm{s}}$.

5.3 shows channel maps of the ZOA-032 cube at two frequencies near the H167α line, plus the final spectra towards G35.6+0.0, using the $minmed_{10}$ and $tsysmin_{10}$ bandpass estimators. The *tsysmin* method shows a significant improvement over *minmed*. It removes the negatives on the Galactic plane and along the longitude direction at W40, and it also recovers more extended emission and renders cleaner spectra, with higher peak values.

After bandpass calibration, a second order polynomial fit to the spectral baseline is removed by . This is to remove large scale curvature and continuum emission from the spectra.

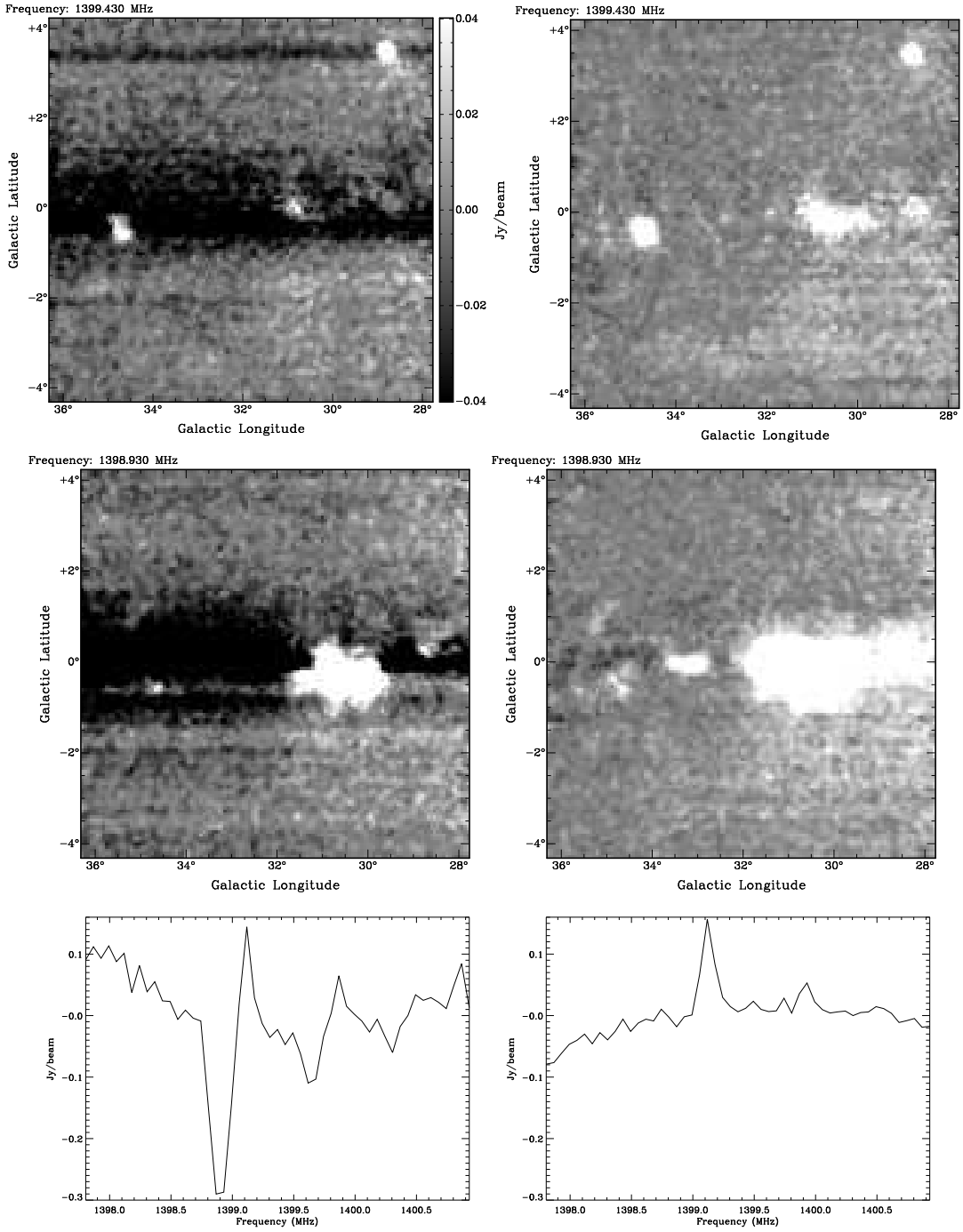

Figure 5.3: Maps of the ZOA-032 datacube processed using $minmed_{10}$ (left) and *tsysmin* (right), at 1399.430 MHz (top) and 1398.930 MHz (middle). The intensity range is −40 to 40 mJy/beam, as indicated in the top-left panel. Negatives are removed using the *tsysmin* method and more extended emission is recovered. The two H167α spectra, taken at (ℓ, b)=(35°.6,0°.0) show that the deep negative left by $minmed_{10}$ is strongly suppressed by the *tsysmin* estimator, shown in the right hand spectrum.

5.1.2 RRL extraction -

Averaging the three RRLs greatly improves the signal-to-noise of the final line (Section 4.1.5). Moreover, removing the baselines before stacking the three spectra gives similar results to stacking and only then removing the baseline, as described in Section 4.1.6. For this reason, and due to the fact that only a portion of the 64 MHz spectrum is used, it was decided to extract each RRL from the bandpass corrected data and either average the three spectra before or during the gridding process.

This algorithm is called and it was included in the distribution for the exclusive treatment of HIPASS/ZOA hydrogen RRLs. reads a bandpass calibrated scan and generates 4 files, 1 for each RRL and one for the combined line, with the same format as the original file but with only a fraction of the channels. The three spectral fragments are Fourier-shifted so that the line rest frequency falls on an integral channel number. They are stacked using a weighted mean of the three RRL spectra, where the weights are proportional to the square root of the bandpass response measured at each line's rest frequency, normalised to unity. The weights are set to 0.26, 0.39 and 0.35 for the H166α, H167α and H168α, respectively, and were measured using several scans selected at random. These values correctly take into account the H ringing and the bandedge effects that affect the H166α and H168α lines, respectively. The error introduced by averaging the lines in frequency rather than in velocity is small, less than 4 per cent of the channel width. The number of channels extracted was set to 51, which is the maximum allowed, due to the proximity of the H166α line to the edge of the band, and is equivalent to an LSR velocity range of $\pm$335 km s^{-1}. Finally, the frequency axis is relabelled as appropriate for the H167α line.

As a result of the procedure, two datacubes can be generated by : one using the files for each individual RRL (split mode) and the other using the stacked line files (combined mode). Examples are given in the next section.

5.1.3 Weighted median gridding

In the analysis of the ZOA-040 datacube, a simple median gridding with no beam normalisation was adopted in order to recover correct fluxes for extended sources (Section 4.1.3). At this stage, a refinement of median gridding is used, the *weighted median* estimator. For each pixel in the output datacube, calculates a weight for each input spectrum based on its angular distance from the pixel and its corresponding system temperature. The beam weighting function is modelled by a Gaussian of FWHM equal to the intrinsic beam, 14.4 arcmin. The value assigned to the pixel is that for which the accumulated weight is half of the total weight (which is summed starting from the lowest). The FWHM of the smoothing top-hat function and the cutoff radius are the same as used before, 12 and 6 arcmin, respectively.

If the gridding process used the mean estimator, gridding and averaging the lines should produce similar results to averaging and then gridding. Fig. 5.4 shows the peak line temperature maps from the ZOA-032 datacube, obtained using the split and combined modes. The two maps are very similar, with approximately the same rms of $\sim$ 3 mJy/beam, which means that median gridding gives equivalent results when the lines are combined before or during the imaging process. In fact, the combined mode produces only slightly better results than the split mode, as the difference map of Fig. 5.4 shows. The maximum line temperature in the combined mode map is 0.96 Jy/beam, compared with 0.90 Jy/beam in the split mode map. For this reason, the combined mode was adopted, so the datacubes are produced using the averaged spectra by .

5.1.4 DC level correction -

Despite the improvement of the spectra through the *tsysmin* bandpass estimator, the ZOA longitude scans cannot provide a real minimum for the bandpass correction on the Galactic plane where emission fills the whole scan. The HIPASS declination scans cross the plane at an angle of $\sim 30^{\circ}$ in the longitude range under study and there-

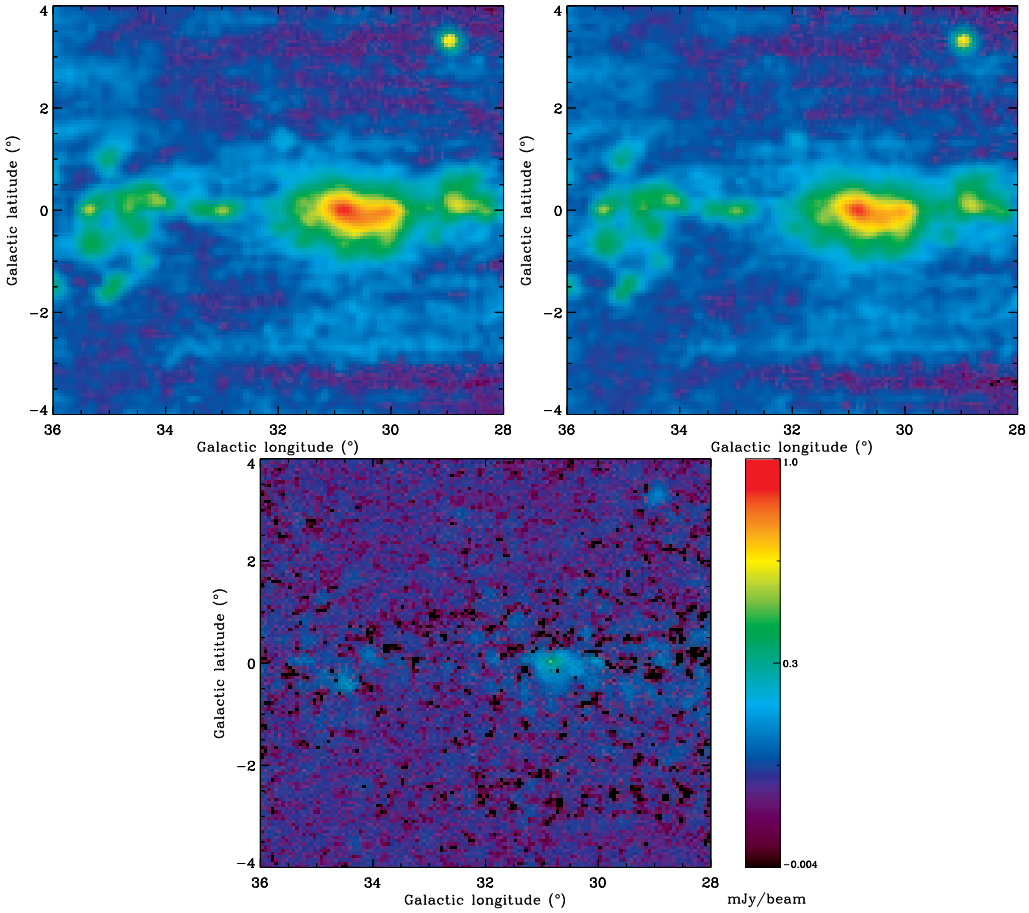

Figure 5.4: Maps of the peak line temperature from the ZOA-032 datacube reduced in the combined (left) and split (right) modes (Section 5.1.2), along with the difference map, combined minus split (bottom). These show the similarity of the results obtained when gridding the averaged or the individual spectra. The three maps are on the same scale.

fore yield a real minimum for the bandpass estimation. This is confirmed by looking at HIPASS and ZOA spectra in Figs. 5.5 (a) and (b): the ZOA spectrum has a significant negative close to the RRL which is not seen in the HIPASS spectrum. The negative is caused by the presence of emission at the frequency of $\sim$ 1399.2 MHz ($V \sim 36$ km s^{-1}) along the ZOA scan, which results in a lower peak temperature for the line, compared with that from the HIPASS spectrum. Fig. 5.6 shows the peak line intensity maps from the ZOA and HIPASS 032 datacubes. The lower integration time of the HIPASS survey is reflected in the rms noise of its spectrum, 27 mJy/beam com-

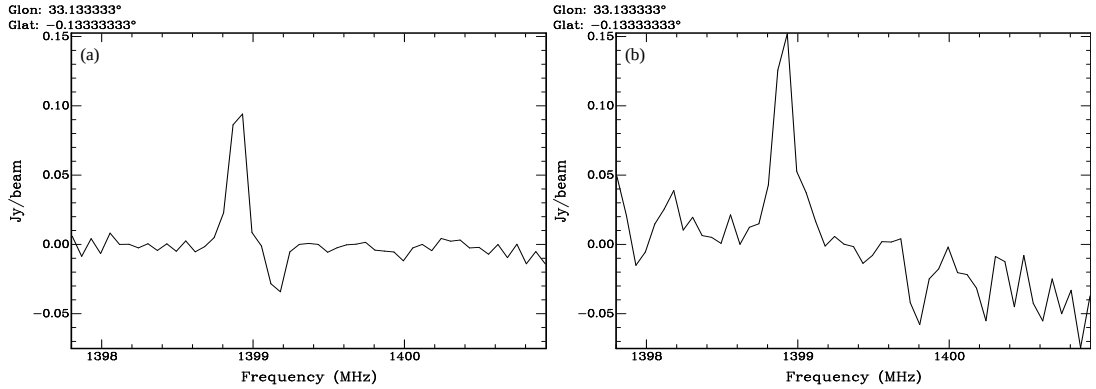

Figure 5.5: Spectra taken at (ℓ, b)=(33°.1,−0°.1) from the ZOA-032 (a) and HIPASS-032 (b) datacubes. Both data sets were reduced as described in Sections 5.1.1, 5.1.2 and 5.1.3.

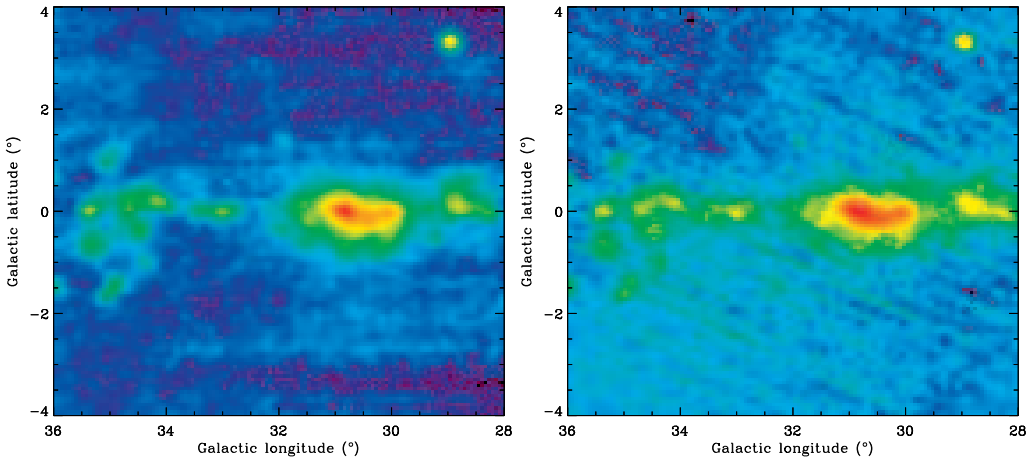

Figure 5.6: Peak line intensity maps from the ZOA-032 (left) and HIPASS-032 (right) datacubes. The intensity scale is the same as in Fig. 5.4.

pared with 6.8 mJy/beam for the ZOA spectrum and in the striations seen in the map along the scanning direction. The rms noise measured away from the Galactic plane in the HIPASS map is 6 mJy/beam, twice the value of the ZOA map. Nevertheless, the HIPASS map recovers more extended emission on the Galactic plane, which is also stronger. A simple averaging of the two datasets would still be affected by the loss of flux from the ZOA survey.

The rms of a spectrum is henceforth defined as the standard deviation estimated from a reference region either side of the line, excluding the datapoints between −20

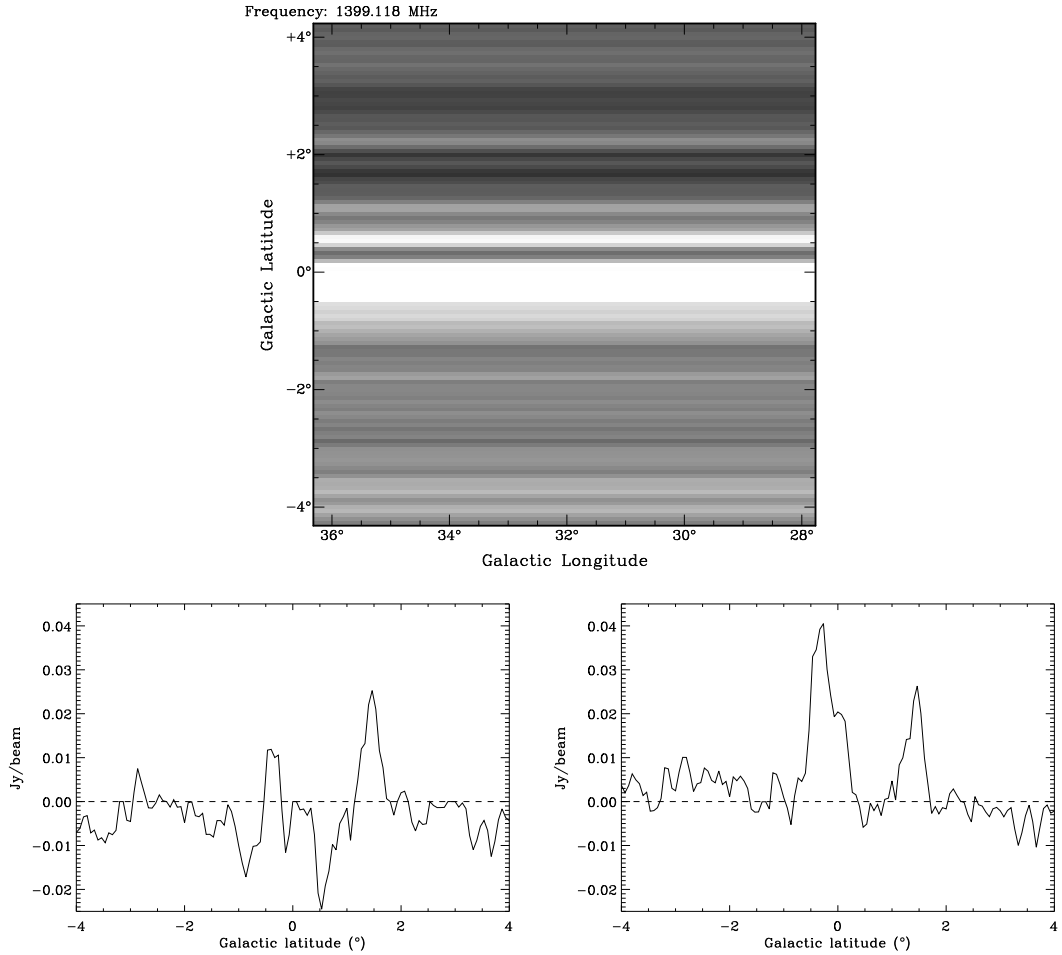

Figure 5.7: (Top) Map of the 032 DC level cube at 1399.118 MHz (53.6 km s^{-1}). The intensity range is from −10 to 20 mJy/beam. (Bottom) The ZOA latitude profiles at $\ell = 32.^\circ 0$ and $V = 53.6$ km s^{-1}, before (left) and after (right) the DC level is added.

and 160 km s^{-1}; the rms of a map is the standard deviation measured in regions away from the Galactic plane, typically at $|b| = 3^\circ - 4^\circ$.

In order to determine the offset of the ZOA survey, the ZOA datacube is subtracted from the HIPASS datacube. The difference cube shows horizontal features, expected due to the different zero levels of the ZOA scans in longitude. The DC level offset added back to the ZOA cube is the median of the difference cube at each Galactic latitude and spectral plane. Fig. 5.7 shows a cut through the $\ell = 32^\circ$ DC level cube at 1399.118 MHz (53.6 km s^{-1}). The map shows that, at this velocity, the offset between

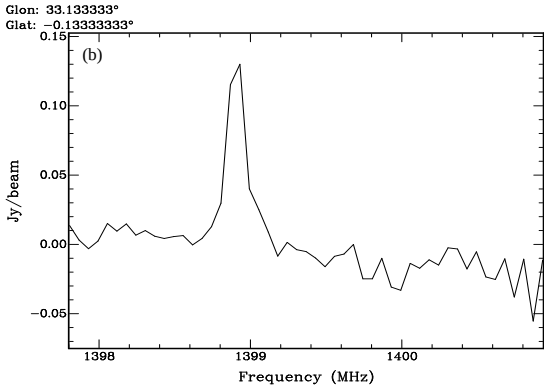

Figure 5.8: ZOA+HIPASS combined spectrum at (ℓ, b)=(33°.1, −0°.1), obtained using equation (5.3).

the ZOA and HIPASS RRL emission is larger at negative latitudes. This is visible comparing the latitude profiles in Fig. 5.7, which show the latitude cuts, at $\ell = 32°.0$ and $V = 53.6$ km s^{-1}, of the ZOA cube before and after DC level correction. The baselevel of the RRL emission at $b < 0°$ becomes positive after an offset of $\sim$ 10 mJy/beam is added. The level of emission on the Galactic ridge is also improved, where it increases by nearly a factor of 4 at $b = -0°.4$ and the negative at $b = +0°.5$ is strongly suppressed. The emission at $b = +1°.5$ in the initial ZOA cube is mainly unchanged by the offset addition, which means that it is detected at a similar level in the HIPASS cube.

The combination of ZOA and HIPASS data

The next step is to combine the ZOA DC level-corrected cube with the HIPASS cube, which is done as follows:

$$COMB = \left(\frac{5 \times (ZOA + DC) + HIPASS}{6}\right). \tag{5.3}$$

This takes into account the fact that the scan density of the ZOA survey is 5 times that of the HIPASS survey. The combined spectrum at (ℓ, b)=(33°.1, −0°.1) is shown in Fig. 5.8. The peak flux of the line increases by $\sim$ 20% compared with the ZOA spectrum of Fig. 5.5 (a) and the negative is greatly reduced. However the rms of the spectrum is degraded from 6.8 to 15.0 mJy/beam and acquires the slope from the

HIPASS spectrum baseline of Fig. 5.5 (b). These effects arise in the the DC level correction where, besides contributing to the signals, the HIPASS data adds noise into the ZOA data. This is more significant for the weak spectra away from the plane, where the baseline curvature of the HIPASS spectra combined with the low integration time create the artifacts seen in the peak line temperature map of Fig. 5.6 (b).

In order to avoid noise contamination of the ZOA spectra, it was decided only to apply the DC level correction in pixels and channels where the DC spectrum differs significantly from the noise. This threshold operation on the DC level spectra is performed after they are Hanning smoothed and baseline fitted, using a 4^{th} order polynomial. For a given pixel and channel, values below the lower threshold, set to 5 mJy/beam, are not applied, whereas those at or above the upper threshold, 15 mJy/beam, are applied. Values in between are applied only if adjacent to a value above the upper threshold. As a result, the DC correction is mainly added to the ZOA spectra for $|b| \lesssim 1^\circ$ and between the frequencies of 1398.8 and 1399.2 MHz ($V \sim 10 - 120$ km s^{-1}), so in the velocity range where the RRL gas is expected to emit.

To further improve the spectra, reducing any remaining spectral negatives and baseline curvature, additional smoothing and baseline fit were applied. The extra smoothing is done with the Tukey filter instead of the Hanning filter, preferred in the initial analysis of the $\ell = 40^\circ$ cube (Section 4.1.2). This gives a final resolution of 20 km s^{-1} (Section 3.2.2). The fit is performed by a function within the distribution, a robust and iterative polynomial baseline fitter. A 4^{th} degree polynomial fit was found to produce more stable baselines as compared to lower order fits. The spectral baseline fit over 3.2 MHz, 51 channels, effectively removes the effect of baseline ripple of period 5.7 MHz (Section 3.2). The DC level correction process described above, including the spectral smoothing and baseline fit of the spectra are performed by a new algorithm, , also included in the distribution.

Figure 5.9 shows the spectrum of the final combined cube towards (ℓ, b)=(33°.1, −0°.1). The negative at 1399.2 MHz in the initial ZOA spectrum of Fig. 5.5 (a) is now at the noise level. The rms of the spectrum is 4.4 mJy/beam. The corresponding peak line

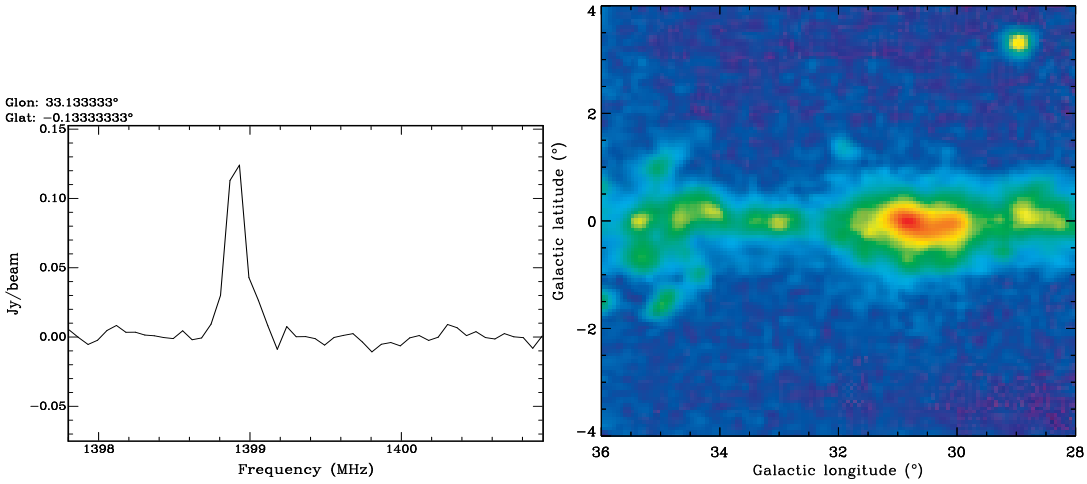

Figure 5.9: The spectrum of the final cube at (ℓ, b)=(33°.1, −0°.1) (left) and the corresponding peak line intensity map (right). The intensity scale is the same as in Fig. 5.6.

intensity map, in Fig. 5.9, shows that more extended emission is recovered on the Galactic plane and that individual sources have higher peak line temperatures. The emission generated by noise and baseline curvature detected away from the plane in the HIPASS map of Fig. 5.6 (b), especially at negative latitudes, has indeed not been propagated into the combined map. The map maximum and minimum line intensities are 948 mJy/beam and −1.8 mJy/beam and the rms away from the Galactic plane is 2.0 mJy/beam.

The previous examples show the improvement of the spectra on the Galactic plane, where the signals are strong and where the DC level is applied. Fig. 5.10 shows how spectra away from the plane change with . Here the DC level is not applied and the final spectra are the weighted mean of ZOA and HIPASS data, Tukey+Tukey smoothed and baseline corrected. The signal at $V \sim 50$ km s^{-1} in Fig. 5.10 (a) is lost in the noise and curvature of the baseline in the original ZOA spectrum with an rms of 11.7 mJy/beam. After the procedure the rms of the spectrum is down by a factor of 2.3, to 5.0 mJy/beam. Fig. 5.10 (b) shows that the RRL signal of amplitude $\sim$ 10 mJy/beam is now at a 2σ level. Figs. 5.10 (c) and (d) show a similar improvement in the spectral baseline of these weak signals out of the Galactic plane. The rms of the

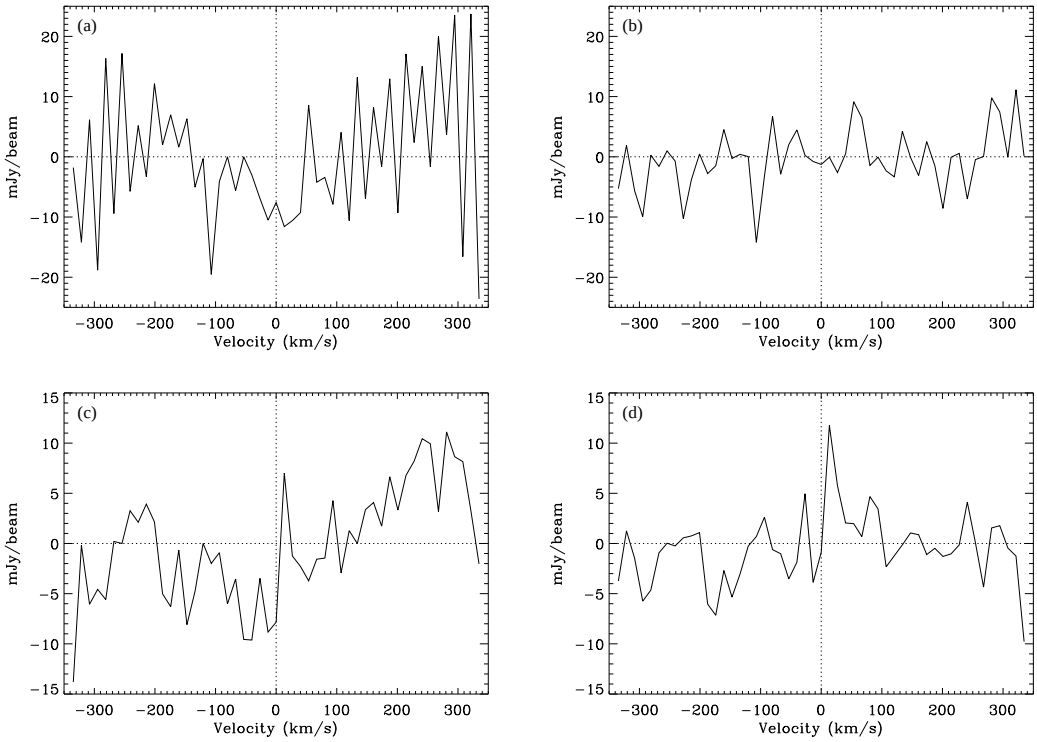

Figure 5.10: Comparison between spectra from the original ZOA (left) and the final (right) 032 cubes for two regions out of the Galactic plane. Spectra in the top and bottom panels are taken at (ℓ, b)=(28°.6, −2°.1) and (ℓ, b)=(29°.4, +2°.4), respectively.

spectrum is also decreased by a factor of two, from 6.0 to 2.9 mJy/beam. A value of $\sim$ 3.5 mJy/beam is found to be the typical rms of -032 spectra at high Galactic latitudes. Still, Figs. 5.10 (b) and (d) also demonstrate that further improvement on the baselines around these weak signals can be achieved if another low-order and localised polynomial fit is applied. This process is described in the next section.

5.1.5 Post-processing baseline removal

In order to leave the spectra from the Galactic plane and other strong H regions unchanged, a mask is computed based on the signal-to-noise ratio of the line. The rms noise is calculated for each spectrum, which is kept unaltered if its signal-to-noise ratio is above a certain value. This value is set to 4.5 after careful visual inspection of the

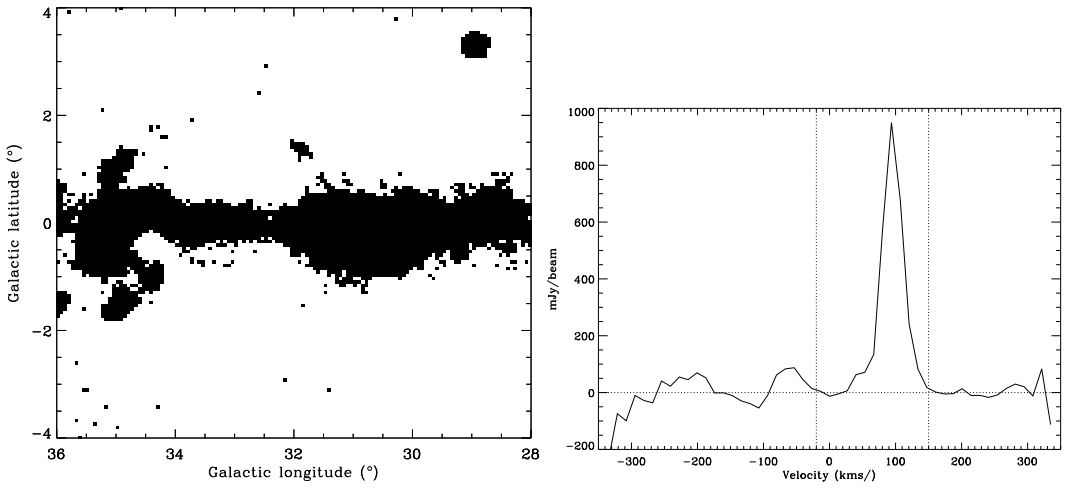

Figure 5.11: The mask created by the signal-to-noise ratio condition, showing in black where the spectra from the -032 cube are left unchanged (left) and the spectrum for the H region W43 (right).

spectra, so as to mask only those that have flat baselines. An example of a masked spectrum is shown in Fig. 5.11 for the H region W43 at (ℓ, b)=(30°.8, 0°.0). The vertical lines depict the velocity range used to calculate the line integral, −20 to 150 km s^{-1}. This range includes RRL emission from local H regions, such as W40 at 0 km s^{-1}, to the highest velocity emitting gas in the $\ell = 32°$ region, at $\sim$ 100 km s^{-1} (Paladini et al. 2003). Even in the case of RRLs at the high velocity end, this integral range excludes the helium and carbon lines (Section 2), as seen in the spectrum of the H region W43. The map in Fig. 5.11 is the mask created by the signal-to-noise ratio threshold. This essentially traces the strong individual H regions.

For the regions that have a line signal-to-noise ratio below the threshold value of 4.5, a second order polynomial fit is applied with two sets of parameters that divide the 130 km s^{-1} range into two sections. If the spectra corrected with the first fit yield negative line integrals, this means that the line is likely to be in the other velocity range, thus the second fit is applied. Because in the $\ell = 32°$ region the bulk of the RRL emission originates in the Scutum spiral arm, the first fit recovers high velocity RRL emission by excluding the velocity range 60 to 120 km s^{-1} and the second fit excludes the RRL range of 0 to 70 km s^{-1}. In both cases, a second order polynomial

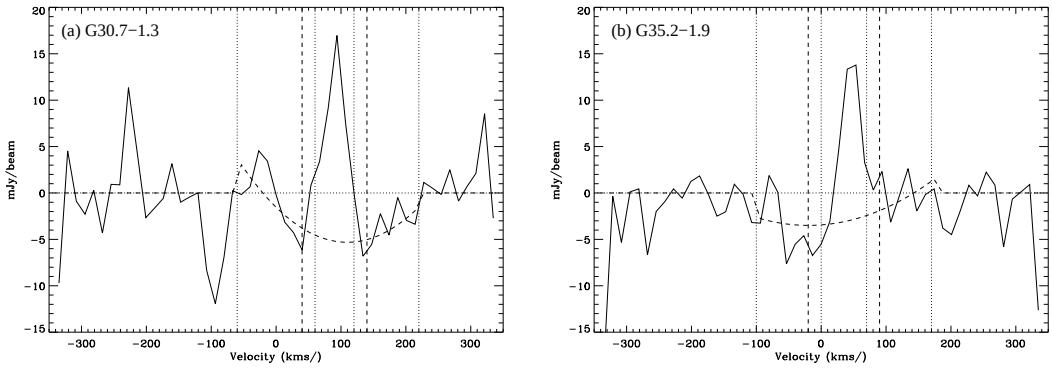

Figure 5.12: The two polynomial fits applied to the spectra of the $\ell = 32°$ cube, if the signal-to-noise ratio is below the defined threshold of 4.5. The outer and inner vertical dotted lines depict the fit and RRL velocity ranges, respectively. The dashed lines are the velocity limits for the line integral calculation.

fit is performed with a ±100 km s^{-1} baseline either side of the RRL range. This set of parameters was chosen after careful inspection of the spectra across the cube, when fitted with different polynomial degrees in various combinations of velocity ranges. Fig. 5.12 (a) shows the spectrum centred on (ℓ, b)=(30°.7, −1°.3), for which the first set of baseline fitting parameters are adequate to recover the $\sim$ 20 mJy/beam line at $V \sim$ 90 km s^{-1}. In the case of the lower RRL velocity, $V \sim 40$ km s^{-1}, in the spectrum of Fig. 5.12 (b), the second fit is applied. This process effectively removes fine structure in the baseline ripple.

The new RRL pipeline described in this chapter was used to produce the cubes 040, 032 and 024. The difference in the reduction of each data cube is on the velocity parameters of the post-processing baseline fit, which were chosen accordingly to the RRL emission velocity at each longitude range. These are presented in Table 5.1.

As a summary of the previous sections, Fig. 5.13 shows a diagram representation of the RRL data reduction process.

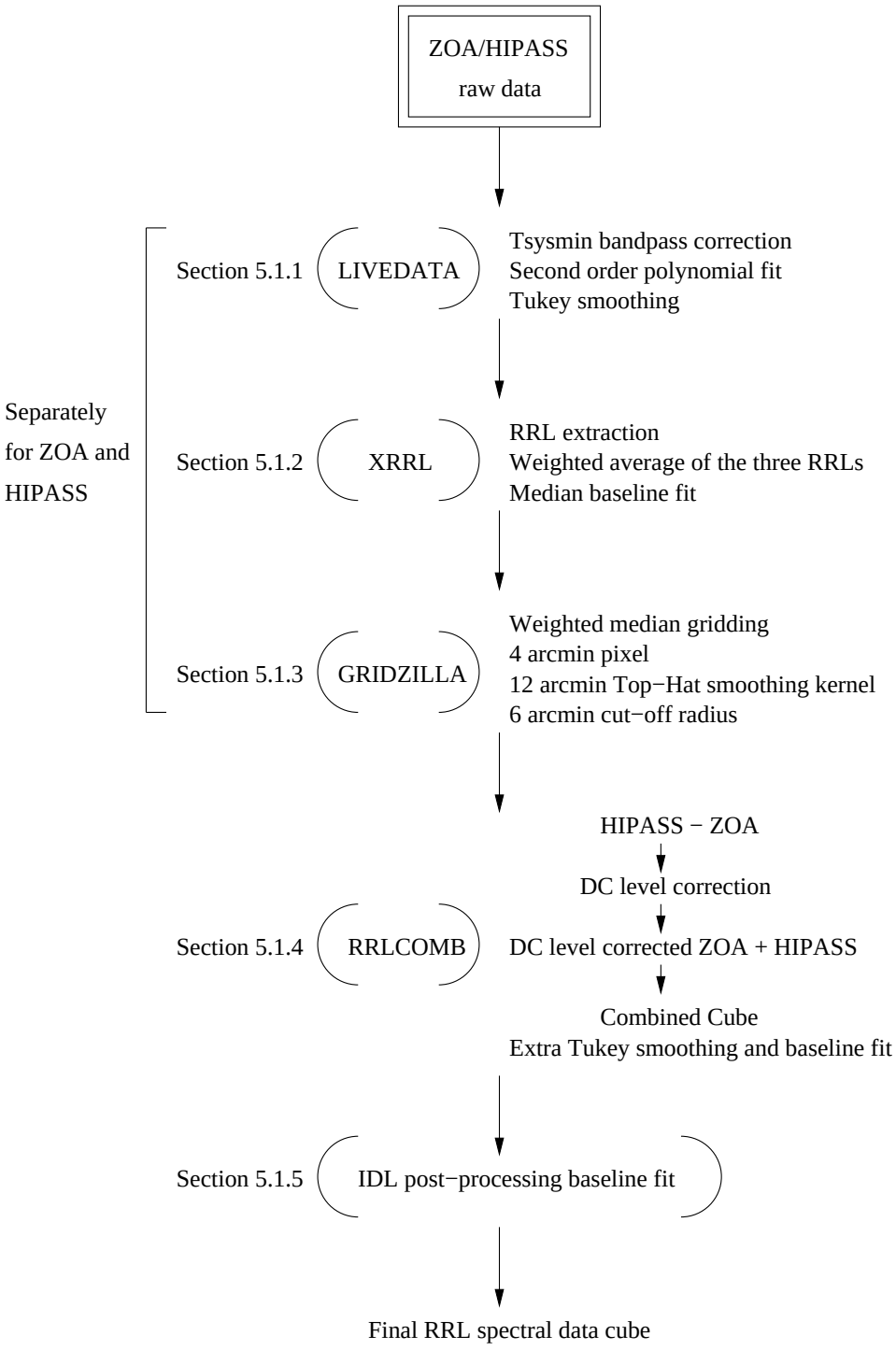

Figure 5.13: Schematic representation of the RRL pipeline described above, from the raw spectra to the final RRL spectral cube.

Table 5.1: The velocity ranges (in km s^{-1}) used in the post-processing baseline removal and line integral, described in this section. Column 2 is the velocity range over which spectra with signal-to-noise ratio above 4.5 are integrated; columns 3 and 6 (RRL) give the velocity range excluded from the fit, which is performed in the velocity range given in columns 4 and 7 (Fit); columns 5 and 8 give the range over which the line is integrated.

	No fit	First fit			Second fit		
Cube	Integral	RRL	Fit	Integral	RRL	Fit	Integral
$\ell = 40°$	$-20, 120$	$10, 100$	$-50, 160$	$-10, 120$	$50, 110$	$-50, 210$	$40, 120$
$\ell = 32°$	$-20, 150$	$60, 120$	$40, 140$	$-10, 120$	$0, 70$	$-50, 210$	$-20, 90$
$\ell = 24°$	$0, 150$	$70, 120$	$-60, 250$	$70, 120$	$10, 70$	$-90, 170$	$10, 70$

5.2 Properties of the final datacubes

Following the different data reduction process presented in this chapter to that used in the previous analysis of the ZOA-040 data cube (Chapter 4), the image properties have changed and significantly improved.

5.2.1 Spectral noise and resolution

The spectral resolution is now 20 km s^{-1}, instead of 27 km s^{-1}, after additional Tukey 25% smoothing is applied to the data, in place of Hanning smoothing. The typical noise level in each channel is 3.5 mJy/beam, or 3.0 mK, which is consistent with the theoretical noise of the ZOA survey (Section 3.1.2). The rms of spectra for strong H regions is $\sim 4 - 5$ mJy/beam, caused by the rise of the continuum emission which produces the baseline ripple.

5.2.2 Spatial resolution

The final spatial resolution, is altered by the different gridding algorithm used and it can be estimated via simulations, which inject false Gaussian sources into the data prior to imaging. The simulations show that for the weighted median gridding algorithm, the broadening of the intrinsic 14.4 arcmin beam is negligible. However the real beams

Table 5.2: The RRL map final beam width. The estimation is made using two sources for which the sizes are obtained from the 2.7 GHz Effelsberg map at 4.3 arcmin resolution (Reich et al. 1990a). The errors are from the fitting procedure .

		RRL map	
Source	Size (arcmin)	Observed Size (arcmin)	Beamwidth (arcmin)
W40	$(6'.0 \pm 0'.3) \times (5'.7 \pm 0'.3)$	$(16'.2 \pm 0'.4) \times (14'.9 \pm 0'.4)$	$(15'.0 \pm 0'.4) \times (13'.8 \pm 0'.4)$
W49	$(2'.9 \pm 0'.2) \times (1'.8 \pm 0'.2)$	$(15'.8 \pm 0'.4) \times (14'.9 \pm 0'.4)$	$(15'.5 \pm 0'.4) \times (14'.7 \pm 0'.4)$

of the telescope can only be accounted for by measuring the sizes of compact sources in the final maps. Ideally, a number of sources should be used but the only isolated H region in the area of the sky under study is W40 (G28.8+3.5). W49 (G43.2+0.0), which is even smaller than W40, can be also used; even though it is on the Galactic plane, this H region is very bright and relatively isolated. The task within is used to fit a Gaussian profile to both sources in the total integrated RRL map and determine the observed sizes. In order to get the beam widths, these are deconvolved with the effective size of the objects, as seen at the higher frequency and higher resolution survey by Reich et al. (1990a). The results, shown in Table 5.2, are consistent within the errors. The average beam size is $14'.8$ with an error of $0'.6$, which is consistent with the intrinsic resolution of 14.4 arcmin and with the simulations. This result shows that the similar widths of the 13 beams (Section 3.1.1) are averaged on the sky to give a final resolution of 14.8 ± 0.6 arcmin.

5.2.3 Data calibration

The spectra, in units of Jy/beam, are calibrated using extragalactic point sources and then converted into units of brightness temperature using equation (3.2). Ω, in equation (3.2), is set to the main beam of 14.8 arcmin, so that the spectra are calibrated in the point source scale. However, due to the fact that no beam normalisation is applied when the data are gridded, the flux for point sources is lowered in the final cubes. This is controlled by the cut-off radius, since the final value for a given pixel is the median

Table 5.3: Correction factors to be applied to the flux measurements made on the images gridded using a 6 arcmin cut-off radius.

FWHM (arcmin)	0	5	10	15	30	60	120
Scale factor	1.20	1.17	1.12	1.09	1.03	1.01	1.01

Table 5.4: Correction factors to be applied to the flux measurements of point sources made on the images gridded using different cut-off radii.

Cut-off radius (arcmin)	6	5	4	3	2	1
Scale factor	1.20	1.12	1.07	1.05	1.03	1.02

of all the data that are within a certain distance from it. Simulations show that for a cut-off radius of 6 arcmin, the peak fluxes of point sources are underestimated by 20%. This is due to the fact that for point sources the data away from the peak are at a lower value, therefore the average is lowered. For extended sources, the effect is less because the data away from the peak are not much lower. Table 5.3 shows the corrections to be applied when gridding with a 6 arcmin radius, as a function of the source size.

Regridding a map with a progressively smaller cut-off radius, should render higher peak fluxes for point sources, since less averaging is performed in the gridding process. Fitting a Gaussian profile to the 032 map at the velocity channel that corresponds to the RRL peak of W40, at 0 km s^{-1}, shows that the peak flux of this compact source increases 17% with decreasing cut-off radius, from 6 to 3 arcmin. However, the peak flux decreases in the 2 and 1 arcmin cut-off radii cubes. Even though the ZOA survey is well sampled, the 032 cube gridded with a 1 arcmin cut-off radius has some empty pixels. Other possible causes of this decrease are the relative position between the pixel and the data that contribute to it, or the increased susceptibility of the final spectra to systematic effects. Table 5.4 shows the correction factors, from simulations, to be applied to point source fluxes, as a function of the cut-off radii used to grid the cubes. Although the peak flux of point sources is only underestimated by 5% if a 3 arcmin cut-off radius is used, compared to 20% using 6 arcmin, the resulting spectra

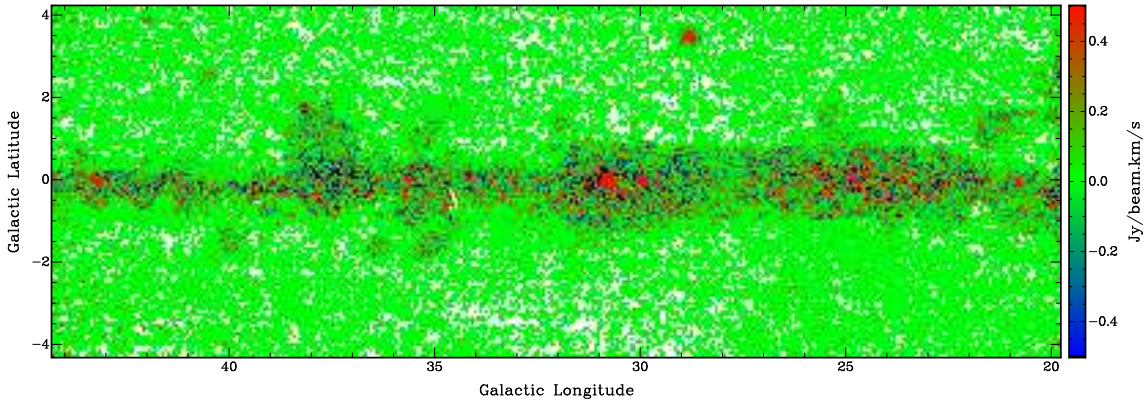

Figure 5.14: Map of integrated RRL emission, in units of Jy/beam km s^{-1} from ℓ = 20° to 44°and $|b| \leq 4°$, from the difference between the 4 arcmin minus the 6 arcmin cut-off radii cubes. This identifies the sources, W49 and W40, where the calibration correction is significant.

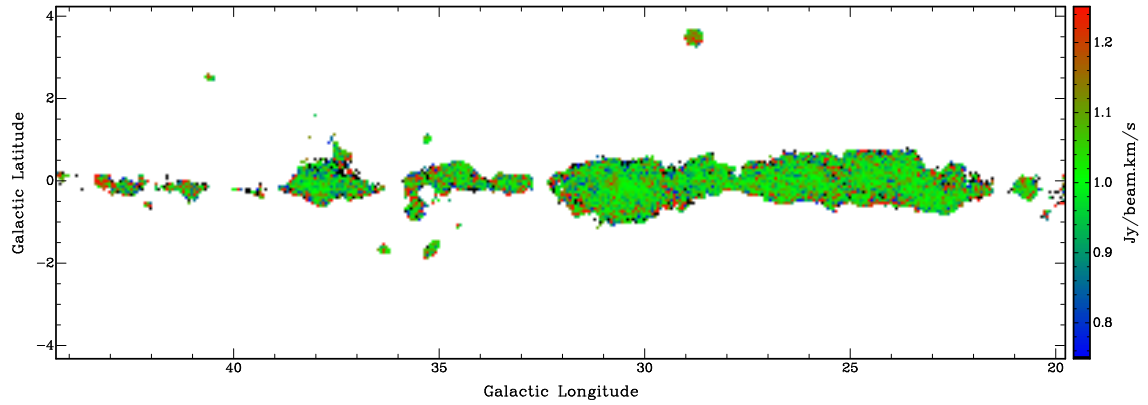

Figure 5.15: Map of the quotient between the RRL integral maps from the cubes reduced with 4 arcmin divided by 6 arcmin cut-off radius, in units of Jy/beam km s^{-1} from ℓ = 20° to 44°and $|b| \leq 4°$.

are noisier. Measurements of the rms of spectra away from the Galactic plane for the 6 and 3 arcmin cut-off radius cubes, give 4.8 mJy/beam and 7.9 mJy/beam, respectively. Also, the rms of the corresponding RRL peak line temperature maps are 2.0 mJy/beam and 3.8 mJy/beam.

Table 5.4 indicates that the 4 arcmin cut-off radius cube produces fluxes for point sources that are 12 per cent higher than in the 6 arcmin cut-off radius cube. Therefore, subtracting the corresponding line integral maps should allow the identification of the regions whose flux needs to be calibrated. Fig. 5.14 shows the difference between the

RRL integral map from the cubes derived with 4 and 6 arcmin cut-off radii. The spectra are integrated 40 km s^{-1} either side of the line using the task which was set to reject spectra below 2σ. The H regions W49 and W40 are identified as well as two H regions in the W43 group, G30.7+0.0 and G29.9-0.0. W43 is an extended group of H regions, the brightest in this region of the Galaxy. The map in Fig. 5.15 is the quotient between the line integral maps from the 4 and 6 arcmin cut-off radii cubes. It indicates that in fact the level of correction in the W43 complex is not greater than 10 per cent. The expected ratio of 12 per cent for point sources is measured at the position of W49 and W40.

Since the bulk of the total RRL emission in the maps is extended, as it will be shown in the next Chapter, I use the 6 arcmin cut-off radius maps with no correction factor applied. This cut-off radius is used because it provides an adequate flux scale with an error of approximately 10 per cent for extended sources in a low noise cube.

5.3 The distribution of RRL emisson from $\ell = 20^\circ$ to 44°

5.3.1 The $\ell = 40^\circ$ cube

The total RRL emission map for the $\ell = 40^\circ$ region is shown in Fig. 5.16. The maximum and minimum of the map are 5.6 and -0.1 K km s^{-1}, respectively and the rms noise away from the Galactic plane is 0.06 K km s^{-1}. This map recovers the individual H regions at a similar level of emission to that derived for $\ell = 40^\circ$ in Chapter 4 using the previous analysis based on the 5 algorithm (Fig. 4.16). Importantly, it is less noisy, with less negatives and striping features. The largest negative is now at a 1.7σ level, whereas before it was at 4σ. More extended emission is recovered on the plane at the high longitude end of the map, where the negative sidelobe next to the strong H region W49 has now disappeared.

The difference map between the present and the previous result is shown in Fig.

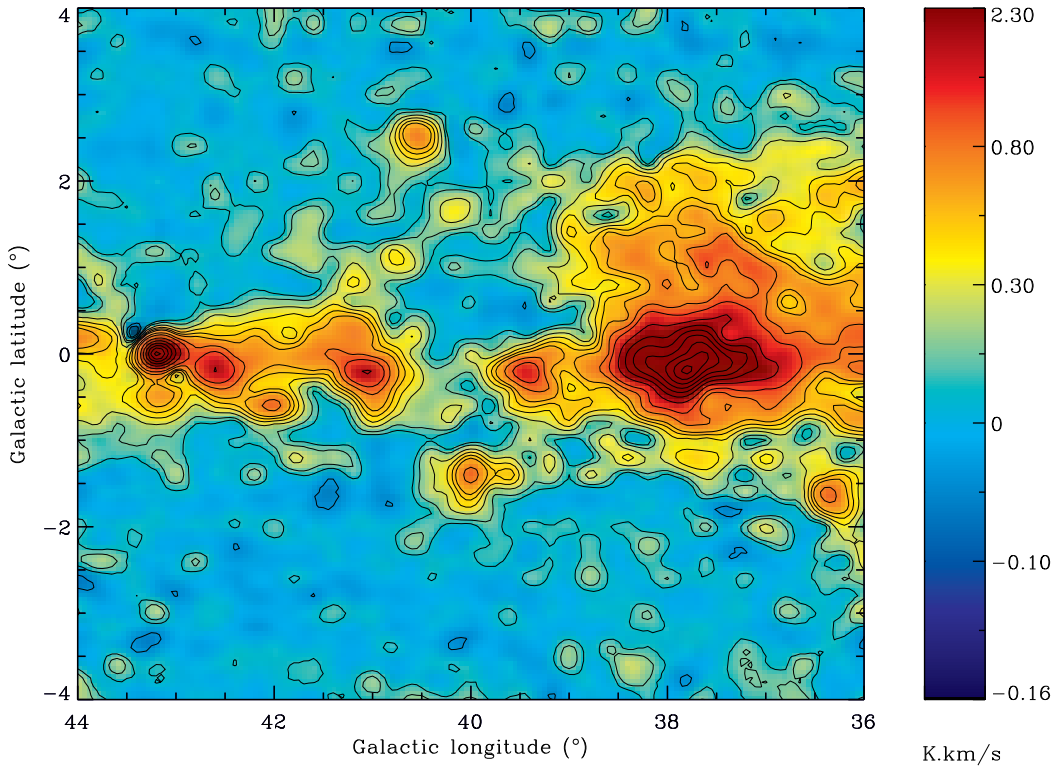

Figure 5.16: Map of the total integrated RRL emission in the ℓ = 40° cube (in K km s^{-1}). The contours and non-linear colour scale are the same as in Fig. 4.16. The resolution of the map is 14.8 arcmin.

5.17. Its rms noise, dominated by the 5 map, is 1.6% of the maximum which corresponds to 0.09 K km s^{-1}. The minimum and maximum are −1.04 K km s^{-1} at (ℓ,b)=(37°.2,+0°.8) and 1.02 K km s^{-1} at (ℓ,b)=(37°.2,+0°.0), respectively. The remaining artifacts in the present map are due to residual baseline effects, but they only affect a small number of pixels for which the optimal baseline fitting parameters cannot recover the whole RRL signal. Another effect contributing to the difference between the two results is the fact that the previous analysis was based on a 4^{th} order polynomial fit to overcome the difficult baselines; this could have slighlty overestimated the RRL signal in some areas. There is ∼ 6% increase in the extended emission at high latitudes in the present map. This is the result of more stable spectral baselines even away from the plane, which also provide the lower rms in the RRL integrated map.

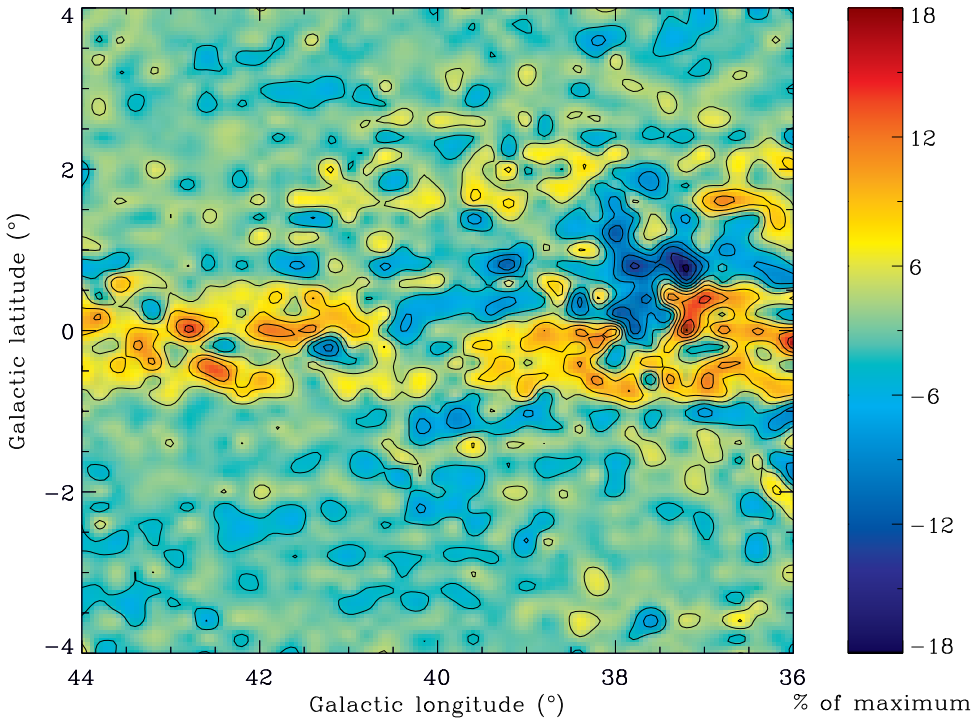

Figure 5.17: The difference map of the total integrated RRL emission at $\ell = 40°$ (in K km s^{-1}) from the present analysis (Fig. 5.16) minus that of the previous analysis (Fig. 4.16), described in Chapter 4. The difference is in percentage units relative to the maximum line integral, which is 5.6 K km s^{-1} for both maps.

5.3.2 The $\ell = 32°$ cube

The map of the total RRL emission in the $\ell = 32°$ region is shown in Fig. 5.18. Well-known H regions are identified in the map, as well as the diffuse RRL emission on the Galactic plane. The maximum and minimum of the map are 26.7 K km s^{-1} and −0.2 K km s^{-1}, respectively, and the rms noise measured away from the Galactic plane is 0.05 K km s^{-1}. Thus, the largest negative of the map at (ℓ,b)=(29°.4,2°.2) is at a 4σ level. Low-level striping at a 1.8σ level is visible below the Galactic plane.

The dynamic range of W40, defined as the ratio between the maximum intensity and the maximum artifact around it, is 34; negative sidelobes are at a the 3σ level. The dynamic range can be caused by noise or systematics. In the case of W40 it is likely that systematic effects, probably related to be sidelobes of the beam, are the main cause. The negative at (ℓ,b)=(34°.7,−0°.4) is caused by the SNR W44, which has

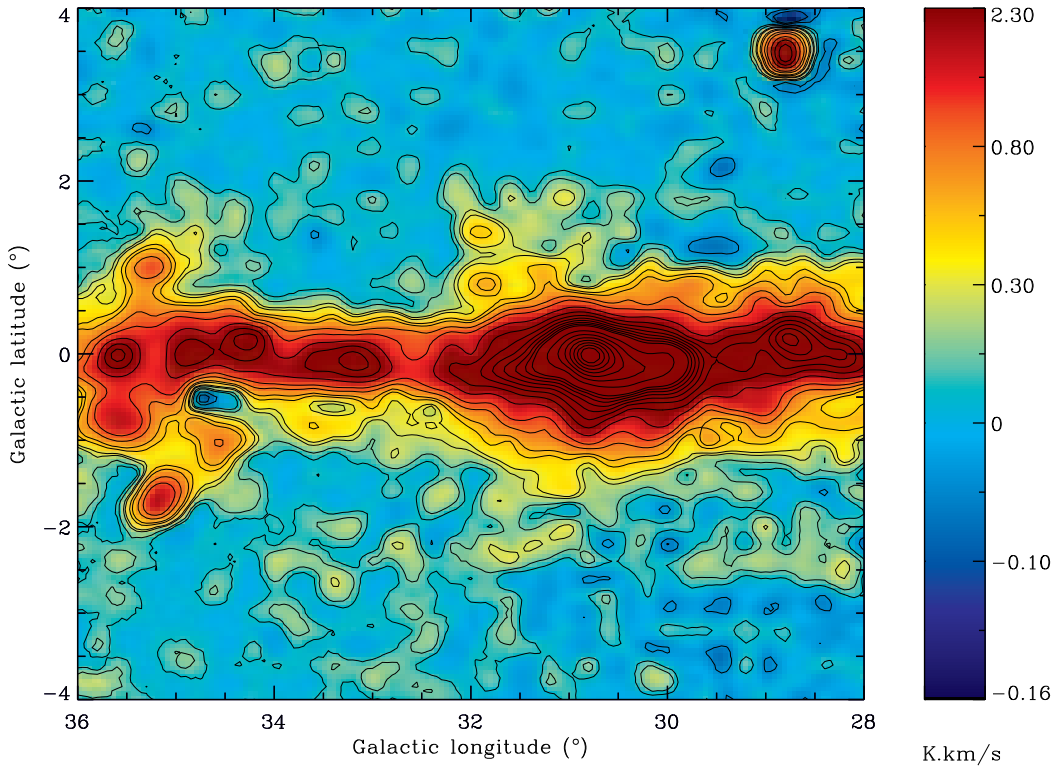

Figure 5.18: Map of the total integrated RRL emission in the ℓ = 32° cube (in K km s^{-1}). Contours and colour scale are the same as in Fig. 5.16, with additional contours at 100, 140, 180, 220, 260, 300, 340 and 380 per cent of 5.29 K km s^{-1}. The resolution of the map is 14.8 arcmin.

a flux density and size at 1.4 GHz of 272 Jy and 23 arcmin (Altenhoff et al. 1970). Therefore, this strong continuum source produces baseline distortions that result in a spectral negative at 1399.8 MHz (~ -95 km s^{-1}) in its surrounding pixels.

5.3.3 The ℓ = 24° cube

The total RRL emission map recovered from the ℓ = 24° cube is shown in Fig. 5.19. The maximum and minimum of the map are 10.2 and −0.1 K km s^{-1}, respectively, and the rms noise is 0.04 K km s^{-1}. The largest negative of the map is at the 2.5σ level, at (ℓ,b)=(25°.2,−3°.8). Individual well-known H regions are recovered, as well as a ridge of diffuse emission between $|b| \simeq 1°$. The RRL emission features that extend to positive latitudes at ℓ = 25°.5 and ℓ = 21°.5 are at a 2.2σ and 3σ level, respectively, and

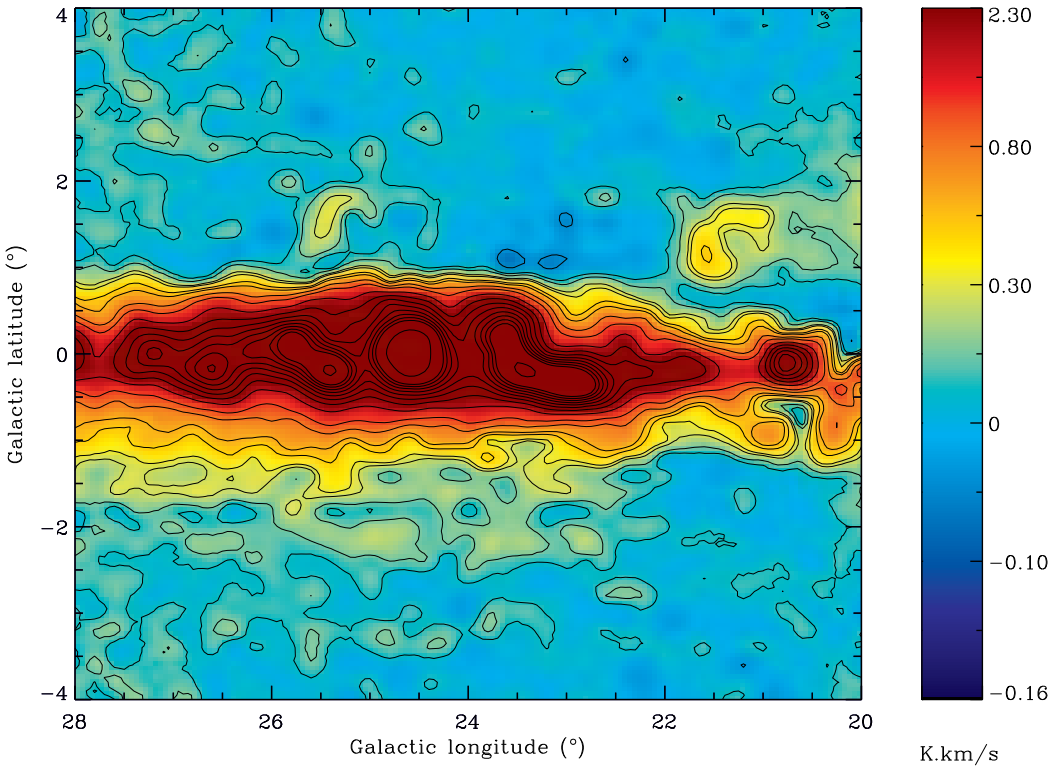

Figure 5.19: Map of the total integrated RRL emission in the $\ell = 24°$ cube (in K km s^{-1}). Contours and colour scale are the same as in Fig. 5.18. The resolution of the map is 14.8 arcmin.

are seen in continuum maps at 1.4 GHz, such as the map presented in the next section (Fig. 5.20). There is a sharp cut-off in RRL emission which causes the contours to lump around $b \sim +1°$; above that latitude the RRL signal is weak, 4 – 5 mK, only $\sim 1.6\sigma$ above the rms noise of the spectra. This asymmetry in latitude is also visible in the continuum map in Fig. 5.20. Despite the similarities, the low diffuse RRL emission above $|b| \sim 1°$ may be partly due to sidelobe effects caused by the strong and narrow continuum emission from the Galactic plane.

5.4 The Parkes 1.4 GHz continuum map

The 1.4 GHz continuum map from the combination of HIPASS and ZOA data, for the region $\ell = 20°$ to 44°, is presented in this section. The analysis of the continuum data

was carried out by Dr. Mark Calabretta. In particular, the ZOA DC level correction and the combination of the HIPASS and ZOA datasets, were adapted from the continuum analysis to the spectral recombination line study. For the continuum map, the bandpass correction uses the minimum-running-median, or $minmed_n$ algorithm, with a box size of 10 integrations. The continuum bandpass-corrected and calibrated files are then gridded using the same parameters, namely the pixel size, the cut-off radius, smoothing kernel and no beam normalisation, as those used in the imaging of the RRL data. Following the gridding of ZOA and HIPASS data, the maps for each $8^\circ \times 8^\circ$ zone are corrected for the DC offset, through an iterative process. First the ZOA and HIPASS datacubes are gridded and subtracted in Galactic coordinates, where the DC levels are averaged in Galactic longitude and then added back to the ZOA cube. Then, the datasets are gridded and subtracted in equatorial coordinates, where, this time, features along the declination direction are averaged. After the iterative process to correct for the zero levels, the final map is gridded in Galactic coordinates using the same parameters in as those used to produce the RRL cubes. Furthermore, the calibration factors in this map are the same as in the RRL maps. No point source correction is applied.

In order to assess the overall calibration of the Parkes continuum map, the integrated flux of a few sources was calculated and compared with the results from the 1.4 GHz Effelsberg map (Reich et al. 1990b). The continuum sources are fitted with a Gaussian profile using the task in both maps, where the Effelsberg map is spatially smoothed from 9.4 to 14.8 arcmin. The results are shown in Table 5.5, along with the corresponding errors from the fitting procedure. The error on the ratios of the weakest sources, W45 and RCW179, is mainly due to the fact that they are surrounded by an extended emission background, which affects the fit. For W40 and W49, the error on the integrated flux is less than 12%. The average ratio between the flux densities for these sources is 1.07 with an rms of 0.13, which shows that the two datasets are consistent. The positive bias of the ratio is due to the fact that the point source correction factor has not been applied to the Parkes continuum map. Therefore the flux

Table 5.5: Integrated intensities and measured sizes of continuum sources fitted from the Effelsberg and the Parkes 1.4 GHz maps. The Effelsberg map (Reich et al. 1990b) is smoothed to the same resolution, 14′.8, of the Parkes continuum map. The errors on the flux density and sizes are from the fitting procedure; the error bars are the same for both dimensions of the source sizes, therefore only one error measurement is given.

Source	Effelsberg (E)		Parkes (P)		Ratio (E/P)
	Flux density (Jy)	Size (arcmin)	Flux density (Jy)	Size (arcmin)	
G28.8+3.5 W40	32 ± 4	(16 × 16) ± 1	26 ± 3	(15 × 14) ± 1	1.23 ± 0.21
G40.5+2.5 W45	8 ± 4	(17 × 16) ± 5	9 ± 4	(18 × 17) ± 5	0.89 ± 0.60
G43.2-0.1 W49	82 ± 5	(22.0 × 15.7) ± 0.9	69 ± 4	(21.0 × 15.3) ± 0.8	1.19 ± 0.10
G41.1-0.3	35 ± 5	(21 × 19) ± 2	36 ± 5	(23 × 21) ± 2	0.97 ± 0.19
G36.3-1.7 RCW179	14 ± 7	(26 × 23) ± 10	13 ± 6	(26 × 23) ± 10	1.08 ± 0.73
					1.07 ± 0.13

densities of compact objects are expected to be underestimated by $\lesssim$ 20%, as indicated in Table 5.3.

The contour map of the 1.4 GHz Parkes continuum for the 24° × 8° region under study is presented in Fig. 5.20, along with the contour plot of the thermal brightness temperature estimated from the RRL line integral. The brightness temperature, T_b, was calculated using 7000 K for the electron temperature, as in Section 4.3.1. Fig. 5.20 shows that the 032 region is the strongest in continuum, as compared to the other two zones. This is mostly due to the W43 H region at (ℓ,b)=(30°.8,+0°.0) and the SNR W44 at (ℓ,b)=(34°.7,−0°.5), that peak at 79 K and 67 K, respectively. Well-known H regions and SNRs can be readily identified by comparing the two maps.

A thorough comparison between these results, as well as comparisons with other datasets at different frequencies and the implications of the adopted value of T_e = 7000 K, will be discussed in the next chapter.

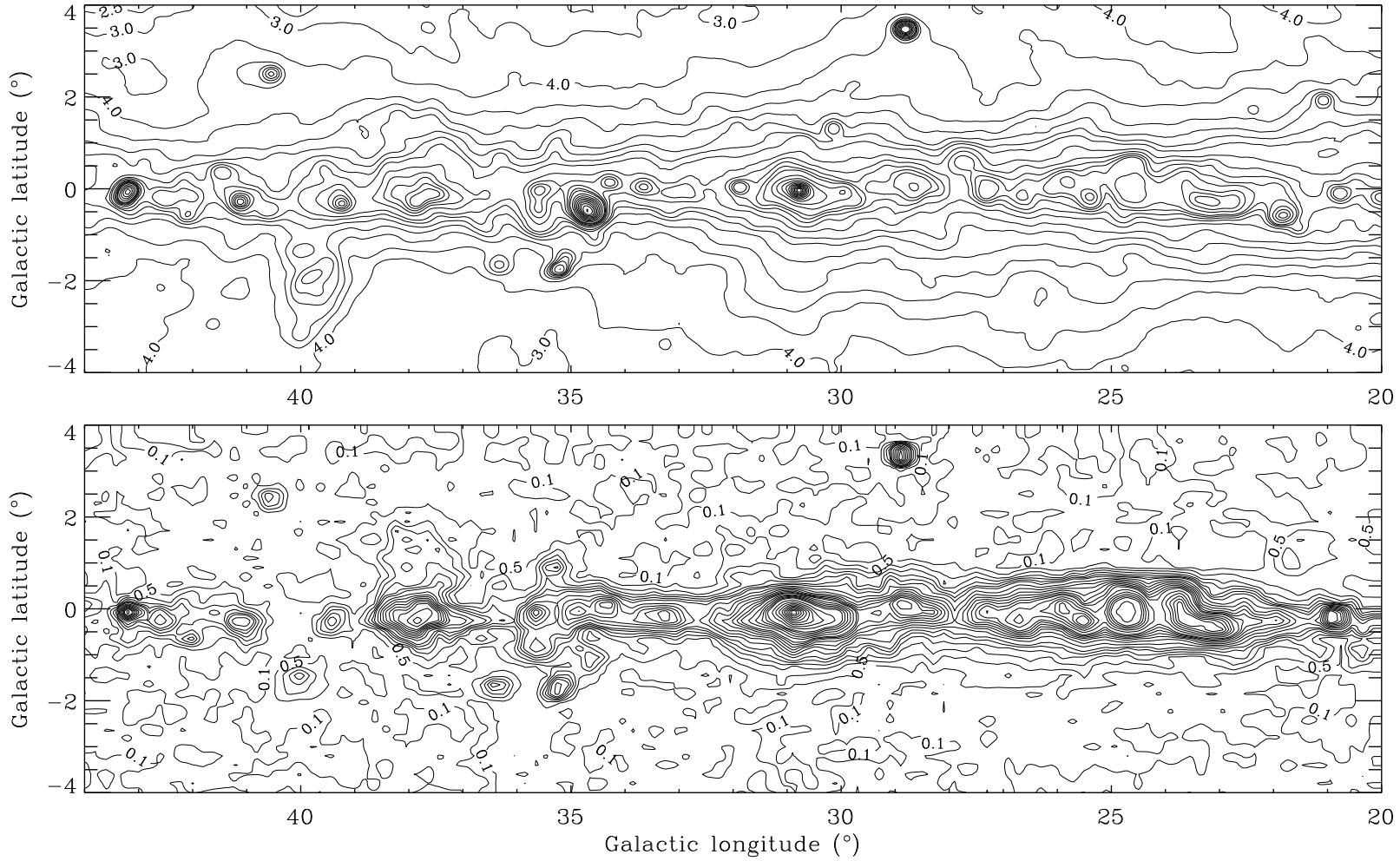

Figure 5.20: Maps of the total (top) and thermal (bottom) brightness temperature at 1.4 GHz for the region $\ell = 20° - 44°$, $|b| \leq 4°$. The continuum map is from the combination of ZOA and HIPASS surveys (see text) and the free-free is estimated from the RRLs with $T_e = 7000$ K. The contours are given at 0.1, 0.5, 1, 1.5, 2 and 2.5 and then at every 1 K from 3 to 10 K, every 2 K from 10 to 20 K and then every 5 K up to 80 K. The first eight contours are labelled in the maps. The resolution of the map is 14.8 arcmin.

6

Implications for Galactic and CMB science

In this Chapter I present the main results of this work and their implications for Galactic and CMB science. It is organised as follows: in section 6.1 the electron temperature of the thermal emission is derived along with the best free-free map for the region $\ell = 20°$ to $44°$. This map, when subtracted from the total continuum, enables the synchrotron emission to be derived for the same region, which is presented in Section 6.2. Sections 6.3 and 6.4 give the list of H regions and SNRs extracted from the free-free and synchrotron maps, respectively. In Section 6.5 I compare the free-free latitude distribution of the thermal emission with WMAP and Hα data. The velocity and radial distribution of the RRL gas in the Galaxy is presented in Section 6.6 and finally Section 6.7 shows two examples of He and C RRLs from the present survey.

6.1 T_e of the thermal emission from $\ell = 20°$ to $44°$

In this Section I present a method of determining the electron temperature for the diffuse ionised component which is used to estimate the final free-free brightness temperature map.

6.1.1 Method to determine T_e

The maps of total and thermal brightness temperature from the ZOA and HIPASS surveys allow the separation between the free-free and synchrotron emission at 1.4 GHz. At this frequency, the emission from the Galaxy is dominated by these two components, thus the synchrotron is the total minus the free-free estimated from the RRL data. Using the total continuum and free-free maps of Fig. 5.20 the synchrotron emission is obtained for a fixed electron temperature of T_e = 7000 K across the region. The longitude distribution at $b = 0^\circ$ of the three components is shown in Fig. 6.1. The decreases in the synchrotron emission indicated by the arrows are correlated with the free-free emission. For those H regions, the assumed T_e = 7000 K for the diffuse emission overestimates the free-free producing an apparent decrease in the synchrotron. When the electron temperature of an H region is higher than 7000 K, as is the case of W40, the derived synchrotron is overestimated which produces an increase.

The variation of T_e in discrete H regions with longitude, or Galactic radius, is well known and can be taken into account by applying the $T_e - R_G$ relationships derived by Shaver et al. (1983) and Paladini et al. (2004) to the RRL integral map, where the Galactocentric distance is calculated using the RRL velocity information and a Galactic rotation curve. Applying the Paladini et al. (2004) relationship to correct the free-free map for T_e, results in the synchrotron distribution given by the dotted line in Fig. 6.1. It can be seen that the decreases are partly suppressed and the synchrotron distribution is smoother. However, there is a spread in T_e at a given Galactocentric radius as shown in Fig. 2.6. Therefore, and in order to apply the appropriate T_e correction for the diffuse H under study, I chose to derive a $T_e - R_G$ relationship using the present continuum and RRL data.

The line-to-continuum ratio is one of the most precise methods of determining the electron temperature of an ionised region (Section 2.5.1) and this survey has the advantage of providing both the line and the continuum data at the same resolution, after going through the same reduction pipeline. However, to use equation (2.41) to cal-

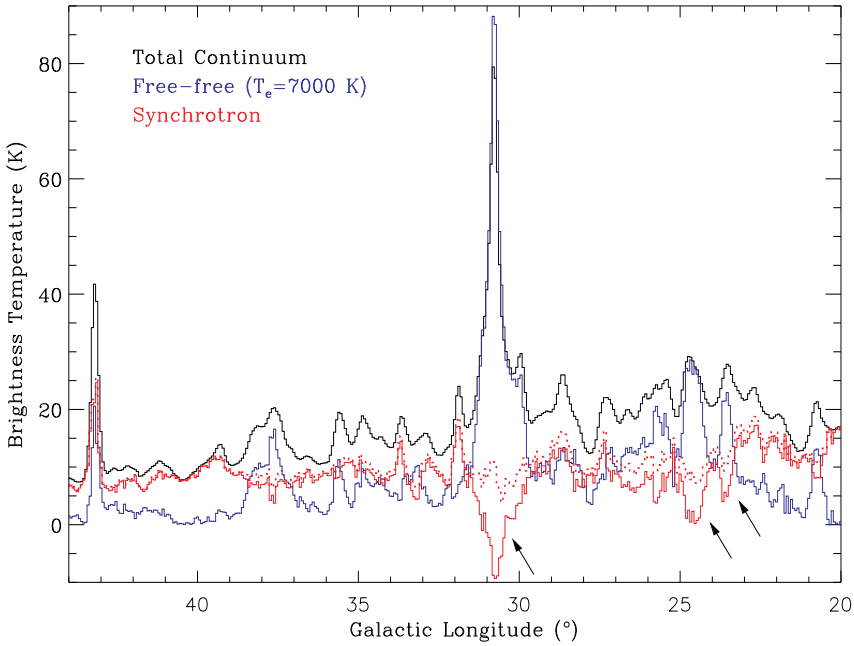

Figure 6.1: Comparison between the total continuum, the free-free estimation from the RRLs and the synchrotron, versus longitude, at $b = 0°$. The full and dotted red lines represent the synchrotron when the free-free is derived firstly using a constant value of $T_e = 7000$ K and secondly using the $T_e - R_G$ relationship from Paladini et al. (2004). The arrows show three regions of decrease in the derived synchrotron emission coincident in shape and position with H regions.

culate T_e, the continuum temperature must correspond to the thermal component only so any remaining synchrotron emission underlying the H region has to be subtracted. The method adopted to deal with this degeneracy problem is based on the fact that the synchrotron longitude distribution is relatively smooth, as shown in Fig. 6.1. Thus, for an H region away from a strong synchrotron emitting source, the background synchrotron emission can be estimated by taking the average of its longitude distribution either side of the source. A detailed description of the method with further examples is given in the next sections.

6.1.2 Examples of T_e variations in the diffuse emission

Figure 6.2 (a) shows the longitude profiles of the total continuum, free-free and synchrotron at $b = 3°.5$, where the free-free is estimated using the constant value of $T_e = 7000$ K. The synchrotron distribution is smooth with an average value of ~ 3.5 K away from the compact object W40. Fig. 6.2 (b) gives a zoom in on the H region W40 centred at $l = 28°.8$. The synchrotron distribution shows an increase correlated with the free-free distribution which indicates that the electron temperature of this H region is higher than 7000 K. The longitude extent of W40 is estimated from its free-free distribution and given by the inner vertical lines. The background synchrotron emission is the average of the synchrotron distribution estimated between the outer and inner vertical lines. This restricted range in longitude is to account for the broad emission component underlying W40 which is considered to be synchrotron emission, since it is not seen in free-free. Sidelobe effects on the RRL map around this strong and compact source are a possible cause of the negatives seen around W40 (Section 5.3.2) but are not likely to suppress the broad emission if it were to be free-free since it is observed in the total continuum from the same survey. The resulting synchrotron background is $T_{sync} = 6.0 \pm 0.6$ K and is shown as the horizontal line between $\ell = 29°.3$ and $28°.3$ in Fig. 6.2 (b). The error on T_{sync}, 0.6 K, is estimated from the rms of the synchrotron map measured away from the Galactic plane.

Figure 6.3 shows the longitude profiles of the total continuum, free-free and synchrotron for two other H regions, G25.8+0.2 and G20.7-0.1. The free-free is estimated using the constant value of $T_e = 7000$ K and the derived synchrotron shows a decrease at the position of each source. These H regions have an electron temperature lower than 7000 K, as it will be shown in Section 6.1.4. The synchrotron background is estimated between the inner and outer vertical lines to exclude the object and is shown as the horizontal lines in each figure.

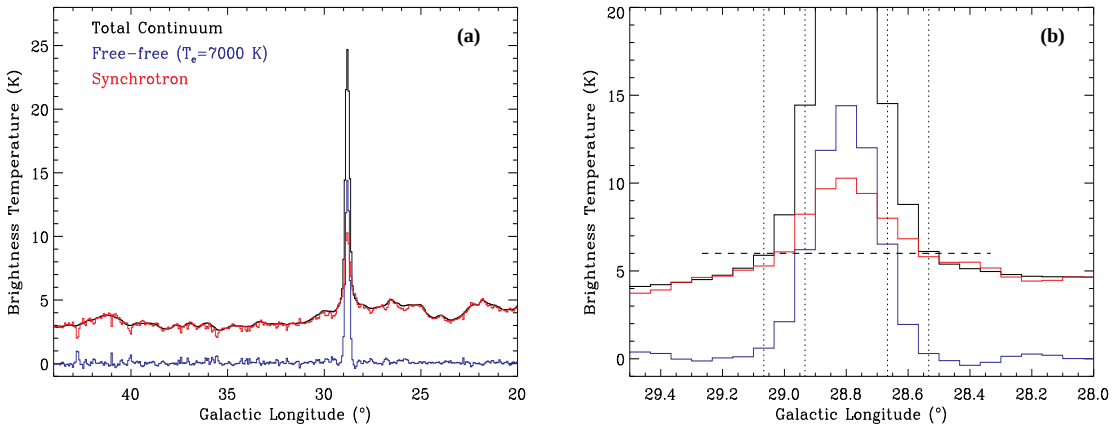

Figure 6.2: Longitude cut at b = 3°.5, through the H region W40. The synchrotron background is the mean estimated between the outer and inner vertical lines in (b), and the result is given by the horizontal line between ℓ = 29°.3 and 28°.3.

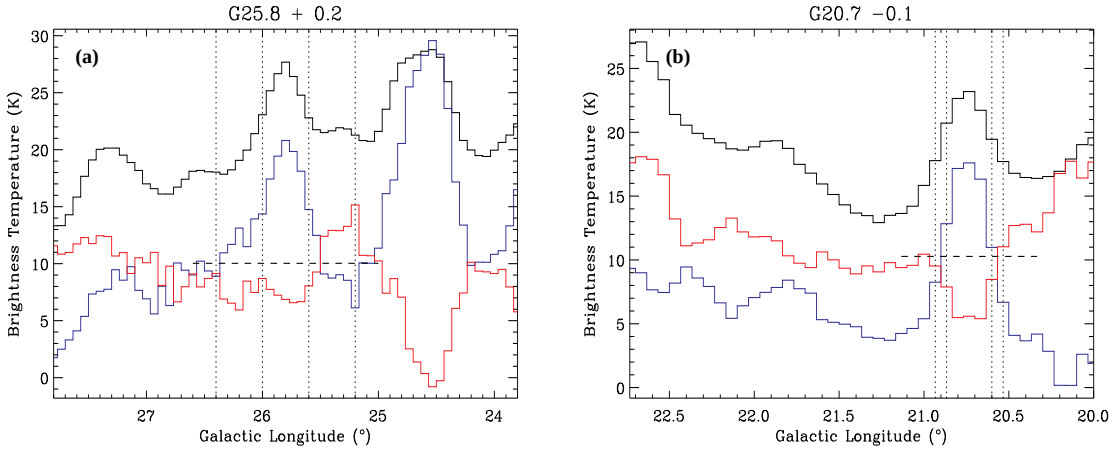

Figure 6.3: Longitude cut at b = +0°.2 and b = −0°.1, through the sources (a) G25.8+0.2 and (b) G20.7-0.1. The black line represents the total continuum, the blue is the free-free with T_e = 7000 K and the red is the synchrotron. The synchrotron background is the mean estimated between the outer and inner vertical lines and the result is given by the horizontal line (Section 6.1.4).

6.1.3 Estimate of the electron temperature

To derive T_e, I use equation (2.41) in the form:

$$T_e = 2847.39 \times \left(\frac{T_C - T_{sync}}{\int T_L \Delta V} \right)^{-1.15} \quad (6.1)$$

where a, in equation (2.12), is assumed to be 1, $\nu_{GHz} = 1.4$ and $\int T_L \Delta V$ is in units of K km s^{-1}. The thermal brightness temperature is the difference between the continuum temperature at the central longitude of the H region and the estimated synchrotron, $T_{ff} = T_C - T_{sync}$. The line integral is also taken at the centre of the source. For W40, $T_C = 24.7 \pm 0.6$ K, $T_{ff} = 18.7 \pm 0.2$ K, $\int T_L \Delta V = 5.1 \pm 0.5$ K km s^{-1}. The error bars on the continuum, free-free, synchrotron and line integral are taken as the rms of the respective maps away from the Galactic plane, which are then propagated into the electron temperature using equation (6.1). The derived electron temperature for W40 is 8770 ± 560 K. Table 6.1 compares published T_e values with the results from this work. It includes W40 and the two H regions in Fig. 6.3, whose T_e was obtained in the same way. There is a good agreement in the results, despite the different angular resolutions and frequencies of the published observations. For example, the H region survey by Quireza et al. (2006) at 8.6 GHz and 3.2 arcmin resolution detects W40 with an angular size of 8.5 arcmin, similar to what is found in this work (see Section 6.3.1).

I have also used the procedure to fit a Gaussian profile to W40 on the continuum and line integral maps. The result is $T_C = 23.0 \pm 0.6$ K, which is equivalent to T_{ff} since a background was subtracted by , and $\int T_L \Delta V = 6.2 \pm 0.1$ K km s^{-1}. Therefore, $T_e = 8770 \pm 250$ K. This result is in good agreement with the previous value of 8770 ± 560 K which shows that the method of estimating the synchrotron using the longitude cuts gives reliable values. A procedure such as would be ideal to subtract the synchrotron background from H regions, but it is less reliable on the Galactic plane due to the strong emission and source confusion.

Table 6.1: Published electron temperatures for the H regions W40, G25.8+0.2 and G20.7-0.1 compared with the values found in this work.

H Region	Downes et al. (1980)	Wink et al. (1983)	Quireza et al. (2006)	This work
W40	-	8000 ± 1400	8450 ± 70	8770 ± 560
G25.8+0.2	6200 ± 2500	5000 ± 800	6120 ± 100	6060 ± 290
G20.7-0.1	5900 ± 2500	7100 ± 900	5590 ± 90	5340 ± 290

6.1.4 The T_e distribution as a function of Galactic radius

In order to obtain the relationship $T_e - R_G$, the discrete H regions used to estimate T_e must cover a wide range of Galactocentric radii. The longitude range $\ell = 20° - 44°$ includes emisson between $V \sim 0 - 100$ km s^{-1}, which is equivalent to $R_G \sim 4 - 8.5$ kpc. The Galactocentric radius of an H region at longitude ℓ and velocity V is obtained by combining equations (2.49) and (2.50):

$$R_G = \frac{221.64 R_0}{\Theta_0 + V/\sin(\ell) + 0.44 R_0} \tag{6.2}$$

where R_G is in kpc, $R_0 = 8.5$ kpc and $\Theta_0 = 220$ km s^{-1} (Section 2.5.1). A group of 16 H regions was selected for this study. Even though there are more objects in the field, these are the H regions with clearer longitude profiles combined with the fact that their RRL spectra have only one velocity component. Table 6.2 lists the H regions with the corresponding velocities and Galactocentric distances, along with T_C, T_{sync}, T_{ff}, $\int T_L \Delta V$ and the derived T_e. The background synchrotron level varies between $\sim 4 - 12.5$ K and increases along the Galactic plane towards lower longitudes, as seen in Fig. 6.1.

The electron temperatures obtained for the 16 H regions are shown in Fig. 6.4 as a function of the Galactocentric distance. The best linear fit to the data gives:

$$T_e = (3467 \pm 463) + (501 \pm 96) R_G \tag{6.3}$$

where the absolute errors on T_e are taken into account by the fitting procedure,

. As shown in Fig. 6.4 this result is in general agreement with the Paladini

Table 6.2: List of H regions selected for the study of the electron temperature variation with Galactocentric distance. R_G is calculated using the RRL central velocity, listed in column 2, and equation (6.2) with $R_0 = 8.5$ kpc. T_C, T_{sync}, T_{ff}, $\int T_L \Delta V$ are obtained from the longitude profiles using the method described in the text for W40; the errors, taken as the rms measured on the maps away from the Galactic plane, are 0.6 K, 0.6 K, 0.2 K and 0.5 K km s^{-1}, respectively. T_e is calculated using equation (6.1).

H Region	V (km s^{-1})	R_G (kpc)	T_C (K)	T_{sync} (K)	T_{ff} (K)	$\int T_L \Delta V$ (K km s^{-1})	T_e (K)
G40.5+2.5	26.8	7.1	9.5	5.0	4.5	1.3	8360 ± 1590
G37.8-0.1	53.6	6.1	21.1	6.4	14.7	6.0	6180 ± 340
G37.7-0.2	53.6	6.1	22.3	7.3	15.0	5.8	6520 ± 350
G36.3-1.7	66.9	5.6	7.0	3.8	3.2	1.3	6210 ± 1480
G35.6+0.0	53.6	6.0	19.4	8.8	10.6	4.0	6650 ± 410
G33.1-0.1	93.7	4.8	15.7	8.6	7.1	3.3	5564 ± 525
G30.9-0.1	93.7	4.6	61.0	8.9	52.1	23.7	5660 ± 190
G30.7+0.0	93.7	4.6	77.3	10.4	66.9	30.9	5580 ± 170
G30.0-0.1	93.7	4.6	61.0	8.9	52.1	23.7	5780 ± 280
G28.8+3.5	0.0	8.4	24.7	6.0	18.7	5.1	8770 ± 560
G27.1+0.0	93.7	4.4	20.9	8.6	12.3	4.8	6500 ± 440
G25.8+0.2	107.1	4.0	27.7	10.0	17.6	7.4	6060 ± 290
G24.8+0.1	107.1	3.9	28.9	8.4	20.5	9.1	5790 ± 240
G23.5+0.0	93.7	4.1	27.4	12.0	15.4	7.4	5400 ± 280
G22.9-0.3	66.9	4.8	33.7	12.5	21.2	9.2	5870 ± 220
G20.7-0.1	53.6	5.0	23.2	10.3	12.9	6.3	5340 ± 290

et al. (2004) and Shaver et al. (1983) results, even though they have larger samples of objects. The difference between the three lines is mainly caused by the lack of data points beyond the solar radius in the present sample and the two higher T_e values from the local H regions W40 and W45. There is an intrinsic scatter at any given R_G in all studies due to the different properties of each H region.

6.1.5 The total free-free brightness temperature

I am now in the position to convert the RRL map into free-free brightness temperature at each pixel using the derived $T_e - R_G$ relationship. In order to automate the calculation of R_G and thus T_e at each position, I use the velocity that corresponds to the maximum

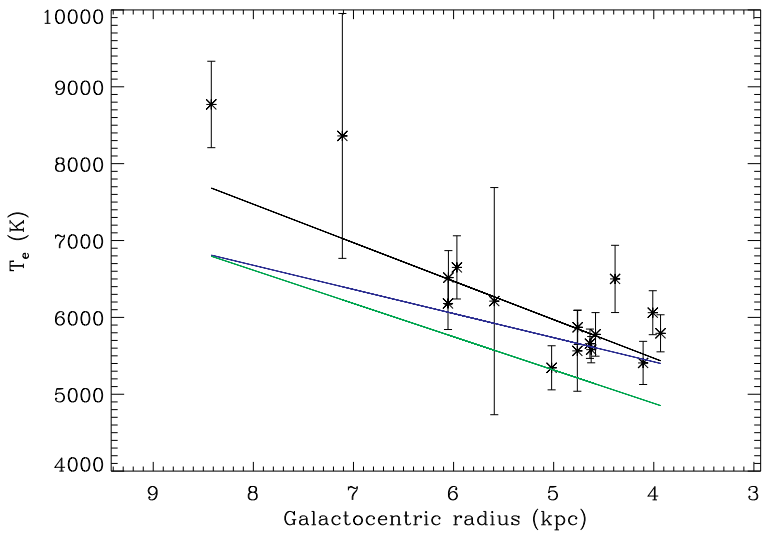

Figure 6.4: The $T_e - R_G$ relationship derived from the results in Table 6.2. The black line gives the best linear fit to the data points (equation (6.3)) and the blue and green lines are the Paladini et al. (2004) and Shaver et al. (1983) results, respectively.

of the RRL spectrum estimated between −30 to 160 km s^{-1} in equation (6.2). Two issues arise with this method. The first is that some spectra have two velocity components, therefore using the peak velocity assigns all the emission to a single radius, and the second is that away from the plane the peak velocities are affected by noise.

For the double-peaked spectra, the electron temperature should be the mean of the two velocity contributions, weighted by the line intensities. However, some lines are blended due to the spectral resolution, which makes it difficult to separate the two line temperatures in an automated way. If one line component, with temperature T_{L_1}, is dominant then the mean T_e is also dominated by T_{e_1}. Only if T_{L_1} and T_{L_2} are comparable does T_e result from a significant contribution from both components. As an example, the spectrum at $(\ell, b) = (25°.4, +0°.1)$ shown in Fig. 6.5, has T_{L_1} = 79 mK at V = 107 km s^{-1} and T_{L_2} = 82 mK at V = 53 km s^{-1}. The corresponding Galactocentric distances are 4.0 kpc and 5.4 kpc, respectively. Using equation (6.3), T_{e_1} = 5470 ± 850 K and T_{e_2} = 6170 ± 980 K. The mean electron temperature at this position is thus 5820 ± 1300. This shows that adopting T_e that corresponds to

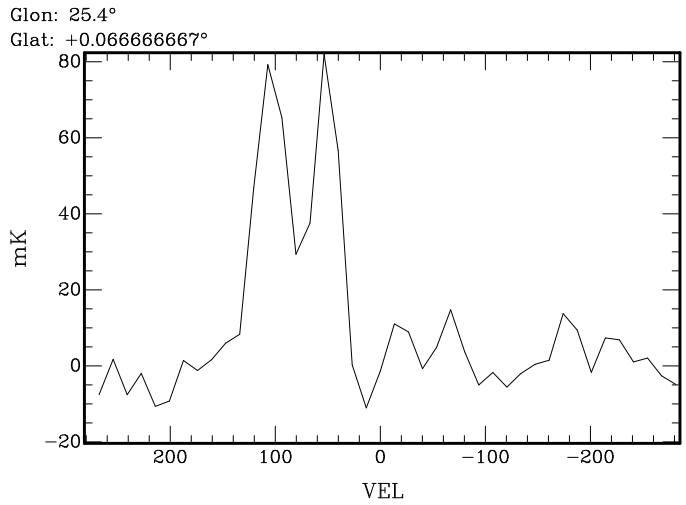

Figure 6.5: Spectrum at $(\ell, b) = (25^\circ.4, +0^\circ.1)$, showing two velocity components, at $V = 107$ km s^{-1} and $V = 53$ km s^{-1}, of similar intensity.

the brightest line component is sufficient given the accuracy on the $T_e - R_G$ relationship with further uncertainties in the estimation of V and R_G. For spectra away from the plane, even though the maximum of the line may correspond to a random velocity within the -30 to 160 km s^{-1} range, the signals are weak therefore the free-free emission is not significantly affected. As a result, the electron temperature map for the region $\ell = 20^\circ - 44^\circ$ derived using equation (6.3) and the RRL velocities has minimum and maximum values of 4900 K and 8590 K, respectively, with an average value at $b = 0^\circ$ of 6080 ± 970 K.

The final and best free-free map, obtained using the $T_e - R_G$ relationship in the conversion of the RRL line integral at each position, is shown in Fig. 6.9. The changes are relatively small compared with the map in Fig. 5.20, where a constant value of $T_e = 7000$ K is used. Fig. 6.6 shows the latitude distribution from both maps, averaged over the 24° longitude range. The latitude profiles are very similar and have the same FWHM of 0°.8. This shows that the free-free emission is a narrow distribution around the plane. The peak of the free-free profile with $T_e = 7000$ K is ~ 1.25 times that of the the free-free with varying T_e, reflecting the lower mean value of $T_e \sim 6000$ K on the plane.

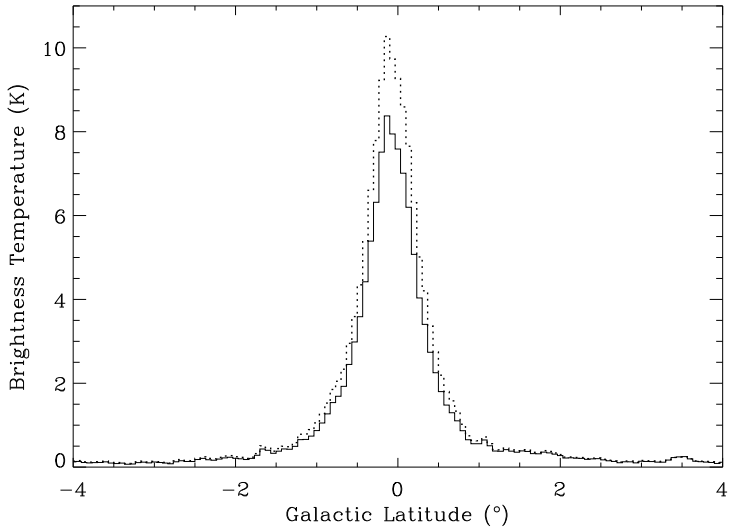

Figure 6.6: The free-free brightness temperature estimated from the RRLs versus latitude, average over the $\ell = 20° - 44°$ longitude range, using 4 arcmin latitude bands. The full line results from using the $T_e - R_G$ relationship in equation (6.3) and the dotted line from adopting the constant value of $T_e = 7000$ K.

6.2 The synchrotron emission

The synchrotron emission can now be obtained by subtracting the free-free estimated from the RRLs with varying electron temperature from the continuum. Fig. 6.7 shows this synchrotron contour map. Well-known SNRs are identified in the map, whose list will be presented in Section 6.4, along with a broad background emission falling to ~ 4 K at $|b| \lesssim 4°$.

There are some positive and negative residuals at the position of a few H regions. W40 and W48 (G35.2-1.7) are likely to be underestimated in free-free emission caused by an underestimation of their electron temperatures. In the case of W40, the broad emission underlying the compact source is thought to be of non-thermal origin (Section 6.1.2). The opposite applies to W47 (G37.8-0.1) and W43 (G30.9-0.1). These are groups of several H regions, unlikely to be characterised by a single T_e value.

Figure 6.8 (a) gives the synchrotron emission versus latitude, averaged over the 24° range in longitude, using 4 arcmin latitude bands. The three lines are the different

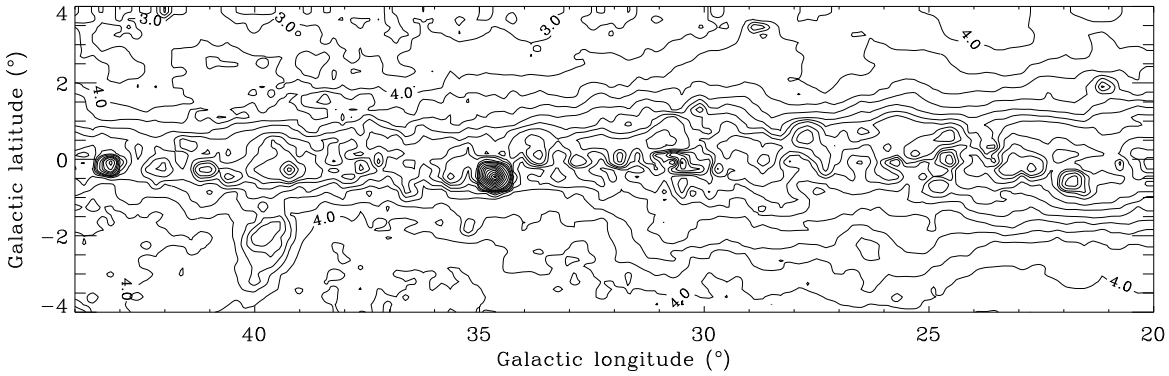

Figure 6.7: Map of the synchrotron emission at 1.4 GHz and 14.8 arcmin for the region $\ell = 20° - 44°$, $|b| \leq 4°$. The contours are given at every 1 K from 3 to 10 K, every 2 K from 10 to 20 K and then every 5 K up to 80 K. The first two contours are labelled in the map.

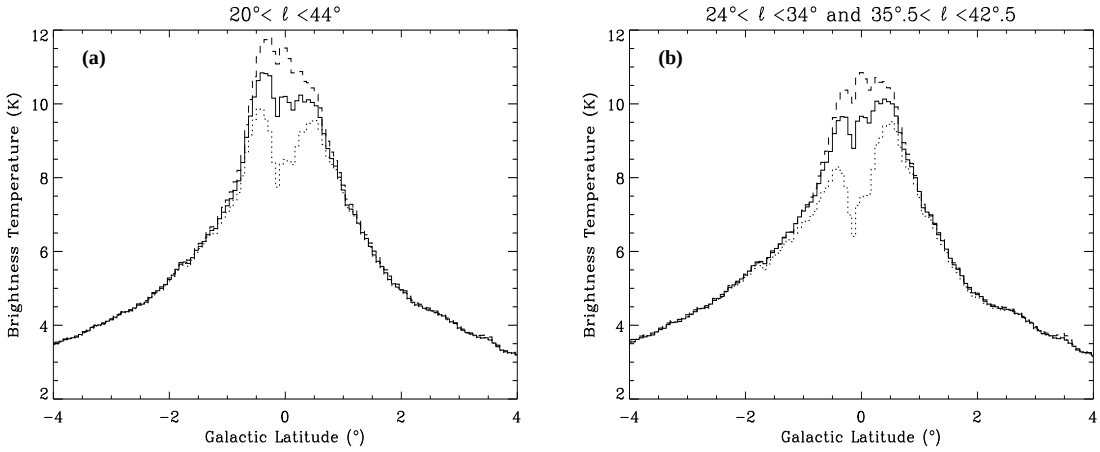

Figure 6.8: The synchrotron emission versus latitude, average over two longitude ranges using 4 arcmin latitude bands. The full line is for the present synchrotron map, obtained with the $T_e - R_G$ relationship, the dotted line is for $T_e = 7000$ K and the dashed line is for $T_e = 5000$ K.

synchrotron results using $T_e = T_e(R_G)$, $T_e = 7000$ K and $T_e = 5000$ K in the free-free estimation. The similarity between the three plots for $|b| \gtrsim 1°$ reflects the fact that the RRL line integral is low away from the plane, and therefore the synchrotron emission is the major contributor at 1.4 GHz for $|b| \gtrsim 1°$. The contribution of the strongest SNR in this region, W44 (G34.7-0.4), is visible at $b \sim -0°.4$. Fig. 6.8 (b) is an average over $\ell = 24° - 34°$ plus $\ell = 35°.5 - 42°.5$ in order to exclude four of

the brightest SNRs: W44, W41 (G23.3-0.3), Kes69 (G21.8-0.6) and W49B (G43.3-0.2). The smoother distribution given by the full and dashed lines in Fig. 6.8, with relation to the dotted line, seems to indicate that the electron temperature of the diffuse ionised gas on the Galactic plane is similar to that of the individual H regions and not higher. The average T_e at $b = 0^\circ$ of $\sim$ 6000 K produces a mean synchrotron level on the plane of $\sim$ 9 K, which increases to $\sim$ 11 K if $T_e = 5000$ K. Therefore, the error of $\sim$ 1000 K on the best fit for the electron temperature at $b = 0^\circ$ produces a difference in the synchrotron amplitude of $\sim$ 2 K.

The free-free map henceforth refers to the result of converting the RRL line integral into brightness temperature using $T_e = T_e(R_G)$, which when subtracted from the continuum produces the synchrotron map.

6.2.1 Comparison with the continuum

Figure 6.9 shows the continuum, free-free and synchrotron emission maps, plotted in the same linear intensity scale. The corresponding latitude distributions are shown in Fig. 6.10, for the ℓ range 20° to 44°, using 4 arcmin bins. It shows that the synchrotron is the dominant emission at high latitudes, where the free-free has fallen to a low value of 0.1 – 0.2 K. On the Galactic plane, the synchrotron accounts for $\sim$ 60% of the total emission.

The synchrotron distribution appears to have two components - one with a FWHM of $\sim$ 10° and a narrow Galactic plane component with a FWHM of $\sim$ 2°. Separation of Galactic thermal and non-thermal components has been performed by means of the correlation between infrared and radio emission (Broadbent et al. 1989) or according to their different spectral indices (Reich & Reich 1988; Paladini et al. 2005; Sun et al. 2011). Sun et al. (2011) use their recent survey at 6 cm, along with the Effelsberg data at 11 (Reich et al. 1990a) and 21 cm (Reich et al. 1990b), to separate thermal and non-thermal emission between $10^\circ \leq \ell \leq 60^\circ$. The derived synchrotron map shows a similar narrow component to that found here. This component is identified here for the

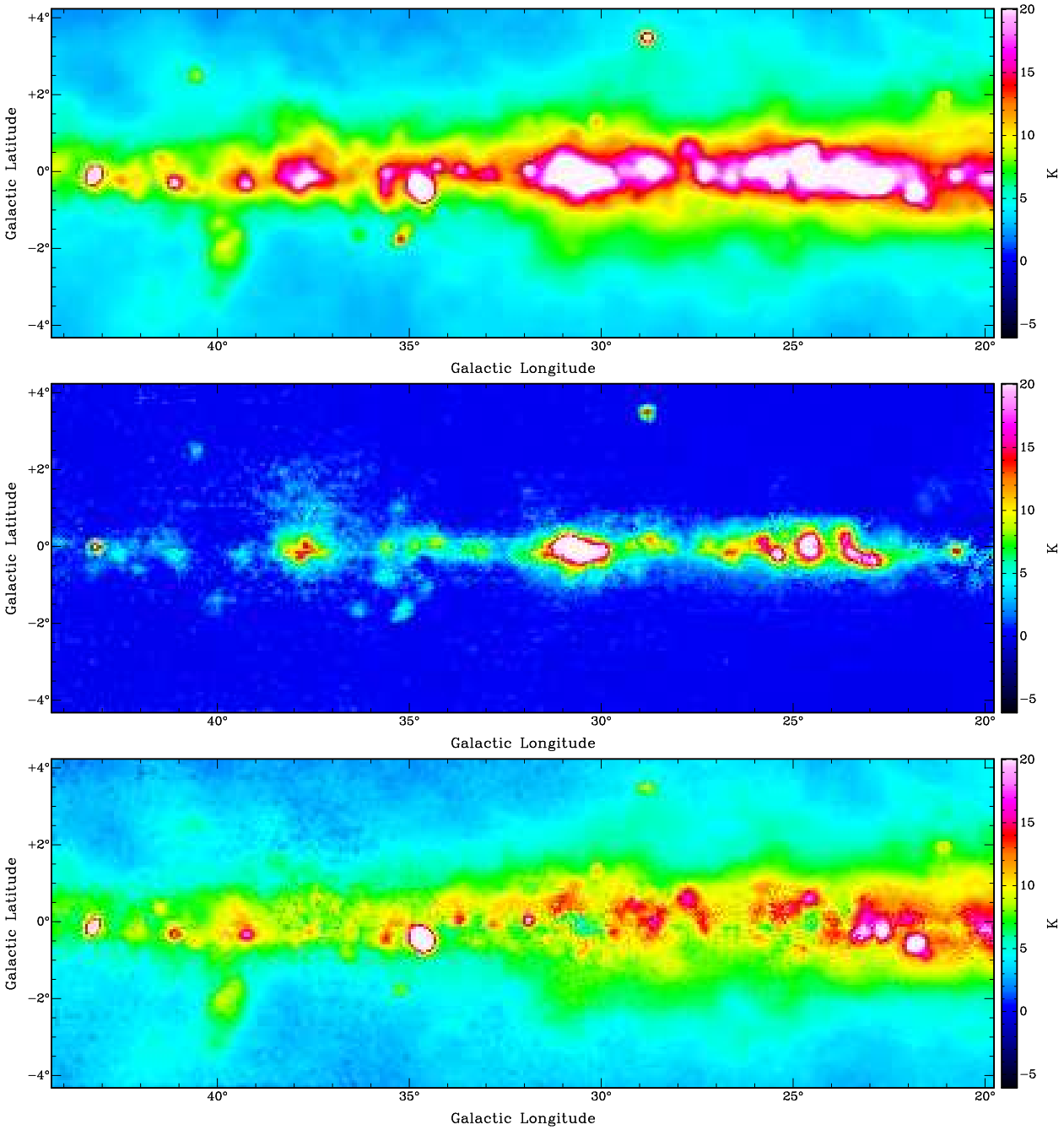

Figure 6.9: Maps of the total continuum (top), free-free (middle) and synchrotron (bottom) emission at 1.4 GHz and 14.8 arcmin resolution. The free-free is estimated from the RRL integral using the $T_e - R_G$ relationship from equation (6.3). The synchrotron is the difference between the continuum and the free-free emission and shows a narrow diffuse emission confined to the plane.

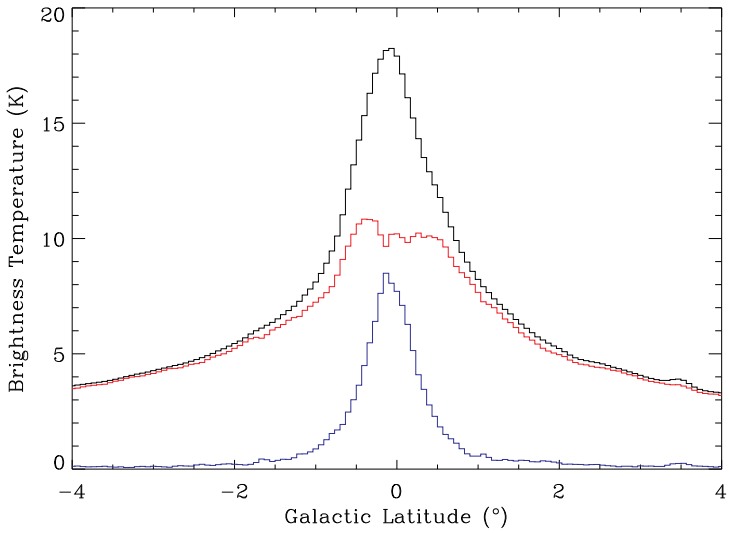

Figure 6.10: Comparison between the total continuum, the free-free and the synchrotron emission, versus latitude, for the longitude range $\ell = 20° - 44°$, using 4 arcmin latitude bands. The black line represents the continuum, the blue is the free-free and the red is the synchrotron.

first time by direct subtraction of the free-free emission.

Once the broad component of ~ 3.5 K is taken off the synchrotron, the contribution from the narrow component is comparable to that of the free-free on the plane.

6.3 Catalogue of H regions

6.3.1 Catalogue from the present work

Using the free-free map from the present work a catalogue of H regions with their angular sizes and fluxes at 1.4 GHz has been created. I have used SExtractor, a source extractor program (Bertin & Arnouts 1996). The main parameters to adjust in SExtractor are the background mesh size, filter function, detection threshold and minimum area. The background size used is 16, which corresponds to the number of pixels of each mesh where the background is estimated. The input map is $24° \times 8°$ with 4 arcmin pixels, so the mesh is $\simeq 1°$. This parameter produces a smooth background map with

the Galactic plane ridge. A Mexican hat filter of width equal to 3 pixels, similar to the 14.8 arcmin beam, was used to allow the detection of weaker and smaller sources. Other filters were tested, such has the Gaussian of same width, but the objects detected are mainly the brightest and most extended. The source has to extend over more than 2 pixels to trigger a detection with a threshold of 2σ above the background rms. The estimated background rms by SExtractor is 0.26 Jy/beam, therefore the threshold limit is 0.53 Jy/beam. SExtractor also performs deblending, to separate possible multiple components, controlled by the contrast parameter which is set to 0.005. The SExtractor parameters were tuned to recover objects on the Galactic plane with sizes consistent with what is seen in the free-free map and known from higher resolution surveys (**?**).

Table 6.3 lists the 57 H regions extracted from the free-free map. The position of each source is found in the filtered map by computing the first order moments of the rectangle which encloses the pixels detected above the threshold. The object is fitted for an elliptical shape whose parameters a and b are computed from the 2^{nd} order moments. They represent the maximum and minimum spatial rms dispersion of the source profile and correspond to the ellipse major and minor axis, respectively. The position angle (P.A.) listed is the angle between the semi-major axis of the source and the longitude axis, measured counter-clockwise. Once the source is detected in the filtered image, its peak flux is measured directly from the input map and subtracted by the background. The error on the peak flux is estimated using the rms errors on the free-free and background maps. I use the peak flux and the observed size to calculate the flux density assuming a Gaussian profile for the source:

$$S = S_{\text{P}} \frac{a \times b}{\text{fwhm}^2} \tag{6.4}$$

where S_{P} is the peak flux in Jy/beam and fwhm is the beam FWHM of 14.8 arcmin. The error on S is estimated using the errors on S_{P} and the errors on a and b, which are given by SExtractor. The maximum error on the observed size is 4 arcmin. A source of 5 arcmin in size is observed by the 14.8 arcmin beam with a diameter of 15.6 arcmin. This small broadening of the beamwidth is difficult to measure, especially for a weak

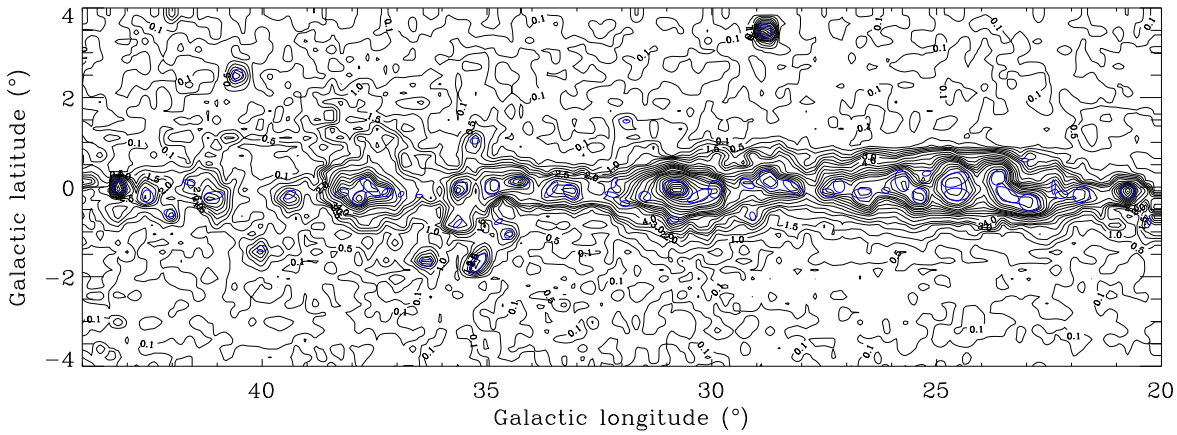

Figure 6.11: The free-free map of the region $\ell = 44°$ to 20°, with the 57 H regions listed in Table 6.3. The ellipses are drawn using the semi-major and minor ellipse parameters and the postion angle. The contours are given at 0.1, 0.5, 1, 1.5, 2 and 2.5 and then at every 1 K from 3 to 10 K, every 2 K from 10 to 20 K and then every 5 K up to 80 K. The first eight contours are labelled in the map.

object within the noise. For the objects whose apparent area is smaller than the beam area, the flux density is the same as the peak, $S = S_{\rm P}$. In such cases, the P.A. has a large uncertainty. Table 6.3 also includes a validation parameter, which is produced by various detection and measurement processes within SExtractor. If the flag is equal to: 1 the object has bright neighbours; 2 the source was originally blended with another one; 3 means that case 1 and 2 apply. Column 9 in Table 6.3 shows that deblending occurs mainly in the H complexes W47 ($\ell \sim 37°.5$), W43 ($\ell \sim 31°$), W42 ($\ell \sim 24°.5$) and at $\ell \sim 23°.5$.

Figure 6.11 shows the position of the 57 extracted H regions on the free-free map. This illustrates the orientation and size of each object detected by SExtractor.

Table 6.3: H regions in the region $\ell = 44^\circ$ to 20°, extracted from the present free-free map using SExtractor. Column 1 numbers each object; columns 2 and 3 are the coordinates; columns 4 and 5 give the angular size of the source, thus *a* and *b* deconvolved with the 14.8 arcmin beam, which is *p* when the object is less than a few ($\sim$ 5) arcmin; column 6 is the angle measured counter-clockwise between the semi-major axis of the source and the longitude axis; columns 7 and 8 give the peak and flux density at 1.4 GHz; column 9 gives the internal flags generated by SExtractor (see text); column 10 identifies a source by its commonly used name as in the Paladini et al. (2003) catalogue.

Number	ℓ ($^\circ$)	b ($^\circ$)	θ_a ($'$)	θ_b ($'$)	P.A. ($^\circ$)	Peak (Jy/beam)	Flux (Jy)	Flag	Name
1	43.18	0.00	10.4	6.3	−45	25.6 ± 3.6	41.2 ± 6.7	0	W49A
2	42.54	−0.21	9.7	*p*	−76	6.0 ± 1.3	6.8 ± 1.8	0	
3	42.06	−0.58	1.7	*p*	−9	3.7 ± 0.9	3.7 ± 0.9	0	
4	41.63	0.10	4.9	*p*	−19	4.7 ± 0.9	4.7 ± 0.9	0	
5	41.08	−0.19	21.7	*p*	11	8.0 ± 1.2	10.1 ± 2.0	0	
6	40.54	2.51	6.1	*p*	68	4.5 ± 1.0	4.5 ± 1.0	0	W45
7	40.00	−1.37	*p*	*p*	0	4.1 ± 1.2	4.1 ± 1.2	0	S74
8	39.38	−0.17	6.8	*p*	33	5.0 ± 1.3	5.0 ± 1.3	2	NRAO591
9	38.23	−0.14	12.2	*p*	19	12.4 ± 2.9	12.4 ± 2.9	1	
10	37.84	−0.25	17.1	1.7	47	17.8 ± 3.9	27.3 ± 6.5	3	W47
11	37.60	−0.01	32.2	*p*	−43	16.6 ± 3.3	32.0 ± 7.3	2	W47
12	37.21	−0.12	5.5	*p*	24	12.0 ± 2.5	12.0 ± 2.5	3	
13	36.91	−0.16	*p*	*p*	46	6.2 ± 2.0	6.2 ± 2.0	0	
14	36.50	−0.20	*p*	*p*	0	3.3 ± 1.8	3.3 ± 1.8	0	
15	36.34	−1.67	2.4	*p*	−9	4.3 ± 1.1	4.3 ± 1.1	0	RCW179
16	35.65	−0.81	5.2	*p*	45	5.0 ± 1.7	5.0 ± 1.7	2	
17	35.59	−0.01	10.1	7.7	86	10.5 ± 2.4	14.4 ± 3.6	0	
18	35.27	1.03	*p*	*p*	0	3.8 ± 1.2	3.8 ± 1.2	0	
19	35.19	−1.69	27.4	*p*	53	7.9 ± 1.4	13.7 ± 3.0	0	W48
20	34.88	0.00	15.9	11.6	69	9.2 ± 2.5	17.1 ± 5.0	0	
21	34.74	−0.77	*p*	*p*	32	3.2 ± 1.7	3.2 ± 1.7	0	W44
22	34.52	−1.05	*p*	*p*	47	3.8 ± 1.2	3.8 ± 1.2	0	
23	34.27	0.13	19.9	*p*	2	12.3 ± 3.0	16.5 ± 4.4	1	W44
24	33.57	−0.06	21.2	*p*	51	7.7 ± 2.4	8.2 ± 2.9	0	
25	33.14	−0.10	16.5	7.9	−45	9.6 ± 2.4	16.4 ± 4.4	0	Ke78
26	32.22	−0.17	12.9	*p*	−15	7.7 ± 2.3	7.7 ± 2.3	1	
27	32.17	0.10	2.4	*p*	70	6.6 ± 2.0	6.6 ± 2.0	1	
28	31.93	−0.37	*p*	*p*	2	8.4 ± 2.5	8.4 ± 2.5	1	

Number	ℓ (°)	b (°)	θ_a (′)	θ_b (′)	P.A. (°)	Peak (Jy/beam)	Flux (Jy)	Flag	Name
29	31.90	1.47	*p*	*p*	0	2.2 ± 0.6	2.2 ± 0.6	0	RCW177
30	31.49	−0.21	6.1	*p*	−9	15.1 ± 3.6	15.1 ± 3.6	3	
31	30.86	−0.74	4.9	*p*	12	8.4 ± 2.8	8.4 ± 2.8	0	
32	30.81	−0.02	29.1	12.2	−11	82.4 ± 16.3	236.3 ± 50.6	1	W43,M51,Ke76
33	30.27	−0.19	31.9	*p*	26	32.4 ± 6.4	66.0 ± 14.7	3	
34	29.93	−0.05	18.2	10.6	83	24.2 ± 4.8	47.5 ± 10.3	2	
35	29.21	0.08	14.0	*p*	−29	10.0 ± 3.2	10.1 ± 3.6	0	
36	29.09	−0.65	*p*	*p*	−73	4.1 ± 2.4	4.1 ± 2.4	0	RCW175
37	28.80	3.49	10.9	5.8	−52	19.0 ± 3.0	30.6 ± 5.4	0	W40
38	28.74	0.17	24.9	11.3	−43	13.1 ± 3.7	32.0 ± 9.6	1	
39	28.18	−0.02	29.0	*p*	−34	10.1 ± 3.1	17.9 ± 6.0	1	
40	27.41	−0.13	6.8	*p*	−18	7.8 ± 3.0	7.8 ± 3.0	3	3C387
41	27.17	0.03	10.6	*p*	−75	13.0 ± 4.5	10.7 ± 3.3	2	3C387
42	26.66	−0.14	21.7	*p*	2	14.9 ± 3.9	22.7 ± 4.5	1	
43	26.13	−0.07	*p*	*p*	0	10.8 ± 4.3	10.8 ± 4.3	3	
44	25.77	0.14	25.0	9.9	−78	16.5 ± 5.5	39.1 ± 13.4	3	
45	25.39	−0.20	14.5	10.6	−64	25.0 ± 7.2	43.1 ± 13.0	3	W42,Ke72
46	25.22	0.31	*p*	*p*	18	8.0 ± 5.8	8.0 ± 5.8	0	Ke71?,RCW173
47	24.58	0.17	33.9	10.1	19	24.0 ± 7.8	72.5 ± 24.3	3	W42
48	24.55	−0.16	29.2	7.1	−2	25.4 ± 7.9	62.1 ± 20.2	3	W42
49	23.62	0.22	17.1	8.6	53	19.1 ± 5.7	33.6 ± 10.5	3	
50	23.43	−0.17	30.6	5.2	−30	22.4 ± 5.8	54.8 ± 15.0	3	W41
51	23.03	0.60	*p*	*p*	0	2.0 ± 2.2	2.0 ± 2.2	0	S57
52	22.93	−0.35	24.7	15.9	−13	23.3 ± 5.3	66.7 ± 16.3	3	W41
53	22.40	−0.00	12.4	*p*	90	7.6 ± 2.2	7.6 ± 2.2	2	
54	22.22	−0.17	7.7	*p*	6	8.5 ± 2.3	8.5 ± 2.3	3	
55	21.78	−0.17	17.9	14.2	37	8.0 ± 1.8	17.4 ± 4.3	0	RCW168
56	20.74	−0.10	13.6	8.1	−14	17.1 ± 3.3	26.5 ± 5.6	0	Ke68
57	20.27	−0.77	*p*	*p*	90	2.9 ± 0.7	2.9 ± 0.7	0	

6.3.2 Comparison with the Paladini et al. (2003) catalogue

In this Section I compare the catalogue of sources from the present work with the Paladini et al. (2003) catalogue, which is the most extensive list of H regions to date. It is the compilation of 1442 objects from 24 previously published lists, containing RRL velocities for ≃ 800 objects and has been used to study the spatial distribution

of H regions in the Galaxy (Paladini et al. 2004). The recent survey by Bania et al. (2010), at a wavelength of 3 cm and 82 arcsec resolution, doubled the number of sources in the longitude range -16° to 67° but the list of objects is not yet publicly available. Such catalogues can be used to study the contamination of H regions at the high CMB observing frequencies (Paladini et al. 2003), but also to separate the contribution of individual sources from the diffuse emission.

The flux densities in the Paladini et al. (2003) catalogue, for the longitude region under study, are essentially from the 2.7 GHz survey by Reich et al. (1984) at a resolution of 4.3 arcmin. I have selected W40 and W49 and also a group of H regions from Table 6.3 to compare with the higher resolution catalogue by Paladini et al. (2003).

Compact H regions

W40 and W49 are the only H regions where a calibration correction of 20 per cent has been applied in Table 6.3, for the reasons discussed in Section 5.2.3.

W40 is listed in the Paladini et al. (2003) catalogue as G28.8+3.5 with a flux density of 34.0 ± 3.4 Jy at 2.7 GHz and size 5.5 ± 2.0 arcmin. Its flux density at 1.4 GHz, 37.3 ± 3.6 Jy, is obtained by extrapolating the 2.7 GHz value using a spectral index $\alpha = -0.1$ ($S \propto \nu^{\alpha}$). The flux density listed in Table 6.3 is 30.6 ± 5.4 Jy and the size is $10'.9 \times 5'.8$. The possible explanation for the remaining discrepancy in S involves $T_{\rm e}$. The possibility of W40 being optically thick at 1.4 GHz, which would generate a lower flux extrapolated from 2.7 GHz, is ruled out. This is based on the spectral index $\alpha = 0.0$ given by Altenhoff et al. (1970), from the flux measurements at 1.4, 2.7 and 5 GHz with a $\sim$ 10 arcmin beam in each case. The electron temperature obtained for W40 in Section 6.1 is 8770 ± 560 K, whereas the actual value used in the conversion of RRL line integral into free-free temperature is 7680 K, from equation (6.3) with $R_{\rm G} = 8.4$ kpc. This difference in $T_{\rm e}$ generates a flux density 1.16 times lower, thus the $T_{\rm e}$-corrected flux is 35.5 ± 6.3 Jy which is consistent with the flux from the Paladini et al. (2003) catalogue.

In the case of W49, the flux density obtained in this work is 41.2 ± 6.7 Jy. The

optically thin assumption in the extrapolation of the 2.7 GHz flux densities from the Paladini et al. (2003) catalogue does not apply to W49 which is a known complex of UCH regions (de Pree et al. 1997). For this object, I use the flux density measured at 1.4 GHz and 9 arcmin resolution by Altenhoff et al. (1970), 47 Jy, as opposed to the scaled flux density from the 2.7 GHz catalogue, 57 Jy. There is a SNR component of W49 10 arcmin away from the H region. They are commonly referred to as W49B and W49A, respectively. For this reason it is difficult to estimate the synchrotron background underlying the H region, therefore I did not estimate its electron temperature in Section 6.1.4. The published T_e for W49 by Quireza et al. (2006) is 8290 ± 64 K whereas the value used in the conversion of RRL line integral into free-free temperature is 7340 K, given by equation (6.3). The Galactic distance used is R_G = 7.7 kpc for a peak line velocity of 13 km s^{-1}. To correct for this, the flux density of W49 is multiplied by $(8290/7340)^{1.15}$ = 1.15. The final value of 47.4 ± 7.7 Jy is consistent with 47 Jy, the flux density given by Altenhoff et al. (1970).

Groups of H regions

In a complex of H regions the 14.8 arcmin beam cannot resolve the individual components, thus comparing the total integrated flux with the individual fluxes from the Paladini et al. (2003) is not straightforward. Moreover, the Paladini et al. catalogue is a compilation of results from various authors, whose surveys were performed with different telescope beam sizes, at several frequencies. On the plane, the large beam from the Parkes survey is likely to produce higher fluxes for a given group of H regions since it includes the diffuse emission around the individual components and also from the possible underestimation of the local background.

The 2.7 GHz survey by Reich et al. (1984), at a resolution of 4.3 arcmin, was used to identify the individual H regions within a group. For example the object G25.77+0.14 listed in Table 6.3 can be seen in the 2.7 GHz map as a group of 2 H regions: G25.7+0.0 and G25.8+0.2. These are listed in the Paladini et al. catalogue with angular sizes of 2.4 ± 1.4 arcmin and 7.6 ± 2.5 arcmin, and velocities 56.3 ±

1.1 km s^{-1} and 110.4 ± 0.9 km s^{-1}, respectively. Their flux densities, extrapolated to 1.4 GHz using $\alpha = -0.1$, are 2.8 ± 0.5 Jy and 15.0 ± 5.0 Jy. The RRL spectrum at $(\ell, b) = (25^{\circ}.8, 0^{\circ}.14)$ has two velocity components, 53.6 and 107.1 km s^{-1}. This means that the emission is indeed arising from these two H regions, but the sum of their fluxes does account for the measured flux of 39.1 ± 13.4 Jy, in Table 6.3, with an angular size of $25' \times 10'$. The large error bar is in part explained by the flag parameter which indicates that this source was initially blended with a bright neighbour, as Fig. 6.11 shows.

6.3.3 The latitude distribution of individual H regions

In this Section I investigate the latitude distribution of the H regions from the higher resolution Paladini et al. (2003) catalogue and compare it with that from the present, lower resolution catalogue.

There are 264 H regions in the Paladini et al. (2003) catalogue in this longitude range, for which fluxes at 2.7 GHz are given, but only 159 of them have RRL velocities. Some of the remaining 105 objects correspond to known or possible SNRs (Section 6.4). The 2.7 GHz flux densities for the 159 objects are extrapolated to 1.4 GHz assuming the free-free is optically thin therefore well approximated by a power law with $\alpha = -0.1$. At a resolution of 14.8 arcmin the free-free emission is mostly dominated by low density, extended H regions, with a small contribution from UCH regions. The example of the H region W49, for which I use the published flux density at 1.4 GHz from Altenhoff et al. (1970), shows that assuming optically thin emission at most affects the results by 20%.

In order to compare the Paladini et al. (2003) catalogue and the present list of sources, the flux densities and sizes are used to simulate Gaussian profiles and create two maps of H regions. These are smoothed to 14.8 arcmin resolution and converted into brightness temperature using equation (3.2). The comparison is shown in Fig. 6.12 (a) as a function of latitude, averaged over the whole longitude range. The two

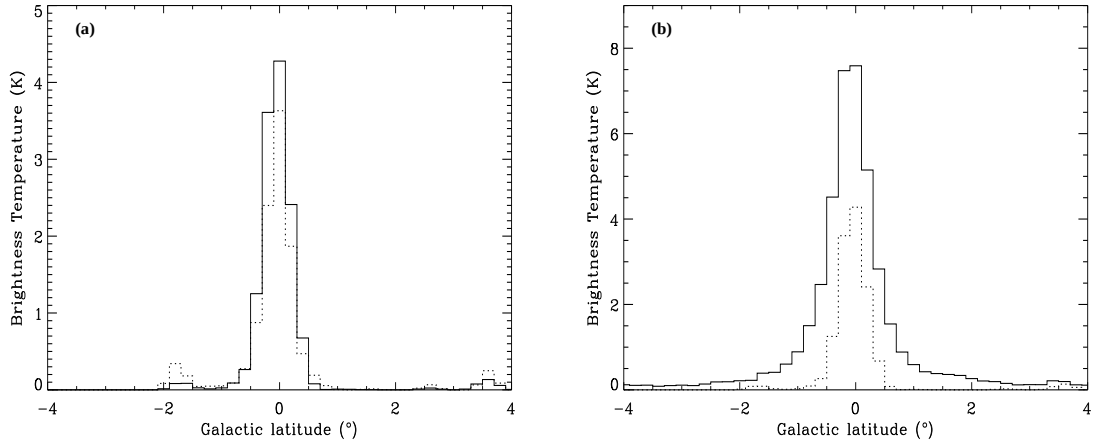

Figure 6.12: (a) Comparison between the contribution from the 159 Paladini et al. (2003) sources (dotted line) and the 57 sources from extrated from this work (full line), versus latitude. (b) Separation between the diffuse emission and the emission from individual H regions at 1.4 GHz. The full line represents the total free-free emission and the dotted is the contribution from the SExtractor H regions. Both plots are for the longitude range 20° to 44° with 0°.2 latitude bins.

distributions are very similar, with FWHM of 0°.48 and 0°.53 for the Paladini et al. and SExtractor lists, respectively. The present catalogue includes the more extended emission around and between features which is not included in the higher resolution Paladini et al. (2003) catalogue, which is missing ~ 20% of the flux.

It is also of interest to quantify how much of the free-free total flux is contributed by the individual H regions, as extracted in this work. Fig. 6.12 (b) compares the latitude distribution of the H regions recovered with SExtractor with that of the total free-free emission, in the longitude range 20° to 44°. It can be seen that the H regions are a narrower distribution than the total diffuse emission, with about half the FWHM. This is consistent with the narrower distribution of the OB stars around the plane, with a FWHM of ~ 70 pc (Bronfman et al. 2000), compared with the thin disk of diffuse H derived from pulsar Dispersion Measures, with a FWHM of ~ 160 pc (Reynolds 1991). The gas in the thin disk is ionised by the UV light from OB stars that escapes the H regions around them. The z-distribution of the diffuse emission is further investigated in Section 6.6.3. The individual H regions account for ~ 30% of the total

free-free emission in this region of the Galaxy.

6.4 Catalogue of SNRs

The synchrotron map derived in this work, as the best measure of synchrotron emission at 1.4 GHz, enables the detection of synchrotron features, most of which are SNRs. The source extractor algorithm SExtractor has been applied to the synchrotron map of Fig. 6.7 in order to create a list of SNRs in the region $\ell = 44^\circ$ to 20°. The background mesh size, the filter function and the detection minimum area are the same as for the free-free map but the detection threshold is decreased from 2 to 1.5σ. The rms of the resulting background map is 0.69 Jy/beam and the threshold limit for a detection is therefore 1.03 Jy/beam. As for the free-free map, the Mexican hat filter only allows for the brightest and more compact SNRs to be detected. Objects like the diffuse and extended SNR W50, which is not detected using this filter function, is recovered if the Gaussian filter is applied since it does not remove large angular scales. Therefore, I use both filters to compile the list of SNRs. Table 6.4 gives the angular size, postion angle, peak and flux density for the 26 SNRs recovered by SExtractor. Their positions and sizes are illustrated in Fig. 6.13.

Green (2009a) gives the most recent compilation of Galactic SNRs along with an online[1] detailed version of the 274 sources, which is regularly updated. This catalogue is based on research in the published data and lists the angular size, flux density at 1 GHz and spectral index for each object. It contains 36 SNRs in the range $\ell = 20^\circ$ to 44°, 23 of which are detected in this survey and listed in Table 6.4. The remaining three sources detected, objects 3, 4 and 10, are not in the Green catalogue and are described in more detail in the next section. The Green catalogue also gives the distance to the SNR, when known. Most of the distances to compact SNRs in this region of the Galaxy have been revised using the Very Large Array (VLA) Galactic Plane Survey (VGPS, Stil et al. 2006) H observations.

[1] http://www.mrao.cam.ac.uk/surveys/snrs

Table 6.4: SNRs in the region $\ell = 44°$ to 20°, extracted from the present synchrotron map using SExtractor. The column descriptions are the same as in Table 6.3. The last column identifies a source by its commonly used name as in the Green (2009a) catalogue. The Flag parameter 16 for the first and last SNR listed means that the object's aperture data are incomplete or corrupted, which is due to this object being near the image boundary. The 7 objects with the star symbol before the number are those extracted using a Gaussian filter.

Number	ℓ (°)	b (°)	θ_a (′)	θ_b (′)	P.A. (°)	Peak (Jy/beam)	Flux (Jy)	Flag	Name
⋆1	43.98	1.60	35.4	25.4	−77	2.0 ± 1.1	10.1 ± 5.8	16.0	
2	43.23	−0.13	16.0	*p*	58	29.8 ± 1.3	49.7 ± 5.5	0.0	W49B
⋆3	42.12	−0.21	51.34	41.1	78	3.8 ± 1.3	40.3 ± 14.4	1.0	
⋆4	41.45	0.39	26.8	20.3	1	4.3 ± 1.4	15.0 ± 5.1	1.0	
5	41.10	−0.30	*p*	*p*	−3	13.3 ± 1.5	16.0 ± 1.8	0.0	3C397
⋆6	40.58	−0.45	34.0	28.0	−13	5.0 ± 1.6	26.9 ± 9.2	3.0	
⋆7	39.78	−2.34	113.4	53.2	73	4.9 ± 1.3	141.3 ± 40.3	17.0	W50
8	39.22	−0.32	4.2	*p*	−14	12.7 ± 1.8	12.7 ± 1.8	0.0	3C396
⋆9	36.61	−0.83	21.0	*p*	−51	2.3 ± 1.4	4.0 ± 2.4	0.0	
10	35.59	−0.44	*p*	*p*	55	6.7 ± 1.5	6.7 ± 1.5	0.0	
11	34.68	−0.44	26.0	15.4	−56	71.2 ± 1.6	208.1 ± 18.6	0.0	W44
12	33.67	0.06	*p*	*p*	43	10.3 ± 1.6	10.3 ± 1.6	0.0	Kes79
⋆13	33.21	−0.51	7.9	*p*	14	2.3 ± 1.4	2.3 ± 1.4	0.0	
14	32.86	−0.05	*p*	*p*	−1	6.5 ± 1.5	6.5 ± 1.5	0.0	Kes78
15	31.89	0.04	3.9	*p*	25	14.7 ± 1.7	14.7 ± 1.7	0.0	3C391
16	29.69	−0.27	*p*	*p*	80	7.9 ± 2.0	9.5 ± 2.4	0.0	Kes75
17	28.61	−0.05	*p*	*p*	−72	8.6 ± 1.8	8.6 ± 1.8	0.0	
18	27.75	0.60	*p*	*p*	0	10.9 ± 1.4	10.9 ± 1.4	0.0	
19	27.37	0.00	*p*	*p*	−51	8.9 ± 1.3	10.7 ± 1.6	3.0	4C-04.71
20	24.73	−0.70	*p*	*p*	90	5.4 ± 1.5	5.4 ± 1.5	0.0	
21	24.58	0.62	10.1	*p*	23	11.4 ± 1.7	12.7 ± 3.2	0.0	
22	23.17	−0.24	8.8	*p*	81	13.0 ± 2.3	14.5 ± 4.1	2.0	W41
23	22.67	−0.24	17.3	2.4	73	15.5 ± 2.0	24.1 ± 5.1	0.0	
24	21.81	−0.57	14.5	7.3	34	32.5 ± 2.0	51.0 ± 6.2	0.0	Kes69
25	21.50	−0.87	*p*	*p*	0	8.2 ± 2.1	9.8 ± 2.5	0.0	
26	19.94	−0.21	17.1	*p*	−47	12.0 ± 1.7	16.4 ± 4.3	16.0	

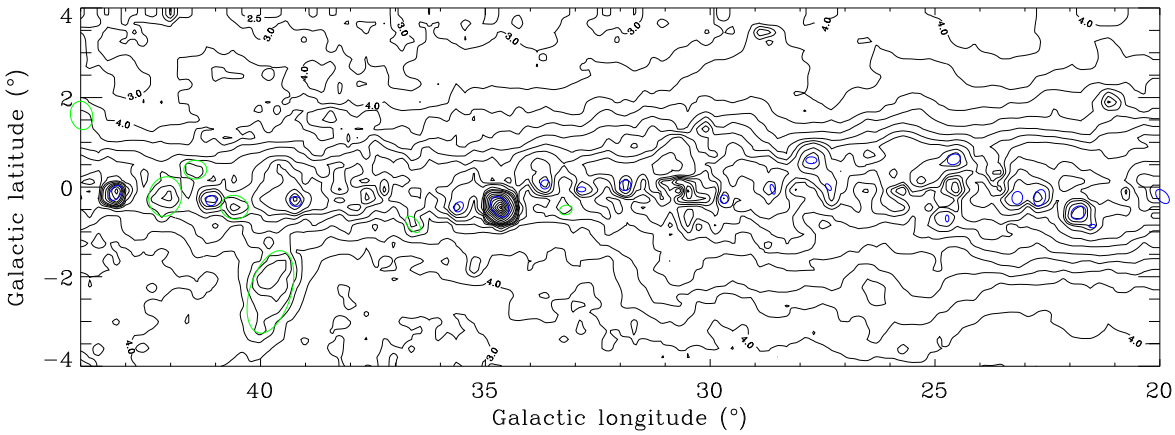

Figure 6.13: The synchrotron map of the region $\ell = 44°$ to 20°, with the 19 SNRs listed in Table 6.4. The ellipses are drawn using the semi-major and minor ellipse parameters and the postion angle. The green ellipses show the 7 SNRs detected using the Gaussian filter. The contours are the same as in Fig. 6.7.

From the 13 SNRs listed by Green (2009a) that are not detected by SExtractor, the brightest object is G26.6+0.3, with flux density at 1.4 GHz of 7.2 Jy and angular size of 10 arcmin. At this position in the synchrotron map there is a decrease of about 37 per cent in flux compared to the local background, which is due to the presence of strong RRL emission, both diffuse and from the H region number 49 in Table 6.3. Green (2009a) points out that this object is not well resolved and is in a complex region. The second brightest SNR, G30.7+1.0, has a flux of 5.2 Jy and size $24' \times 18'$. This SNR is on a ridge of emission on the synchrotron map, therefore is difficult to detect. The remaining SNRs are mostly diffuse and have flux densities below 2.7 Jy, which is comparable with the lowest flux density in Table 6.4, detected by SExtractor. Some SNRs in the Green list are poorly defined, without angular sizes or flux measurements.

The flux densities listed in Table 6.4 are subject to calibration factors due to the imaging process. Since the synchrotron map is the difference between the continuum and free-free maps, it is not straightforward to identify the synchrotron sources to be corrected as it was performed in Section 5.2.3 for the free-free objects. I use the angular sizes listed in the Green catalogue to identify the objects that are less than 5 arcmin in size, thus whose flux in Table 6.4 is increased by a factor of 1.2. These are SNRs 2,

5, 16, 19 and 25. The corrected flux density of 9.5 ± 2.4 Jy for Kes75 agrees with the value given by Green (2009a), 7.9 Jy, when extrapolated to 1.4 GHz using the listed spectral index $\alpha = 0.7$. The flux density of 49.5 ± 5.5 Jy for W49B is 50% higher than the value given by Green (2009a), 32.3 Jy. This is due to the size of $\sim 16' \times 5'$ fitted to this source, which is $4' \times 3'$ in the Green catalogue, and also because W49B is likely confused with its thermal counterpart W49A.

Most of the sources in Table 6.4 are smaller than the beam, their sizes and flux densities are in overall agreement with the values in the Green catalogue. For example the strongest SNR in this region of the Galaxy, W44, is fitted in the present synchrotron map with a size of $26'.0 \times 15'.4$ and a flux density of 208.1 ± 18.6 Jy. The flux density given by Green (2009a) for W44 is 203 Jy at 1.4 GHz, extrapolated from 1 GHz with the listed spectral index $\alpha = 0.37$, and the angular size is $35' \times 27'$.

6.4.1 Comments on individual synchrotron sources

G42.12-0.21 and G41.45+0.39 – These objects in Table 6.4 correspond to two of the three SNR candidates by Kaplan et al. (2002). The angular sizes and flux densities found here are larger than the values obtained by Kaplan et al. (2002) using the 1.4 GHz NRAO VLA Sky Survey (NVSS, Condon et al. 1998) data, which may resolve out some of the emission. This can also be due to the fact that these two faint objects are recovered with the Gaussian filter, thus are likely to be confused with the strong background on the plane. Moreover, they are both flagged as having bright sources nearby. The third possible SNR in Kaplan et al. (2002), G43.5+0.6, is too faint in the NVSS to derive a flux density and it is indeed only marginally visible, at a $\sim 1.2\sigma$ level, in the present synchrotron map.

G35.6-0.4 – The SNR G35.6-0.4 has been recently re-identified by Green (2009b), using VGPS and data from other single-dish surveys at higher frequency to confirm the non-thermal spectral index of this object. The SNR is seen in the VGPS map with a size of $\sim 15' \times 11'$ and has an flux density of 7.8 Jy. These results are consistent with

what is found in this work, 6.7 ± 1.5 Jy for a relatively compact source of size similar to the beam.

The resolution of the 2.7 GHz data (Reich et al. 1984) is very similar to that of the 100 μm data by Miville-Deschênes & Lagache (2005). This is ideal to investigate the spatial coincidence between dust and radio continuum emission, which can be used to distinguish between H regions and SNRs (Haslam & Osborne 1987; Broadbent et al. 1989). The radio to dust ratio is higher for SNRs than for H regions, since dust is not usually associated with synchrotron emission. This correspondence helps us understand that the artifacts seen in the synchrotron map around the H region complexes W47, W43 and W42 are correlated with individual H regions, and are thus caused by electron temperature variations. On the other hand, the lack of significant dust emission for a radio emitting source points toward a non-thermal origin. This is the case of the sources at $(\ell, b) = (30^\circ.1, +1^\circ.3)$ and $(\ell, b) = (21^\circ.0, +2^\circ.0)$ in Fig. 6.13, which show strong emission in the 2.7 GHz map but have no 100 μm counterpart. Both sources are extragalactic, even though only $(\ell, b) = (21^\circ.0, +2^\circ.0)$ is currently identified as such in the literature.

The double-lobed radio source $(\ell, \mathbf{b}) = (\mathbf{30^\circ.13}, +\mathbf{1^\circ.34})$

The contour map of Fig. 6.14 (a) is the VGPS 1.4 GHz emission of the radio source. At this survey of resolution 1 arcmin a double-peaked feature is clearly visible. The elongated structure of this source has been detected at lower frequencies, in particular at 74 MHz in the VLA Low-Frequency Sky Survey (VLSS, Cohen et al. 2007). The catalogue from this survey gives a flux density of 41.97 ± 4.24 Jy and an angular size of $2'.05 \times 0'.59$ with a 1.3 arcmin beam. At 1.4 GHz, the survey by Reich et al. (1990b) at 9.4 arcmin resolution gives a flux density of 4.62 ± 0.05 Jy for a slightly extended source of angular size less than 11 arcmin. The higher resolution survey at 2.7 GHz (Reich et al. 1984) detects a source of $7'.4 \times 4'.3$ size and flux density of 3.57 ± 0.04 Jy. Combining the three measurements results in a spectral index of $\alpha = -0.71 \pm 0.05$, which is within the observed values for a SNR (Green 2009a). Nevertheless, the shape

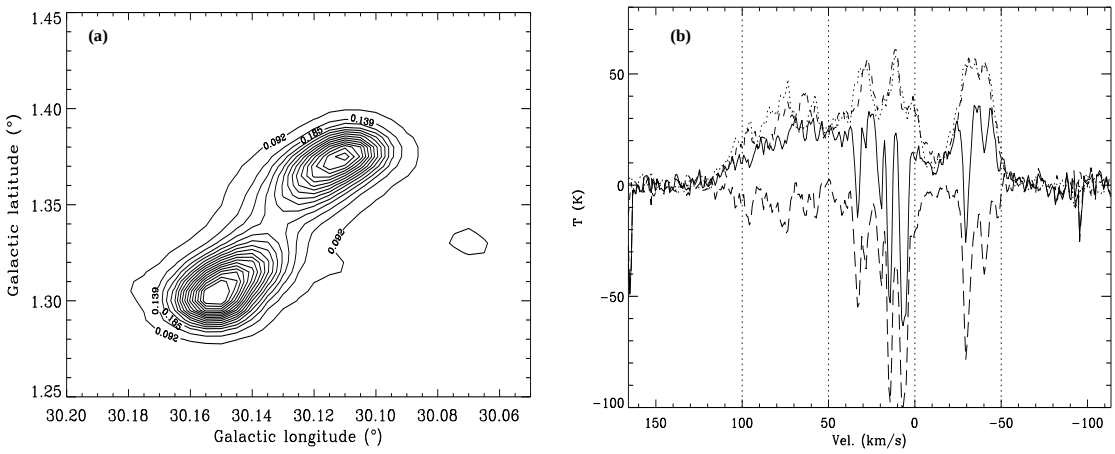

Figure 6.14: (a) Contour map of the radio source $(\ell, b) = (30^{\circ}.13, +1^{\circ}.34)$ from the VGPS survey at 1.4 GHz and 1 arcmin resolution. The contours are given at every 5% from 5 to 90% of 0.92 Jy, which corresponds to the maximum on the southern lobe. The first 4 contours are labelled. (b) The H spectrum from the VGPS survey against the radio source, taken at $(\ell, b) = (30^{\circ}.15, 1^{\circ}.31)$ (full line). The dotted and dashed lines are the off source spectra, measured at the same latitude and longitudes of $31^{\circ}.13$ and $31^{\circ}.17$, respectively. The thick long-dashed line is the absorption spectrum of the source which shows that absorption is detected at all velocities, inside and outside the Solar circle, confirming its extragalactic origin.

of the radio source and its angular size points toward an extragalactic origin. Helfand et al. (1992), on their 20 cm study with the VLA and identification of 1457 compact sources near the Galactic plane, also suggest that this is an extragalactic object. If this is the case, such a bright and extended object, has probably been missed from extragalactic source catalogues due to its proximity to the Galactic plane.

I have used VGPS H data to confirm that $(\ell, b) = (30^{\circ}.13, +1^{\circ}.34)$ is a radio galaxy. The latitude coverage of the VGPS H spectral cube, $|b| \lesssim 1^{\circ}.315$, only includes the southern lobe of the source, which is enough to obtain and compare spectra on and off the source. These are shown in Fig. 6.14 (b). H absorption against the object is detected at all velocities including negative velocities, which gives the confirmation that $(\ell, b) = (30^{\circ}.13, +1^{\circ}.34)$ is outside the Galaxy.

This interesting object deserves further study at higher angular resolution.

6.5 The free-free latitude distribution of T_b - Comparison with other data

In Section 6.1.5 the distribution of free-free emission was derived on and near the Galactic plane. In this Section, other data are used to compare and extend our analysis of the free-free emission, namely Hα, WMAP total power and maximum entropy method (MEM) estimate of the free-free. In order to provide a more sensitive determination of the latitude distribution up to $|b| = 4°$, the free-free emission is averaged in longitude.

6.5.1 The Hα latitude distribution

I follow the approach of Dickinson et al. (2003) to derive the Hα latitude distribution. WHAM, the sensitive Hα survey of the northern sky provides a map with accurately determined baselines at a resolution of ~ 60 arcmin (Haffner et al. 2003). This map is then corrected for absorption by Galactic dust using the Schlegel et al. (1998) 100 μm map corrected to a fixed dust temperature of 18.2 K. The total absorption (for an extragalactic object) at the wavelength of Hα is estimated as $(0.0462 \pm 0.0035)D^{\rm T}$ magnitudes where $D^{\rm T}$ is the 100 μm temperature-corrected intensity in MJy sr^{-1}. Dickinson et al. find that the effective absorption for Galactic emission is ~ 0.3 of this value, so the corrected Hα intensity is $I^{corr}_{\rm H\alpha} = I_{\rm H\alpha} \times 10^{\rm D_T \times 0.0185 \times f_d}$. This 0.3 factor, f_d, represents the relative distribution of the gas (Hα) and dust in the line of sight at intermediate and high Galactic latitudes. When the effective absorption reaches 1 magnitude, the correction becomes uncertain and the estimate of the true Hα intensity is unreliable.

The Hα intensity $I_{\rm H\alpha}$ is converted to T_b using the formula given in equation (2.17), Section 2.1.3. The conversion is equivalent to 3.87 mK/R for $T_e = 7000$ K and $\nu = 1.4$ GHz. I use the electron temperature relationship of equation (6.3) for $|b| \leq 4°$ and assume a constant T_e of 7000 K for $4° < |b| \leq 30°$. As a result, the conversion between corrected Hα intensity and T_b varies between 3.17 and 4.35 mK/R, for T_e of 4900 K

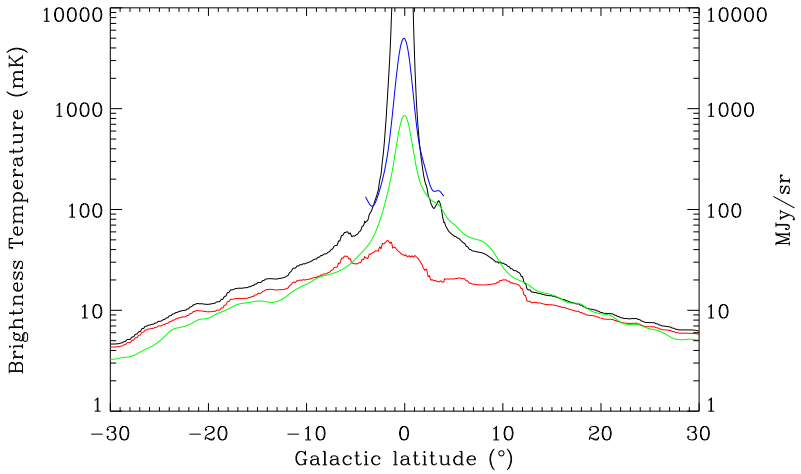

Figure 6.15: The Hα latitude distribution, uncorrected (red) and corrected for dust absorption (black) as well as the free-free estimated from the RRLs (blue), averaged for the whole 24° longitude range. The $D^{\rm T}$ distribution is also shown (green) in units of MJy/sr, read from the right-hand vertical axis. The WHAM intensity is corrected for dust absorption and converted to brightness temperature using the $T_{\rm e}$ relationship from equation (6.3) plus a constant $T_{\rm e}$ of 7000 K for $|b| > 4°$, $\nu = 1.4$ GHz and f_d values of 0.55 and for 0.32 the negative and positive sides of the distribution, respectively. Note the logarithmic vertical scale.

and 8590 K, respectively.

Figure 6.15 shows the latitude distribution of $T_{\rm b}$, between $b = -30°$ to 30° averaged over the longitude range $\ell = 20°$ to 44°, for the uncorrected Hα (red line), the corrected Hα (black line), the RRLs free-free estimation (blue line) and the $D^{\rm T}$ dust (green line). The angular resolution of the data used in Fig. 6.15 is 60 arcmin. I use the free-free map smoothed to 1° and the Hα data to derive the f_d value that best fits the two distributions between latitudes of $|b| = 3°$ to 4°. The correct Hα intensity is calculated for a grid of f_d values ranging from 0 to 1, every 0.01, and compared with the free-free estimated from the RRLs. The best fit f_d values corresponds to the minimum chi-squared (χ^2) and the errors are estimated from the χ^2 curve, as half its width at 1σ. For the negative and positive sides of the latitude distribution f_d is $0.48^{+0.36}_{-0.33}$ and

$0.32^{+0.05}_{-0.26}$, respectively. The Hα data in Fig. 6.15 are corrected for dust absorption using the derived f_d values. The effective absorption is about 1 magnitude at $|b| \simeq 5^\circ$ and increases to 2 magnitudes at $|b| \simeq 3^\circ$. At this latitude, the brightness temperature from the Hα and RRLs is $\sim$ 120 mK. A uniform mixing of gas and dust corresponds to an f_d value of 0.5. Our derived values at $|b| = 3^\circ$ to 4° are similar to uniform mixing. However, at lower latitudes the values determined from the Hα data are far higher than the observed free-free emission from RRLs. This would appear to indicate that the Schlegel et al. (1998) dust model for $D^{\rm T}$ for a fixed dust temperature of 18.2 K overestimates the absorption produced by the warm (40 K) dust on the Galactic ridge. This is not unexpected since the dust properties such as temperature, composition, ISM radiation field, along this deep line of sight through the Galaxy are different from those at intermediate latitudes covered by the Schlegel et al. (1998) model.

This shows that the RRL data can be combined with Hα data to overcome the high dust obscuration on the Galactic plane on creating a full-sky map of the free-free emission.

6.5.2 WMAP free-free MEM model

The WMAP team has estimated the contribution of synchrotron, thermal dust and free-free emission, at each band and at 1° resolution, using a Maximum Entropy Method (MEM) (Gold et al. 2011). The MEM is an iterative procedure that fits for the emission of each component and also the synchrotron spectral index, assuming that the dust and free-free temperature follows a power law with $\beta = +2$ and $\beta = -2.14$ ($T \propto \nu^\beta$), respectively. Where the WMAP's S/N is low, templates made from external data are used as priors. These templates are: the Haslam 408 MHz map (Haslam et al. 1982) for the synchrotron, the extinction-corrected Hα map (Finkbeiner 2003) for the free-free and the Model 8 of Finkbeiner, Davis, & Schlegel (1999) map for the thermal dust.

Figure 6.16 shows, for three longitude ranges, the brightness temperature estimation from the RRLs (dotted line) with an assumed $T_{\rm e}$ given by equation (6.3) and a

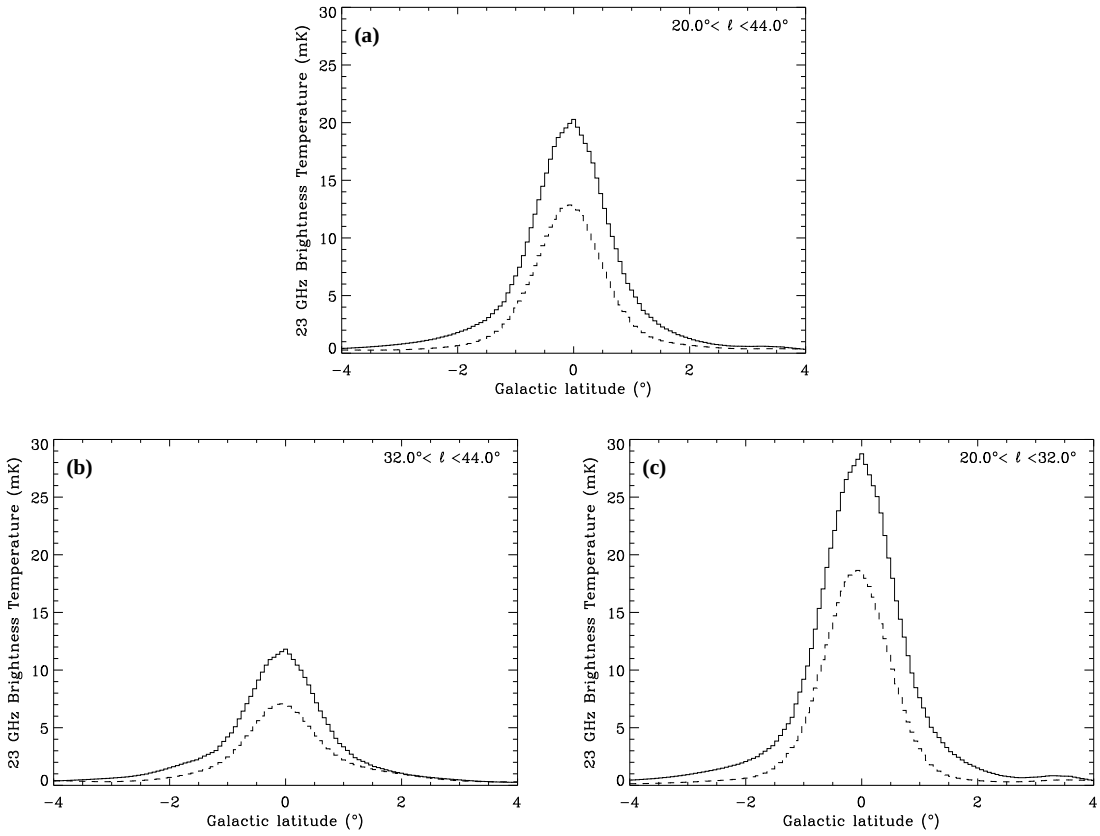

Figure 6.16: Free-free emission estimated from the RRLs and from the WMAP 23 GHz MEM versus latitude, averaged over three longitude ranges. The full line represents the WMAP MEM and the dotted line is the free-free emission from the ZOA smoothed to 1° resolution and an assumed T_e given by equation (6.3).

spectral index $\beta = -2.13$ and WMAP's MEM (full line), at 23 GHz[2]. The peak of the MEM distribution is always higher than that of the RRLs, for the three longitude ranges. For the brighter longitude range $\ell = 20°$ to 32°, Fig. 6.16 (c), the MEM estimation is about 48 per cent higher than the RRL prediction. In this region, the mean electron temperature on the plane is $\sim$ 5700 K which would have to be increased to about 8000 K for the two peaks to agree. The FWHM of the RRL latitude distribution is $\sim 1°.32$, slightly narrower than that of the MEM, $1°.47$. This reflects the narrow RRL distribution seen in Fig. 5.19 and the possible systematic effects of the sharp slope

[2]Downloaded from the website http://lambda.gsfc.nasa.gov.

for $|b| \gtrsim 1^\circ$, over this strong continuum emitting region (Section 5.3.3). The largest difference is for the range $\ell = 32^\circ$ to 44°, Fig. 6.16 (b), where the MEM predicts ~ 67 per cent more emission at $b = 0^\circ$ than the RRLs. This implies that T_e should go from the mean T_e of 6400 K to around 10000 K for the RRL free-free peak to agree with that of the MEM. On the other hand, both distributions have approximately the same FWHM of $\sim 1^\circ.52$. This longitude range is mostly dominated by individual H regions rather than groups of H regions, as the lower longitude range of the region is. If a 30% contribution by individual and compact ($\sim 5'$) H regions is assumed (Section 6.3.3), for example W49, it needs to be corrected by 20% due to the imaging process (Section 5.2.3). This small correction is enough to reduce the MEM overprediction above the RRLs by $\sim$ 10%. This reflects the importance of the separation between diffuse and compact free-free emission and subsquent correction depending on angular scale.

Planck Collaboration et al. (2011b) recently reported a similar result using *Planck* data. They showed that the MEM free-free estimate on the Galactic plane is higher than what is predicted by their model of the multi-phase ISM, which recovers $\sim$ 80% of the WMAP MEM emission at 23 GHz. With the restricted frequency range of WMAP in separating at least 4 components, there is some uncertainty in the MEM separation of the synchrotron and the free-free components.

6.5.3 WMAP: 23 to 94 GHz - identification of the four foreground components

Our determination of the free-free emission from the RRL data makes a significant contribution to the derivation of the Galactic foregrounds on the Galactic plane at higher frequencies. The WMAP 7-year (Jarosik et al. 2011) data at 23, 33, 41, 61 and 94 GHz have the resolutions of $\sim$ 49, 37, 29, 20 and 13 arcmin respectively, which are adequate to investigate the Galactic latitude distribution which has a width of $\sim 1^\circ$ in the longitude range of the present study. I use the 1° resolution WMAP data for each of the five frequency bands.

The synchrotron component is given by the 408 MHz survey (Haslam et al. 1982), made with a resolution of 51 arcmin; its brightness temperature spectral index is assumed to be $\beta = -3.0$ (Banday et al. 2003; Davies et al. 2006). The free-free emission is that derived from the RRLs with a resolution of 14.8 arcmin, assuming an electron temperature given by equation (6.3). Its spectral index is assumed to be $\beta = -2.13$ over the frequency range of WMAP. A spectral index of $\beta = -2.10$ is used to correct the synchrotron map for free-free emission at 408 MHz. Both the synchrotron and the free-free templates are smoothed to 1° for this comparison.

Figures 6.17 (a) to (e) show the latitude cuts at each WMAP frequency for the longitude range 20° to 44°. The black line gives the total WMAP brightness temperature, while the green line gives the total minus the free-free (in red) and minus the synchrotron (in blue), at each frequency. It is seen immediately that the synchrotron is a minor contributor at WMAP frequencies - amounting to only 6 per cent at 23 GHz and correspondingly less at higher frequencies falling to only 1 per cent at 94 GHz. The green line represents the anomalous emission. At 23, 33 and 41 GHz this excess emission is 58, 57 and 55 per cent, respectively, of the total emission. Expressed more physically, the anomalous emission at these three frequencies is 1.6, 1.4 and 1.3 of the free-free emission. Assumptions on the free-free and synchrotron spectral indices, electron temperature and calibration errors do not affect the results on the anomalous emission detection by more than 20 per cent.

At 61 and 94 GHz the thermal (vibrational) dust emission is a significant contributor. On the plane this dust is warmer ($T_D \simeq 40$ K) than at intermediate latitudes (20 K) having been heated by the radiation field responsible for ionising the ISM to produce the free-free. At 94 GHz the excess emission is 3 times the free-free. If a thermal dust emissivity spectral index of $\beta = +2.0$ is assumed, it will contribute 38 per cent of the observed excess at 61 GHz. On the other hand, if $\beta = +1.5$, it contributes 48 per cent and will have a significant contribution, 20%,at 41 GHz.

A critical test for the spinning dust model is that the width of the observed anomalous radio emission should be similar to that of the (warm) dust. The 100 μm IRIS

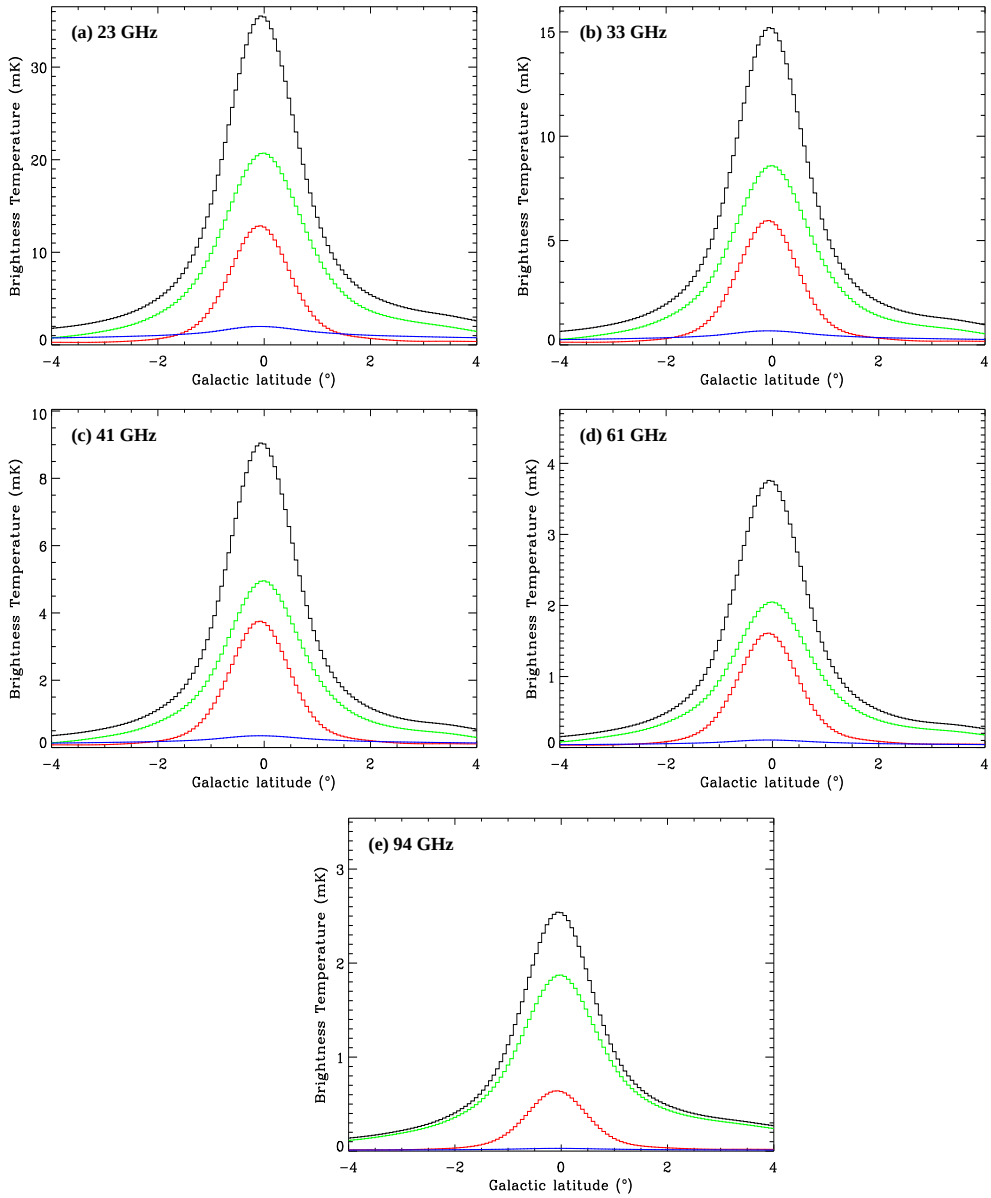

Figure 6.17: Comparison between WMAP, free-free and synchrotron versus latitude, at each frequency (23 GHz (a) to 94 GHz (e)), averaged over the longitude range 20° to 44°, at 1° resolution. The black line represents the WMAP temperature (I) 7-year data; the green line is the result of WMAP minus the the free-free and minus the synchrotron; the blue line is the 408 MHz data scaled with a spectral index $\beta = -3.0$. The assumed electron temperature in the free-free estimation is given by equation (6.3).

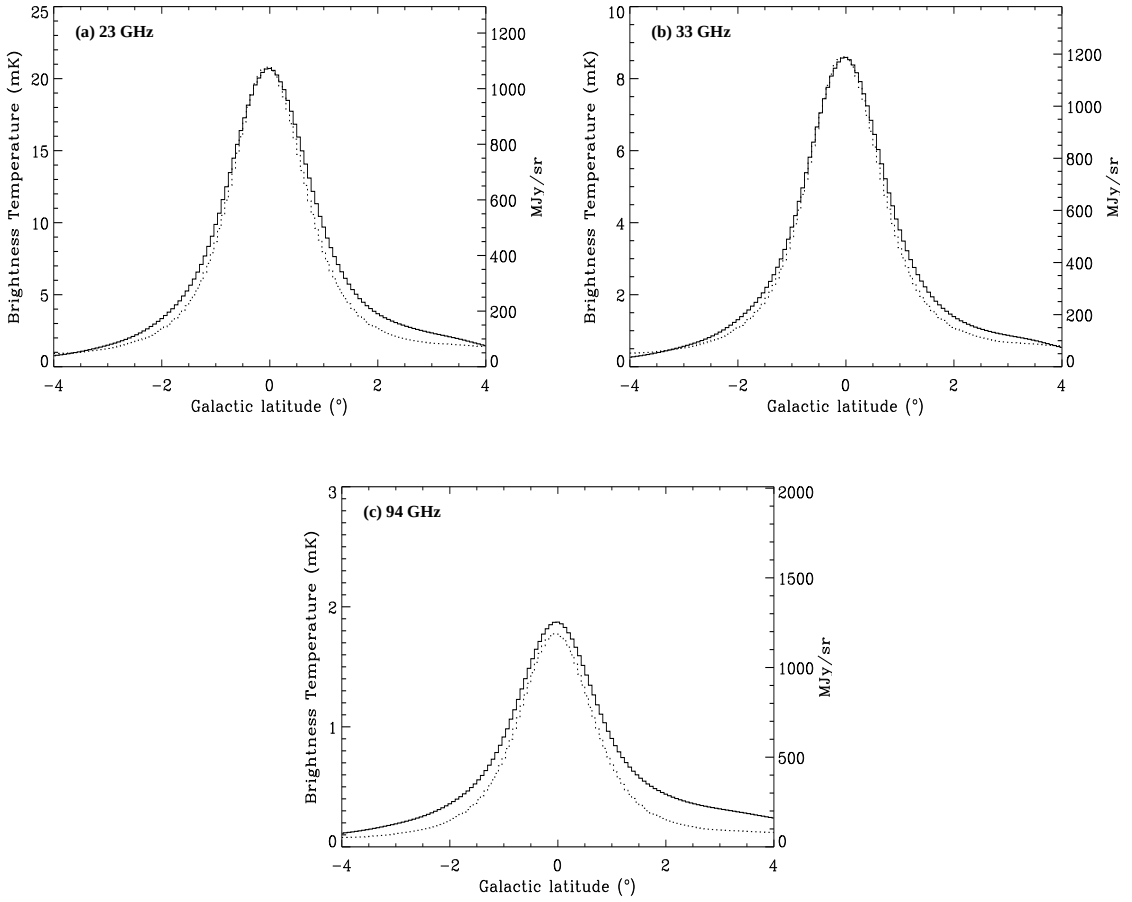

Figure 6.18: The anomalous emission (i.e., total minus free-free minus synchrotron) latitude distribution for the longitude range 20° to 44° at 23 GHz (a), 33 GHz (b) and 94 (c) GHz (full line), compared with the 100 μm surface brightness distribution (dotted line). The assumed electron temperature in the free-free estimation is given by equation (6.3).

data (Miville-Deschênes & Lagache 2005), again smoothed to 1°, are compared with the WMAP data in Figs. 6.18 (a), (b) and (c) at 23, 33 and 94 GHz, for the longitude range 20° to 44°. The latitude distributions of the radio (full line) and dust emissions (dotted line) are clearly similar both at 23 and 33 GHz (spinning dust) and at 94 GHz (thermal dust). The half power widths are 1°.69, 1°.89, 1°.83 and 1°.87 for 100 μm, 23 GHz, 33 GHz and 94 GHz respectively. The ratio of 33 GHz to 100 μm brightness is 9.5 μ K(MJy sr^{-1})$^{-1}$, a value similar to that found at intermediate latitudes (Davies

et al. 2006). These WMAP data are in agreement with models of spinning dust.

6.6 Galactic Structure

RRL surveys of H regions have provided information on the kinematics and location of the ionised gas in the Galaxy, tracing the spiral arms and sites of recent star formation. The combination of the Paladini et al. (2003) catalogue with the new objects detected by Bania et al. (2010) give the best current picture of the longitude-velocity distribution of Galactic H regions, with unambiguous evidence for an ordered pattern of Galactic structure. The present RRL survey is unique for it provides equivalent information for the total point source and diffuse ionised gas on the Galactic plane between 20° and 44°.

6.6.1 Distribution of RRL emission in longitude and velocity

Figure 6.19 shows the contours of RRL temperature in velocity-longitude space, for spectra averaged in 0°.5 in longitude within 1° of the Galactic plane. The first positive contour (full line) is at $\sim 1\sigma$ (Section 5.2.1). It shows that there is no emission at negative velocities in this longitude range, knowing that the low-level features at ℓ = 38° and between ℓ = 23° and 31° are associated with carbon and helium lines (Section 6.7). This result is very similar to that found in the H166α line survey by Lockman (1976), shown in Fig. 1.6. This RRL survey at a resolution of 21 arcmin, detected emission in all the 1° intervals from 4° to 44°. Both longitude-velocity maps show a minimum of emission at $\ell \sim 40°$, no emission at 0 km s^{-1} and a large change in emission with longitude.

6.6.2 Radial distribution of Galactic ionised emission

The RRL velocity of the free-free emission, when converted into a distance to the Galactic centre, can be used to obtain the radial distribution of the ionised gas. This

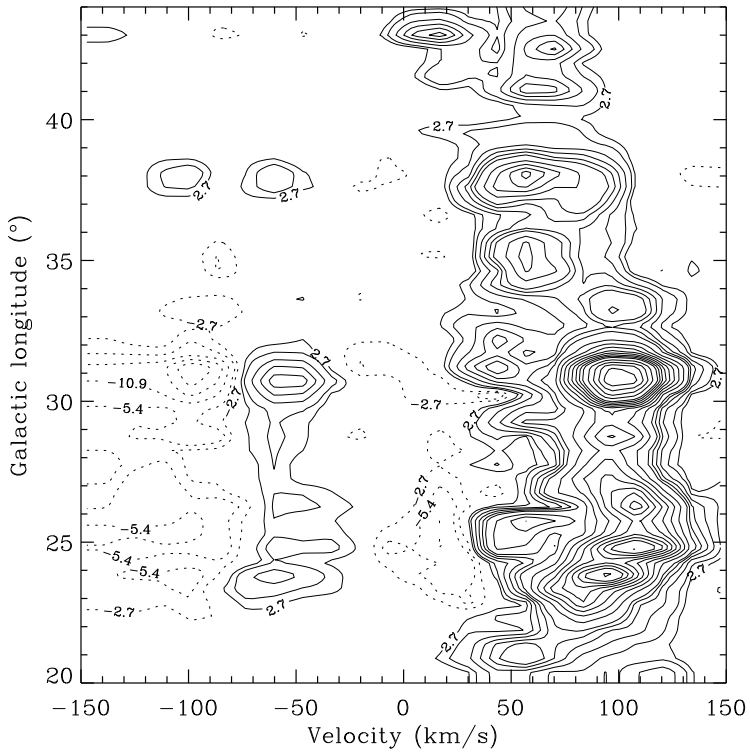

Figure 6.19: The longitude-velocity distribution of RRL brightness temperature within 1° of the Galactic plane. Contours are at ±8, ±6, ±4, ±2, ±1 and 10 per cent, then at every 5 per cent from 10 to 50 per cent and every 10 per cent from 60 to 90 per cent of the maximum line temperature observed, 272 mK. The first 4 contours are labelled and the dotted lines correspond to the negative contours.

is shown in Fig. 6.20 as the full line histogram. The RRL spectra are averaged into a 12 arcmin pixel grid, to reduce the correlation between the points, for the longitude range $\ell = 20°$ to 44° and $|b| \leq 1°$. The Galactocentric radius R_G is calculated as in Section 6.1.5 using equation (6.2), with $R_0 = 8.5$ kpc, and the velocity that corresponds to the peak of the line for each spectrum. Fig. 6.20 also shows the distribution of the 145 H regions from the Paladini et al. (2003) catalogue that are within the same region of the sky (dotted line, scale by a factor of 4). The two distributions are very similar and show narrow peaks at $\sim$ 4.4 kpc and 5.9 kpc that correspond to the Scutum and Sagittarius spiral arms, respectively. This indicates that the diffuse emission follows the same radial distribution as the H regions.

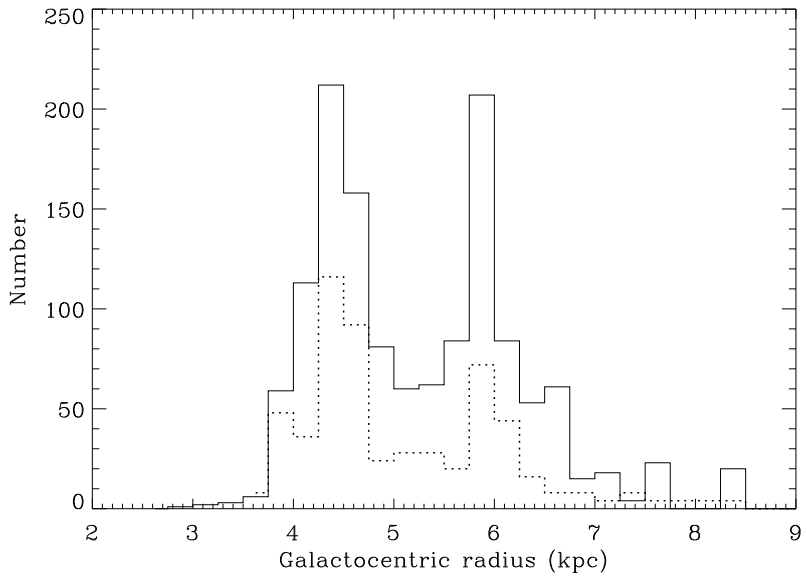

Figure 6.20: Radial distribution of the ionised emission (full line) and the Paladini et al. (2003) H regions (dotted line) between $\ell = 20°$ and 44° and $|b| \leq 1°$. The Galactocentric radius of the averaged 12×12 arcmin^2 RRL spectra is calculated as described in Section 6.1, using $R_0 = 8.5$ kpc. The Paladini et al. (2003) histogram is scaled by a factor of 4 for a better comparison and both distributions are plotted with 0.25 kpc wide bins. The two spiral arms, Scutum and Sagittarius, show as narrow peaks at 4.4 kpc and 5.9 kpc.

The radial distribution obtained by Bania et al. (2010), using the 602 H regions detected in their survey, also shows two peaks at 4.3 kpc and 6.0 kpc. These values of R_G correspond to tangent points in longitude of 30° and 45° and terminal velocities of 110 km s^{-1} and 63 km s^{-1}, respectively. The fact that the present survey covers $\ell \leq 44°$ suggests that it is missing part of the emission from the tangent point of the Sagittarius arm. This can be partly responsible for the narrower peak of this spiral arm, $\sim$ 0.5 kpc, compared with that of the Scutum arm, $\sim$ 1 kpc. Another important factor is the channel width and spectral resolution of the present survey, that limits the determination of R_G and in particular the fact that only one velocity is assigned to each pixel, therefore not accounting for a possible second component of emission. Moreover, there is a spread of velocities in the spiral arms due to non-circular motions,

less than a few per cent of the rotational velocities, of about 10 km s^{-1}. At the distance and radial velocity of the Sagittarius arm, the error on $R_{\rm G}$ due to the 20 km s^{-1} spectral resolution is about 0.5 kpc. Nonetheless, as a similar width of the Sagittarius arm is seen in the distribution of H regions, this is likely to be a real feature.

6.6.3 The z-distribution of the diffuse ionised gas

Having identified the Sagittarius and Scutum arms in the $R_{\rm G}$ and velocity space, I am now able to separate the emission from each of the spiral arms and investigate their azimuthal extent. Figs. 6.21 (a) and (b) show the integrated RRL emission over 50 km s^{-1}, from 80 to 130 km s^{-1} and from 30 to 80 km s^{-1}, respectively. Fig. 6.21 (a) shows the narrow distribution of the high-velocity emission from the Scutum arm that covers mainly $\ell \lesssim 34^\circ$. The lower emission for $\ell > 34^\circ$ originates in the wings of RRLs at $V \sim 80$ km s^{-1}. The emission from the Sagittarius arm covers the whole longitude range and has a broader distribution around the plane. Fig. 6.21 (c) shows that the RRL emission at $V \sim 0$ km s^{-1} is attributed to the W49 and W40 H regions, with some emission from W45, at $V \sim 25$ km s^{-1} and from the positive latitude extent of the W47 complex.

The latitude profiles of Figs. 6.21 (d) and (e) show the narrower z-distribution of the Scutum arm, with a FWHM of $\simeq 0^\circ.78$, compared with the slightly broader distribution of the Sagittarius arm, with FWHM of $\simeq 0^\circ.85$. The Galactocentric distances to the tangent points give a mean distance to the Sun of 6.0 and 7.3 kpc for the Sagittarius and Scutum arms, respectively. Using the observed FWHM of the latitude profiles gives a z-thickness of about 100 pc, $\sigma \sim 45$ pc, for the diffuse ionised gas about the Galactic plane. This compares with $\sigma \sim 70$ pc, the value found by Reynolds (1991) using pulsar Dispersion Measures and reflects the fact that emission measures trace the densest parts of the ionzed gas, EM $\propto n_{\rm e}^2$, compared to dispersion measures which trace $n_{\rm e}$. The latitude distribution of the Sagittarius arm, Fig. 6.21 (e), shows a broader component of FWHM $\simeq 2^\circ$ that corresponds to the emission from the near

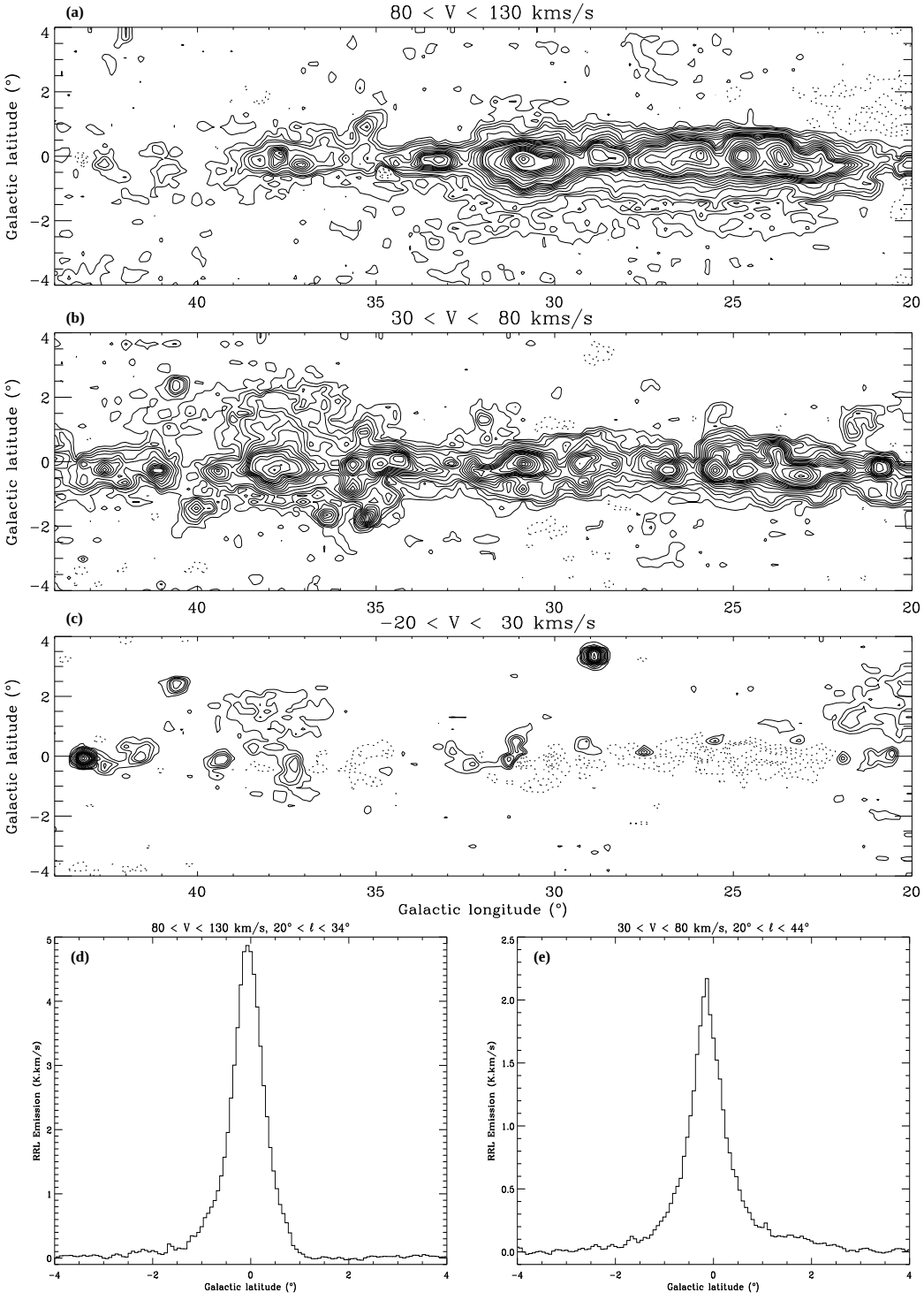

Figure 6.21: Maps of RRL emission integrated over 50 km s^{-1}, centred at 105 km s^{-1} (a), 55 km s^{-1} (b) and 5 km s^{-1} (c), at a resolution of 14.8 arcmin. Contours are given at every 0.1 K km s^{-1} from −0.4 to 0.4 K km s^{-1}, every 0.2 K km s^{-1} from 0.4 to 2 K km s^{-1} and then at 2.5, 3, 4, 5, 6, 7, 8, 9, 10, 15, 20, 25 K km s^{-1}. The negative contours are dotted. Figs. (d) and (e) are the latitude profiles that correspond to maps (a) and (b), respectively, averaged over the longitude ranges indicated.

side, whereas emission from the far side is responsible for the narrow component. The negative mean value of the peak in both latitude distributions is consistent with the result from Reed (1997) that the Sun lies above the Galactic mid-plane.

6.7 Helium and Carbon RRLs

Helium and Carbon RRLs are observed in the HIPASS/ZOA spectra. The expected velocity separation of 122.1 km s^{-1} and 149.5 km s^{-1} between the hydrogen RRL and the helium and carbon lines, respectively, allow their identification. Due to the spectral resolution of 20 km s^{-1}, these two RRLs are sometimes blended. When the carbon RRL is amplified by maser emission by foreground gas, it shifts towards lower velocities and the two can be separated.

Figure 6.22 shows two examples of spectra, for which helium and carbon lines are detected, toward the H regions W47 and W40. These RRLs are baseline corrected by fitting a polynomial to the spectrum between the hydrogen and the helium lines and to the equivalent portion of the spectrum at lower velocities. The polynomial is of second and fourth orders for the W47 and W40 H regions, respectively. Fig. 6.22 (b) shows the helium and carbon RRLs for W47, which has a velocity of 67 km s^{-1}. The helium line is detected at its expected separation from the hydrogen line, but the carbon RRL is clearly shifted toward lower velocities, by $\sim$ 30 km s^{-1}. This is expected if cold gas between us and the Sagittarius spiral arm, where W47 is located, is contributing to the carbon line emission. Gaussian fits to the lines give line widths of 25 km s^{-1} and 18 km s^{-1}, and temperatures of 15 $\pm$ 4 mK and 20 $\pm$ 10 mK for the helium and carbon RRLs respectively, and 159 $\pm$ 8 mK for the hydrogen line. The abundance of ionised helium in this H region, given by the ratio between the He and H line temperatures, is 0.09 $\pm$ 0.02, consistent with the values found in the literature (Section 2.4.2).

In the case of W40, which is a local H region, the C line is $\sim$ 150 km s^{-1} from the H line. The line width given by the Gaussian fit is broad, 47 km s^{-1}, which shows that C and He RRLs are blended. The W40 H region has been widely studied at various

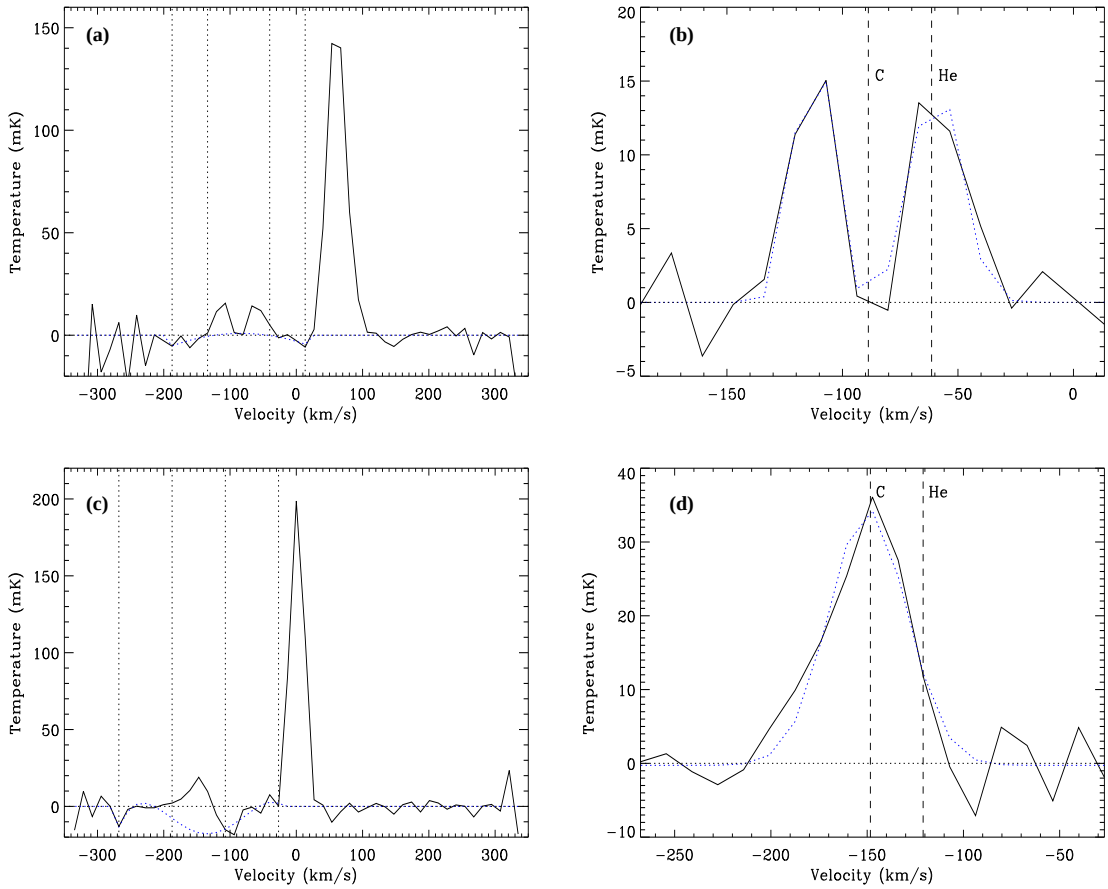

Figure 6.22: Spectra for the H regions W47 $(\ell, b) = (37.^{\circ}8, -0.^{\circ}3)$ (top) and W40 (bottom), averaged over 12×12 arcmin^2. A fit to the baseline is performed between the dotted lines, excluding the helium/carbon feature, and is shown as the blue dotted line. The right panels show the baseline corrected helium and carbon RRLs, with their rest velocities given by the vertical dashed lines; here the blue dotted line is the Gaussian fit to the RRLs. The carbon line is amplified by maser emission by the foreground gas toward W47, at $V = 67$ km s^{-1} and for W40 is is blended with the weaker helium RRL.

wavelengths and in particular for carbon RRLs at 21 cm by Pankonin et al. (1977) and 9 and 4.6 cm by Vallée (1987). Using these three frequencies, Vallée (1987) derives an electron temperature and density of 100 K and 1 cm^{-3}, respectively, for the C region that lies between the molecular cloud and the H region of W40. The high spatial and spectral resolution observations by Vallée (1987), at 4.3 arcmin and 2.7 km s^{-1}, respectively, show that the C line is actually ~ 6 km s^{-1} away from its rest velocity, at

6.5 ± 0.2 km s^{-1}, and at the same velocity as the CO molecular cloud, 6.7 km s^{-1} (Blitz et al. 1982). The difference between the H and C velocities suggests that the H gas originates from the edge of the C region (Vallée 1987), in what is called a *blister* model of the region.

He and C RRLs are detected along the Galactic plane in the $\ell = 20°$ to $44°$ region. Even though they have low signal-to-noise ratio further investigation and analysis should provide a statistical measure of the ionised helium abundance along the Galactic plane.

7

Conclusions and future work

In this Chapter I give an overview and summary of the results from this work, followed by the plans for the future of this project.

7.1 Overview of the results and conclusions

The main goal of this project is to estimate the free-free emission on the Galactic plane using RRLs from the HIPASS/ZOA survey. This survey contains three RRLs which can be averaged to provide a high sensitivity map of the RRL emission at an angular resolution of 14.8 arcmin. The velocity resolution of 20 km s^{-1} is sufficient to be able to identify the free-free emission from the Local, Sagittarius and Scutum spiral arms.

The data cube centred at $(\ell, b) = (40°, 0°)$ was used to illustrate the viability of such an investigation and has demonstrated that the 1.4 GHz ZOA survey is of sufficient sensitivity to be able to provide a map of free-free emission on the Galactic plane in this longitude range. An important upgrade on the data analysis was the inclusion of a new bandpass algorithm and the combination of ZOA and HIPASS data to correct for the zero levels on the Galactic plane. This resulted in a major improvement of the final spectra. The ZOA+HIPASS combined datacubes and corresponding RRL line integral maps covering ℓ from 20° to 44° and $|b| \leq 4°$ were reduced using the upgraded pipeline.

In order to convert the RRL line integral to a free-free brightness temperature it is necessary to have a value of the electron temperature T_e. Using the HIPASS/ZOA continuum and line data I was able to calculate the electron temperature for 16 H regions from the survey and to derive the T_e variation with Galactocentric radius. I found agreement with previous results (Shaver et al. 1983; Paladini et al. 2004) that have a larger longitude coverage. The derived T_e variation was used to convert the RRL line integral to free-free brightness and to obtain the first direct measurement of the free-free emission on the Galactic plane between $\ell = 20°$ and 44°. When this map is subtracted from the continuum map, the synchrotron emission is derived for this region of the Galaxy, at 1.4 GHz. The latitude distribution of the synchrotron emission was used to show that the electron temperature of the diffuse ionised gas is similar to that of the individual H regions, with a mean of $\sim$ 6000 K on the Galactic plane. The synchrotron distribution appears to have a narrow component, detected for the first time at this frequency clear of the free-free emission. It has FWHM of $\sim$ 2°, presumably arising from the SNRs on the Galactic plane.

Using the source extractor algorithm SExtractor on the synchrotron map, I was able to detect 23 well-known SNRs listed in the Green (2009a) catalogue, plus two SNR candidates and one recently re-identified.

A list of H regions was extracted from the free-free map with SExtractor. The flux densities given for the present 14.8 arcmin survey of H regions are accurate to the 10 per cent level. The list of H regions is used to derive their contribution to the total free-free emission in this region of the Galaxy, of $\sim$ 30%. The individual H regions have a latitude distribution with about half the width of the total free-free distribution, $\sim$ 0°.5 at half power. This can be converted into a z-distribution for the H emission at known distances and is consistent with previous results (Reynolds 1991; Bronfman et al. 2000) on the distribution of OB stars and the width of the thin disk from Dispersion Measures.

The clear determination of the free-free emission in the ℓ-range 20° to 44°, allows the investigation of the anomalous microwave emission in this section of the Galactic

plane by using WMAP data along with the 408 MHz synchrotron template. I have shown that the excess (above the free-free and synchrotron) emission has the same latitude distribution as the 100 μm far-infrared emission. This is expected for a dust-correlated component of emission. The lower WMAP frequencies (23 and 33 GHz) fit a spinning dust model for very small dust grains, whose emission is about 58 per cent of the total and 1.5 of the free-free emission, in this longitude range. The highest WMAP frequency (91 GHz) emission includes the long wavelength tail of the thermal emission from large dust grains which is three times the free-free emission. The 61 GHz emission is composed of roughly equal amounts from both the free-free and thermal dust mechanisms.

7.2 Future work

7.2.1 Mapping the full ZOA RRL survey

Using the upgraded RRL pipeline described in Chapter 5, the RRL data can be readily reduced to produce spectral cubes with low noise and stable baselines for the brightest regions. I reduced each of the 27 ZOA zones and combined with the respective HIPASS data, resulting in a RRL cube covering the Galactic plane between $\ell = 196^\circ \rightarrow 52^\circ$. Fig. 7.1 shows the line integral for the inner Galaxy region, from $\ell = -50^\circ$ to 50°. The preliminary map is obtained using the task , set to calculate the integral 40 km s^{-1} either side of the line after rejecting spectra that are below 15 mJy/beam. Even without a careful analysis and correction of the spectral baselines, this map shows high significance detection of RRL emission from individual H regions and from extended diffuse emission.

A deeper and thorough analysis, similar to that described in Chapter 5 for each of the three zones under study, is needed for this larger area in order to recover the weaker signals away from the Galactic plane and estimate the free-free emission throughout the inner Galaxy.

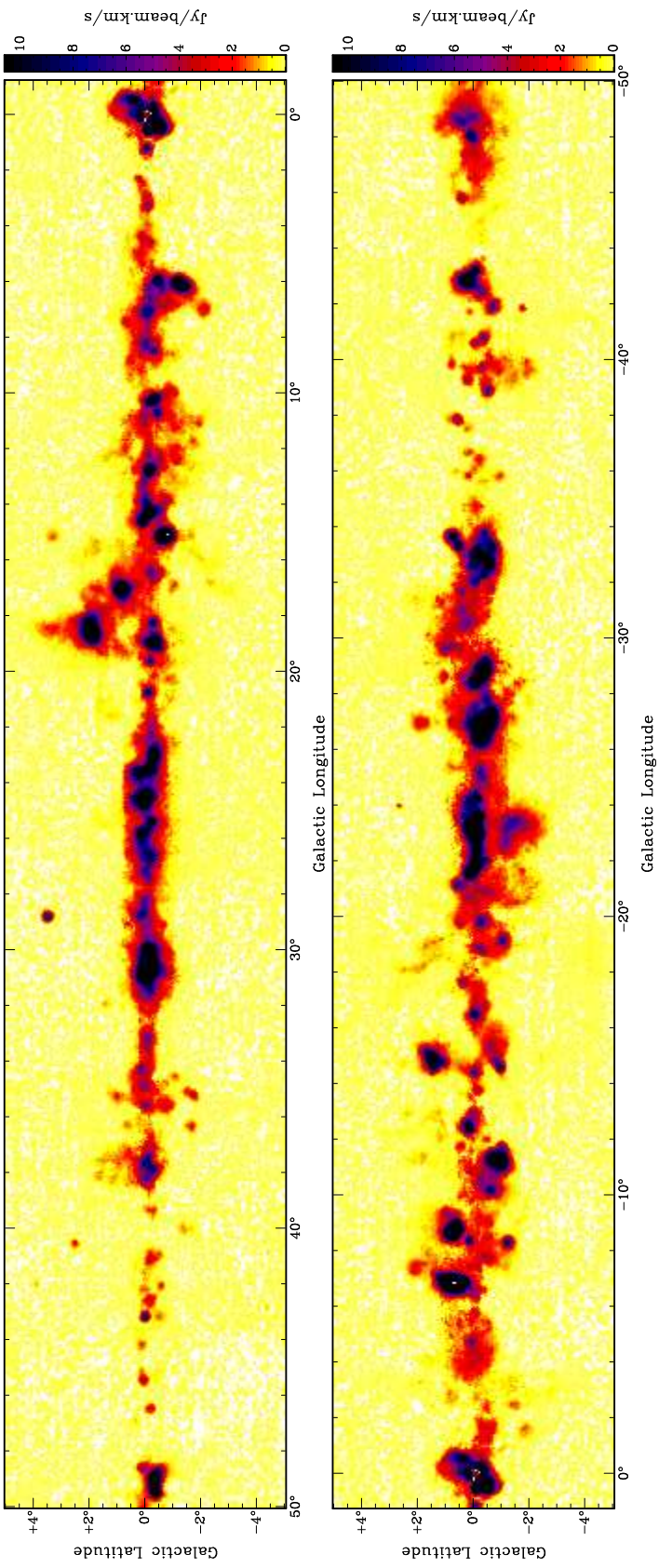

Figure 7.1: Preliminary maps of RRL integrated emission (in units of Jy/beam km s^{-1}) from the combination of ZOA and HIPASS data for the region $\ell = -50^\circ$ to 50° and $|b| \leq 5^\circ$.

7.2.2 The distribution of ionised gas

The present RRL survey provides unique information on the velocity of the diffuse emission. Figure 7.2 shows the velocity at peak of the RRL spectra on the Galactic plane between $\ell = -50°$ and 50°. It shows a clear gradient as expected, with positive velocities increasing from ~ 50 km s^{-1} at $\ell = 50°$ to ~ 100 km s^{-1} at $\ell \approx 30°$, where the line of sight passes through the Scutum spiral arm, and then becomes negative in the fourth quadrant of the Galaxy. This larger area will allow the radial distribution of the diffuse gas to be better determined and compared with the distribution of H regions given by the Paladini et al. (2003) and the Bania et al. (2010) samples, shown in Fig. 7.3. However, as described in Section 6.1.5 some spectra have more than one velocity component, which are not straighforward to separate due to the spectral resolution of this survey. In order to improve the Galactic radius calculation in Fig. 6.20, a careful analysis and separation of the velocity components has to be performed.

The velocity information of the ionised gas is of great importance for the Galaxy inversion models (Paladini et al. 2007; Planck Collaboration et al. 2011b). These aim at constructing the 3D distribution of the various components of the ISM in the Galaxy and determining the properties of dust and gas in the different environments in the Milky Way. At the present these models lack of information on the diffuse ionised gas distribution.

7.2.3 Other regions of interest at intermediate latitudes

The large-scale diffuse ionised gas at intermediate and high latitudes is observed in Hα since RRLs are too weak to be detected. However, bright H regions and ionised extended features in the local Gould's Belt system have been observed in RRLs, such as Barnard's Arc (Gaylard 1984). For an electron temperature of 7000 K at 1.4 GHz, 1 R of Hα line intensity corresponds to 3.87 mK of free-free brightness temperature (Section 2.1.3). From equation (2.39) it follows that in those conditions and for a typical RRL of width 25 km s^{-1}, its line temperature is ~ 1.4 per cent of the continuum.

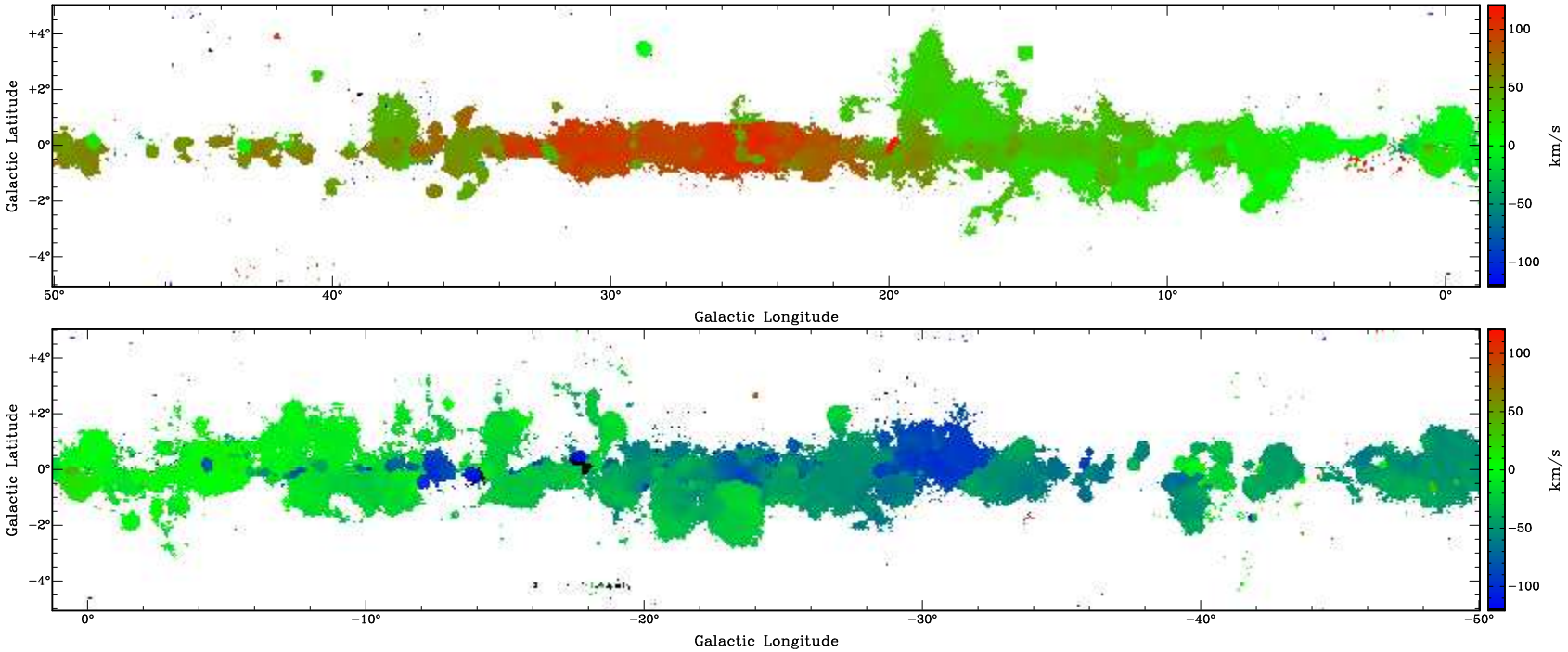

Figure 7.2: Preliminary maps of the peak RRL velocity (in units of km s^{-1}) from the combined ZOA+HIPASS RRL data cube for the region $\ell = -50^\circ$ to 50° and $|b| \leq 5^\circ$.

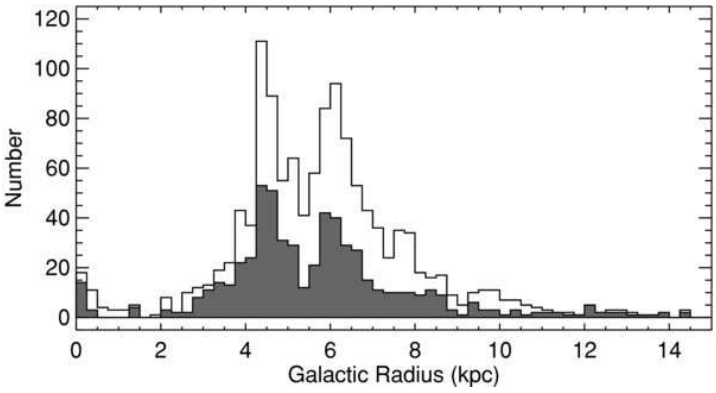

Figure 7.3: Radial distribution of Galactic H regions from the sample of 602 new nebulae found by Bania et al. (2010) (filled histogram) combined with the Paladini et al. (2003) sample (open histogram). From Bania et al. (2010).

Therefore, the Barnard's Arc region which is $\sim$ 200 R in Hα, should be detected in RRLs with a temperature $\sim$ 10 mK. This region of the sky at $b \approx -20^{\circ}$ is not covered by the ZOA survey, which combined with the HIPASS survey renders spectral cubes with a typical noise level per channel of 3 mK (Section 5.2.1). Nevertheless, a line of $T_{\rm L} = 10$ mK can still be detected using HIPASS data only, which is twice the noise of the ZOA data, so with a rms noise per channel of $\sim$ 6 mK.

There is an increasing interest on the fraction of scattered Hα light at high latitudes. Recent results by Witt et al. (2010) suggest that about half of the total Hα intensity observed in many diffuse, translucent and dark dust clouds is due to scattering of Hα photons present in the Galatic interstellar radiation field that originate in emission regions elsewhere. This explains the excess of surface brightness in Hα light, compared to the surrounding sky, that has been observed toward high latitude dust structures (Mattila et al. 2007). The free-free emission estimated from RRLs at intermediate latitude ionised regions can be used to compare with Hα measurements to constrain the amount of dust and scattered light.

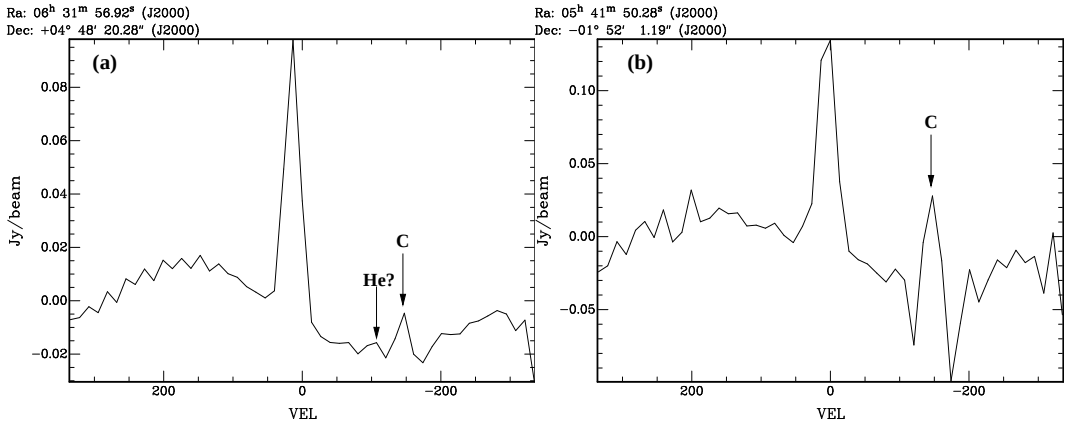

Figure 7.4: Average spectra for the (a) Rosette and (b) Orion B nebulae, showing carbon RRLs at . Note the strong C RRL from the Orion B region, detected in the curved and noisy baseline. The same curvature is seen in the Rosette nebula's spectrum, but with a lower rms due to the contribution of ZOA data.

7.2.4 Helium and Carbon Lines

Using the HIPASS and ZOA individual scans in , the $30° \times 30°$ RRL datacube centred at (RA, δ) = ($5^{\rm h}.87, 2°.00$) was reduced. This covers the Orion A and B regions, Bernard's arc and the Rosette nebula and shows high significance RRL detections. Barnard's arc is seen with $T_{\rm L} \approx 20 - 30$ mK. Fig. 7.4 shows the spectra for the Rosette nebula G206.2-2.1, which is within the ZOA survey coverage, and for the Orion B nebula G205.5-16.4. Both spectra show carbon RRLs, at ~ -150 km s^{-1} away from the hydrogen line, as expected. It is difficult to estimate the C RRL intensity which is seen to vary relative to the H RRL for the two examples shown here. Since there is no significant shift in velocity, the C line is likely to be amplified by maser emission by the continuum emission from the associated H region that lies behind the C region. In order to study the physical properties of the C region, observations of C RRLs over a range of frequencies are needed to compare with models.

The HIPASS survey will allow the investigation of C/He RRLs on bright H features at intermediate latitudes whereas the deeper ZOA survey along the Galactic plane will also provide information on the C/He RRLs from the the diffuse ionised gas in the inner Galaxy.

7.2.5 A full-sky template of free-free emission

With the advent of large-area Hα surveys, such as WHAM and SHASSA, templates for the free-free emission at high and intermediate latitudes became available (Dickinson et al. 2003; Finkbeiner 2003). Before the Hα data can be converted into a free-free brightness temperature, they have to be corrected for dust absorption. At $|b| \lesssim 5^\circ$ this correction breaks down and accordingly the Hα surveys cannot be used for this purpose along the Galactic plane. RRLs in contrast to Hα give a direct measure of the free-free with no dust absorption or contamination, thus can be used to complement the Hα templates on the Galactic plane.

In Section 6.5.1 the combination of Hα and RRL data for the region $\ell = 20^\circ$ to 44° gives an indicative value of the effective dust in the line of sight that is absorbing the optical line. More importantly, it shows that the RRL prediction of the free-free agrees with that of the Hα at $b \approx 4^\circ$. A full-sky free-free template is the ultimate goal of this project. For that each ZOA $8^\circ \times 8^\circ$ RRL datacube still has to be carefully analysed in order to recover the weak signals away from the Galactic plane, at $|b| = 2^\circ - 4^\circ$.

A full-sky free-free template will be useful for CMB experiments such as *Planck*, in particular for component separation. It is also important to understand the synchrotron emisson for the first time on the Galactic plane. A clean synchrotron map at 1.4 GHz helps to define the spectral index variation, namely to constrain the observed turnover in spectral index (Banday et al. 2003; Davies et al. 2006).

References

Ali-Haïmoud, Y., Hirata, C. M., & Dickinson, C. 2009. A refined model for spinning dust radiation. MNRAS, 395, 1055

Altenhoff, W. J., Downes, D., Goad, L., Maxwell, A., & Rinehart, R. 1970. Surveys of the galactic plane at 1.414, 2.695 and 5.000 GHz. A&AS, 1, 319

Altenhoff, W. J., Mezger, P. G., Wendker, H., & Westerhout, G. 1960. . Veröff Sternwärte Bonn, 59, 48

Alves, M. I. R., Davies, R. D., Dickinson, C., Davis, R. J., Auld, R. R., Calabretta, M., & Staveley-Smith, L. 2010. Diffuse radio recombination line emission on the Galactic plane between l = 36° and 44°. MNRAS, 405, 1654

Anantharamaiah, K. R. 1985a. A survey of recombination line emission from the Galactic plane at 325 MHz. Journal of Astrophysics and Astronomy, 6, 177

——. 1985b. Low density ionized gas in the inner Galaxy - Interpretation of recombination line observations at 325 MHz. Journal of Astrophysics and Astronomy, 6, 203

——. 1986. On the origin of the Galactic ridge recombination lines. Journal of Astrophysics and Astronomy, 7, 131

Balick, B., Gammon, R. H., & Hjellming, R. M. 1974. The structure of the Orion nebula. PASP, 86, 616

Ball, J. A., Cesarsky, D., Dupree, A. K., Goldberg, L., & Lilley, A. E. 1970. Detection and Identification of Recombination Lines from an H Region. ApJ, 162, L25

Banday, A. J., Dickinson, C., Davies, R. D., Davis, R. J., & Górski, K. M. 2003. Reappraising foreground contamination in the COBE-DMR data. MNRAS, 345, 897

Bania, T. M., Anderson, L. D., Balser, D. S., & Rood, R. T. 2010. The Green Bank Telescope Galactic H Region Discovery Survey. ApJ, 718, L106

Barnes, D. G. et al. 2001. The H Parkes All Sky Survey: southern observations, calibration and robust imaging. MNRAS, 322, 486

Bennett, C. L. et al. 2003. First-Year Wilkinson Microwave Anisotropy Probe (WMAP) Observations: Preliminary Maps and Basic Results. ApJS, 148, 1

——. 1992. Preliminary separation of galactic and cosmic microwave emission for the COBE Differential Microwave Radiometer. ApJ, 396, L7

Bertin, E., & Arnouts, S. 1996. SExtractor: Software for source extraction. A&AS, 117, 393

Blitz, L., Fich, M., & Stark, A. A. 1982. Catalog of CO radial velocities toward galactic H regions. ApJS, 49, 183

Broadbent, A., Osborne, J. L., & Haslam, C. G. T. 1989. A technique for separating the galactic thermal radio emission from the non-thermal component by means of the associated infrared emission. MNRAS, 237, 381

Brocklehurst, M., & Salem, M. 1977. Radio recombination lines from H^+ regions and cool interstellar clouds: computation of the bn factors. Computer Physics Communications, 13, 39

Brocklehurst, M., & Seaton, M. J. 1972. On the interpretation of radio recombination line observations. MNRAS, 157, 179

Bronfman, L., Casassus, S., May, J., & Nyman, L.-Å. 2000. The radial distribution of OB star formation in the Galaxy. A&A, 358, 521

Bronfman, L., Cohen, R. S., Alvarez, H., May, J., & Thaddeus, P. 1988. A CO survey of the southern Milky Way - The mean radial distribution of molecular clouds within the solar circle. ApJ, 324, 248

Brown, M. L. et al. 2009. Improved Measurements of the Temperature and Polarization of the Cosmic Microwave Background from QUaD. ApJ, 705, 978

Caswell, J. L., & Haynes, R. F. 1987. Southern H regions - an extensive study of radio recombination line emission. A&A, 171, 261

Cersosimo, J. C., & Magnani, L. 1990. Non-LTE effects in radio recombination lines from H regions at 18 CM. A&A, 239, 287

Cersosimo, J. C., & Onello, J. S. 1991. Radio recombination lines from diffuse interstellar gas in the Galaxy. ApJ, 370, 225

Cesarsky, C. J., & Cesarsky, D. A. 1971. Interpretation of Recombination-Line Emission from the Interstellar Medium. ApJ, 169, 293

Churchwell, E., Mezger, P. G., & Huchtmeier, W. 1974. Helium Abundance in Galactic H Regions. A&A, 32, 283

Churchwell, E., & Walmsley, C. M. 1975. Are the electron temperatures of H regions a function of galactic radius. A&A, 38, 451

Cohen, A. S., Lane, W. M., Cotton, W. D., Kassim, N. E., Lazio, T. J. W., Perley, R. A., Condon, J. J., & Erickson, W. C. 2007. The VLA Low-Frequency Sky Survey. AJ, 134, 1245

Condon, J. J., Cotton, W. D., Greisen, E. W., Yin, Q. F., Perley, R. A., Taylor, G. B., & Broderick, J. J. 1998. The NRAO VLA Sky Survey. AJ, 115, 1693

Davies, R. D., Dickinson, C., Banday, A. J., Jaffe, T. R., Górski, K. M., & Davis, R. J. 2006. A determination of the spectra of Galactic components observed by the Wilkinson Microwave Anisotropy Probe. MNRAS, 370, 1125

Davies, R. D., Watson, R. A., & Gutierrez, C. M. 1996. Galactic synchrotron emission at high frequencies. MNRAS, 278, 925

de Pree, C. G., Mehringer, D. M., & Goss, W. M. 1997. Multifrequency, High-Resolution Radio Recombination Line Observations of the Massive Star-forming Region W49A. ApJ, 482, 307

Delhaye, J. 1965, in Stars and Stellar System, Vol. 5, Galactic Structure, ed. A. Blaauw

& M. Schmidt, Chicago: University of Chicago Press, 61

Desert, F., Boulanger, F., & Puget, J. L. 1990. Interstellar dust models for extinction and emission. A&A, 237, 215

Dickinson, C., Davies, R. D., & Davis, R. J. 2003. Towards a free-free template for CMB foregrounds. MNRAS, 341, 369

Donley, J. L. et al. 2005. The H Parkes Zone of Avoidance Survey: The Northern Extension. AJ, 129, 220

Downes, D., Wilson, T. L., Bieging, J., & Wink, J. 1980. H110-alpha and H2CO survey of galactic radio sources. A&AS, 40, 379

Draine, B. T., & Lazarian, A. 1998. Diffuse Galactic Emission from Spinning Dust Grains. ApJ, 494, L19

——. 1999. Magnetic Dipole Microwave Emission from Dust Grains. ApJ, 512, 740

Draine, B. T., & Li, A. 2001. Infrared Emission from Interstellar Dust. I. Stochastic Heating of Small Grains. ApJ, 551, 807

Dravskikh, Z. V., & Dravskikh, A. F. 1964. . Astron. Tsirk, 282, 2

Dupree, A. K. 1974. Carbon Recombination Lines and Interstellar Hydrogen Clouds. ApJ, 187, 25

Einstein, A. 1916. Strahlungs-Emission und Absorption nach der Quantentheorie. Deutsche Physikalische Gesellschaft, 18, 318

Fich, M., Blitz, L., & Stark, A. A. 1989. The rotation curve of the Milky Way to 2 R(0). ApJ, 342, 272

Field, G. B., Goldsmith, D. W., & Habing, H. J. 1969. Cosmic-Ray Heating of the Interstellar Gas. ApJ, 155, L149

Finkbeiner, D. P. 2003. A Full-Sky Hα Template for Microwave Foreground Prediction. ApJS, 146, 407

Finkbeiner, D. P., Davis, M., & Schlegel, D. J. 1999. Extrapolation of Galactic Dust Emission at 100 Microns to Cosmic Microwave Background Radiation Frequencies Using FIRAS. ApJ, 524, 867

Finkbeiner, D. P., Schlegel, D. J., Frank, C., & Heiles, C. 2002. Tentative Detection of Electric Dipole Emission from Rapidly Rotating Dust Grains. ApJ, 566, 898

Gaensler, B. M., Madsen, G. J., Chatterjee, S., & Mao, S. A. 2008. The Vertical Structure of Warm Ionised Gas in the Milky Way. Publications of the Astronomical Society of Australia, 25, 184

Gaustad, J. E., McCullough, P. R., Rosing, W., & Van Buren, D. 2001. A Robotic Wide-Angle Hα Survey of the Southern Sky. PASP, 113, 1326

Gaylard, M. J. 1984. Detection of the H 142-alpha line from the Barnard Loop. MNRAS, 211, 149

Georgelin, Y. M. 1975, PhD thesis, , Univ. Provence, Obs. de Marseille, (1975)

Georgelin, Y. M., & Georgelin, Y. P. 1976. The spiral structure of our Galaxy determined from H regions. A&A, 49, 57

Gillett, F. C., Forrest, W. J., & Merrill, K. M. 1973. 8 - 13-micron spectra of NGC 7027, BD +30 3639, and NGC 6572. ApJ, 183, 87

Gold, B. et al. 2011. Seven-year Wilkinson Microwave Anisotropy Probe (WMAP) Observations: Galactic Foreground Emission. ApJS, 192, 15

Goldberg, L. 1968, Theoretical intensities of recombination lines., ed. Goldberg, L.

Goldberg, L., & Dupree, A. K. 1967. Population of Atomic Levels by Dielectronic Recombination. Nature, 215, 41

Goldwire, Jr., H. C. 1968. Oscillator Strengths for Electric Dipole Transitions of Hydrogen. ApJS, 17, 445

Gordon, M. A. 1976. Radial-velocity corrections for earth motion. Methods of Experimental Physics, 12, 277

Gordon, M. A., Brown, R. L., & Gottesman, S. T. 1972. The Latitude Extent of Diffuse Ionization in the Galaxy. ApJ, 178, 119

Gordon, M. A., & Cato, T. 1972. A Longitude Survey of Radio Recombination Lines from the Diffuse Interstellar Medium. ApJ, 176, 587

Gordon, M. A., & Sorochenko, R. L., eds. 2009, Astrophysics and Space Science Library, Vol. 282, Radio Recombination Lines

Gottesman, S. T., & Gordon, M. A. 1970. Radio Recombination Lines from Diffuse Interstellar Gas. ApJ, 162, L93

Green, D. A. 2009a. A revised Galactic supernova remnant catalogue. Bulletin of the Astronomical Society of India, 37, 45

——. 2009b. Re-identification of G35.6-0.4 as a supernova remnant. MNRAS, 399, 177

Griem, H. R. 1967. Stark Broadening by Electron and Ion Impacts of NA Hydrogen Lines of Large Principal Quantum Number. ApJ, 148, 547

Haffner, L. M., Reynolds, R. J., & Tufte, S. L. 1999. WHAM Observations of Hα, [S II], and [N II] toward the Orion and Perseus Arms: Probing the Physical Conditions of the Warm Ionized Medium. ApJ, 523, 223

Haffner, L. M., Reynolds, R. J., Tufte, S. L., Madsen, G. J., Jaehnig, K. P., & Percival, J. W. 2003. The Wisconsin Hα Mapper Northern Sky Survey. ApJS, 149, 405

Hanson, M. M., Luhman, K. L., & Rieke, G. H. 2002. A Near-Infrared Survey of Radio-selected Ultracompact H Regions. ApJS, 138, 35

Hart, L., & Pedlar, A. 1976. A survey of radio recombination line emission from the galactic plane. MNRAS, 176, 547

Haslam, C. G. T., & Osborne, J. L. 1987. The infrared and radio-continuum emission of the Galactic disk. Nature, 327, 211

Haslam, C. G. T., Salter, C. J., Stoffel, H., & Wilson, W. E. 1982. A 408 MHz all-sky continuum survey. II - The atlas of contour maps. A&AS, 47, 1

Heiles, C., Koo, B., Levenson, N. A., & Reach, W. T. 1996a. Radio Recombination Lines from Inner Galaxy Diffuse Gas. I. High-Sensitivity Observations: He +/H + and Carbon. ApJ, 462, 326

Heiles, C., Reach, W. T., & Koo, B. 1996b. Radio Recombination Lines from Inner Galaxy Diffuse Gas. II. The Extended Low-Density Warm Ionized Medium and the "Worm-ionized Medium". ApJ, 466, 191

Helfand, D. J., Zoonematkermani, S., Becker, R. H., & White, R. L. 1992. Compact

radio sources near the Galactic plane. ApJS, 80, 211

Henning, P. A. et al. 2000. H -bright Galaxies in the Southern Zone of Avoidance. AJ, 119, 2686

Hill, J. K. 1977. Narrow radio recombination lines from ionization fronts. ApJ, 212, 692

Hinshaw, G. et al. 2009. Five-Year Wilkinson Microwave Anisotropy Probe Observations: Data Processing, Sky Maps, and Basic Results. ApJS, 180, 225

Hjellming, R. M., Gordon, C. P., & Gordon, K. J. 1969. Properties of Interstellar Clouds and the Inter-Cloud Medium. A&A, 2, 202

Hoglund, B., & Mezger, P. G. 1965. Hydrogen Emission Line $n_{110} \rightarrow n_{109}$: Detection at 5009 Megahertz in Galactic H Regions. Science, 150, 339

Hummer, D. G. 1988. A fast and accurate method for evaluating the nonrelativistic free-free Gaunt factor for hydrogenic ions. ApJ, 327, 477

Hummer, D. G., & Storey, P. J. 1987. Recombination-line intensities for hydrogenic ions. I - Case B calculations for H I and He II. MNRAS, 224, 801

Jarosik, N. et al. 2011. Seven-year Wilkinson Microwave Anisotropy Probe (WMAP) Observations: Sky Maps, Systematic Errors, and Basic Results. ApJS, 192, 14

Jones, A. P. 2009. Microwave emission from dust revisited. A&A, 506, 797

Kalberla, P. M. W. et al. 2010. GASS: The Parkes Galactic All-Sky Survey. II. Stray-Radiation Correction and Second Data Release. ArXiv e-prints

Kaplan, D. L., Kulkarni, S. R., Frail, D. A., & van Kerkwijk, M. H. 2002. Deep Radio, Optical, and Infrared Observations of SGR 1900+14. ApJ, 566, 378

Kardashev, N. S. 1959. On the Possibility of Detection of Allowed Lines of Atomic Hydrogen in the Radio-Frequency Spectrum. Soviet Astronomy, 3, 813

Kerr, F. J., & Lynden-Bell, D. 1986. Review of galactic constants. MNRAS, 221, 1023

Kilborn, V., Webster, R. L., & Staveley-Smith, L. 1999. HI mass function from HIPASS. Publications of the Astronomical Society of Australia, 16, 8

Kogut, A., Banday, A. J., Bennett, C. L., Gorski, K. M., Hinshaw, G., Smoot, G. F., & Wright, E. I. 1996. Microwave Emission at High Galactic Latitudes in the Four-Year DMR Sky Maps. ApJ, 464, L5

Koo, B., Kim, K., Lee, H., Yun, M., & Ho, P. T. P. 1996. The H Region Complex G5.48-0.24: Radio Continuum, H , and CO Observations. ApJ, 456, 662

Kovac, J. M., Leitch, E. M., Pryke, C., Carlstrom, J. E., Halverson, N. W., & Holzapfel, W. L. 2002. Detection of polarization in the cosmic microwave background using DASI. Nature, 420, 772

Krugel, E., & Tenorio-Tagle, G. 1978. The ionization of the interstellar medium by X-rays. A&A, 70, 51

Kurtz, S. 2005, in IAU Symposium, Vol. 227, Massive Star Birth: A Crossroads of Astrophysics, ed. R. Cesaroni, M. Felli, E. Churchwell, & M. Walmsley, 111–119

Kurtz, S. E., Watson, A. M., Hofner, P., & Otte, B. 1999. Ultracompact H Regions with Extended Radio-Continuum Emission. ApJ, 514, 232

Lang, K. R. 1974, Astrophysical formulae: A compendium for the physicist and astro-

physicist, ed. Lang, K. R.

Larson, D. et al. 2011. Seven-year Wilkinson Microwave Anisotropy Probe (WMAP) Observations: Power Spectra and WMAP-derived Parameters. ApJS, 192, 16

Leitch, E. M., Readhead, A. C. S., Pearson, T. J., & Myers, S. T. 1997. An Anomalous Component of Galactic Emission. ApJ, 486, L23

Lilley, A. E., Menzel, D. H., Penfield, H., & Zuckerman, B. 1966a. Detection of Hydrogen Emission Lines $n_{159} \rightarrow n_{158}$ and $n_{157} \rightarrow n_{156}$ in Galactic H Regions. Nature, 209, 468

Lilley, A. E., Palmer, P., Penfield, H., & Zuckerman, B. 1966b. Radio Astronomical Detection of Helium. Nature, 211, 174

Lockman, F. J. 1976. A survey of ionized hydrogen in the plane of the galaxy. ApJ, 209, 429

——. 1989. A survey of radio H regions in the northern sky. ApJS, 71, 469

Lockman, F. J. 1990, in Astrophysics and Space Science Library, Vol. 163, IAU Colloq. 125: Radio Recombination Lines: 25 Years of Investigation, ed. M. A. Gordon & R. L. Sorochenko, 225

Lockman, F. J., Blundell, K. M., & Goss, W. M. 2007. The distance to SS433/W50 and its interaction with the interstellar medium. MNRAS, 381, 881

Lockman, F. J., & Brown, R. L. 1975. The radio recombination line spectrum of Orion A - Observations and analysis. ApJ, 201, 134

Lockman, F. J., Pisano, D. J., & Howard, G. J. 1996. Detection of 130 "Diffuse" Galactic H Regions. ApJ, 472, 173

Longair, M. S. 1994, High energy astrophysics. Vol.2: Stars, the galaxy and the interstellar medium, ed. M. S. Longair

Madsen, G. J., Reynolds, R. J., & Haffner, L. M. 2006. A Multiwavelength Optical Emission Line Survey of Warm Ionized Gas in the Galaxy. ApJ, 652, 401

Massardi, M. et al. 2011. The Australia Telescope 20 GHz (AT20G) Survey: analysis of the extragalactic source sample. MNRAS, 412, 318

Mather, J. C., Fixsen, D. J., Shafer, R. A., Mosier, C., & Wilkinson, D. T. 1999. Calibrator Design for the COBE Far-Infrared Absolute Spectrophotometer (FIRAS). ApJ, 512, 511

Mathis, J. S., Rumpl, W., & Nordsieck, K. H. 1977. The size distribution of interstellar grains. ApJ, 217, 425

Matthews, H. E., Pedlar, A., & Davies, R. D. 1973. Radio recombination line emissionfrom the galactic plane. MNRAS, 165, 149

Mattila, K., Juvela, M., & Lehtinen, K. 2007. Galactic Dust Clouds Are Shining in Scattered Hα Light. ApJ, 654, L131

Menzel, D. H. 1968. Oscillator Strengths for High-level Transitions in Hydrogen. Nature, 218, 756

——. 1969. Osciliator Strengths, f, for High-Level Transitions in Hydrogen. ApJS, 18, 221

Meyer, M. J. et al. 2004. The HIPASS catalogue - I. Data presentation. MNRAS, 350, 1195

Mezger, P. G., Altenhoff, W., Schraml, J., Burke, B. F., Reifenstein, III, E. C., & Wilson, T. L. 1967. A New Class of Compact H Regions Associated with OH Emission Sources. ApJ, 150, L157

Mezger, P. G., & Henderson, A. P. 1967. Galactic H Regions. I. Observations of Their Continuum Radiation at the Frequency 5 GHz. ApJ, 147, 471

Mezger, P. G., & Smith, L. F. 1976, in Stars and Galaxies from Observational Points of View, ed. E. K. Kharadze, 369–382

Mezger, P. O. 1978. The Galactic Extended Low-density HII Region and Its Relation to Star Formation and Diffuse IR Emission. A&A, 70, 565

Miville-Deschênes, M., & Lagache, G. 2005. IRIS: A New Generation of IRAS Maps. ApJS, 157, 302

Murphy, E. J. et al. 2010. The Detection of Anomalous Dust Emission in the Nearby Galaxy NGC 6946. ApJ, 709, L108

Nordgren, T. E., Cordes, J. M., & Terzian, Y. 1992. The scale height of the galactic free electron cloud. AJ, 104, 1465

Onello, J. S., & Phillips, J. A. 1995. Radio Recombination Line Observations of Partially Ionized Gas in Galactic H II Regions. ApJ, 448, 727

Oster, L. 1961. Emission, absorption, and conductivity of a fully ionized gas at radio frequencies. Rev. Mod. Phys., 33, 525

Osterbrock, D. E. 1989, Astrophysics of gaseous nebulae and active galactic nuclei, ed. Osterbrock, D. E.

Paladini, R., Burigana, C., Davies, R. D., Maino, D., Bersanelli, M., Cappellini, B., Platania, P., & Smoot, G. 2003. A radio catalog of Galactic HII regions for applications from decimeter to millimeter wavelengths. A&A, 397, 213

Paladini, R., Davies, R. D., & DeZotti, G. 2004. Spatial distribution of Galactic HII regions. MNRAS, 347, 237

Paladini, R., De Zotti, G., Davies, R. D., & Giard, M. 2005. Analysis of the thin layer of Galactic warm ionized gas in the range $20^\circ < \ell < 30^\circ$, $-1.5^\circ < b < 1.5^\circ$. MNRAS, 360, 1545

Paladini, R., Montier, L., Giard, M., Bernard, J. P., Dame, T. M., Ito, S., & Macias-Perez, J. F. 2007. A broadband study of galactic dust emission. A&A, 465, 839

Palmer, P., Zuckerman, B., Penfield, H., & Lilley, A. E. 1967. Detection of a New Microwave Spectral Line. Nature, 215, 40

Pankonin, V., Walmsley, C. M., Wilson, T. L., & Thomasson, P. 1977. A study of the partially ionized medium in the vicinity of the H regions NGC 2024 and W 3. A&A, 57, 341

Penzias, A. A., & Wilson, R. W. 1965. A Measurement of Excess Antenna Temperature at 4080 Mc/s. ApJ, 142, 419

Petuchowski, S. J., & Bennett, C. L. 1993. Galactic fine-structure lines - Morphologies of the warm ionized interstellar medium. ApJ, 405, 591

Pikelner, S. B. 1967. Heating of the Interstellar Gas by Subcosmic Rays, and the Formation of Clouds. AZh, 44, 915

Planck Collaboration et al. 2011a. Planck Early Results: Dust in the diffuse interstellar

medium and the Galactic halo. ArXiv e-prints, 1101.2036

——. 2011b. Planck Early Results: Properties of the interstellar medium in the Galactic plane. ArXiv e-prints, 1101.2032

——. 2011c. Planck Early Results: Statistical properties of extragalactic radio sources in the Planck Early Release Compact Source Catalogue. ArXiv e-prints, 1101.2044

——. 2011d. Planck Early Results: New Light on Anomalous Microwave Emission from Spinning Dust Grains. ArXiv e-prints, 1101.2031

Putman, M. E. et al. 2002. HIPASS High-Velocity Clouds: Properties of the Compact and Extended Populations. AJ, 123, 873

Putman, M. E., & Gibson, B. K. 1999. First results from the Parkes Multibeam High-velocity Cloud Survey. Publications of the Astronomical Society of Australia, 16, 70

Putman, M. E. et al. 1998. Tidal disruption of the Magellanic Clouds by the Milky Way. Nature, 394, 752

Putman, M. E., Staveley-Smith, L., Freeman, K. C., Gibson, B. K., & Barnes, D. G. 2003. The Magellanic Stream, High-Velocity Clouds, and the Sculptor Group. ApJ, 586, 170

Quireza, C., Rood, R. T., Bania, T. M., Balser, D. S., & Maciel, W. J. 2006. The Electron Temperature Gradient in the Galactic Disk. ApJ, 653, 1226

Reed, B. C. 1997. The Sun's Displacement from the Galactic Plane: Limits from the Distribution of OB-Star Latitudes. PASP, 109, 1145

Reich, P., & Reich, W. 1988. Spectral index variations of the Galactic radio continuum emission - Evidence for a Galactic wind. A&A, 196, 211

Reich, W., Füerst, E., Haslam, C. G. T., Steffen, P., & Reif, K. 1984. A radio continuum survey of the Galactic Plane at 11 CM wavelength. I - The area L = 357.4 to 76 deg, B = -1.5 to +1.5 deg. A&AS, 58, 197

Reich, W., Füerst, E., Reich, P., & Reif, K. 1990a. A radio continuum survey of the Galactic Plane at 11 CM wavelength. II - The area L = 358-76 deg, B = -5 to 5 deg. III. A&AS, 85, 633

Reich, W., Reich, P., & Füerst, E. 1990b. The Effelsberg 21 CM radio continuum survey of the Galactic plane between L = 357 deg and L = 95.5 deg. A&AS, 83, 539

Reichardt, C. L. et al. 2009. High-Resolution CMB Power Spectrum from the Complete ACBAR Data Set. ApJ, 694, 1200

Reifenstein, E. C., Wilson, T. L., Burke, B. F., Mezger, P. G., & Altenhoff, W. J. 1970. A Survey of H109Hα Recombination Line Emission in Galactic HN Regions of the Northern Sky. A&A, 4, 357

Reynolds, R. J. 1985. The forbidden line of S II lambda 6716 in the galactic emission-line background. ApJ, 294, 256

——. 1991. Line integrals of N_E and n_E-squared at high Galactic latitude. ApJ, 372, L17

Reynolds, R. J., Haffner, L. M., & Tufte, S. L. 1999. Evidence for an Additional Heat Source in the Warm Ionized Medium of Galaxies. ApJ, 525, L21

Reynolds, R. J., Sterling, N. C., Haffner, L. M., & Tufte, S. L. 2001. Detection of [N II] λ5755 Emission from Low-Density Ionized Interstellar Gas. ApJ, 548, L221

Roelfsema, P. R., & Goss, W. M. 1992. High resolution radio recombination line observations. A&A Rev., 4, 161

Rohlfs, K., & Wilson, T. L. 2000, Tools of radio astronomy, ed. Rohlfs, K. & Wilson, T. L.

Salem, M., & Brocklehurst, M. 1979. A table of departure coefficients from thermodynamic equilibrium b_n factors for hydrogenic ions. ApJS, 39, 633

Scaife, A. M. M. et al. 2009. AMI observations of Lynds dark nebulae: further evidence for anomalous cm-wave emission. MNRAS, 400, 1394

——. 2010. Microwave observations of spinning dust emission in NGC6946. MNRAS, 406, L45

Schlegel, D. J., Finkbeiner, D. P., & Davis, M. 1998. Maps of Dust Infrared Emission for Use in Estimation of Reddening and Cosmic Microwave Background Radiation Foregrounds. ApJ, 500, 525

Schmidt, M. 1965, in Galactic Structure, ed. A. Blaauw & M. Schmidt, 513

Seaton, M. J. 1964. Recombination spectra, III. MNRAS, 127, 177

Sejnowski, T. J., & Hjellming, R. M. 1969. The General Solution of the b_n Problem for Gaseous Nebulae. ApJ, 156, 915

Shaver, P. A. 1976. Interpretation of low-frequency recombination line observations of the interstellar medium. A&A, 49, 1

——. 1979. Pressure broadening of radio recombination lines from multiple-component H regions. A&A, 78, 116

——. 1980a. Accurate electron temperatures from radio recombination lines. A&A, 91, 279

——. 1980b. Why is observable radio recombination line emission from galactic H regions always close to LTE. A&A, 90, 34

Shaver, P. A., McGee, R. X., Newton, L. M., Danks, A. C., & Pottasch, S. R. 1983. The galactic abundance gradient. MNRAS, 204, 53

Smoot, G. F. et al. 1992. Structure in the COBE differential microwave radiometer first-year maps. ApJ, 396, L1

Sorochenko, R., L., & Borozich, E. V. 1965. . Dokl. Akad. Nauk SSSR, 163, 603

Spitzer, L. 1998, Physical Processes in the Interstellar Medium, ed. Spitzer, L.

Spitzer, Jr., L., & Tomasko, M. G. 1968. Heating of H Regions by Energetic Particles. ApJ, 152, 971

Staveley-Smith, L. et al. 1998. New H -detected Galaxies in the Zone of Avoidance. AJ, 116, 2717

Staveley-Smith, L., Kim, S., Calabretta, M. R., Haynes, R. F., & Kesteven, M. J. 2003. A new look at the large-scale H structure of the Large Magellanic Cloud. MNRAS, 339, 87

Staveley-Smith, L. et al. 1996. The Parkes 21 CM multibeam receiver. Publications of the Astronomical Society of Australia, 13, 243

Stil, J. M. et al. 2006. The VLA Galactic Plane Survey. AJ, 132, 1158

Storey, P. J., & Hummer, D. G. 1995. Recombination line intensities for hydrogenic ions-IV. Total recombination coefficients and machine-readable tables for Z=1 to 8. MNRAS, 272, 41

Sun, X. H., Reich, W., Han, J. L., Reich, P., Wielebinski, R., Wang, C., & Müller, P. 2011. A Sino-German λ6 cm polarization survey of the Galactic plane. III. The region from 10° to 60° longitude. A&A, 527, A74

Sunyaev, R. A., & Zeldovich, Y. B. 1970. Small-Scale Fluctuations of Relic Radiation. Ap&SS, 7, 3

Taylor, J. H., & Cordes, J. M. 1993. Pulsar distances and the galactic distribution of free electrons. ApJ, 411, 674

Todorović, M. et al. 2010. A 33-GHz Very Small Array survey of the Galactic plane from ℓ = 27° to 46°. MNRAS, 406, 1629

Vallée, J. P. 1987. The warm C II region between the hot ionized region S 64 = W 40 and the cold molecular cloud G 28.74 + 3.52. A&A, 178, 237

Valls-Gabaud, D. 1998. Cosmological applications of Hα surveys. Publ. Astron. Soc. Aust., 15, 111

van de Hulst, H. C. 1945. . Nederladsch Tidjischrift voor Naturkunde, 11, 230

Verschuur, G. L., & Kellermann, K. I. 1988, Galactic and extra-galactic radio astronomy, ed. G. L. Verschuur & K. I. Kellermann

Walmsley, C. M. 1990. Level populations for millimeter recombination lines. A&AS, 82, 201

Walsh, A. J., Burton, M. G., Hyland, A. R., & Robinson, G. 1998. Studies of ultracompact HII regions - II. High-resolution radio continuum and methanol maser survey. MNRAS, 301, 640

Watson, R. A., Rebolo, R., Rubiño-Martín, J. A., Hildebrandt, S., Gutiérrez, C. M., Fernández-Cerezo, S., Hoyland, R. J., & Battistelli, E. S. 2005. Detection of Anomalous Microwave Emission in the Perseus Molecular Cloud with the COSMOSOMAS Experiment. ApJ, 624, L89

Williams, D. R. W. 1973. Studies of four regions for use as standards in 21 CM observations. A&AS, 8, 505

Wilson, T. L., Mezger, P. G., Gardner, F. F., & Milne, D. K. 1970. A Survey of H 109 α Recombination Line Emission in Galactic H Regions of the Southern Sky. A&A, 6, 364

Wink, J. E., Wilson, T. L., & Bieging, J. H. 1983. An H76-alpha survey of galactic H regions - Electron temperature and element gradients. A&A, 127, 211

Witt, A. N., Gold, B., Barnes, F. S., DeRoo, C. T., Vijh, U. P., & Madsen, G. J. 2010. On the Origins of the High-latitude Hα Background. ApJ, 724, 1551

Wong, O. I. et al. 2006. The Northern HIPASS catalogue - data presentation, completeness and reliability measures. MNRAS, 371, 1855

Wood, D. O. S., & Churchwell, E. 1989. Massive stars embedded in molecular clouds - Their population and distribution in the galaxy. ApJ, 340, 265

Wood, K., & Mathis, J. S. 2004. Monte Carlo photoionization simulations of diffuse

ionized gas. MNRAS, 353, 1126

Zubko, V., Dwek, E., & Arendt, R. G. 2004. Interstellar Dust Models Consistent with Extinction, Emission, and Abundance Constraints. ApJS, 152, 211

Zuckerman, B., & Ball, J. A. 1974. On Microwave Recombination Lines from H Regions. ApJ, 190, 35

Zwaan, M. A. et al. 2003. The 1000 Brightest HIPASS Galaxies: The H Mass Function and Ω_{HI}. AJ, 125, 2842